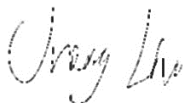# Low Temperature Synthesis and Characterisation of Novel Complex Carbide- and Boride-Based Materials

Submitted by Cheng Liu to the University of Exeter
as a thesis for the degree of
Doctor of Philosophy in Engineering
In May 2019

I certify that all material in this thesis which is not my own work has been identified and that no material has previously been submitted and approved for the award of a degree by this or any other University.

Signature: ……………………………………………………………..

Abstract

This thesis work dealt with four novel types of carbide- and boride-based materials which are considered to be candidate materials for a variety of important applications. They were synthesized by using a low temperature "universally" applicable molten salt synthesis technique, and characterised systematically.

In the first part of this thesis work, phase pure well-dispersed $Al_8B_4C_7$ particles with the average size of about 200 nm were synthesized from Al, B_4C and C after firing in NaCl-NaF at 1250 °C for 6 h. Under the optimal condition, Al initially diffused rapidly through the molten salt onto the surface of C to form Al_4C_3, and also diffused through the salt rapidly onto the surface of B_4C and reacted with it to form Al_3BC and AlB_2. B from the decomposition of AlB_2 and Al_3BC also slightly dissolved in the salt, diffused onto the surface of Al_4C_3 formed earlier (from the Al-C reaction and decomposition of Al_3BC), and reacted with it to form $Al_8B_4C_7$. Compared to the conventional synthesis techniques, the synthesis temperature in the present case was about 500 °C lower, which was attributable to the great accelerating-effect of the molten salt containing NaF.

In the second part of this thesis work, molybdenum aluminum boride (MoAlB) fine powders were synthesized from Al, B and Mo in molten NaCl. The effects of key processing parameters on the phase evolution and morphology of product powder were investigated and the relevant reaction mechanisms discussed. As-prepared MoAlB

1

particles exhibited three different morphologies: rounded particles (1~3 μm), plate-like particles (<5 μm in diameter) and columnar crystals with various lengths (up to 20 μm) and diameters (up to 5 μm), resultant from different reaction routes. The optimal synthesis condition for synthesis of phase pure MoAlB was: using 1. 4 times excessive Al and firing at 1000 °C for 6 h. This synthesis temperature was much lower than required by other synthesis techniques. Under the optimal condition, Mo initially reacted with Al and B, forming respectively Al_8Mo_3 and MoB which further reacted with excessive Al to form MoAlB and Al-rich Al-Mo phases (such as Al_4Mo). The latter further reacted with the residual B and form secondary MoAlB. The molten salt played an important role in the whole synthesis process by improving the mixing between the reactant species and facilitating their diffusion processes.

The third part of this thesis work deals with nanocarbon supported tungsten carbide nanocatalysts for hydrogen generation. By using WO_3, Mg and C as starting materials and KCl as reaction media, tungsten carbides (WC with W_2C) nanoparticles (< 5 nm) were *in-situ* formed/anchored on nanosized carbon black (CB) and carbon nanotube (CNT). Owing to this special hybrid structure, both the exposed surface area of active species and the electrical conductivity of the catalysts were increased effectively, making the catalysts perform considerably better in HER than pure WC and WC based catalysts prepared *via* other conventional routes. WC nanocrystals *in-situ* formed/anchored on CNTs showed small overpotential (90 mV), low Tafel slope (69 mV dec^{-1}), high current density (93.4 and 28 mA cm^{-2} at 200 and 300 mV, respectively) and excellent stability

2

(remaining stable even after 3000 cycles). Such a performance is one of the best among those of WC based electrocatalysts developed to date. We demonstrate here significantly improved HER performances of inexpensive tailored WC materials, along with a facile synthesis strategy which could be also readily extended to prepare a range of other types of mono-dispersed nanocatalysts for more potential applications.

In the final part of this thesis work, novel 2D SiC nanosheet (SNS), ZrC nanosheet (ZNS), and SiC- and ZrC-coated graphite nanoplatelets were successfully prepared at relatively low temperatures. The effects of processing parameters such as firing temperature, time, and salt on the reaction/synthesis processes were examined, and the relevant mechanisms proposed. In all the cases, Si or Zr slightly dissolved in the molten salt and diffused rapidly through it onto the surface of graphite nanoplatelet, and then reacted *in-situ* to form SiC or ZrC which retained the morphology and size of the original graphite nanoplatelet, i.e., a template growth mechanism had functioned in all the cases and the original graphite nanoplatelet acted as the template. In the initial stage, as no barrier layer was built up on the surface of the graphite nanoplatelet, so the reaction was rapid. However, with the enhancement in the reaction extent, more and more carbide product would be formed, leading to the formation of a carbide barrier layer the remaining graphite nanoplatelet. Then, the reaction process would be controlled by the diffusion process of the metal and/or carbon. Nevertheless, as the molten salt medium could improve the mixing between the metal and the graphite nanoplatelet, and accelerate the diffusion process of the metal dissolved in it, the overall reaction still remained very

3

rapid, as verified by the much lowered synthesis temperature, especially in the case of ZrC formation where Zr has a sufficiently "high" solubility in the molten salt (1250 and < 850 ºC respectively in the cases of SiC and ZrC formation). By controlling the ratio between the metal and graphite nanoplatelet, both carbide nanosheets and carbide-coated graphite nanoplatelet/graphene nanosheets could be readily synthesized.

4

Table of contents

7

9

Acknowledgements

I would like to express my sincere gratitude to the all those who offered me greatly valuable assistance during my PhD study.

My deepest gratitude goes first and foremost to Prof. Shaowei Zhang for his kind support, encouragement and guidance throughout my PhD time. His valuable suggestions on both academic and personal levels are priceless. He has walked me through all the stages of the writing of this thesis. Without his consistent and illuminating instruction, this thesis could not have reached its present form. I would also like to thank Prof. Yanqiu Zhu and Dr. Yongde Xia for their kind assistance allowing me to use some facilities in his lab.

I am also very grateful to the people in my research group: Dr. Wei Xie, Dr. Yan Wen, Prof. Liangxu Lin, Dr. Jianke Ye, Dr. Juntong Huang, Dr. Bao Ke, Dr. Zhaoping Hou, Dr. Donghai Ding and Dr. Benjun Cheng for sharing the knowledge and experience (especially Prof. Liangxu Lin and Dr. Yan Wen for XPS test/analyzing and instructions in Chapter Six). Special thanks to Dr. Hong Chang, Dr. Lesley Wears and Dr. Judith Bannerman for the technical support and help on the characterization work.

A special thanks to my parents, my wife and my children. I would never have been able to complete my PhD thesis without their companionship and encouragement. This dissertation is written for all of my family members.

List of figures

12

14

15

16

17

18

19

List of tables

Chapter 1. Introduction

Work of this thesis mainly dealt with low temperature synthesis and characterisation of complex carbide- and boride-based materials which have received a great deal of attention, especially in recent years. As working tools, four novel types of them (referred to as "target materials"), $Al_8B_4C_7$ (or Al_3BC_3), MoAlB, carbon nanotube (CNT) and carbon black (CB) supported WC/WC_2 nanoparticles, and SiC and ZrC coated multi-layered graphene/graphite nanoplatelets, were synthesized by using a modified "universally" applicable molten salt synthesis method, and characterised in detail.

1.1 Target materials investigated by this thesis work

The first two types of target materials, $Al_8B_4C_7$ (or Al_3BC_3) and MoAlB, are considered to be important ceramic materials for both structural and functional applications, because of their varieties of excellent properties. The former possesses excellent hydration resistance, high hardness, high melting point, relatively low density, low thermal expansion coefficient, good thermal conductivity, and excellent erosion and corrosion resistance [1-4]. These outstanding properties make it suitable for many important applications, e.g., in high temperature structural components, sintering processes (as a sintering agent) of some other high temperature ceramics such as SiC, ZrB_2 and B_4C [5-9], carbon-containing refractories (as an antioxidant) [4,10-13] and new generation nuclear reactors (as an absorber) [14]. The latter also exhibits several excellent properties,

23

e.g., good oxidation resistance, high compressive strength, high electrical and thermal conductivity, low thermal expansion coefficient and stability up to at least 1400 °C in an inert atmosphere [15-21].

The third type of target material investigated was tungsten carbide (WC or W_2C), belonging to the so-called ultra-high temperature ceramics family, with a melting point as high as around 3000 K [22]. WC has a high thermal conductivity, low coefficient of thermal expansion [23-24], high hardness [23-26] as well as similar electrical resistivity to some metals [23]. W_2C has a high hardness and electrical resistivity of 9 $\mu\Omega\cdot m$. The traditional application areas of tungsten carbide-based materials are mainly in cutting and mining tools, ammunitions, grinding media, and etc. One of the interesting applications of tungsten carbide-based materials explored recently is in electrochemical catalysis, in particular for hydrogen generation from water [27-36]. Nanosized tungsten carbide particles exhibited very high catalytic activity in hydrogen evolution reaction (HER), with an overpotential of 145 to 500 mv and tafel slope of 69 to 137 mV dec^{-1} [refs].

The fourth type of target material investigated was 2D carbide nanosheet/2D carbide coated graphene. These materials have unique morphologies and possess combined properties of carbon and carbide constituent materials, and so are regarded as a new class of materials potentially applicable to many areas, e.g., reinforced composites. Carbon based materials have high thermal conductivity, low thermal expansion coefficient, high

24

specific strength (carbon fiber) and non-wettability by molten metal and slag (especially graphite). On the other hand, carbide materials such as SiC and ZrC have high decomposition/melting point, high hardness, high mechanical strength, high thermal conductivity, low thermal expansion coefficient, excellent thermal shock resistance and good chemical inertness/resistance [23, 37-41].

The four types of target materials have been prepared previously by using various techniques/methodologies. In the case of $Al_8B_4C_7$/Al_3BC_3, the thermal reduction method and the direct reaction method were the most commonly used. By using Al or carbon as a reducing agent [42-45], boron containing oxides could be used as a boron source. With this method, inexpensive boron-containing oxides can be used to replace much more expensive boron or boron carbide (and sometimes aluminum). However, a high synthesis temperature is often required to complete the reactions, and some byproducts or intermediate phases such as Al_2O_3 and Al_4O_4C/Al_2OC could still remain in the final product powders which were heavily agglomerated together. Apart from this thermal reduction method, the direct reaction method was often used, in which case, a mixture of Al/B/C [46], $Al/B_4C/C$ [2-3,47-50] or Al_4C_3/B_4C [51] was used as starting materials. The synthesis/reaction process is much more straightforward than in the case of thermal reduction. However, excessive aluminum had to be used to compensate for its evaporation loss at high reaction temperatures. Moreover, more expensive raw materials were used, and a high synthesis temperature was required. In addition, like in the case of thermal reduction, the final product powders suffered from heavy agglomeration.

25

The synthesis methods for MoAlB included mainly, the Al flux method, hot pressing, sparking plasma sintering and the conventional mixed powder route. The Al flux method required a very high synthesis temperature 1400~ 1800 °C. It was mainly used to grow MoAlB single crystals larger than 100 μm [52-54]. SPS [56] and hot pressing [16,20-21] were often used to prepare bulk MoAlB from MoB and Al (always 20 % to 30 % excessive) raw materials. The synthesis temperature was generally low (1100~1200 °C). but a high pressure was required. The only method attempted to synthesize MoAlB powder was the conventional mixed powder route [19,57], i.e., by directly heating a mixture of MoB and Al (always 30 % to 60 % excessive) at 1100 °C. Unfortunately, with this technique it was difficult to prepare high quality (phase pure, good dispersion and fine size) MoAlB powders, as some impurity phases (e.g. MoB_2) almost always remained in the final agglomerated product powders [19,57].

The conventional mixed powder method initially used to prepare WC catalysts, also exhibited several disadvantages, such as high firing temperature and long reaction time, uncontrollable sintering/heavy agglomeration of product particles and poor catalytic activity [58]. To avoid these problems, a gaseous carbon source was used instead. Although the synthesis temperature was reduced to 800-1000 °C [59-64], a carbon film was always deposited on the WC catalyst particles, separating them from the reactant species, reducing their catalytic activity. Considering this, a so-called "removable ceramic coating method" [65] was attempted to fabricate well-dispersed WC NPs free

26

from carbon covering. Unfortunately, it still suffered from several drawbacks such as a complicated process, long processing time, the use of hazardous material precursors and low production yield.

As for 2D carbide nanosheets and SiC and ZrC coated multi-layered graphene/graphite nanoplatelets, there have been not much work carried out on their synthesis so far. Although several coating techniques, including high speed impacting [66-67] and CVD [68-70], have been developed previously to prepare carbide coatings on different substrates such as graphite, they were not suitable for the synthesis of the fourth types of target material.

Clearly, it is crucial to develop an alternative synthesis method to address the issues with the conventional synthesis methods/techniques. As a response to this, in this thesis work, a low-cost "universal" molten salt synthesis (MSS) technique, was further developed to fabricate the four types of target materials, aiming to reduce the preparing temperature, and achieve high purity and good dispersion of the final products. The effects of key processing parameters on the synthesis process and microstructures and properties of the materials were examined, and the relevant reaction/synthesis mechanisms clarified. Based on these, the synthesis conditions were also optimized under which high quality target materials were prepared, and subsequently characterised systematically.

Based on the results from this thesis work, one paper on WC-based nanocatalyst for

hydrogen generation from water has already been published, and two other papers on

the synthesis and characterization of $Al_8B_4C_7$ and MoAlB have been drafted and will be

submitted for publish soon. The fourth paper on the synthesis and characterisation of 2D

carbide nanosheets and carbide coated graphene is in preparation. It is believed that the

findings from this thesis work would be beneficial to many industrial sectors, in

particular, structural ceramics/refractories, and aerospace industries.

1.2 Aims/Objectives of this thesis work

1) Develop a low-cost low-temperature MSS technique "universally" applicable to the

   synthesis of binary and ternary carbide- and boride-based materials.

2) Examine the effects of key processing parameters on the MSS process and the quality

   of product powders.

3) Understand the science underpinning the MSS process, based on which optimize the

   synthesis conditions

4) Prepare the four novel types of target materials under the optimal conditions and

   characterise their microstructures and properties.

1.3 Thesis Outline

This thesis consists of eight chapters. Chapter 1 provides an overall introduction to the

thesis, including brief background about of the target materials studied and the

aims/objectives of the work. Chapter 2 presents a comprehensive literature review, with a focus on the structures, properties and current preparation techniques of the target materials and the recent research work on MSS. In chapter 3, the main characterisation techniques used are described. Chapter 4 and 5 describe the synthesis and characterisation work on $Al_8B_4C_7$ and MoAlB fine powders, respectively. The effects of processing parameters on the MSS process and microstructures/morphologies of product powders are discussed, and the relevant reaction mechanisms proposed. Chapter 6 is focused on the results from the preparation and characterisation of CNT/CB supported tungsten carbide catalysts for hydrogen generation from water. Chapter 7 gives the main results from fabrications and characterisations of SiC and ZrC nanosheets, and SiC- and ZrC-coated graphene/graphite nanoplatelets, along with detailed discussions on the relevant reaction mechanisms. Finally, Chapter 8 draws conclusions from this thesis work and recommends some future work.

Chapter 2. Literature review

2.1 Crystal structures, properties and applications

In terms of the so-called "four major components" of materials science and engineering, physicochemical properties of a material are determined by its structures on all the scales (from atomic scale to macroscale), and they themselves determine the performance of the material during the service. In this section, crystal structures, properties and applications of several novel types of carbide/boride based materials investigated by the thesis work are reviewed.

2.1.1 Aluminum boron carbide ($Al_8B_4C_7$/Al_3BC_3)

$Al_8B_4C_7$, or Al_3BC_3, is a complex carbide crystallized in $P6_3$/mcm [1,51] or $P6_3$/mmc [46] space group (Fig 2.1). Similar XRD results were obtained in both compositions. Some researchers consider that $Al_8B_4C_7$ was a binary compound of Al_4C_3 and B_4C [71] while some other researchers believed it was actually Al_3BC_3 containing some residual Al and B [48]. No detailed information about the crystal structure of $Al_8B_4C_7$ is available, but it is supposed to be similar to the wurtzite structure [72]. In the crystal structure of Al_3BC_3, Al_3C layers are interleaved by linear C-B-C chains along the c-axis [46, 73-78]. The B-C distance (1.44 Å) in this parallel C-B-C unit is shorter than that in C-B-C chains in Sc_2BC_2 (1.48 Å) [79]. This may explain why Sc_2BC_2 has metallic properties while

30

Al$_3$BC$_3$ does not [46]. Vibrational spectroscopy results [46] revealed that this C–B–C unit has a strong covalent bond. Based on carbon's coordination polyhedra, crystal structure of Al$_3$BC$_3$ can be described as an Al$_3$CBCAl$_3$ double tetrahedral with a shared corner in a staggered orientation. Boron atom connects the terminal Al atoms of A1$_3$C layers in CAl$_5$ bipyramids (also tetrahedrally coordinated with Al-C distance of 2.00 Å - 2.06 Å). Due to the formation of the superstructure, coordination tetrahedra of the equatorial Al atoms are slightly distorted with distances of three Al-C bonds of 1.98 Å and one of 2.23 Å. Al$_8$B$_4$C$_7$ /Al$_3$BC$_3$ has some superior properties such as excellent oxidation resistance [1-2], high hardness [1,3,48,74,78,80], moderate melting point [81-82], relatively low density [1,74,83] and thermal expansion coefficient [1], good thermal conductivities [1], thermal stability (up to 1830 ^{o}C) [50], chemical stability [1], hydrolysis resistance [2,46], and excellent erosion and corrosion resistance [1]. The properties of aluminum boron carbide are listed in Table 2.1. These properties make aluminum boron carbide a candidate material for many important applications. For example, it can be used as a high temperature structural material due to its relatively high melting point (above 1800 ^{o}C), good mechanical properties, and low density compared with other ternary carbides such as Ti$_3$AlC$_2$ (4.24 g/cm^3) [84], AlZrC$_2$ (5.12 g/cm^3) [85], Ti$_3$SiC$_2$ (4.53 g/cm^3) [86] or Mo$_2$BC (8.74 g/cm^3) [87]. Its moderately high melting point also makes it a good sintering aid for some high temperature materials such as SiC, ZrB$_2$ and B$_4$C [5-9]. Because of its much better hydration resistance than Al and Al$_4$C$_3$ and its chemical properties (its oxidation product B$_2$O$_3$ can react with MgO to form 3MgO·B$_2$O$_3$ (M$_3$B) and give a M$_3$B-MgO eutectic low melting phase to prevent the oxygen diffusion while

31

another oxidation product Al_2O_3 can easily react with MgO in M$_3$B-MgO liquid phase to form spinel ($MgAl_2O_4$) to enhance the mechanical properties and slag corrosion resistance), it can be used as a good antioxidant for carbon-containing refractories such as MgO-C refractories bricks [4,10-13]. Its addition presents carbon-containing refractories from oxidation as effectively as addition of binary Al + B_4C antioxidant (which can improve simultaneously oxidation resistance, corrosion resistance and mechanical properties of carbon-containing refractories) but does not suffer from the drawbacks in the case of the latter (cracking caused by gaseous CH_4 and H_2 from hydration of Al and/or Al_4C_3 formed on heating [88-89]). In addition to the properties stated above, $Al_8B_4C_7$/Al_3BC_3 is semiconductive and could be potentially used as an absorber in a new generation nuclear reactor [14].
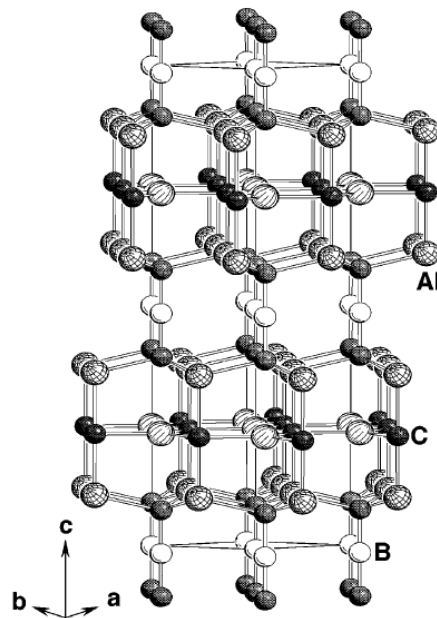
Fig. 2.1 crystal structure of Al_3BC_3 [78].

32

Table 2.1 Typical properties of $Al_8B_4C_7$/Al_3BC_3

Properties	$Al_8B_4C_7$	Al_3BC_3
Density (g/cm^3)	2.69	2.658
Lattice parameters (Å)	a=5.906, c=15.901	a=5.9, c=15.89
Crystal structure	Hexagonal	Hexagonal
Space group	P6$_3$/mcm	P6$_3$/mmc
Hardness (GPa)	12.1-15.2	11.1-20.7
Melting point (°C)	Above 1800	Above 2100
Thermal conductivity	29.2 Wm^{-1}K^{-1}	-
Thermal expansion coefficient	6.67×10^{-6} per K	-

2.1.2 Tungsten carbides (WC, W_2C)

Two tungsten carbides, WC and W_2C, have recently attracted a great deal of attention. Their crystal structures are illustrated in Figs. 2.2, 2.3 and 2.5. In general, W and C atoms in tungsten carbides are covalently bonded [90], while still maintaining a degree of metallic electrical and thermal conductivity. Lower tungsten carbide, W_2C, has four modifications which are low-temperature β''-W_2C, intermediate β'-W_2C, high-temperature β-W_2C [91], and ε-W_2C [92-93] (the latter three phases are also called α-W_2C, β-W_2C and γ-W_2C) [94-96]. All four W_2C modifications have an hcp metallic sublattice of W atoms with half octahedral interstitials occupied by C atoms. The distribution of C atoms determines different W_2C structural modifications as well as whether W_2C is ordered or disordered [97]. Higher carbide, WC, has a hexagonal

33

structure δ-WC (or α-WC [98] or simply WC [99]) and cubic phase γ-WC$_{1-x}$ (designated

also as β-WC [98] or α-WC$_{1-x}$ [99] or simply WC$_{1-x}$).

According to Rudy et al. [22,97], β-W$_2$C has a L'3-type hexagonal structure with space

group of $P63/mmc(D^4_{6h})$ which is a completely disordered phase. (Fig. 2.2). The L'3-

type structure is a typical structure of most nonstoichiometric lower carbides and nitrides

of V, Nb and Ta except V$_2$N [100-102]. Crystal structure of β-W$_2$C can be described

[103] as two tungsten atoms occupy the 2(c) positions with coordinates of (1/3 2/3 1/4)

and (2/3 1/3 3/4) and one carbon atom randomly occupies the position between 2(a)

position with coordinates of (0 0 0) and (0 0 1/2) in a probability of 1/2. The W atoms

layers A and B alternate with the nonmetallic lattice sites C layers in the form of

ACBCACBC. β-W$_2$C is stable from 2670 to 2720 K up to its melting temperature of

3000–3050 K [103].

All the four modifications of W$_2$C have similar hexagonal metallic sublattices and hence

have similar XRD patterns (Fig. 4). The β'-W$_2$C has a rhombic symmetry with ζ-Fe$_2$N

type and space group of Pbcn (D$^{14}_{2h}$) [22,91,97,104]. The carbon atoms occupy 4(c)

positions with coordinates of (0 3/8 1/4) and the tungsten atoms occupy 8(d) positions

with coordinates of (1/4 1/8 1/12) [103]. β'-W$_2$C exists stably between 2370 K to 2670–

2750 K [103]. The β''-W$_2$C has the C6 (anti-CdI$_2$)-type structure [97] with the space

group of P$\bar{3}$m1(D$^3_{3d}$). Its structure [103] contains two tungsten atoms which occupy 2(d)

positions with coordinates of (1/3 2/3 1/4) and (2/3 1/3 3/4), one carbon atom occupies

34

in 1(a) position with coordinates of (0 0 0) and a vacant site is in 1(b) position with coordinates of (0 0 1/2). It decomposes to give WC and W at temperature lower than 1523K [103]. The ε-W$_2$C phase [92-93] has a trigonal structure and belongs to space group P31m (D$^1_{3d}$). Tungsten atoms are in 6(k) positions with coordinates (1/3 0 1/4) and carbon atoms occupy 1(a) and 2(d) positions with coordinates of (0 0 0) and (1/3 2/3 1/2) respectively, while positions 1(b) and 2(c) remain vacant with coordinates of (0 0 1/2) and (1/3 2/3 0) respectively [103].

δ-WC [103] has hexagonal type B$_h$ (the WC-type) structure with space group of P6m2 (D$^1_{3h}$). Tungsten atoms occupy 1(a) positions with coordinates of (000) and carbon atoms occupy 1(d) positions with coordinates of (1/3 2/3 1/2) [105]. In this structure, tungsten and carbon atoms form simple hexagonal sublattices and carbon atoms occupy the centers of interstitials of the tungsten trigonal prismatic sublattice (Fig. 2.5). γ-WC$_{1-x}$ [22] has a cubic B1 (NaCl) type structure with space group of Fm3m (O^5_h) (Fig. 2.6), which is a typical structure of all nonstoichiometric carbides and nitrides of Group IV and V transition metals. In this structure, carbon atoms can occupy all octahedral interstitials in the face centered cubic (fcc) sublattice of tungsten.

Tungsten carbides (WC and W$_2$C) are highly refractory, with a melting point as high as about 3000 K [22]. WC has a high thermal conductivity and low coefficient of thermal expansion [23-24]. It is extremely hard with a hardness of 22-26 GPa [23-26]. It has Young's modulus and shear modulus of approximately 530–720 GPa [23-24,106-107]

35

and 262-274 GPa [23,108] respectively, with Poisson's ratio around 0.2 [107,109]. The electrical resistivity of tungsten carbide is close to that of a metal (0.22 $\mu\Omega\cdot$m) [23]. For ditungsten carbide, W_2C [110], it has a hardness of 17.1 GPa, Young's modulus of 444 GPa, electrical resistivity of 9 $\mu\Omega\cdot$m and Poisson's ratio of 0.286. The detailed properties of WC and W_2C are listed in Table 2.2.

The applications of tungsten carbides are mainly based on their good mechanical properties. Typical application areas include cutting tools, mining tools, ammunitions, grinding tools, etc. In recent years, electrochemical catalytic properties of tungsten carbides, especially in the case of hydrogen generation from water, has been investigated [27-36]. They showed good catalytic activity in hydrogen evolution reaction with an overpotential of 145 to 500 mv and tafel slope of 69 to 137 mV dec[-1].
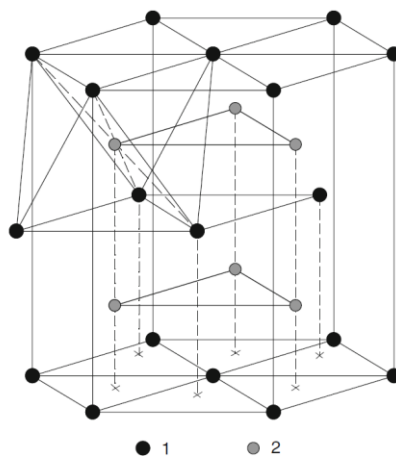
Fig. 2.2 Crystal structure of β-W_2C [103].

36
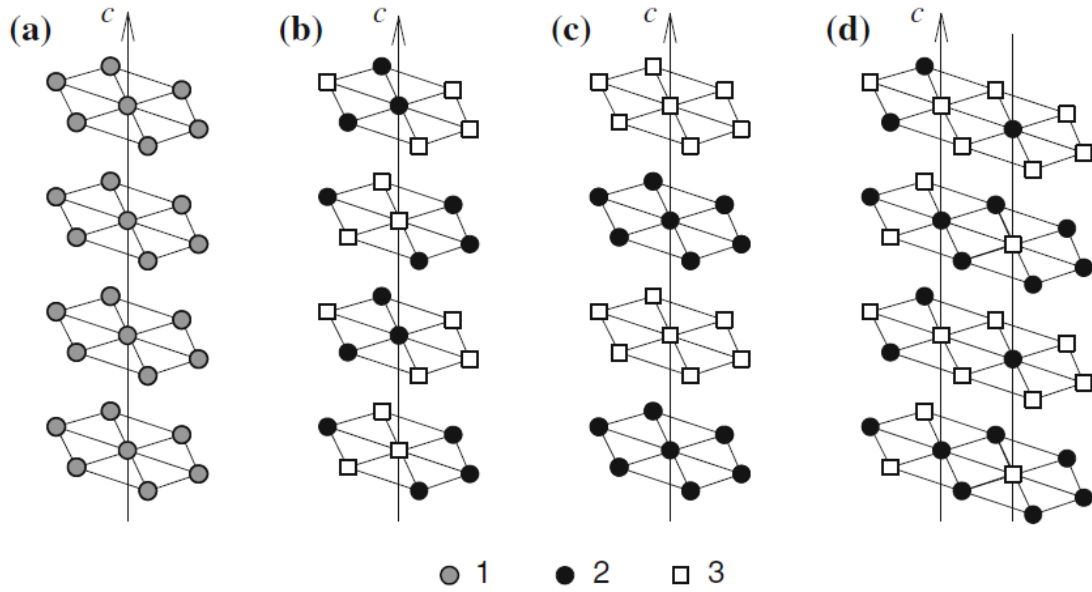
Fig. 2.3 Distribution of carbon atoms in lower carbides (a) β-W$_2$C, (b) β'-W$_2$C, (c) β''-W$_2$C and (d) ε-W$_2$C; 1: the positions randomly occupied by carbon atoms with a probability of 1/2, 2: carbon atoms, 3: vacancies [103].
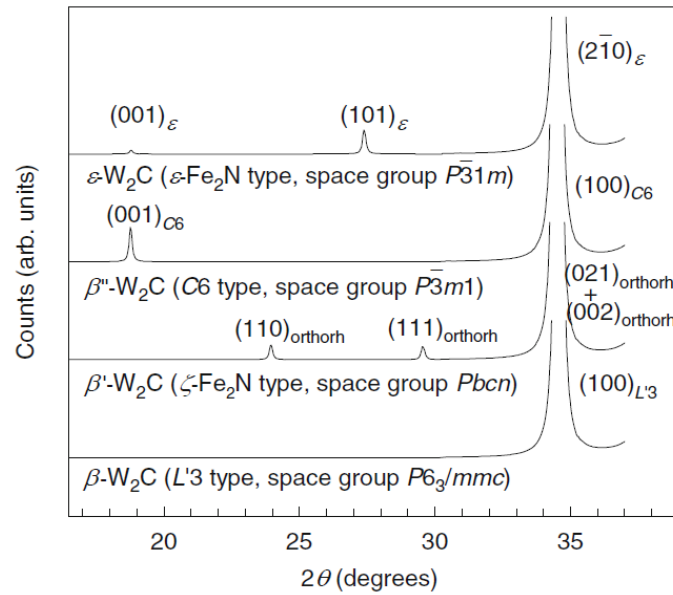
Fig. 2.4 XRD patterns of β-W$_2$C, β'-W$_2$C, β''-W$_2$C and ε-W$_2$C [103].
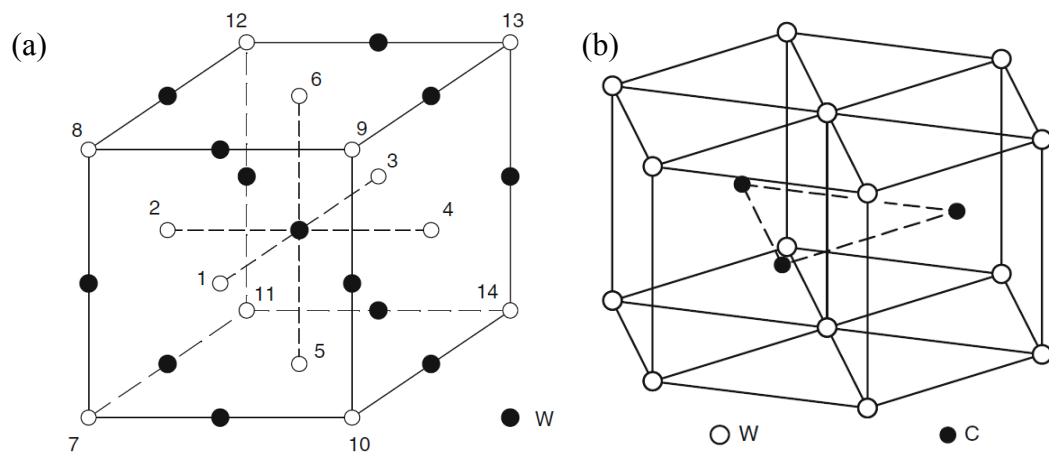
Fig. 2.5 Crystal structures of (a) cubic γ-WC$_{1-x}$ and (b) hexagonal δ-WC [103].

Table 2.2 Typical properties of WC and W$_2$C

Properties	WC	W$_2$C
Density (g/cm^3)	15.8	17.17
Lattice parameters (Å)	(γ) a=4.215-4.266 (δ) a=2.906, b=2.837	(β) a=2.997, c=4.7279 (β') a=4.728, b=6.009, c=5.193 (β'') a=2.985, b=4.717, c=3.001 (ε) a= 5.184, c= 4.721
Crystal structure	(γ) cubic (δ)hexagonal	(β) hexagonal (β') orthorhombic (β'') trigonal (ε) trigonal
Space group	(γ) Fm$\bar{3}$m (O^5_h) (δ) P$\bar{6}$m2 (D$^1_{3h}$)	(β) $P6_3/mmc$(D$^4_{6h}$) (β') Pbcn (D$^{14}_{2h}$) (β'') P$\bar{3}$m1(D$^3_{3d}$) (ε) P$\bar{3}$1m (D$^1_{3d}$)
Modulus of elasticity (GPa)	530-720	444
Hardness (GPa)	22-26	17.1
Melting point	3058K	3058K
Electrical resistivity ($\mu\Omega$·m)	0.22	9
Thermal conductivity (Wm^{-1}K^{-1})	63 or 110	
Thermal expansion coefficient (per K)	a: 5.2×10^{-6} c: 7.3×10^{-6}	

2.1.3 MoAlB

Ternary transition metal borides M_2AlB_2 (M = Cr, Mn, Fe) and MAlB (M = Mo, W) [52] have similar structures to those of MAX phase materials (Fig. 2.6). Among them, MoAlB has attracted particular attention because of its excellent oxidation resistance. MoAlB [111] has a layered structure in which an aluminum monolayer is located between two MoB layers (Fig. 2.6). Its crystal structure [15-17,111] can be described as edge-sharing Mo_6B trigonal prisms interleaved by two Al planar layers with zigzag chains of B atoms with space group of Cmcm or D_{2h}^{17} [112]. The Mo_6B trigonal prismatic array has two B atoms and one Al atom outside its rectangular faces. The prisms have axes parallel to the b direction, while the zigzag chains formed by B atoms are parallel to the c direction. The wrinkled metal layers of Al atoms interleaved the Mo_6B trigonal prisms (or Mo double layers). MoAlB has strong directional AlMoBBMoAl covalent-bond slab parallel to the b direction bonded by weaker Al-Al bonds [113]. Its unique nanolaminated structure increases the fractural toughness [18-19,113]. Compared with MoB, the introduction of aluminum bilayers improves the oxidation resistance due to formation of a dense alumina scale on heating [15-16,20-21]. MoAlB has relatively low hardness, high compressive strength (1940 ± 103 MPa), high electrical/thermal conductivity, and low thermal expansion coefficient [15-19]. MoAlB is stable up to at least 1400 °C in an inert atmosphere [16]. The main properties of MoAlB are listed in Table. 2.3.

40

Table 2.3 Typical properties of MoAlB

Properties	MoAlB
Density (g/cm^3)	6.45
Lattice parameters (Å)	a=3.212, b=13.985, c=3.102
Crystal structure	Orthorhombic
Space group	Cmcm
Hardness (GPa)	9.3–13
Melting point	>1708 K (decompose)
Electrical resistivity	0.36-0.49 μΩm
Thermal conductivity	29.21-35 Wm^{-1}K^{-1}
Thermal expansion coefficient	9.5×10^{-6} per K
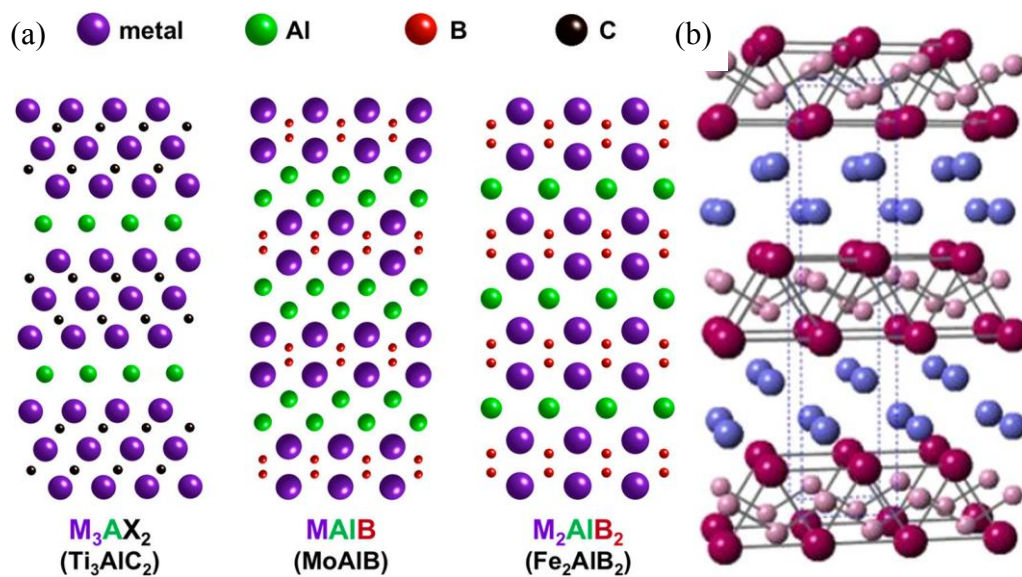
Fig. 2.6 (a) Crystal structure relations between MAX phases, MAlB-type MAB phases

and M$_2$AlB$_2$-type MAB phases [52] and (b) crystal structure of MoAlB [111].

2.1.4 SiC

Due to its many excellent properties, silicon carbide (SiC) has been extensively used in many important areas as a structural and functional ceramic. Si and C atoms in SiC are covalently bonded [114]. It has about 250 crystalline modifications [115], and among them, four crystalline modifications are well-known [116-117], i.e., β-SiC (3C), 2H-SiC, 4H-SiC and 6H-SiC which have the space groups of $F\bar{4}3m$, $P6_3mc$ and $C6mc$ (latter two modifications) respectively [118-119]. Structures of these four crystalline forms of SiC [120] are illustrated in Fig. 2.7. Polymorphs of SiC result from varied periodic stacking sequences of bilayers (Fig. 2) which contain two close packed planes [120]. There are six different kinds of bilayers (*bA, cA, aB, cB, aC,* and *bC*) (Fig. 2) which can stack to form vertex-sharing Si_4C/SiC_4 tetrahedral. 3C-SiC, 2H-SiC, 4H-SiC and 6H-SiC have the bilayers stacking orders of cAaBbC, bAaB, bAaBbCcB and bAaBbCcBaCcB respectively. These periodic stacking sequences have little influence on bond lengths and bulk density [121]. Hexagonal SiC (α-SiC) has even numbers of bilayers in its unit cell while cubic and rhombohedral SiC (β-SiC) have odd numbers.

SiC [23] has high decomposition point, high hardness, high mechanical strength, high thermal conductivity, low thermal expansion coefficient, good chemical inertness and excellent thermal shock resistance. It also has semi-conductivity which can be tailored/controlled *via* doping with different atoms [123]. Both n-type (by N or P) and p-type (by Be, B, Al, or Ga) SiC can be prepared. Table 2.4 lists the main properties of

42

SiC. Because of these excellent properties, SiC based materials find applications in many important areas, e.g., refractories, abrasive and cutting tools, high temperature sensors, Power electronic devices, LEDs and heating elements.

Table 2.4 Main properties of SiC

Properties	SiC
Density (g/cm^3)	3.2
Lattice parameters (Å)	(3C) a=4.36 (2H) a=3.08, c=5.03 (4H) a=3.08, c=10.06 (6H) a=3.08, c=15.09
Crystal structure	(3C) cubic (2H, 4H, 6H) hexagonal
Space group	(3C) F-$\bar{4}$3m (2H, 4H, 6H) P6$_3$/mc
Hardness (GPa)	24.5-28.2
Melting point	2830 ºC
Thermal conductivity (Wm^{-1}K^{-1})	25.5-490
Thermal expansion coefficient	3.8-5.12×10^{-6} per K

SiC Polytypes

(a)

Fundamental Bilayers

b_A

c_A

a_B

c_B

a_C

b_C

(b)

Close Packing in Plane

A-B Stacking

A-C Stacking

A ●

B ⬡

C ▢

(c)

3C (∞)

c_A
a_B
b_C

2H (11)

b_A
a_B

4H (22)

b_A
a_B
b_C
c_B

6H (33)

b_A
a_B
b_C
c_A
a_C
c_B
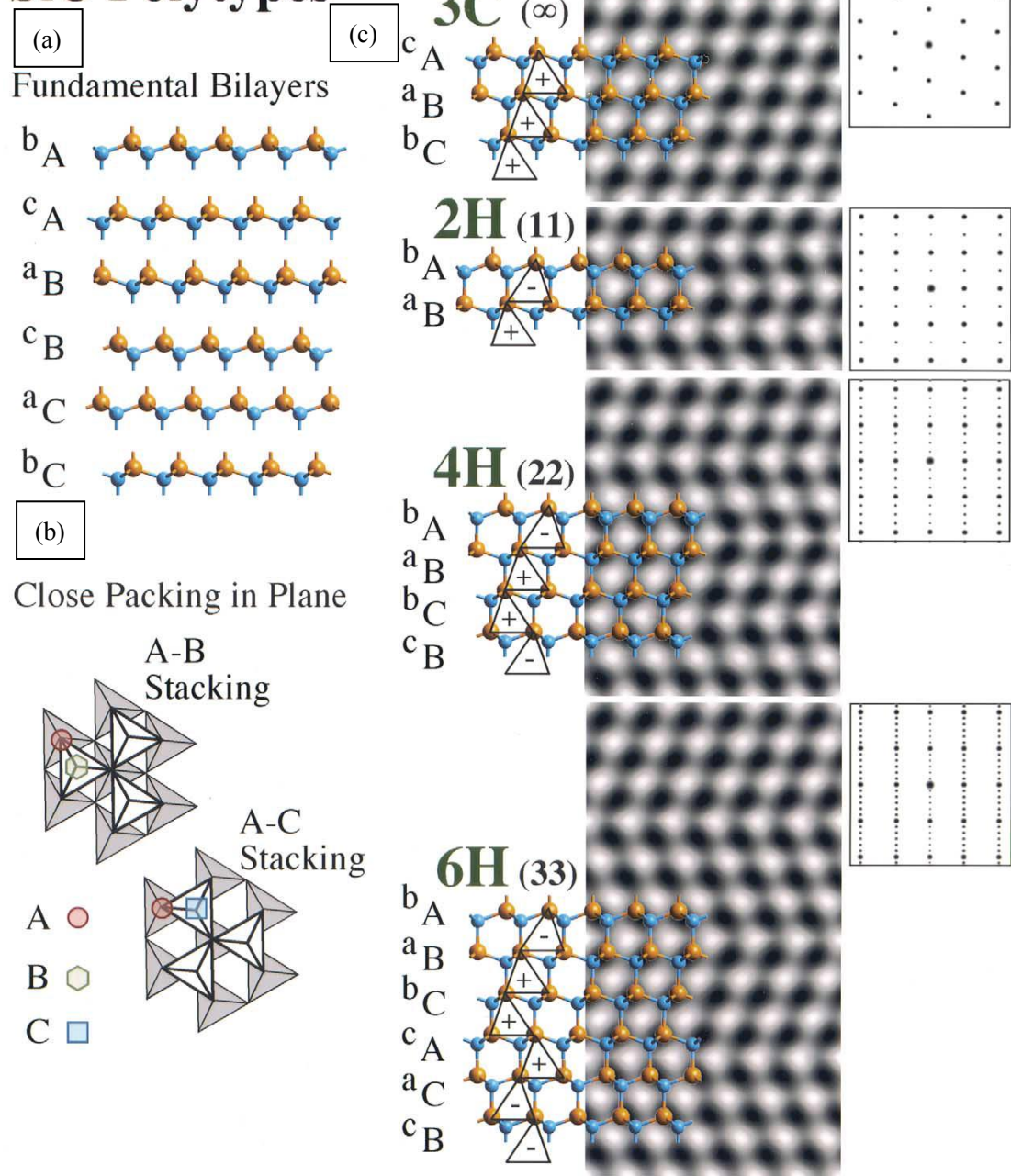
Fig. 2.7 (a) Six fundamental bilayers of SiC; (b) three principle close packed planes and (c) structures of 3C-SiC, 2H-SiC, 4H-SiC and 6H-SiC and their corresponding HR-TEM lattice images and diffraction patterns [120].

2.1.5 ZrC

Borides, carbides and nitrides of some of the group IVB and VB transition metals have melting point above 3000 °C, so they are defined as the so-called ultra-high-temperature ceramics (UHTCs) [122-125]. Zirconium carbide (ZrC) is one of the UHTCs carbides, with a cubic rock-salt (NaCl-type) with a space group of Fm3m [126-127] (Fig. 2.8). The Zr atoms in its structure occupy the face centered cubic (FCC) lattice sites with coordination of (0,0,0) and the carbon atoms fill the octahedral interstitial sites with coordination of (1/2,1/2,1/2). Apart from high melting point (3460 -3490 °C) [37], ZrC has several other excellent properties, including high hardness (16-22 GPa) [38], good thermal conductivity (20.5 $Wm^{-1}K^{-1}$) [39], low thermal expansion coefficient ($6.99*10^{-6}$ per K) [40], high strength at room temperature and elevated temperatures (up to 2400 °C) [41], high Young's modulus of 195-549 GPa [38, 128-130], relatively low density (6.73 g/cm^3) and good corrosion resistance to HCl and NaOH at room temperature. Table 2.5 lists some of the main properties of ZrC. These excellent properties make it suitable for structural applications, especially at a high temperature. For example, it is a potential candidate for aerospace applications or armor applications due to its high melting point, good thermal properties, relatively low density and high strength at high temperature [131-132]. Although its oxidation resistance is poor [133], it could be overcome by combining with some other materials such as SiC and ZrB_2 + SiC [134-135]. In addition, its high hardness makes it suitable for making cutting tools and abrasive components.
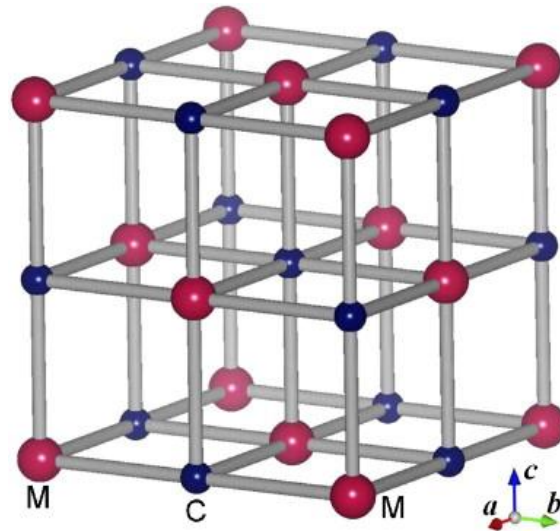
Fig. 2.8 Crystal structure of ZrC [126].

Table 2.5 Main properties of ZrC

Properties	ZrC
Density (g/cm^3)	6.73
Lattice parameters (Å)	a=4.691
Crystal structure	cubic
Space group	$\overline{Fm3m}$
Modulus of elasticity (GPa)	195-549
Hardness (GPa)	25
Melting point	3530 °C
Thermal conductivity	20.5 Wm^{-1}K^{-1}
Thermal expansion coefficient	6.7*10^{-6} per K

2.1.6 Coated carbon materials

Carbon materials, such as carbon black, graphite, graphene and carbon fiber, have many superior properties including high thermal conductivity, low thermal expansion coefficient, high specific strength (carbon fiber) and non-wettability by slag (especially graphite). Therefore, they are extensively used in many important industrial sectors, e.g., refractory, automotive, and aerospace industries. However, they generally suffer from poor water-wettability/dispersivity and oxidation resistance, which limits their service lives.

To solve these problems, several coating techniques were introduced. An oxide or carbide coating material can be formed on the surface of carbon *via* physical or chemical routes. For example, the water-wettability/dispersivity of carbon was improved by coating it with TiC/SiC/oxides [136-138], as proved by zeta potential test or castable flowability test (Fig. 2.9). TG test [137, 139-140] revealed that a dense coating could effectively decrease the diffusion of oxygen and thus protect carbon materials from oxidation (Fig. 2.10).

47
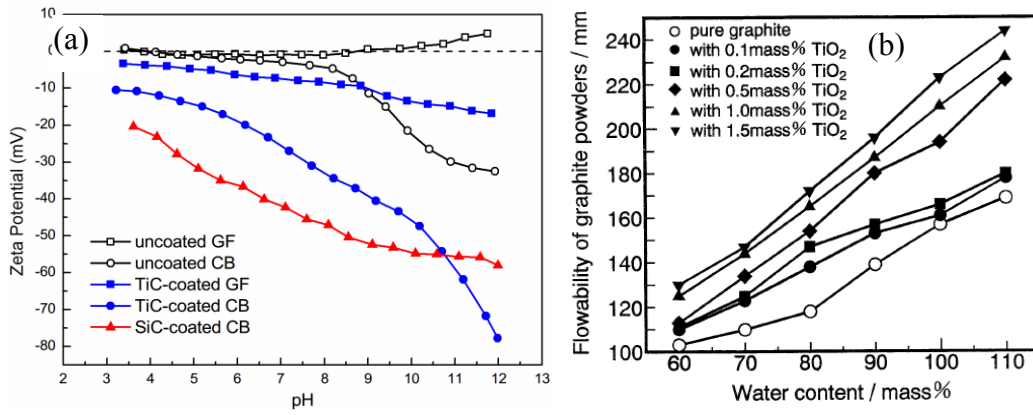
Fig. 2.9 (a) Zeta potential of carbon and TiC or SiC coated carbon [137]; (b)

flowability of graphite and TiO$_2$ coated graphite [138].
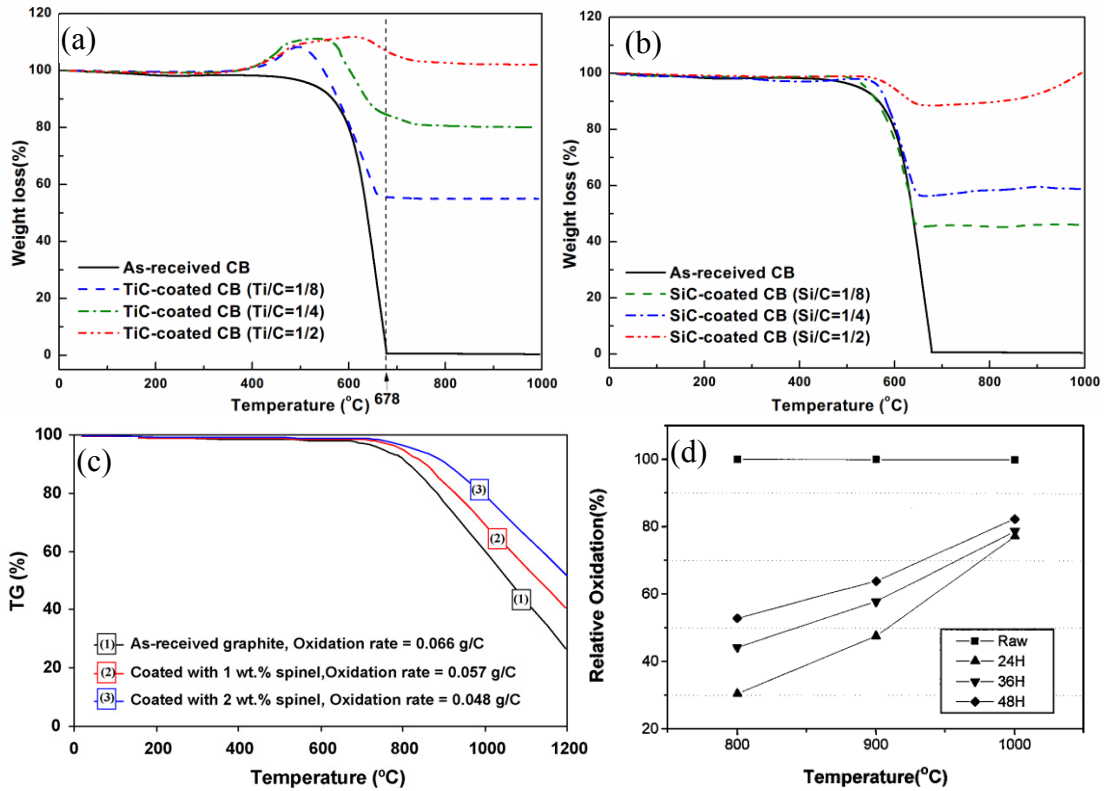
Fig. 2.10 Weight changes of (a) CB and TiC coated CB, (b) CB and SiC coated CB, (c)

graphite and spinel coated graphite [137]; and (d) relative oxidation rate of graphite

and ZrO$_2$ coated graphite [139].

48

2.2 Synthesis of tungsten carbide-carbon composite

Tungsten carbide-carbon composites are mainly prepared *via* reduction-carbonization routes. This section reviews and evaluates synthesis of WC and W_2C powders using different reducing agents and carbon and tungsten sources.

The reduction-carbonization route is involved with initial reduction of tungsten oxides (or other tungsten oxides containing raw materials) and subsequent carbonization of the formed tungsten. Several reduction agents could be used for this synthesis method. The commonly used reducing agents include carbon, carbon monoxide, hydrogen, metals, CH_4 or combinations of different reducing agents. For carbonization, carbon (such as graphite, carbon black, carbon nanotube or carbon fiber), carbon monoxide, CH_4 or some organic gaseous carbon sources are always used.

2.2.1 Hydrogen (H_2) and Carbon based reducing agents (C, CO and CH_4)

WC was firstly prepared *via* carbothermal reduction of WO_3 (Reaction (2.1)) which has been using extensively since [141-142]. This reaction is endothermic and takes place only at elevated temperatures. In this case, carbon acts as both reducing agent (Reaction (2.2) and (2.3)) and carbon source (Reaction (2.4) and (2.5)). With this technique, large tungsten carbide particles are generally produced at a relatively high temperature.

49

$$WO_3 + 4C = WC + 3CO \qquad (2.1)$$

$$2WO_3 + 7C = W_2C + 6CO \qquad (2.2)$$

$$WO_3 + 3C = W + 3CO \qquad (2.3)$$

$$W + C = WC \qquad (2.4)$$

$$2W + C = W_2C \qquad (2.5)$$

Apart from carbon, H_2 was used to reduce WO_3 [142-143]. As reported in Ref. 143, at 700-1000 °C, WO_3 could be reduced by H_2, forming W (particle size 0.5-5 μm) and H_2O (reaction 2.6). The formed W subsequently reacted with carbon to form WC of 0.5-20 μm at about 2000 °C (Fig. 2.11). By coating WO_3 with carbon *via* heating poly propylene gas (C_3H_6) and further reaction with carbon black under H_2 + Ar, WC with the average size of 0.5 μm was formed at 1100-1400 °C [144]. The carbon coating was believed to provide intimate WO_3-C contact and promote the diffusion of C.

$$WO_3 + 3H_2 = W + 3H_2O \qquad (2.6)$$
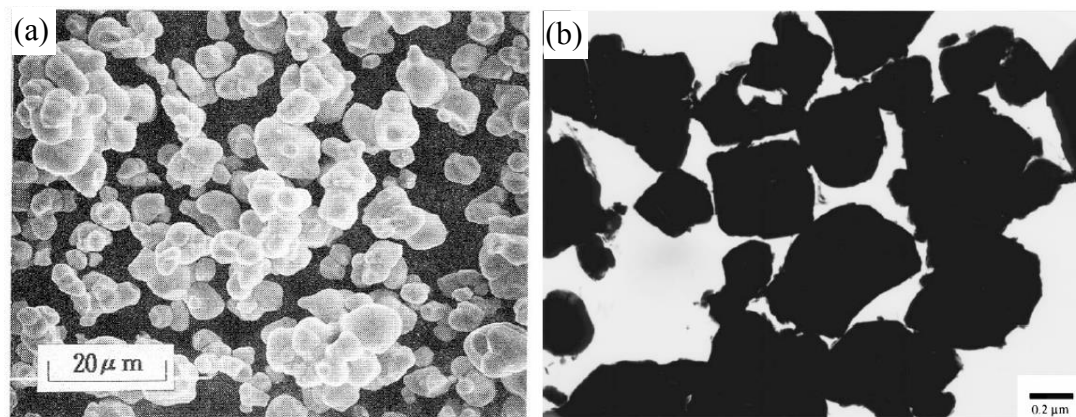
Fig. 2.11 (a) SEM image of WC powder from [143] and (b) TEM image of WC powder from [144].

50

CO is a common reducing agent for many reactions. Although the reduction of WO_3 to W by CO (Reaction 2.7) was assumed to occur by some researchers [145-146], CO was rarely used as a reducing agent in this case. According to Kozyrev's work [147] on the WO_3-CO and WO_3-C reactions, the calculated Gibbs free energy values indicate that the three WO_3-CO reactions (Reactions (2.7), (2.8) and (2.9)) are not favored thermodynamically.

$$WO_3 + 3CO = W + 3CO_2 \tag{2.7}$$

$$WO_3 + 5CO = WC + 4CO_2 \tag{2.8}$$

$$2WO_3 + 8CO = W_2C + 7CO_2 \tag{2.9}$$
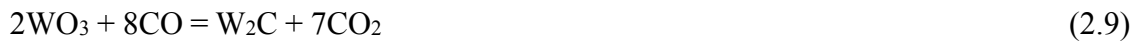
Oro et al [148] compared the effectiveness of CO, C and H_2 in the preparation of WC. Unlike H_2, CO can only reduce WO_3 to $W_{18}O_{49}$ rather than W at 1300 °C. This may explain why CO was used together with other reducing agents. Both H_2 and CO can lower the formation temperature of tungsten carbide when used together with C. Single WC phase or mixtures of WC and W_2C can be produced at 1000 -1100 °C depending on the carbon type and atmosphere. Similarly to that mentioned above [143], product powders prepared *via* the WO_3-H_2-C route had larger average size than that of the powders produced *via* the WO_3-C-CO (this work) and WO_3-C routes.
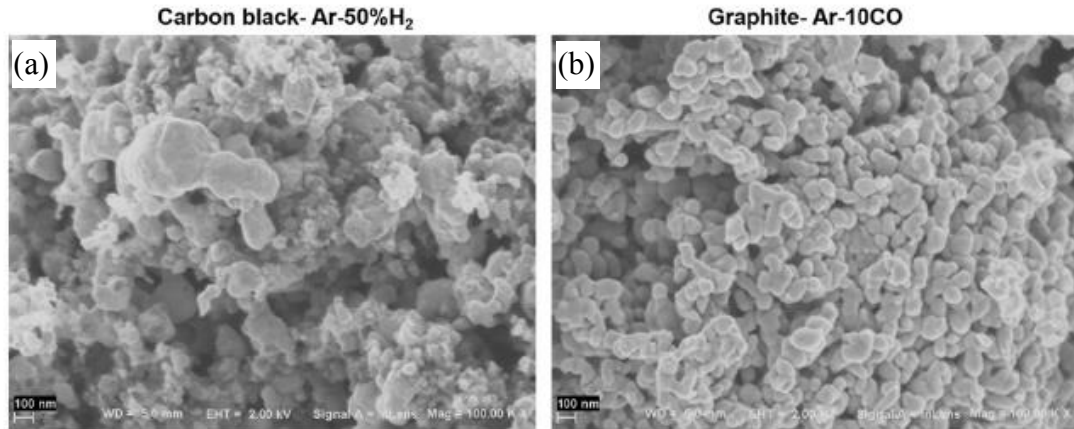
Fig. 2.12 SEM images of samples heated at 1100 °C: (a): WO_3 + C in $Ar-50H_2$, (b): WO_3 + C in Ar-10CO [148].

CH_4 was also used as both reducing agent and carbon source in the reduction-carbonization route. The role of CH_4 in WC preparation was investigated extensively [149-152]. At 850 and 900 °C, WO_2 and W were the reduction products of WO_3 (Reactions (2.10) and (2.11)). At 1000 °C, W_2C began to appear (Reaction 2.12) and with prolonged reaction time or elevated temperature single WC phase could be obtained (Reaction (2.13)).

$$CH_4 + 3WO_3 = 3WO_2 + CO + 2H_2O \tag{2.10}$$

$$CH_4 + WO_3 = W + CO + 2H_2O \tag{2.11}$$

$$2W + CH_4 = W_2C + 2H_2 \tag{2.12}$$

$$W + CH_4 = WC + 2H_2 \tag{2.13}$$

2.2.2 Magnesiothermal reduction with different carbon sources

Magnesium is widely used as a reducing agent for many important reduction reactions. A relatively low reduction temperature is required by the magnesiothermal reduction-carbonization approach. The exothermic WO_3-Mg reaction also makes it possible to synthesize WC *via* self–propagation high–temperature synthesis (SHS) or mechanical ball milling. One of the main drawbacks of this method, however, is that repeated acid leaching/water washing is required to remove the byproduct MgO formed from the reduction reaction. Also, product powders suffer from some other problems such as carbon covering and poor dispersivity.

Tan et al [153] used magnesiothermal reduction combined with mechanical ball milling to prepare tungsten carbide nanopowders. WO_3, Mg and graphite were used as raw materials. The mixtures together with milling balls were placed in a milling jar under H_2-Ar atmosphere with ball-powder weight ratio of 20: 1 to 50: 1 and milling speed of 250 rev min^{-1}. The final products were nanocomposite powders comprising cubic and hexagonal WC, and W_2C with 4-20 nm in size (Fig. 2.13).
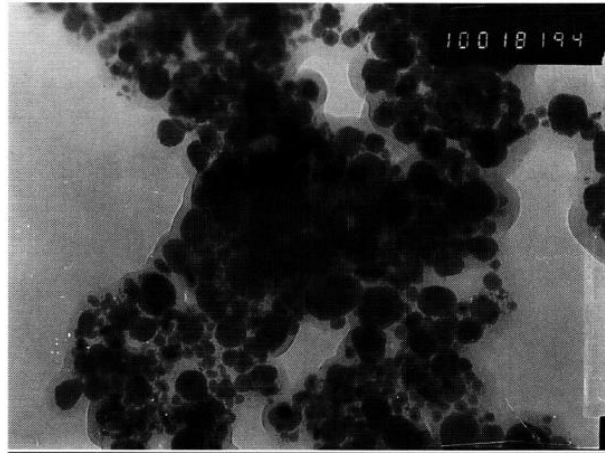
Fig. 2.13 TEM images of as milled nanocrystalline tungsten carbide powder mixture

[153].

Kirakosyan et al [154] synthesized tungsten carbides *via* a combustion method using

WO_3, carbon black and magnesium as the raw materials. The maximum temperature of

combustion wave was 1850 ℃ and 2050 ℃ for samples with W to C atomic ratio of 1:1

and 1:2 respectively. The resultant powders were rinsed by HCl solution. A mixture of

WC and W_2C with particle size of 50-300 nm was obtained (Fig. 2.14). Similar results

were also achieved by Borovinskaya et al [155] and Won et al [156].
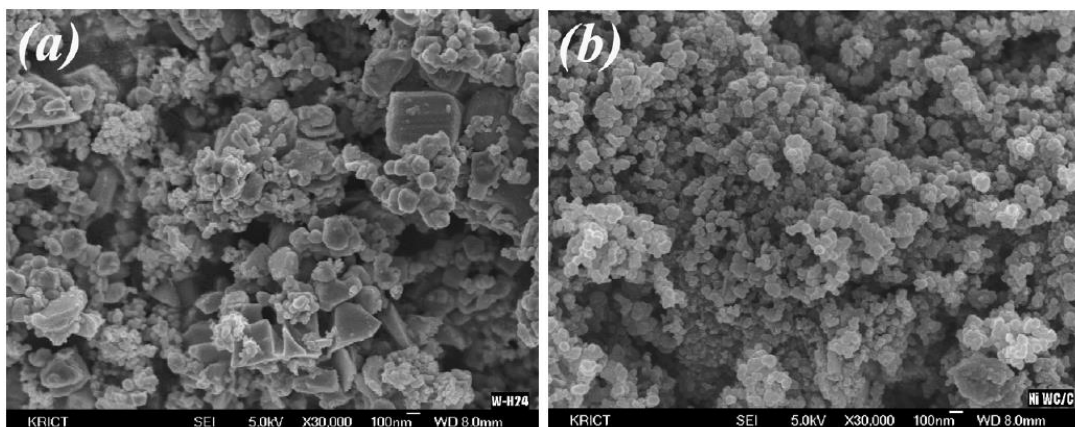
Fig. 2.14 SEM images of (a) WC-W_2C–C (main phase: WC) and (b) W_2C–WC-C

(main phase: W_2C) powders synthesized *via* SHS [154].

54

To further reduce the synthesis temperature and to synthesize nanosized particles, some researchers used gaseous carbon source instead of solid carbon (an autoclave was always needed). However, a carbon film was always deposited on the surface of WC nanoparticles (NPs), separating them from the reactant species, and reducing their catalytic activity. Singla et al [61] and Kumar et al [62] prepared WC-C nano-composites by using anhydrous acetone (C_3H_6O) as the carbon source. WO_3, Mg and anhydrous C_3H_6O were added into a sealed autoclave and heated to 600 ^oC for 1-2 h, followed by a series of washing steps: using HCl to remove MgO, distilled water to remove HCl, NaOH to remove residual oxides and deionised water to remove NaOH. The resultant products had an average size of 35 nm (Fig. 2.15). The relevant reactions are as follows:

$$3WO_3 + C_3H_6O + 5Mg = WC + W_2C + 5MgO + CO_2 + 3H_2O \qquad (2.14)$$

ΔH = -1548.32 kJ/mol, ΔG = -1567.76 kJ/mol

$$3WO_3 + C_3H_6O + 6Mg = WC + W_2C + 6MgO + CO + 3H_2O \qquad (2.15)$$

ΔH = -1866.92 kJ/mol, ΔG = -1879.86 kJ/mol

55
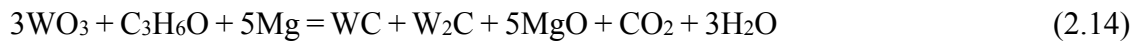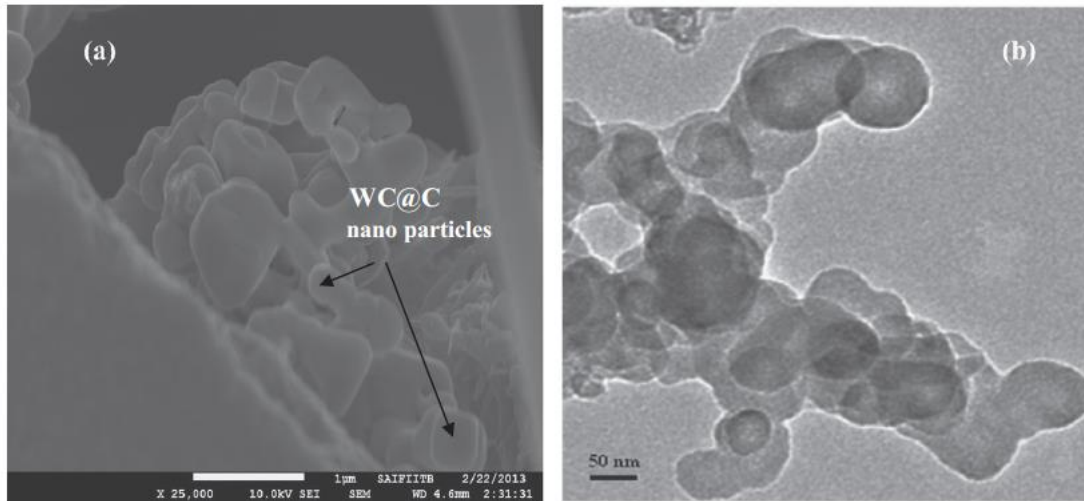
Fig. 2.15 (a) SEM and (b) TEM images of the as prepared WC with C_3H_6O as the

carbon source [61].

Such a method was also applied using CO (derived from oxidation of activated charcoal, acted as both carbon source and reducing agent), Mg and scheelite ($CaWO_4$) as starting materials [63]. After 50 h heating at 800 °C, WC particles of 20-100 nm were synthesized (Fig. 2.16).
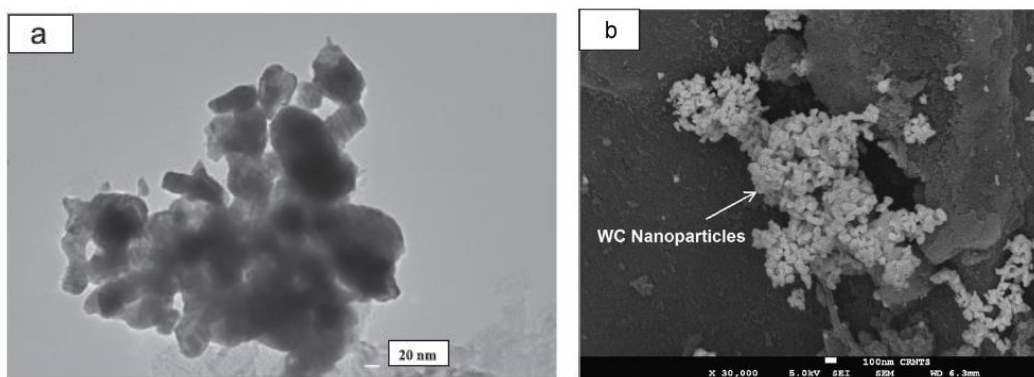
Fig. 2.16 (a) TEM and (b) SEM images of WC prepared from CO, Mg and scheelite

raw materials [63].

2.2.3 Reduction-carbonization of tungsten salts *via* CVD

A tungsten salt also can be used as a tungsten source to replace W oxide. For example, WCl_6 reacted with methane and hydrogen gases [157], forming WC according to Reaction (2.16). The corresponding Gibbs free energy is -469 to -630 kJ at 800–1200 °C, indicating that the reaction is thermodynamically favored.

$$WCl_6 + H_2 + CH_4 = WC + 6HCl \tag{2.16}$$
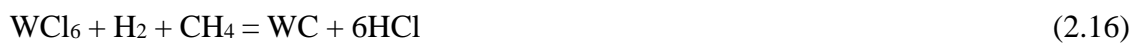
Compared with the conventional solid-solid reaction process, a chemical vapor deposition (CVD) process is generally quicker and requires a much lowered operation temperature. Moreover, high purity nanosized product powders can be prepared. W salts used to prepare WC included tungsten hexachloride (WCl_6) [158], tungsten hexafluoride (WF_6) [159], WCl_4 [160] and tungsten hexacarbonyl ($W(CO)_6$) [161] while the gaseous carbon sources included propane (C_3H_8) [161], acetylene (C_2H_2) [163], urea [160] and methane (CH_4) [164-165]. Hojo et al [158], Tang et al [162] and Won et al [163] prepared nanosized tungsten carbide powder *via* CVD using WCl_6, hydrocarbon (CH_4, C_3H_8 or C_2H_2), and H_2. Hojo et al. [158] obtained 40–50 nm WC powders at 400 °C, and 80–110 nm powders at above 1000 °C. To form phase pure WC, excess amount of methane and a high temperature above 1400 °C were required. Won [163] et al. produced mixture powders of WC and W_2C with size from 100 nm to 1 μm. Tang et al. [162] synthesized WC at >1400 °C using excess amount of C_3H_8.

57
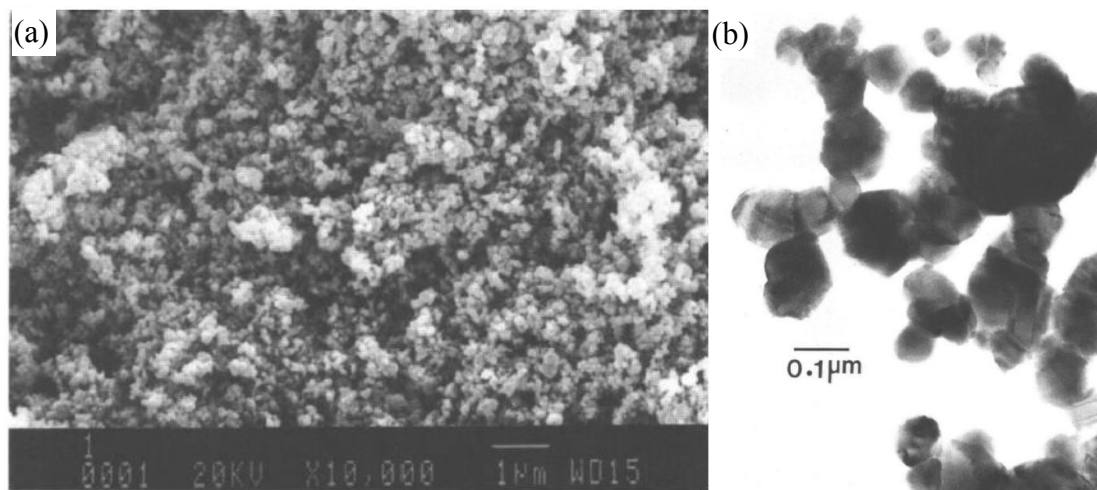
Fig. 2.17 (a): SEM and (b) TEM images of WC prepared from WCl_6 *via* CVD [163].

Kim and Kim [161] used tungsten hexacarbonyl [$W(CO)_6$] and carbon monoxide (CO) to synthesize WC. The former decomposed to W and CO at 150–205 °C. The subsequent carburization of W by CO and C ($2CO = C + CO_2$) occurred at 600 to 800 °C, forming WC_{1-x} particles smaller than 50 nm.
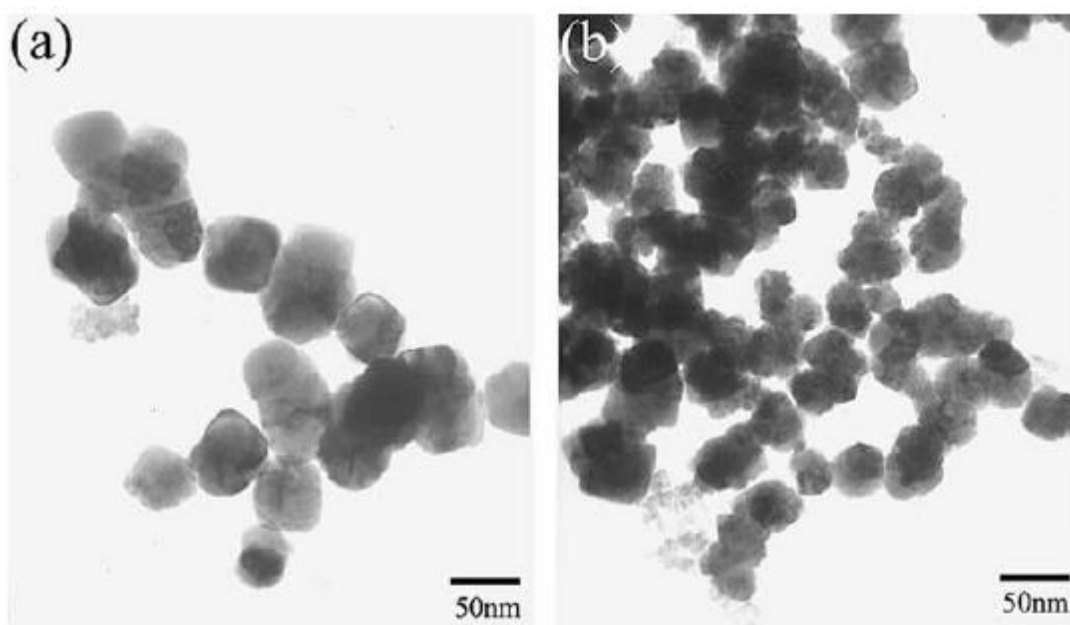
Fig. 2.18 SEM images of WC prepared from $W(CO)_6$ *via* CVD at (a) 600 °C and (b)

700 °C, respectively [161].

58

Giordano et al [160] prepared tungsten carbide nanoparticles by a so-called urea-glass route. Urea, as the carbon source, was mixed with WCl_4 and alcohol to form a polymer-like amorphous precursor. On heating to 1000 °C, WC or WC/W_2C (depending on the urea/WCl_4 ratio) was obtained. SEM and TEM images (Fig. 2.19) revealed that the overall particle size of WC was about 4 nm.
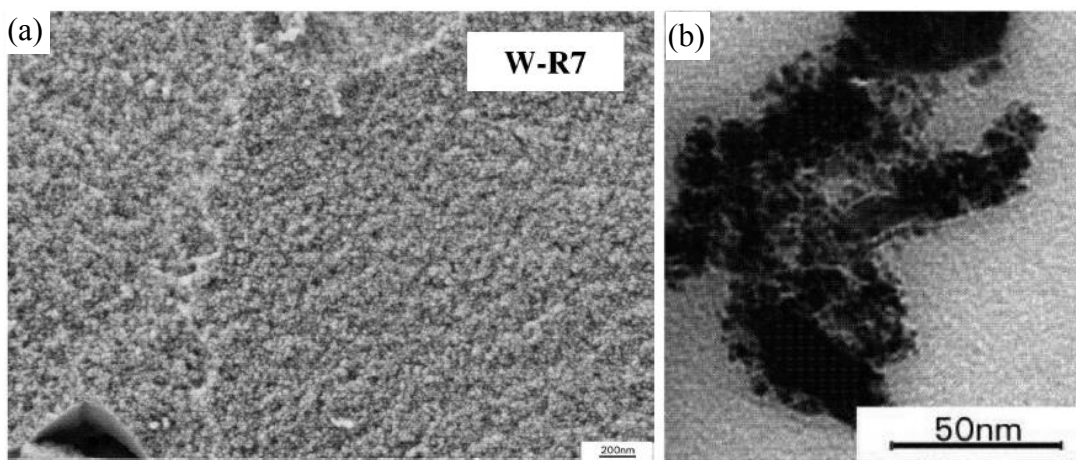
Fig. 2.19 (a) SEM and (b) TEM images of WC prepared from WCl_4 *via* CVD [160].

Ma et al [166] also used Mg to reduce W chlorides. Mg and WCl_6 were placed in an autoclave and heated at 800 °C. Mg reduced simultaneously WCl_6 and CO_2 derived from Na_2CO_3. After purification of the resultant powder with an HCl solution, phase pure WC powder of 20 nm in size was obtained.

Despite its advantages stated above, the CVD method suffers from several disadvantages such as use of expensive and/or hazardous raw materials, low production yield and complex processing conditions.

2.2.4 Direct carbonization of metallic tungsten

Direct solid-solid phase reaction between elemental W and graphite (at 1400~1600 °C) was another straightforward method used by many researchers to make WC [142,167-168]. Apart from firing at a high temperature, the mechanical alloying (or high-energy ball mill) [169] method was used to enable the WC formation reaction. In this case, W and C were mixed in the molar ratio of 1:1. The mixture combined with stainless steel balls (in the weight ratio of 10:1) was sealed in a stainless steel vial in a glove box under Ar and milled together at room temperature for an appropriate period of time. Phase pure WC particles with sizes of 70-90 nm were obtained.
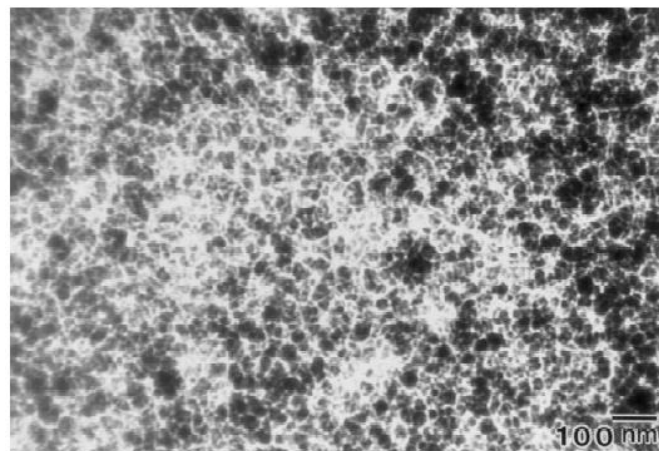
Fig. 2.20 TEM image of WC particles prepared *via* the mechanical alloying method [169].

2.3 Synthesis of aluminum boron carbide

Aluminum boron carbide ($Al_8B_4C_7$ or Al_3BC_3) is prepared *via* simple heating or hot pressing of powder raw materials. There are two main synthesis routes: reduction route and direct reaction route.

2.3.1 Reduction method

When Al or carbon is used as a reducing agent, boron containing oxides could be used as a boron source for preparation of aluminum boron carbide. The main advantage of this reduction method is using cheap raw materials instead of expensive boron or boron carbide. However, the main problem with it is the requirement of high reaction temperature and remaining of some byproducts like Al_2O_3 and Al_4O_4C/Al_2OC.

Zhu et al. [43] prepared $Al_8B_4C_7$ powder by reducing B_2O_3 with Al and carbon at 1700 °C. Powders with sizes of 2-4 μm were prepared, comprising primary phases of $Al_8B_4C_7$ and Al_2O_3, and minor phases of Al_2OC and Al_4O_4C. Deng et al [44] used $Na_2B_4O_7 \cdot 10H_2O$ instead of B_2O_3 to synthesize $Al_8B_4C_7$ and obtained similar results. Cui et al [45] achieved better results by using similar raw materials (activated charcoal as carbon source) and subsequent firing at 1800 ºC for 2 h. Hexagonal plate-like particles having an average size of ~100 μm and containing minor byproduct Al_2OC were obtained. Lee et al [45] prepared pure Al_3BC_3 by using $Al(OH)_3$, B_2O_3 and phenolic resin as raw

61

materials. After a complicated mixing, drying of slurries, carbonization of phenolic resins, crushing and pressing, the formed pellets were fired at 1725 °C for 4 h. According to Lee et al, the whole synthesis process could be divided into three stages. Firstly, under 1650 °C the Al_2O_3-C reactions occurred and most Al was transferred into Al_4C_3 and Al containing gas phases (Al and Al_2O). Next, when the temperature was increased to 1650 °C, B_2O_3 vapor reacted with Al_4C_3 and C at their interfaces to form Al_3BC_3. Then the boron- and aluminum- containing gases diffused through the Al_3BC_3 and Al_4C_3 and reacted with C.

$$Al_2O_3 + 2C = Al_2O + 2CO \tag{2.17}$$

$$Al_2O_3 + 3C = 2Al + 3CO \tag{2.18}$$

$$2Al_2O_3 + 9C = Al_4C_3 + 6CO \tag{2.19}$$

$$2Al_2O + 5C = Al_4C_3 + 2CO \tag{2.20}$$

$$4Al + 3C = Al_4C_3 \tag{2.21}$$

$$3Al_4C_3 + 2B_2O_3 + 9C = 4Al_3BC_3 + 6CO \tag{2.22}$$

$$3Al_2O + B_2O_3 + 12C = 2Al_3BC_3 + 6CO \tag{2.23}$$

$$6Al + B_2O_3 + 9C = 2Al_3BC_3 + 3CO \tag{2.24}$$
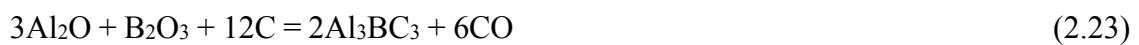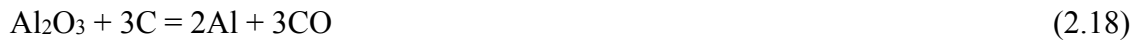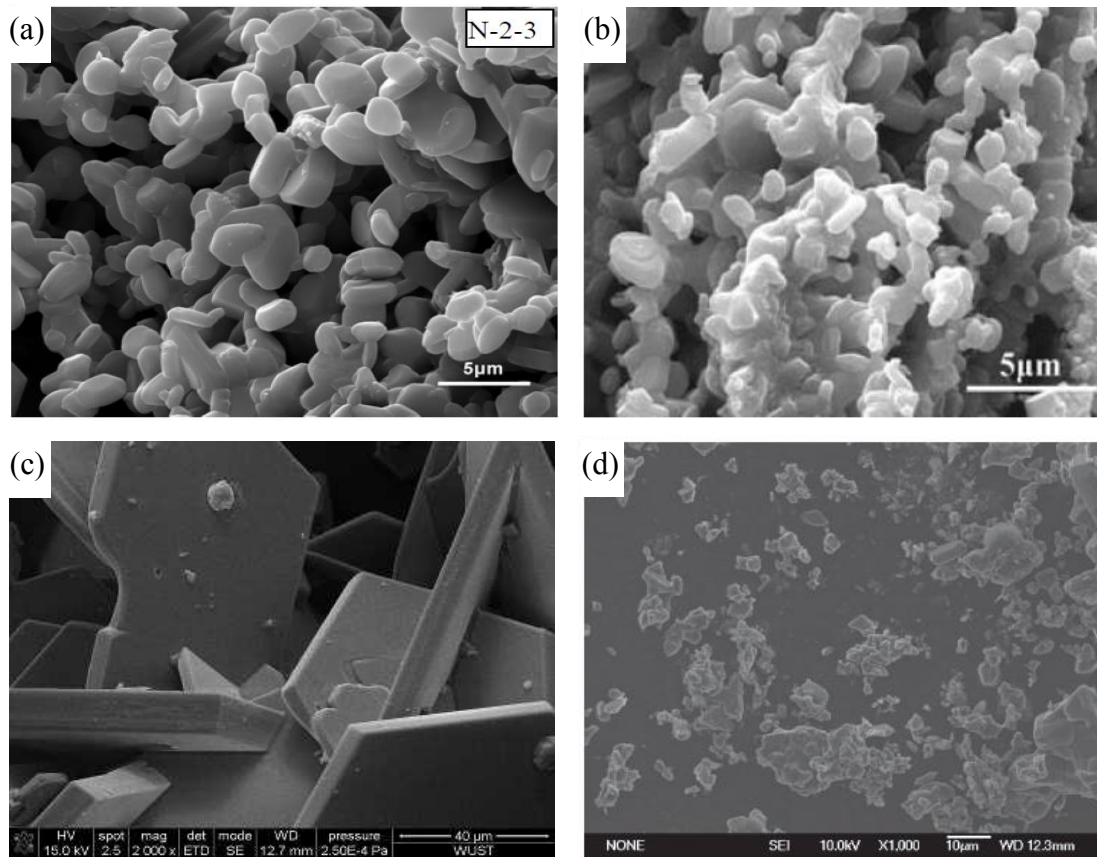
Fig. 2.21 SEM images of $Al_8B_4C_7$/Al_3BC_3 synthesized *via* the aluminothermal

reduction route [42-45] under different conditions: (a) borax as B source, at 1700 ^{o}C

[43], (b) B_2O_3 as B source, at 1700 ^{o}C [42] and (c) B_2O_3 as B source, at 1800 ^{o}C [44];

and (d) *via* carbothermal reduction route using $Al(OH)_3$ and B_2O_3 as reactants at 1800

^{o}C [45].

(a) below 1,050°C, (b) 1,500–1,600°C, (c) 1,600–1,650°C, (d), (e) above 1,650°C and (f) 1,800°C.
($\square$: Al$_2$O$_3$, $\blacksquare$: B$_2$O$_3$, $\blacksquare$: C, $\equiv$: Al$_4$C$_3$, $\boxtimes$: Al$_3$BC$_3$)
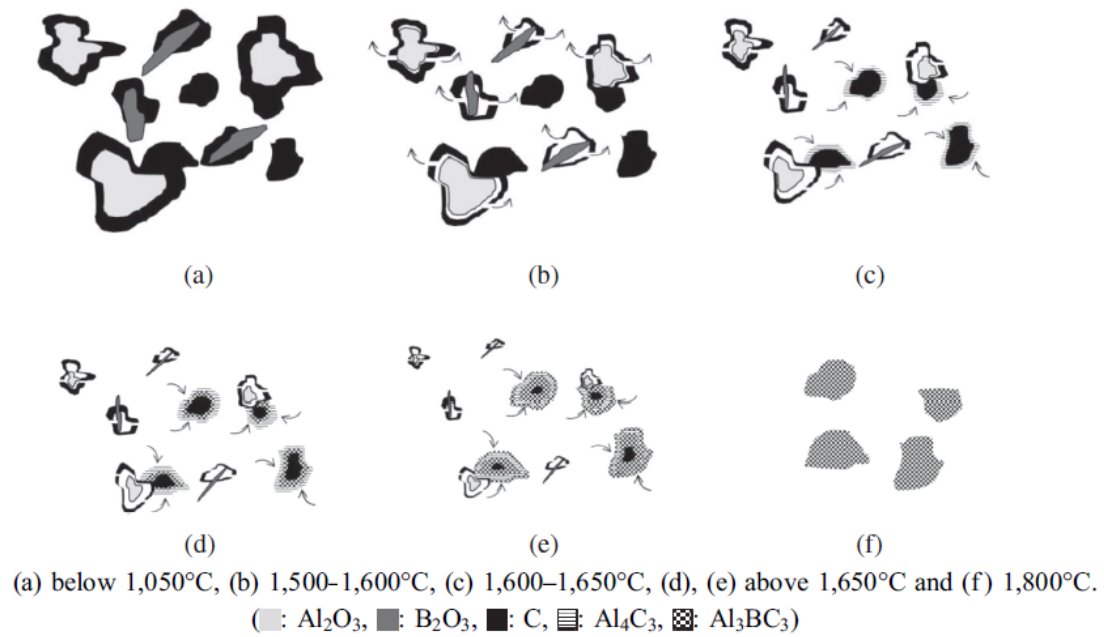
Fig. 2.22 Schematic of reaction mechanisms in the carbothermal production of Al$_3$BC$_3$ [45].

2.3.2 Direct chemical reaction

Another main synthesis route is direct chemical reaction, i.e., heating a mixture of Al/B/C, Al/B$_4$C/C or Al$_4$C$_3$/B$_4$C at an appropriate temperature. In this case, evaporation of aluminum is the only possible reason responsible for the loss of raw material. Therefore, there is no need to use excessive B (or B$_4$C) and C and it is easier to study the reaction process than in the case of carbothermal reduction described above. However, the raw materials are generally more expensive, and the firing temperature still remains high.

Hillebrecht et al [46] heated a mixture of Al, B and C in the molar ratio of 40:2:3 (Al

64

flux method) at 1500 °C. This liquid aluminum medium led to formation of single crystals of Al_3BC_3 along with byproducts of Al_4C_3 and AlB_2 (Al_3BC_3 single crystal was obtained after removing Al by HCl leaching and separating byproducts under the microscope). Inoue et al [51] synthesized $Al_8B_4C_7$ *via* heating Al_4C_3 and B_4C at 1800 °C, and heating a mixture of Al, B and C at 1400 °C followed by further heating 1830 °C. Al, B_4C and C were also used as raw materials. Yuanfei Gao et al [50], Hashimoto et al [3] and Wang et al [2] synthesized $Al_8B_4C_7$ by heating Al, B_4C and C with particle sizes of 5-7 μm at 1600 °C for 3 h, 1600 °C for 1 h and 1800 °C for 2 h respectively. Li et al [74], Che et al [49] and Lee et al [48] synthesized Al_3BC_3 dense body by heating directly Al, B_4C and C at 1800 °C. It was found that at 1300 °C large amounts of Al_4C_3 still remained and the reactions between carbides were slow even at an elevated temperature, due to probably lack of liquid phase. Lee et al [169] also synthesized Al_3BC_3 powders at 1500 °C for 1 h and proposed the responsible synthesis mechanism. At 660 ~1000 °C, Al_4C_3 layers were formed from the reaction of carbon and melted Al. With increasing temperature to >1100 °C, Al_4C_3 increased but dissolved in the aluminum melt in which B_4C also dissolved. With crystallization and growth of Al_3BC_3 in the melt, most of the aluminum was consumed. Then the residual carbides and carbon reacted *via* a solid–solid reaction route (beyond 1340 °C), and aluminum vapor and B/C reacted *via* a gas–solid reaction route (above 1340 °C) (Fig. 2.24).

65
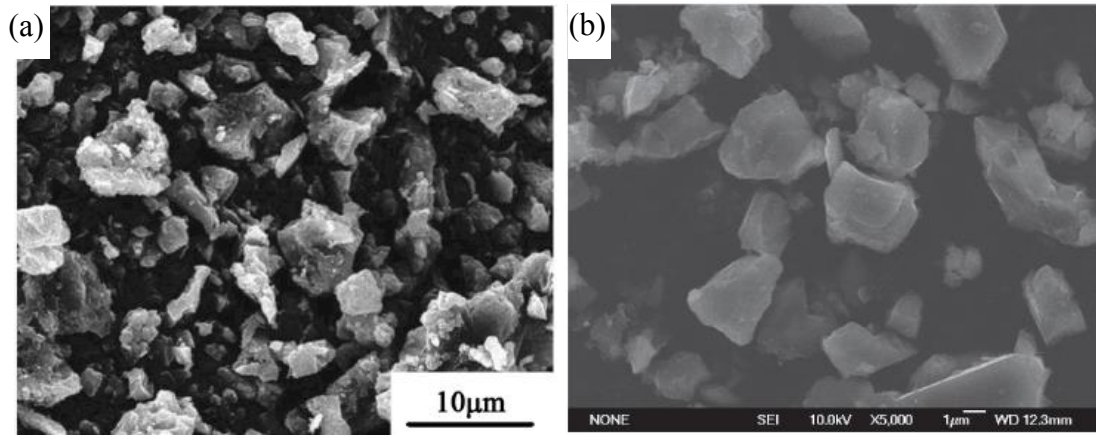
Fig. 2.23 SEM images of aluminum boron carbide prepared *via* direct chemical

reaction, (a)$Al_8B_4C_7$ [50] and (b) Al_3BC_3 [169].
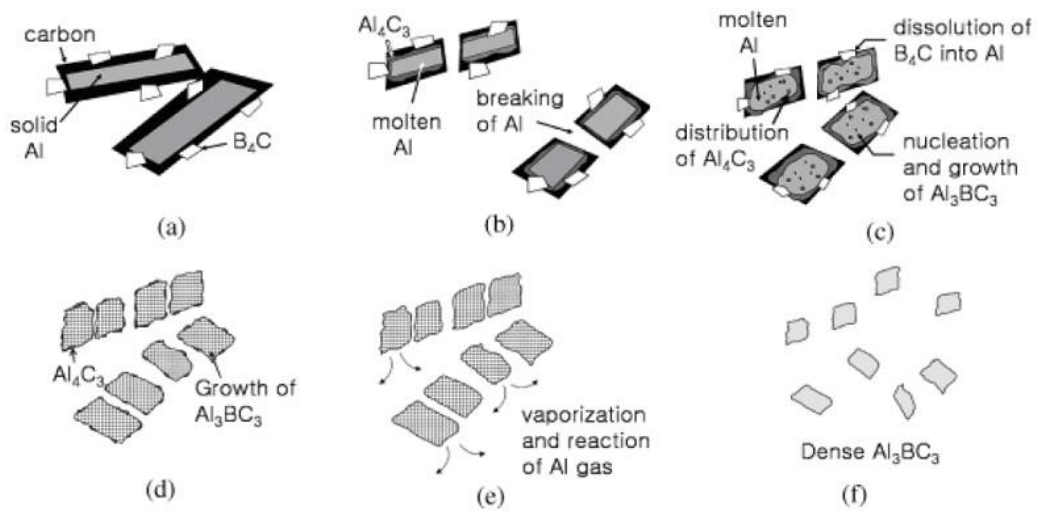
Fig. 2.24 Schematic of reaction mechanisms in the synthesis of Al_3BC_3 *via* direct

chemical reaction [169].

2.4 Synthesis of MoAlB

2.4.1 Al flux method

The metal flux method is widely used in the synthesis of intermetallic compounds [170]. Due to its low melting temperature, large gap between melting point and boiling point and removability well as instability of its binary alloys at high temperatures, aluminum is used as a flux for the synthesis of MoAlB single crystal. Jeitschko prepared MoAlB single crystal (Fig. 2.25) by using an Al bath method from Mo, B and Al in the molar ratio 1:6:1 at 1800 ºC [53]. Okada [54] mixed molybdenum and boron powders, and aluminum chips, in the molar ratio of 1:1:53.3. The mixed reactants were placed in an alumina crucible and heated at 1500 ºC in argon for 10 hours. The residual aluminum was removed by 7 days leaching with HCl (6mol/L). The same method was also used, though under slightly different conditions (molar ratio of Mo:B:Al = 1:1:53.3, fired at 1400 ºC for 10 hours [52]; molar ratio of Mo:B:Al = 1:1:30 - 1:1:150, fired at 1500 ºC for 24 hours [55]).
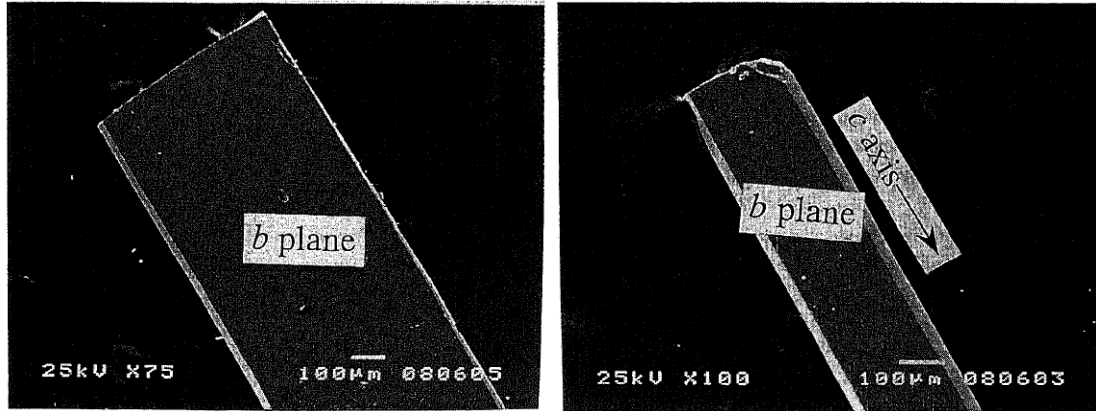
Fig. 2.25 SEM images of MoAlB single crystals synthesized *via* the Al flux method

[54].

However, due to use of too much excessive aluminum, this method is only suitable for small-scale production of MoAlB single crystals.

2.4.2 Reaction between MoB and Al

Dense bulk MoAlB could be prepared by hot pressing using MoB and Al as starting materials. As reported in Refs. 16, 20 and 21, MoB and Al were mixed in the molar ratio of 1:1.3 for 24 h, and placed in a graphite die which was heated at 1200 °C (with a heating rate of 300 °C/h) for 5-5.8 hours under the pressure of 39 MPa [16] (or 30 MPa [20] and 25 MPa [21]).

Apart from hot pressing, direct heating was also used to prepare MoAlB. MoB and Al in the molar ratio of 1:1.2 were ball milled for 6 minutes and then cold pressed [57]. The green sample was heated at 750 °C for 2 h and then 1550 °C for 2 h in argon. A pure

68

MoAlB bulk sample was obtained. Xu et al [19] ball milled MoB and Al for 8 h. The powder mixture was placed in an alumina crucible and heated at 1100 °C for 1 h in argon. Excessive aluminum was removed by washing with 8 wt% hydrochloric acid solution. The as-prepared powder was highly agglomerated with size of 0.5-4 μm and could be used as a raw material for producing bulk samples.
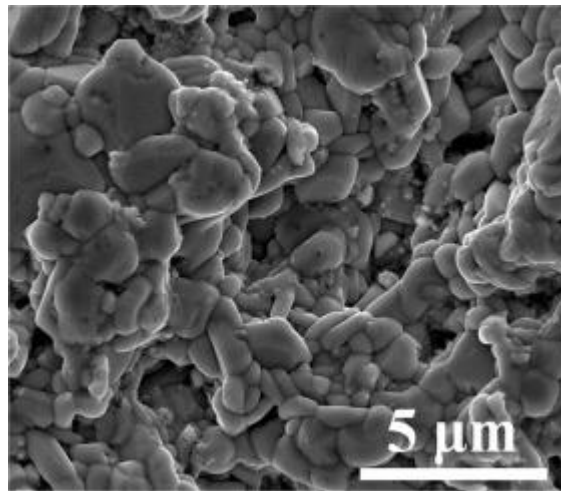
Fig. 2.26 SEM image of bulk MoAlB prepared by direct heating [19].

Sparking plasma sintering is another feasible way to prepare bulk MoAlB [56]. MoB and Al (in the molar ratio of 1:1.1) were ball milled with ethanol for 24 hours. After 5 h drying at 70 °C, the powder mixture was placed in a graphite die and sparking plasma sintered in argon for 8 min at a temperature of 1100 -1200 °C and at a pressure of 50 MPa or 100 MPa. The heating rate and pressure increasing rate were 100 °C/min and 40 MPa/min respectively and initial pressure was 20 MPa. Finally, a dense body was prepared.

The methods described above suffer from various drawbacks. Bulk MoAlB directly prepared *via* SPS or hot pressing contained residual Al which left pores in it after acid leaching. To solve this problem, MoAlB powders free from Al need to be used to prepare dense bodies. However, impurity MoB_2 almost always remained in the product sample. Therefore, an alternative method needs to be developed.

2.5 Synthesis of ceramic-coated carbon

2.5.1 Impact method

High speed impact of a mixture of SiC and graphite is a less expensive coating method [66-67]. The high-speed impact leads activation of graphite surface and absorption of SiC onto the graphite surface, so SiC coated graphite could be prepared. This process is very easy to operate, but the coating prepared is only physically adsorbed (weakly attached) to the surface of graphite, and so easily peels off during prolonged mixing.

2.5.2 CVD

CVD method used to synthesize some material powders (as mentioned earlier) also can be used to prepare high quality coatings on carbon-based materials. For example, by using MMT (CH_3SiCl_3), H_2 and Ar as a source material, a carrier gas and diluent, a sealing gas, respectively, a uniform SiC coating with thickness of ~0.1-0.2 μm was

70

prepared on carbon fiber (CF) [68].
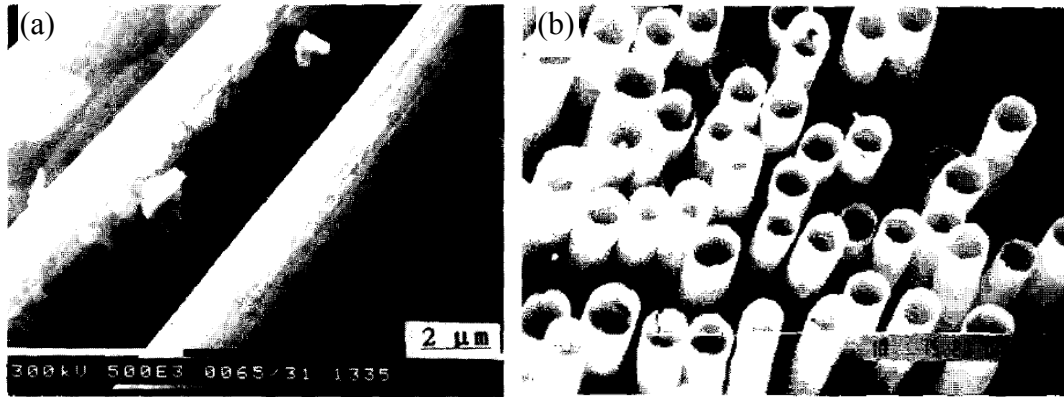
Fig. 2.27 (a) SiC coated carbon fiber prepared *via* CVD and (b) SiC hollow tubes [68].

Hopfe et al [69] used laser CVD (LCVD) to prepare a TiC coating on carbon fibers. Upon heating $TiCl_4$ and H_2 raw materials, a mixture of gaseous $TiCl_3$ and HCl were obtained. Similarly to those in the preparation of SiC coated carbon fibers, H_2 and Ar were also used respectively as carrier gas and diluent, and the sealing gas. After LCVD process, a coating with thickness of 40-50 nm was formed. Adding C_6H_6 or C_2H_2 had little effect on the reaction rate or morphology but decreased the thermal stress between the coating and the fiber.
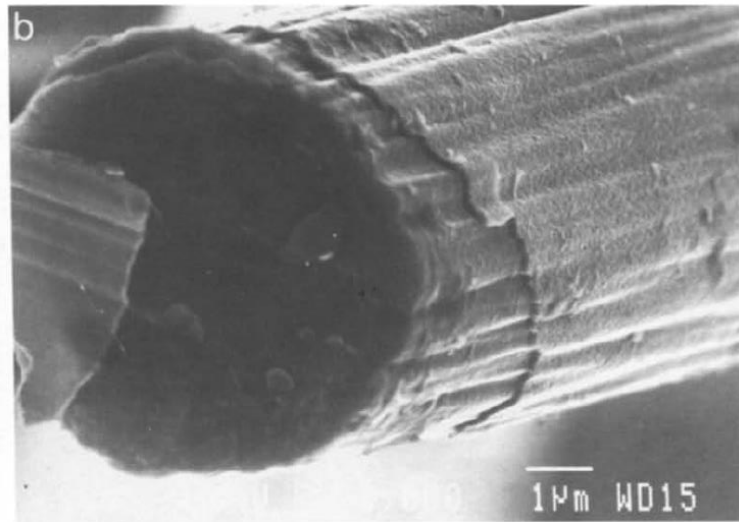
Fig. 2.28 TiC coated carbon fiber prepared *via* CVD [69].

For fabrication of a hafnium carbide coating, hafnium powder and fluoride-containing gases were used along with Ar carrier gas [70]. The coating process was carried out at 1200–1300 K for 1 h at the total pressure of 100 Pa. There were two approaches to fabricate the SiC/HfC coated carbon fibers. One was similar to what was used to make a HfC coating but silicon powder and fluorine-containing gases were used as raw materials. Another one was dipping the fibers into solutions of polysilethynes or polycarbosilanes in chloroform, followed by drying and subsequent pyrolyzing in argon at 293–1200 K.
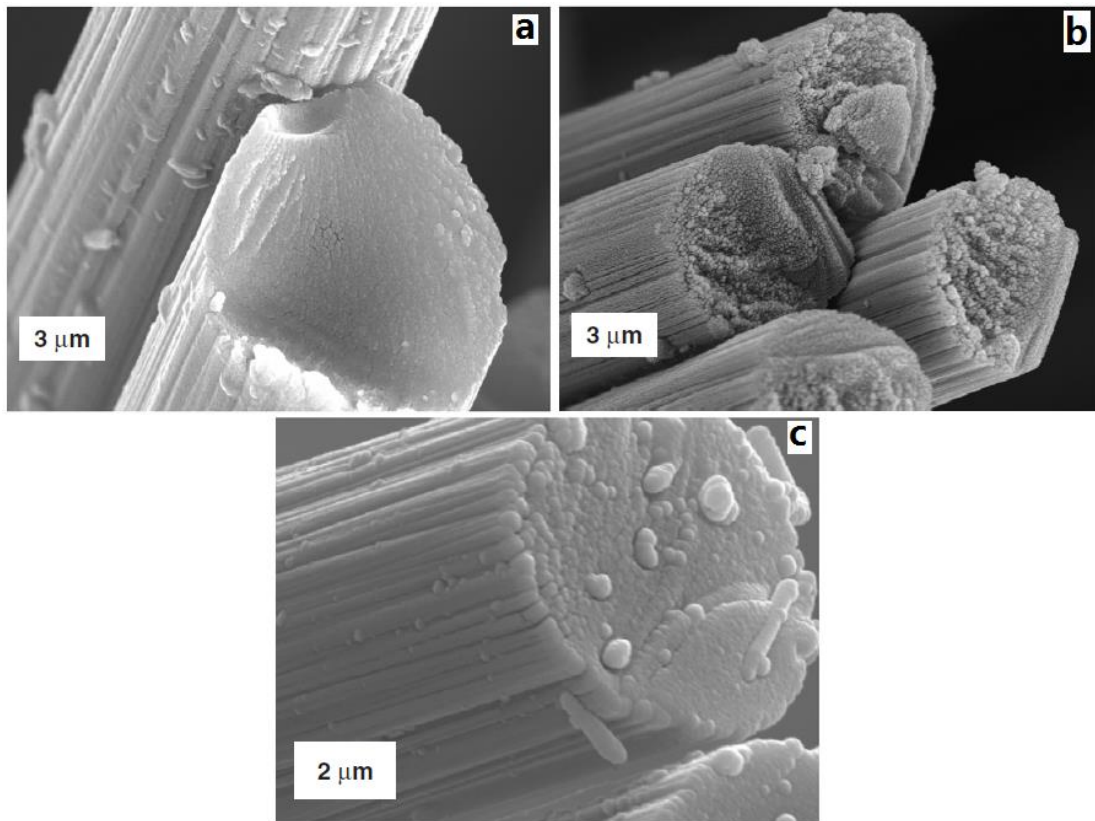
Fig. 2.29 SEM images of (a) carbon fiber (CF), (b) HfC coated CF and (c) HfC/SiC

coated CF [70].

The main drawbacks of CVD method, as described above, included the use of expensive

toxic gases as well as the complex process.

2.5.3 Sol-gel

Several researchers made varieties of oxides coatings on graphite using a sol-gel method.

Zhang et al [171] made SiO_2, Al_2O_3 and $SiO_2 + Al_2O_3$ coatings on graphite surface from

TEOS and $Al(OC_3H_7)_3$ precursors. After drying at 120 ^{o}C and further heating at 500 ^{o}C,

the sols transferred into amorphous gel coatings. Water wettablity was evidently improved, especially in the case of SiO_2 coated graphite. Oxidation resistance was also enhanced.

Sunwoo et al [139] coated graphite with ZrO_2 derived from hydrolysis of $ZrOCl_2.8H_2O$ aqueous solution. PVA (polyvinyl alcohol) was added to enhance the Zr ion adsorption on graphite surface. Zeta potential of ZrO_2 coated graphite increased and oxidation resistance was improved.

Yu et al [138] obtained TiO_2 coated graphite by heating a mixture of titanium alkoxide $(Ti(OC_4H_9)_4)$ (Fig. 2.30) and graphite. Water-wettability, flowability and oxidation resistance of graphite powders were greatly improved after the coating.

$$(C_4H_9O)_4Ti + H_2O \rightarrow (C_4H_9O)_3TiOH + C_4H_9OH$$
$$(C_4H_9O)_4Ti + 2H_2O \rightarrow (C_4H_9O)_2Ti(OH)_2 + 2C_4H_9OH$$
$$(C_4H_9O)_3TiOH + HOTi(OC_4H_9)_3 \rightarrow (C_4H_9O)_3Ti-O-Ti(OC_4H_9)_3 + H_2O$$
$$(C_4H_9O)_4Ti + HOTi(OC_4H_9)_3 \rightarrow (C_4H_9O)_3Ti-O-Ti(OC_4H_9)_3 + C_4H_9OH$$
$$(C_4H_9O)_3Ti-O-Ti(OC_4H_9)_3 \xrightarrow{(C_4H_9O)_3TiOH} Ti[O-Ti(OC_4H_9)_2]_nOTi(OC_4H_9)_3$$
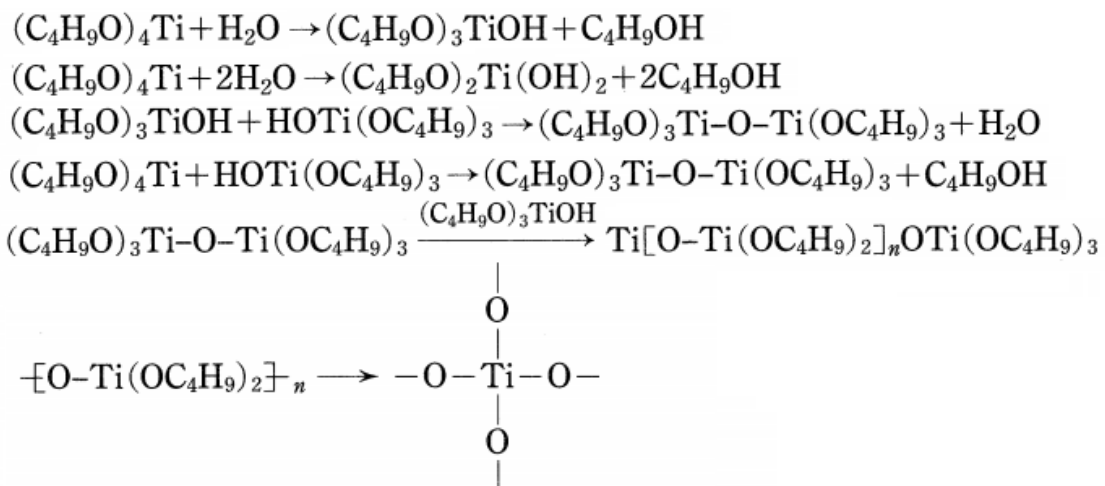
Fig. 2.30 TiO_2 derived from hydrolysis of titanium alkoxide [138].

Kawabata et al [172] made several types of Al_2O_3 based coatings ($Al_2O_3 + CaO$, Al_2O_3

74

+ ZrO_2, Al_2O_3 + TiO_2, Al_2O_3 + SiO_2 and Al_2O_3). The precursors were ethyl acetoacetate aluminum diisopropoxide, calcium acetate monohydrate, titanium tetra-isopropoxide, zirconium tetran-butoxide and tetraethyl orthosilicate. The slurries of graphite coated with Al_2O_3 + CaO and Al_2O_3 + TiO_2 had higher while those with Al_2O_3 + ZrO_2, Al_2O_3 + SiO_2 and Al_2O_3 had lower viscosity with addition of a dispersion agent.

Nanostructured calcium aluminate coatings were prepared on graphite surface by Mukhopadhyay et al [173-175] using calcium carbonate and reactive alumina (or alkoxide and hydrated calcium nitrate) as raw materials. The zeta potential was increased in the case of PH > 7. The oxidation resistance of graphite was improved as well.

Saberi et al [176] developed $MgAl_2O_4$ spinel coating on graphite by using Magnesium nitrate, aluminum nitrate, citric acid and ammonia solution. The water wettability of graphite was enhanced as proved by floating ratio (FR), volume of sediment (SV), contact angle and zeta potential. TG exhibited that the oxidation resistance of graphite was also improved upon coating.

However, this method is not suitable for preparing carbide coated carbon materials due to the high carbothermal reaction temperature and carbon loss arising from the carbothermal reaction.

2.5.4 Molten salt

Carbides like SiC and TiC were successfully coated on graphite and carbon black using a molten salt synthesis (MSS) method based on the template growth mechanisms. When carbon, metal (or oxides) and salt (NaF, NaCl, KF, LiCl and KCl) were used as raw materials, upon firing, the salt would melt first, forming a liquid reaction medium. Then the metal would dissolve slightly into the molten salt medium. The dissolved metal would diffuse through the molten salt rapidly to the surface of graphite/carbon black, and react *in-situ* with the remaining undissolved carbon, forming a carbide coating on its surface.
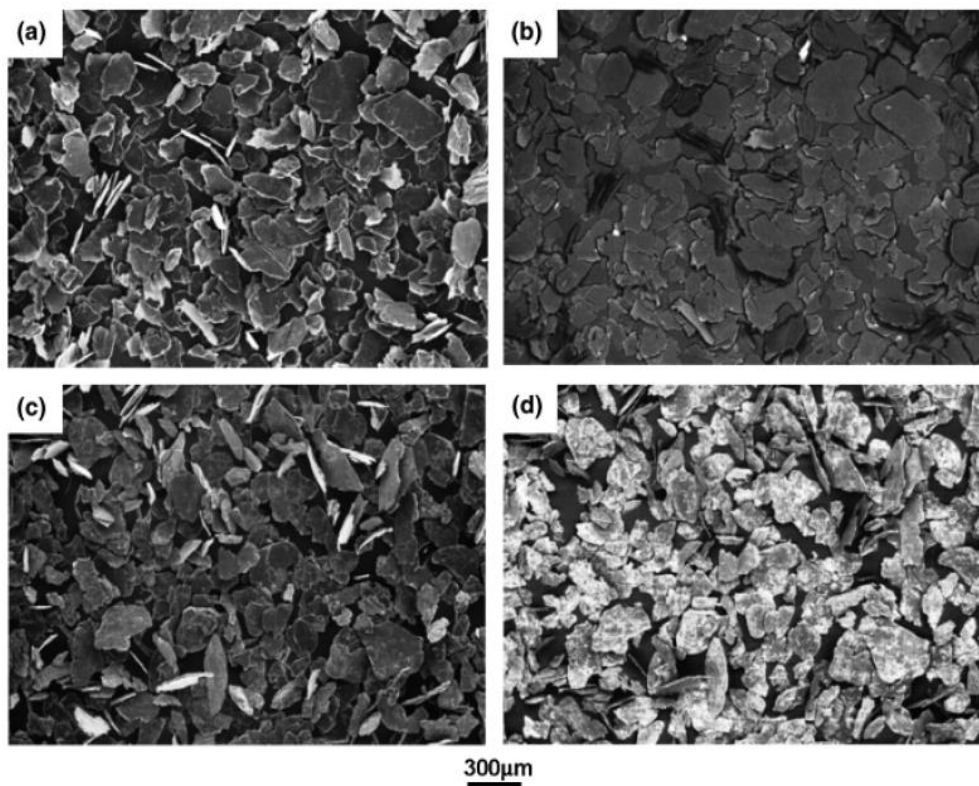
Fig. 2.31 SEI of (a) graphite and (c) TiC coated graphite, and BEI of (b) graphite and

(d) TiC coated graphite [177].
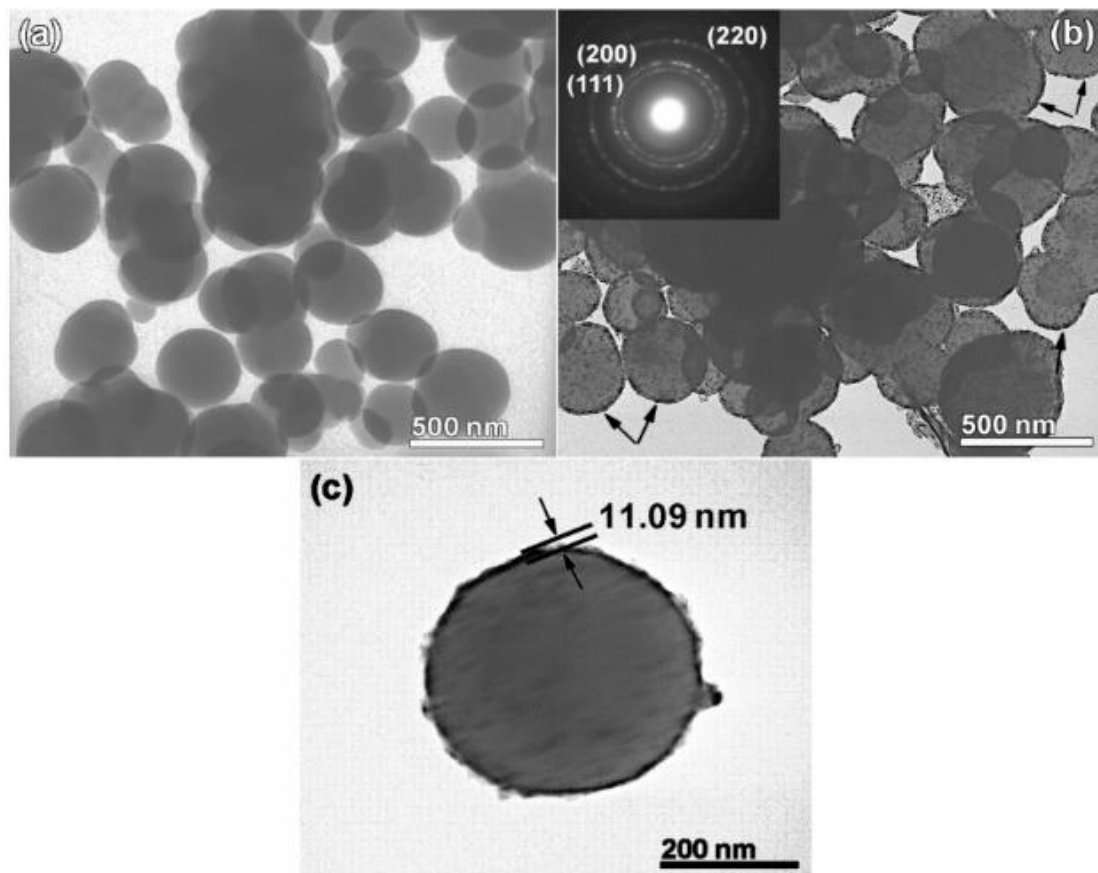
Fig. 2.32 TEM images of (a) CB, (b) TiC coated CB and (c) an individual TiC coated

CB [137].

Due to the high solubility of Ti in KCl, TiC coated graphite [177] and carbon black [137]

were prepared at as low as 900 °C. When complex salt systems containing KCl, KF and

LiCl were used, TiC coating could also be formed on carbon fibers [178] at 900 °C. Due

to relatively low solubility of silicon or tantalum, toxic fluorides were always needed in

the molten salt synthesis of relevant carbides. Also higher temperatures were always

required. For example, NaF and KF were used for preparing SiC and TaC coating

respectively and the temperatures for SiC-graphite [179], SiC-carbon black [136] and

TaC-carbon fibers [180] were 1300 °C, 1100 °C, and 1100 °C, respectively.

77

2.6 Molten Salt Synthesis

As mentioned above, the molten salt synthesis (MSS) technique can be used to form carbide coatings on a carbon substrate. It is actually also an effective way to synthesize various types of ceramic powders. Appropriate amounts of salts (a single salt or mixture of several salts) are introduced to form a melt when heated above the melting point (single salt) or eutectic point (mixed salts). The molten salts, as ionic liquids with ionized anions and cations [181], can act as a reaction medium to enhance diffusion of reactants or sometimes be the reactants directly taking part in the synthesis. Compared with the traditional solid state synthesis method, mass transport is facilitated by introducing these ionic liquid phases. Therefore, MSS leads to lowered synthesis temperature, higher purity, lower agglomeration and controllable sizes and shapes.

2.6.1 Selection of salts

In the MSS technique, salt selection is an important issue. The requirements of the salts used for MSS are listed below [218].

i) The salt should be stable, inexpensive and readily available.

ii) The salt must be water (or other inexpensive solvent) soluble so that it can be easily removed by rinsing and washing after synthesis.

iii) The salt must not produce undesirable phases during synthesis, neither with reactants nor products. The byproducts must be easily removed, e.g., by hydrochloric acid

78

leaching.

iv) The salt should have an appropriate melting point for the synthesis process. Generally, a salt with a low melting point is preferred. In some cases, it is better to use a mixture of different salts to lower the overall melting point and/or adjust/tailor the salt properties (e.g., viscosity). However, in some cases where the synthesis reaction requires a relatively high temperature, a salt with an appropriately high melting point has to be used.

v) The salt should have a low vapor pressure (to prevent the rapid vaporization) and a low viscosity to enhance the convection at the firing temperatures.

vi) The solubility of each reactant in the molten salt at the firing temperatures has to be considered, as it affects significantly the diffusion of species in the salt and overall reaction rate. Also, the differences in the solubility of reactants in the molten salt determine the relevant reaction mechanisms. Salts in which all the reactants are insoluble are ineffective in the synthesis process and should not be selected.

2.6.2 Mechanisms

Two main mechanisms, dissolution-precipitation mechanism and template-growth mechanism, are generally involved in the MSS process, depending on the solubility differences of the reactants in the molten salt [182] (Fig. 2.33). In the MSS dominated by the dissolution-precipitation mechanism, all the reactants have sufficiently high solubility, so they slightly dissolve and react in the molten salt media, precipitating an

79

insoluble or almost insoluble solid product (Fig. 2.33a). On the other hand, in the MSS

governed by the template-growth mechanism, the reactant with higher solubility slightly

dissolves in the molten salt and diffuse through it onto the surface of the insoluble or

much less soluble reactant and then react *in-situ*, forming a solid product which largely

retains the shape and size of the latter (Fig. 2.33b).
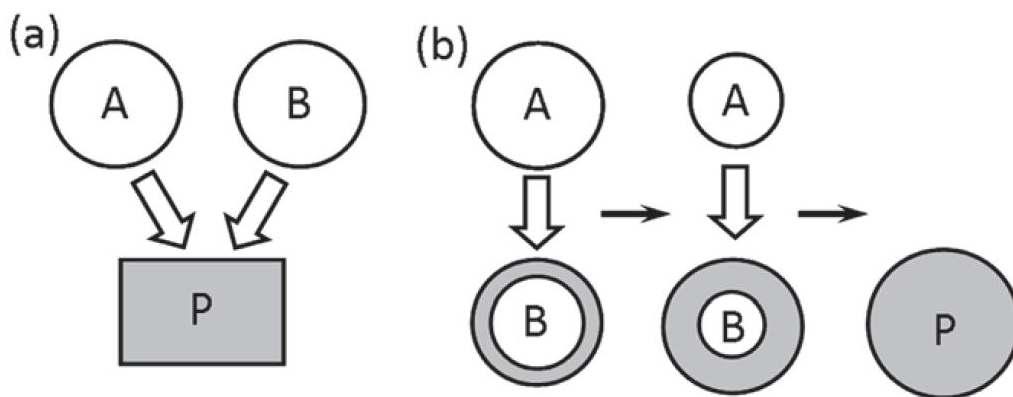
Fig. 2.33 Schematic showing (a) the dissolution-precipitation mechanism and (b) the

template-growth mechanism involved in MSS [182].

2.6.2.1 Molten salt synthesis based on the dissolution-precipitation mechanism

Many complex oxide materials have been synthesized so far based on the dissolution-

precipitation mechanism. One example is with the synthesis of Bi_2SiO_5 [183]. Fig. 2.34

shows SEM images of the as-received raw SiO_2 and Bi_2O_3 powders, and Bi_2SiO_5 product

particles synthesised at 625 °C for 1 h in Na_2SO_4-NaCl. Although rod like Bi_2O_3 and

irregular shaped SiO_2 particles were used, the synthesized Bi_2SiO_5 particles showed

plate-like shapes, indicating dominance of the dissolution-precipitation mechanism in

80

the synthesis process. Both of the reactants were reported to have relatively high solubility in molten NaCl or Na_2SO_4. So at the test temperatures, they dissolved partially in the molten $NaCl/Na_2SO_4$, which improved significantly the mixing between the two (homogeneous mixing at the atomic level had been achieved). Furthermore, their diffusion was also facilitated considerably in the molten salt medium, becoming much more rapid than in the case of solid state. Therefore, the dissolved Bi_2O_3 and SiO_2 reacted in the molten salt much more rapidly than in the case of conventional solid state reaction. Bi_2SiO_5 crystals started to precipitate from the molten salt media when it is oversaturated. Due to this, the product Bi_2SiO_5 did not retain the shape and size of either of the original reactant particles.
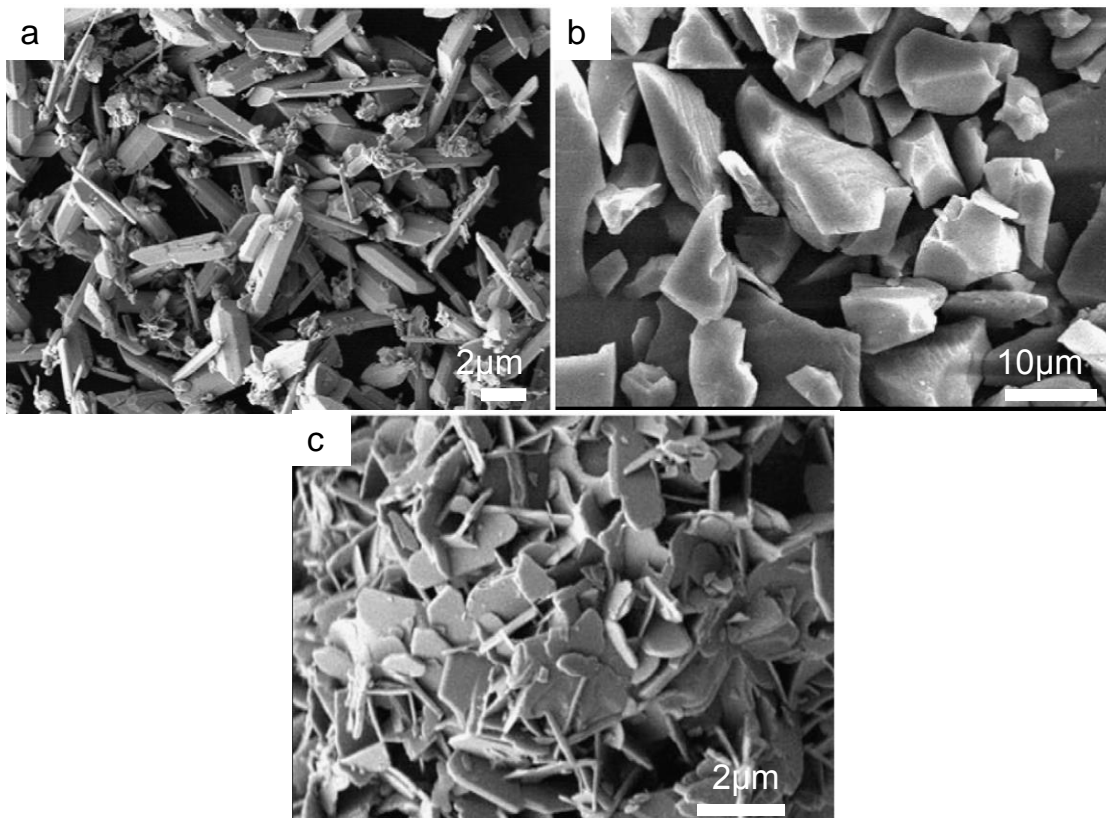
Fig. 2.34 SEM images of (a) SiO_2, (b) Bi_2O_3 and (c) molten salt synthesized Bi_2SiO_5 powders [183].

Another example is with the molten salt synthesis of LaAlO$_3$ in a NaCl based salt containing small amounts of NaF [262]. As La$_2$O$_3$ and Al$_2$O$_3$ reactants have some solubility in the molten salt, the dissolution-precipitation mechanism dominated the synthesis process. So the as-prepared LaAlO$_3$ exhibited different morphology and size than those of the starting material powders (Fig. 2.35)
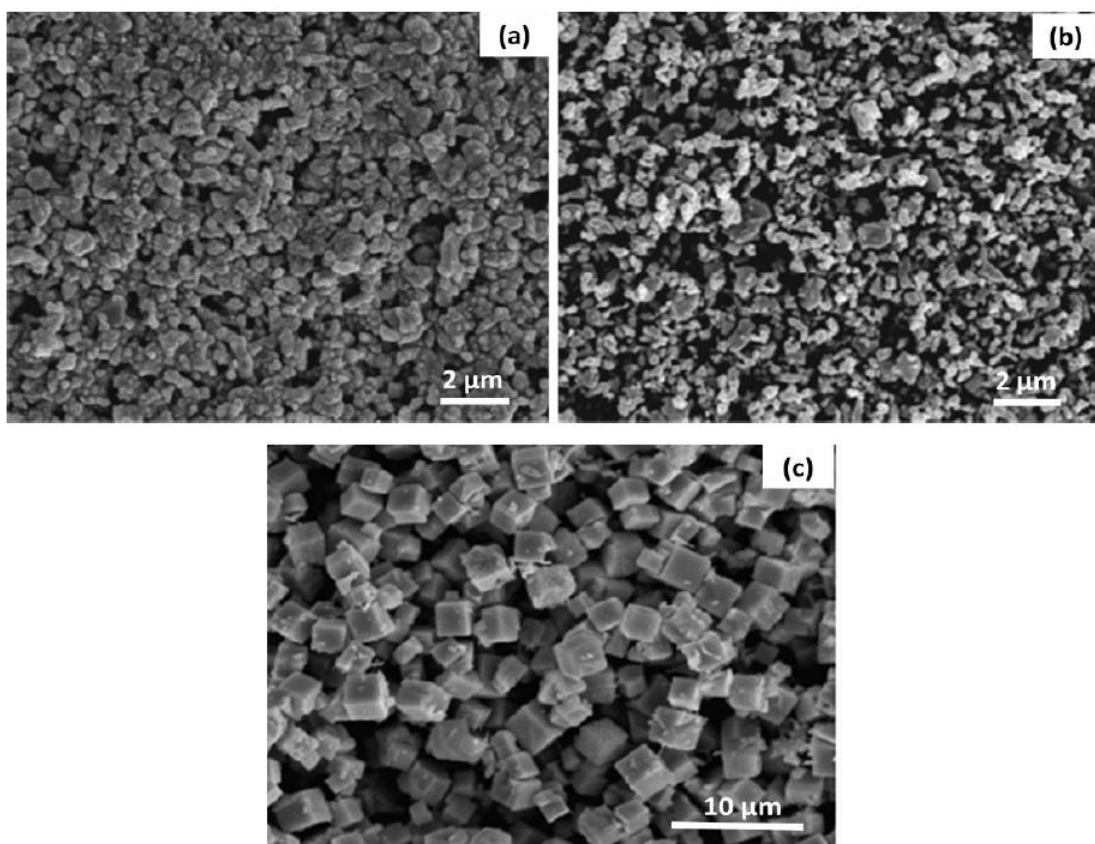
Fig. 2.35 SEM images of (a) La$_2$O$_3$; (b) Al$_2$O$_3$, and (c) LaAlO$_3$ synthesised in NaCl-NaF at 630 $^{\circ}$C for 3 h, showing different morphologies and sizes of the reactant and product particles [262].

2.6.2.2 Molten salt synthesis based on the template-growth mechanism

The template-growth mechanism has also been used to synthesise many materials with interesting morphologies and novel properties. Fig. 2.36, as an example, presents microstructural images of molten salt synthesised $ZnAl_2O_4$ powder and the starting material precursors [184], revealing that , the as-prepared $ZnAl_2O_4$ particles largely retained the morphology and size of the raw material Al_2O_3 which had much lower solubility than ZnO in the molten salt used. BSI of the cross-sections of the resultant powders, along with X-ray dot maps of Zn and Al (Fig. 2.36-c) reveal a core-shell structure, providing further evidence supporting the dominance of the template-growth mechanism.
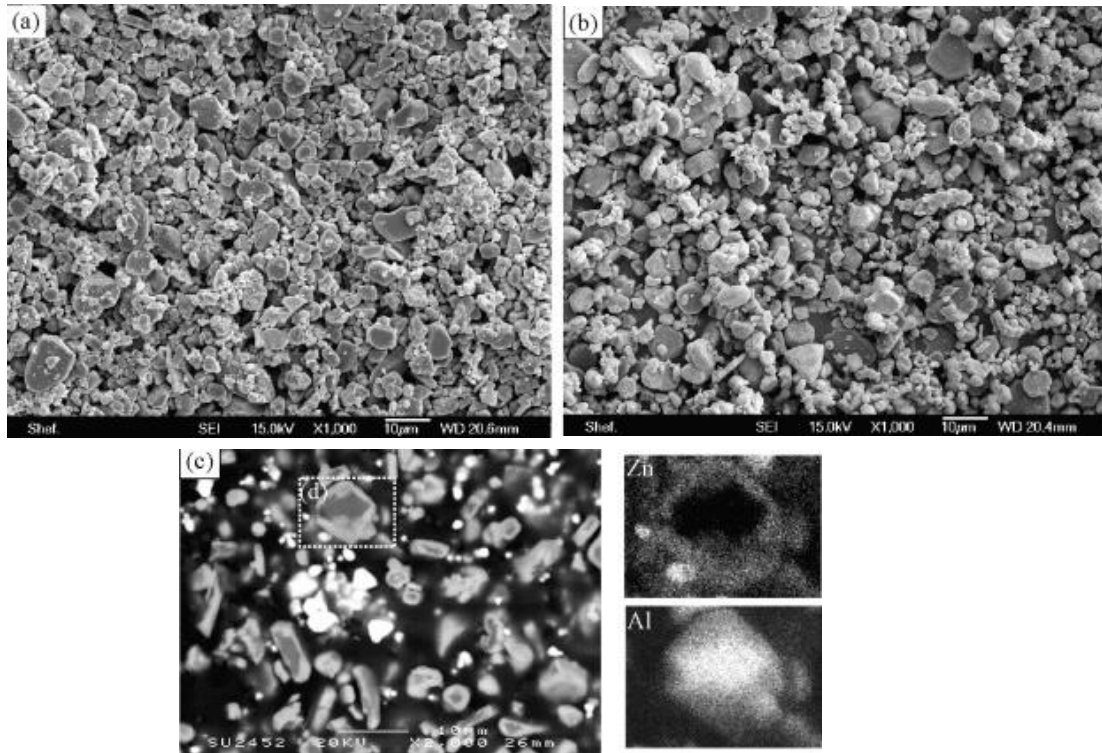
Fig. 2.36 SEI of (a) Al_2O_3, (b) as-prepared $ZnAl_2O_4$ powders, (c) BEI of some resultant powders and (d) EDS mapping of selected area in (c) [184].

83

Apart from complex oxides, many useful carbide-based materials can be also prepared based on the template-growth mechanism, this is largely due to the insolubility of carbon in molten salt under normal synthesis conditions. In addition to carbide coating formation on a carbon substrate, various types of carbide powders and nanorods, in particular, TiC and SiC, have been synthesized in molten salt [136-137,177-179,214,218,263]. Fig. 2.37, as an example, shows microstructural images of SiC nanorods prepared in molten NaCl - NaF by using carbon nanotubes as the template, revealing that as-prepared SiC nanorods largely retained the shape and size of the original carbon nanotubes [263].
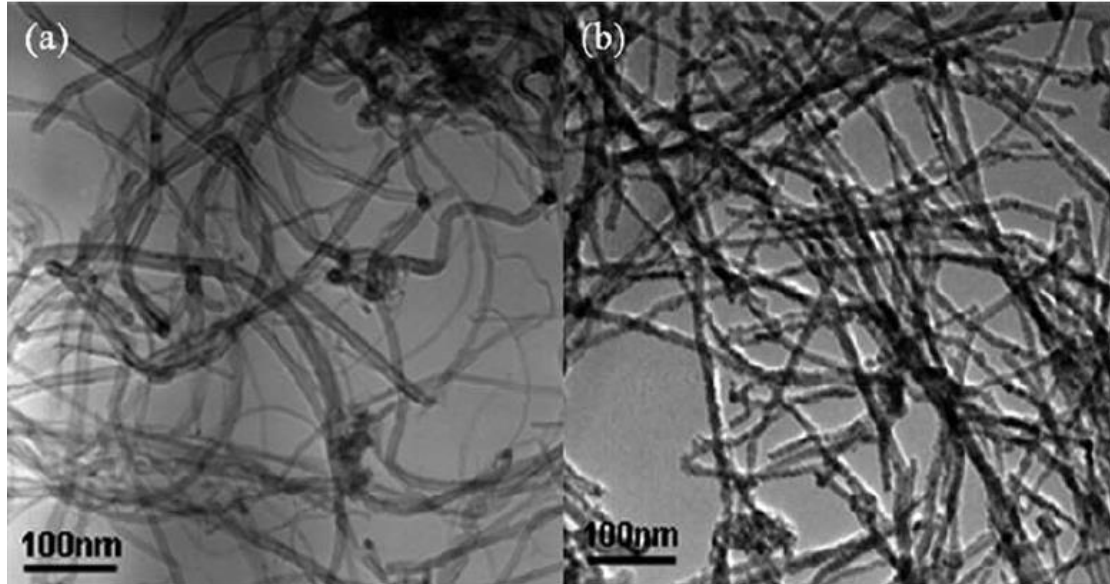
Fig. 2.37 TEM images of (a) as-received MWCNTs and (b) the resulting SiC nanorods synthesised in NaCl-NaF at 1200 ºC for 4 h, showing similar morphologies and sizes of the reactants and products [263]

2.6.3 Advantages and disadvantages of molten salt synthesis

Compared with the conventional synthesis techniques, the MSS technique exhibits the following main advantages [218].

i) Because of the presence of the molten salt medium, the reaction rate is remarkably accelerated and hence the synthesis temperature can be significantly lowered and the reaction time shortened, especially when compared with the case of using the conventional solid-state reaction route.

ii) Compared with other low temperature synthesis methods such as sol-gel, the MSS process is simple, inexpensive and suitable for large-scale production. Furthermore, there is little restriction on the choice of precursors, so cheap natural raw materials can be used directly as the starting materials.

iii) As-prepared powders are homogenous and well dispersed with high surface reactivity, which is beneficial to the future sintering/densification process and makes the molten salt synthesized powders more suitable for making dense structural components.

iv) In the case of synthesis based on the template-growth mechanism, shape and size of the final product can be easily controlled/tailored. Many interesting morphologies (e.g., spheroidal, platelet-like, or lath/needle-like), and sizes from nano-scale to micro-scale can be achieved by using an appropriate template. Materials with complex shapes, which are difficult to fabricate by other conventional methods can be readily prepared by the MSS method.

85

Despite these advantages, the MSS method also suffers from the following disadvantages, which need to be addressed properly.

i) Due to the evaporation of the molten salt at high temperature for a prolonged time period, large amounts of salt have to be used to compensate for it.

ii) MSS is not suitable to prepare products which react with leaching/washing agents (water, hydrochloric acid or Ethanol), e.g., AlB_2, MgB_2 and Al_4C_3.

iii) MSS cannot be used to synthesise materials corrodible by the selected molten salt.

iv) If all the reactants are insoluble or have too much low solubility in the salt, the MSS method would not be useful or effective for the material synthesis.

v)Large amounts of leaching agents (e.g., water and acid) need to be used to remove the residual salt, byproducts and other impurity phases.

Chapter 3. Characterisation Techniques

In this chapter, the main characterisation techniques employed in this thesis work are described.

3.1 X-ray diffraction (XRD)

X-ray diffraction (XRD) is a useful technique for identifying phase composition and crystalline structures. Crystalline materials are composed of regular arrays of atoms which can scatter X-ray which is considered as an electromagnetic wave with a wavelength comparable to lattice distances of crystals. Therefore, every crystalline substance gives a certain diffraction pattern *via* XRD technique, no matter whether it is a single phase or in a multi-phase mixture [185]. An X-ray beam incident on a crystalline substance will be scattered in all directions by the atom's electrons. In some certain directions, an increased intensity is observed. This phenomenon is because of the constructive interference of the waves scattered from lattice planes, which occurs when the difference between the path lengths of the two waves is an integer number of the wavelength (Figure 3.1). This is the Bragg's law:

$n\lambda = 2d\sin\theta$

where d is the interplanar spacing, θ is the incident angle (the angle between the diffraction beam and the transmitted one is 2θ), λ is the wavelength of the X-ray beam and n is a positive integer.

87
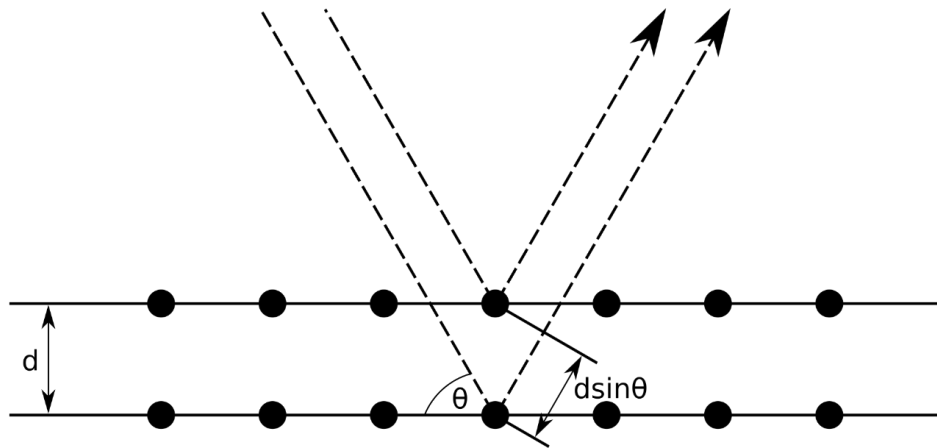
Fig. 3.1 Schematic illustration of Bragg's law [186].

To study phase composition and atomic structures, the positions, intensities and profiles of the peaks in a diffraction pattern are important information. The peak positions are related to the crystal structure and symmetry while the peak intensities exhibit the total scattering from each lattice plane which is determined by the crystal structure and phase composition [187]. The peak width can be used to calculate the crystalline size *via* the Scherrer equation [188]:

$$D=K\lambda/(\beta\cos\theta)$$

where D is the average crystallite size, β is the half-width at half-maximum intensity of the peak, θ is the incident angle, K is a dimensionless shape factor and λ is the wavelength of the X-ray beam.

Besides qualitive phase analysis, quantitative phase analysis is also available *via* four methods [188].

1. Method with external standard: $I_i^s(hkl)/I_i^p(hkl)=V_i^s*\mu^p/\mu^s$

($I_i(hkl)$: measured intensity (s: within the sample, p: the pure phase), V_i^s: volume fraction,

88

μ: absorption coefficients (s: the sample, p: the pure phase)).

2. Method with internal standard: $W_i = K_{ij} * W_j * I_i(hkl)/I_j(hkl)$

(W: mass concentration (of phase i or j, both within the sample), I(hkl): intensity of hkl peak (of phase i or j), K_{ij}: a factor that can be measured experimentally).

3. Method of intensity ratio: $V_i = \Sigma_j(I_j(hkl)/I_i(hkl) * R_i(hkl)/R_j(hkl))^{-1}$

(V_i: volume fraction, I(hkl): intensity of hkl peak (i: selected phase, j: other phases), R(hkl): factors that can be measured experimentally (i: selected phase, j: other phases)).

4. Rietveld method: a whole pattern method fitting structure refinement. The measured XRD pattern is refined with a calculated pattern with several structural, microstructural, and experimental parameters.

3.2 Scanning electron microscopy (SEM)

Scanning electron microscope (SEM) is a useful instrument for examination of microstructure and phase morphology. Information such as grain size, shape, distribution and chemical composition (see 3.4) can be obtained. A high-energy electron beam is generated from the electron gun and focused to form a fine probe through electromagnetic lenses (Fig. 3.2). This probe scans the surface of the specimen continuously and gives the information of microstructure in the form of pictures. The electron beams penetrate the surface of specimens and interact with atoms to produce varieties of signals including secondary electrons (SE), cathodoluminescence (CL), backscattered electrons (BSE), Auger electrons (AE) and X-rays (Fig. 3.3).
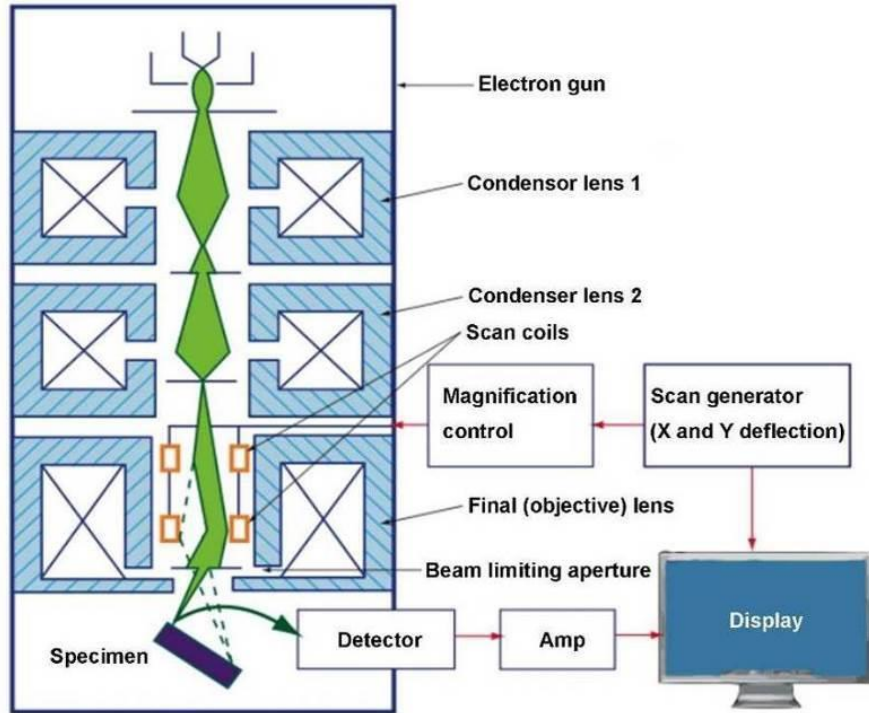
Fig. 3.2 Schematic of the major components of a typical SEM [189].
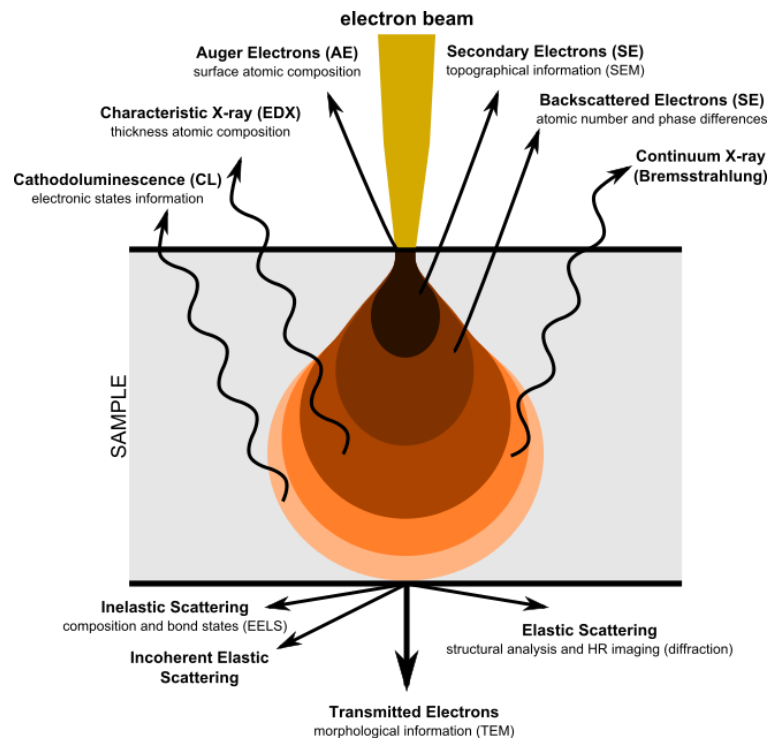
Fig. 3.3 Various electron signals emitted from different parts of the interaction volume

[190].

Among these signals, SE and BSE are most commonly used to form SEM images. Secondary electrons are ejected by inelastic scattering interactions between the k-shell of the specimen atoms and electrons beam. Due to the low energy of 3-5 eV, emission depth of these electrons is a few nanometers from the sample surface [191]. The brightness of the images depends on the amounts of secondary electrons collected by the detector. Increasing incident angle leads to increased interaction volume and more secondary electrons emission. Therefore, images of steep surfaces are brighter than flat surfaces, which makes SE suitable to observe the morphology of the specimens such as texture and roughness.

Backscattered electrons (BSE) are high-energy electrons generated from elastic scattering interactions between back-scattered electrons beam and atoms of specimens. The brightness of images is affected by different elements, this is because elements with high atomic number (having more positive charges on the nucleus) backscatter the electrons beams more strongly than those with low atomic number. Therefore, images obtained *via* BSE show the contrast between areas with different chemical compositions [191]. Because of greater emission depth of BSE than that of SE, images with worse resolutions are always achieved.

3.3 Transmission electron microscopy (TEM)

Transmission electron microscope (TEM) is widely used to study the microstructure of electron transparent specimen at atomic level resolution. Basic principle of TEM is the same as that of optical microscope except using high-energy electrons beam instead of light. A TEM typically contains the electrons beam source (electron gun), lensing system (an electron lens and objective lenses), apertures, and a fluorescent screen or a CCD camera (Fig. 3.4).
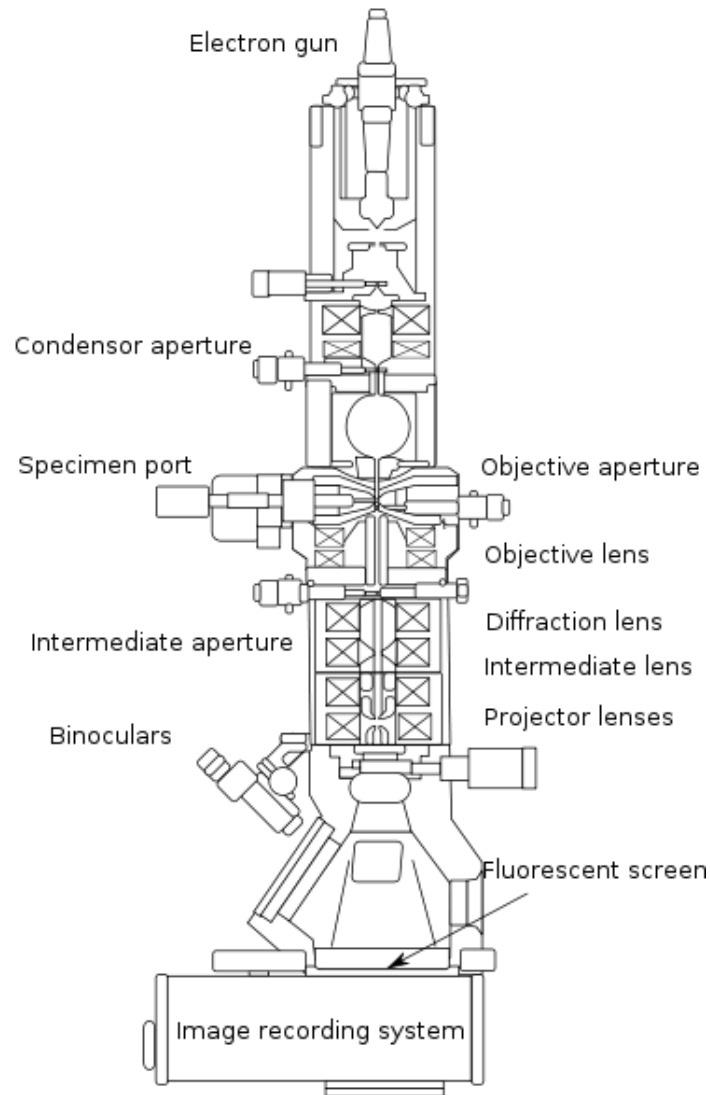
Fig. 3.4 Schematic of a basic TEM [192].

The working process of TEM is as follows: electrons are accelerated to several hundred kV and thus have a decreased wavelength which leads to higher resolution. The difference of wavelength between light and electrons is responsible for the much higher resolution of TEM than optical microscope. The accelerated electrons are projected onto the specimen through the condenser lens system and penetrate it. Then they are taken by the objective lenses, dispersed to give a diffraction pattern (Fig. 3.5) and recombined to give an image (Fig. 3.5). If the object plane is set as the image plane by adjusting the intermediate lens, an image is generated and displayed onto the fluorescent screen or the CCD camera. Otherwise if the back focal plane acts as the object plane, the diffraction pattern is projected onto the fluorescent screen or the CCD camera.
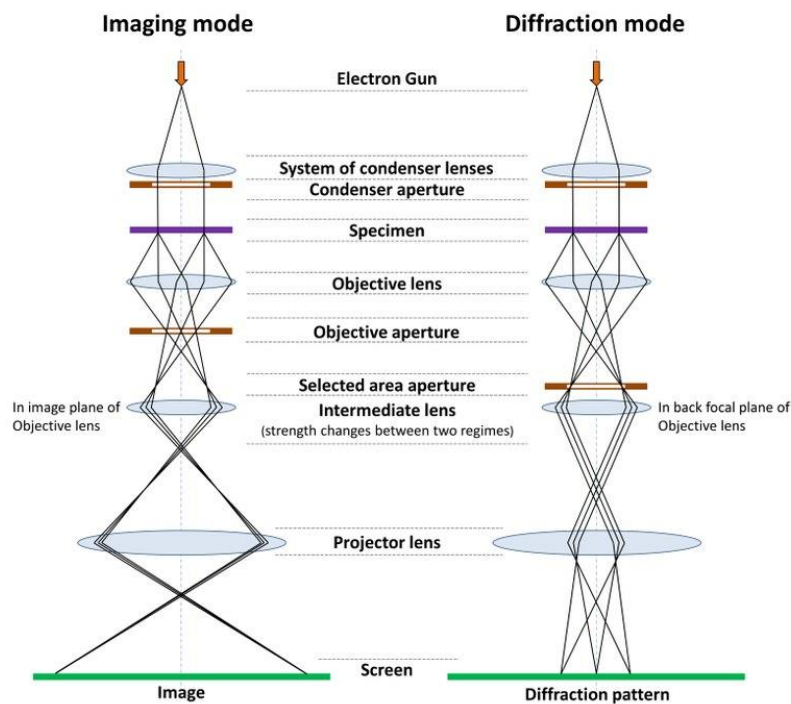
Fig. 3.5 Simplified diagram of the two basic operations of the TEM imaging system involve: left: imaging mode; and right: diffraction mode [193].

93

3.4 Energy Dispersive X-ray Spectroscopy (EDS)

Energy-dispersive X-ray spectroscopy (EDS) is a widely used non-destructive technique for elemental analysis of a specimen. It is often linking with an SEM or TEM. As described above, interaction between the high-energy electrons and atoms of specimen leads to emission of X-ray. The production of characteristic X-ray process is illustrated in Fig. 3.6. Besides the excitation sources, EDS always consists of three other parts, the X-ray detector, the pulse processor and the analyzer. The X-ray energy is converted to voltage signals by the detector, then the signal is received and measured by the pulse processor before being sent to the analyzer for analysis. Due to the unique atomic structure of each element, unique peaks on its electromagnetic emission spectrum are obtained and thus the composition is characterized. EDS can also be used for elemental composition quantitative analysis by comparison with standard reference materials.
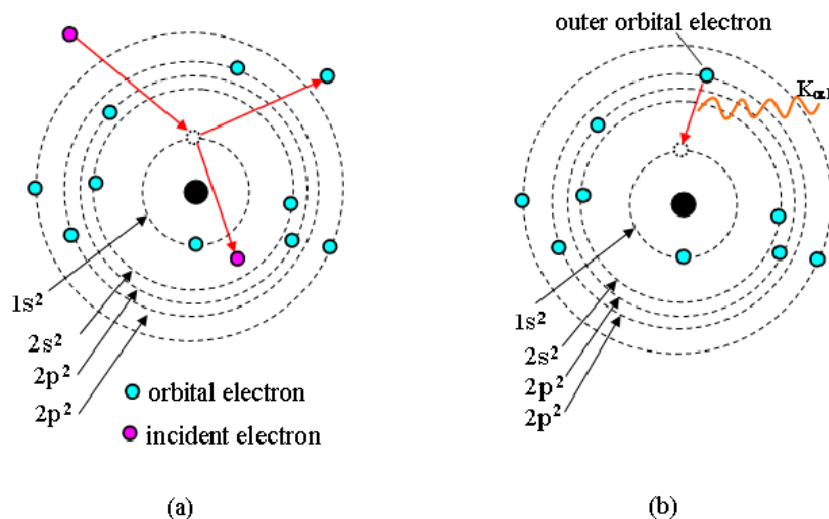
Fig. 3.6 The process of X-Ray production in EDS (a) an inner orbital electron is ejected out (b) the production of characteristic X-Rays from the transition of an electron [194].

3.5 Selected area electron diffraction (SAED)

In diffraction pattern mode of TEM, a selected area electron diffraction (SAED) pattern can be obtained by inserting an SAED aperture into the image plane. SAED pattern reflects crystal structure of the specimen. Because of the very small incident angle caused by small wavelength or high-energy electrons, $\sin\theta$ could be considered approximately equal to θ. Therefore, the Bragg's law can be simplified as follows:

$\lambda=2d\theta$

When related the incident angle to the camera length and the distance between the diffraction spots and camera length (Fig. 3.7), a formula is given:

$\tan2\theta=R/L$

Where R is the distance the diffraction spots and L is the camera length. Due to distance between the diffraction spots is very small, $\tan2\theta$ could be considered approximately equal to 2θ. Therefore, the law could be further modified as:

$\lambda L=Rd$

Because λ and L are constants of the camera, R and d are inversely proportional.

A diffraction pattern gives the information such as lattice distance and possible crystal system (according to the shape) which can support the XRD results. It also reveals whether the specimen is single crystal (spots), polycrystalline (concentric rings, radius represents the distance the diffraction spots) or amorphous (halo ring).

95
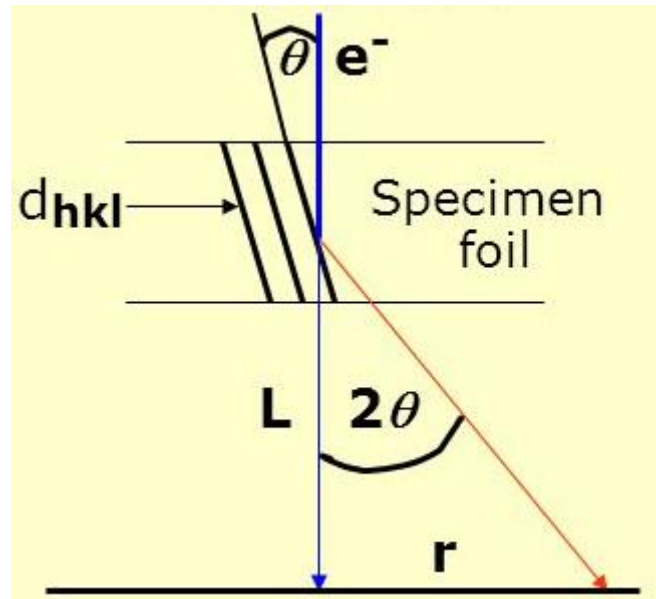
Fig. 3.7 Schematic illustration of the geometry of SAED [195].

3.6 Electrochemical measurements
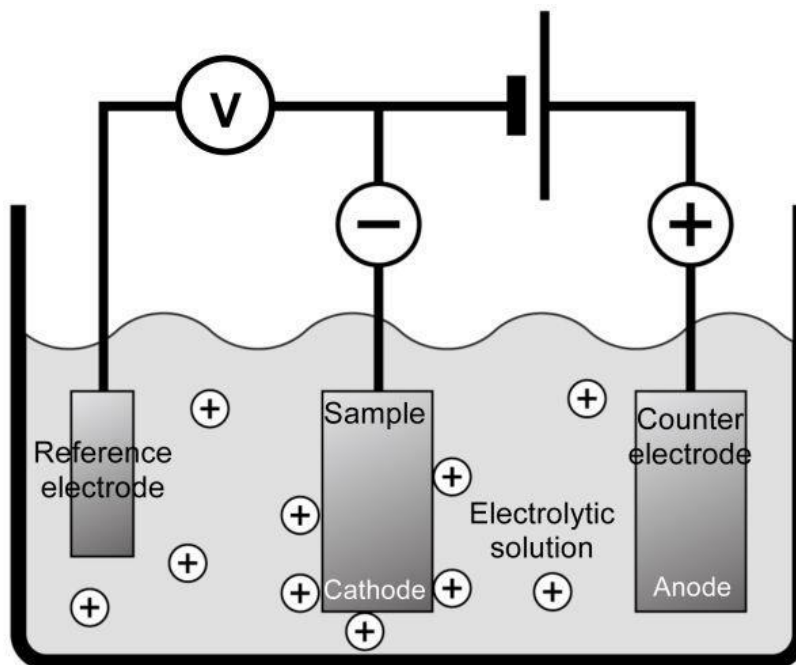
Fig. 3.8 Schematic of an electrochemical workstation.

An electrochemical workstation is a digital potentiostat/galvanostat instrument widely used to monitor/control the change of current and potential in electrochemical studies. In studies of hydrogen evolution reaction, a three-electrode system is used to test the properties of a catalyst. This three-electrode workstation contains three electrodes: a counter (auxiliary) electrode (e.g., Pt electrode), a working electrode (e.g., glassy carbon or Au electrode) and a reference electrode (e.g., Ag/AgCl electrode). The working electrode is used to carry the samples and form a circuit by connecting with the counter electrode. The reference electrode has a highly stable electrode potential. Therefore, the potential of the working electrode can be easily measured. Many testing techniques such as cyclic voltammetry (CV), linear sweep voltammetry (LSV) and Tafel test are based on this three-electrode system. In this thesis work, a CHI 602D instrument was used to test all the electrochemical properties.

Tafel plots of log current versus overpotential (measured value + 0.059*PH value + reference electrode potential (0.2223 V for Ag/AgCl in 1M KCl)) are used to obtain kinetic parameters for the HER. According to Tafel equation, $\eta = b \cdot lg(j/j_0)$, Tafel slope b and current density at a certain potential can be obtained. A good HER catalyst should have high current density and small Tafel slope. An example of Tafel plots is shown in Fig. 3.9.
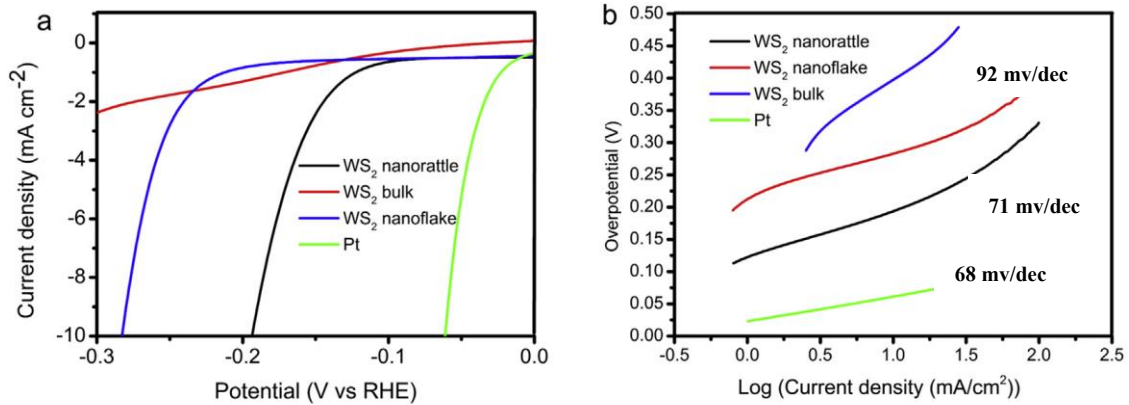
Fig. 3.9. (a) Polarisation curves in [231]; (b) Corresponding Tafel plots;

Cyclic voltammetry (CV) is an electrochemical measurement that the working electrode potential is ramped linearly versus time. The effectively active surface area could be represented by the double layer capacitance (Cdl) of the catalyst. This capacity can be calculated based on the plot of $\Delta j = j_a - j_c$ (where j_a and j_c are current densities at a certain potential) against the CV scan rate. A larger Cdl (which means catalytically active sites) always represents improved HER performance. An example of CV plots is shown in Fig. 3.10.
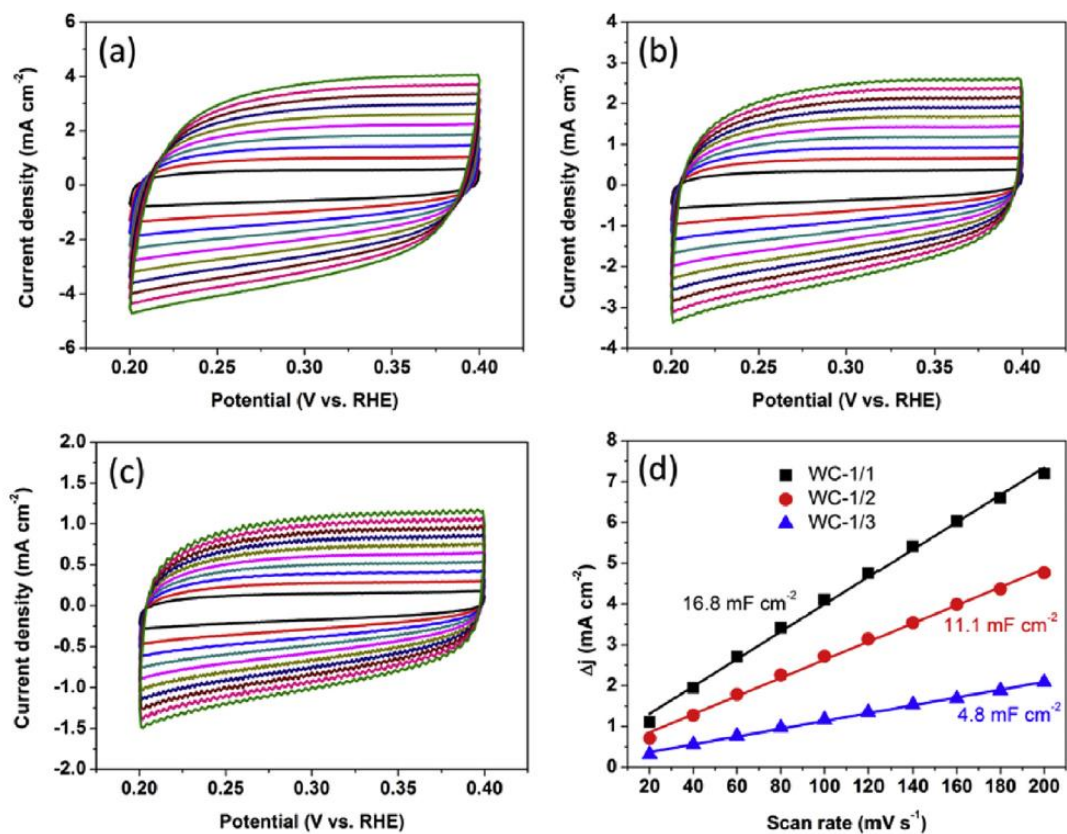
Fig. 3.10. (a-c) CV curves in [29]; (d) Corresponding Cdl;

Electrochemical Impedance Spectroscopy (EIS) is a frequency domain measurement made by applying a voltage to a system. The impedance (the frequency dependant resistance) at a given frequency is related to processes occurring at timescales of the inverse frequency. Due to the response of electrochemical systems is nonlinear, the results are always displayed in the form of Nyquist plots (Imaginary Impedance vs Real Impedance). In HER process, the charge transfer resistances (Rct) can be obtained in this test. A lower Rct always represents better HER performances as well as higher electrical conductivity. An example of EIS results is shown in Fig. 3.11.
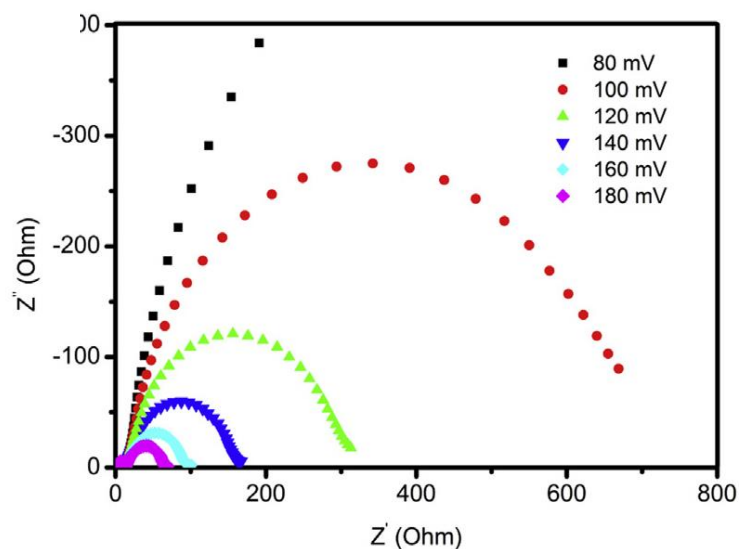
Fig. 3.11. EIS responses in the form of Nyquist plots [231];

3.7 X-ray photoelectron spectroscopy (XPS)

X-ray photoelectron spectroscopy (XPS) is a quantitative spectroscopic technique that can measure the elemental composition, empirical formula, chemical state and electronic state of the elements of a material. The spectra are obtained by illuminating a material with an X-ray beam and synchronously measuring the kinetic energy and number of photoelectrons emitted from 1 nm to 10 nm below the surface of the material.

An XPS system typically includes an X-ray source, an ultra-high vacuum (UHV) chamber, UHV pumps, an electron collection lens, an electron energy analyzer, an electron detector system, a sample introduction chamber, a sample stage, and a set of stage manipulators (Fig. 3.12).

100
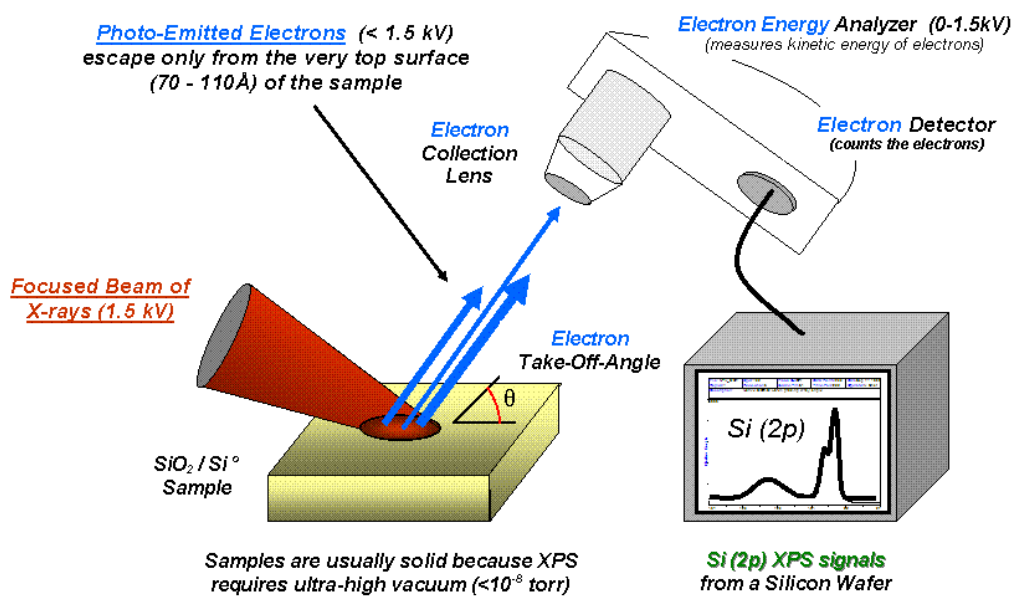
Fig. 3.12 Schematic illustration of basic components of a monochromatic XPS system [196].

Chapter 4. Low temperature molten salt synthesis and characterisation of $Al_8B_4C_7$ powder

4.1 Background

As reviewed in chapter 2, aluminum boron carbide ($Al_8B_4C_7$) is considered as an important candidate material for a variety of important applications such as high temperature structural ceramics, antioxidants in carbon-containing refractories [4,10-13] and sintering aids for SiC, ZrB_2 and B_4C materials [5-9], because of its superior properties including good oxidation resistance, high hardness (15.2 GPa) , high melting point (1900 °C), low density (2.69 g/cm^3) and thermal expansion coefficient ($6.67x10^{-6}$ per K), high thermal conductivity (29.2 W/m/K), and excellent corrosion resistance [1-4].

Several techniques have been developed to date to synthesize $Al_8B_4C_7$ powder. Among them, the thermal reduction method and the direct reaction method were most commonly used. In the former, Al or carbon is used as a reducing agent [42-45], to reduce boron containing oxides to element boron. The main advantage of this is that inexpensive oxide materials can be used to replace much more expensive boron or boron carbide (B_4C). However, a high synthesis temperature (1700 °C~1800 °C) is required to complete the reaction. Also, some by-products, e.g., Al_2O_3 and Al_4O_4C/Al_2OC, often remain in the

102

final product powder. In the case of the latter, Al, B$_4$C and C are used as raw materials, but the synthesis temperature required is still 1600~1800 ºC [2-3,47-50]. Apart from the requirement of high synthesis temperatures (>1600 ºC), the product powders prepared by using these two techniques are heavily agglomerated and have relatively large sizes (>5 μm). To overcome these drawbacks, it is necessary to develop alternative techniques.

In response to this, in the work presented in this chapter, a novel molten salt synthesis method was developed. Phase pure and well-dispersed submicron-sized Al$_8$B$_4$C$_7$ particles were successfully synthesized using B$_4$C, Al and C as starting materials, at a much lowered temperature. The effects of key factors such as firing temperature and salt type/composition were investigated and the synthesis conditions were optimized. Furthermore, the formation mechanism of Al$_8$B$_4$C$_7$ was proposed.

4.2 Experimental procedure

4.2.1 Raw materials

Al (powder, 99.7%, <25 micron), B$_4$C (powder, 99.98%), and C (carbon black powder, ≥99%, <250 nm) powders from Sigma-Aldrich (Gillingham, UK) were used as raw materials, and NaCl (≥99%) and NaF (≥98%) used to form a molten salt medium.

4.2.2 Sample preparation

Al, B$_4$C and C were mixed in the stoichiometric molar ratios of 8:1:6 (1.35 g, 0.35 g and 0.53 g, respectively) corresponding to Reaction (4.1) and further combined with 20g salts (1g NaF + 19g NaCl) by using an agate mortar. The mixed powder batch was contained in a graphite crucible covered with a graphite lid, and placed in an alumina tube furnace. The furnace was heated to a given temperature between 1100 °C and 1250 °C in argon (5 °C/min up to 1000 °C, 3 °C/min up to 1200 °C and then 1 °C/min) and held at the temperature for 6 h.

$$8Al + B_4C + 6C = Al_8B_4C_7 \tag{4.1}$$

To assist investigating the reaction/synthesis mechanisms, Al and B$_4$C (1.35 g and 0.35 g) with the molar ratio of 8:1 were heated initially in 19g NaCl + 1g NaF at 1250 °C for 6 h. Then the unwashed fired sample was milled with carbon black (0.53g, molar ratio of Al/B$_4$C/C = 8:1:6) and 19g NaCl + 1g NaF, and reheated at 1250 °C for 6 h. In another test, Al$_4$C$_3$ (prepared *via* reacting Al with C in 19g NaCl + 1g NaF at 1150 °C for 6 h) was heated with B and carbon black (molar ratio of Al/B$_4$C/C = 8:1:6) at 1250 °C for 6 h.

To study the effects of salt on the formation of Al$_8$B$_4$C$_7$, the raw materials with the stoichiometric ratio were mixed and combined with 20g NaCl or 19.5g NaCl + 0.5g NaF,

104

and then heated at 1250 ºC for 6 h.

The fired samples were directly stored in a sealed container to prevent hydration of Al_4C_3, or washed repeatedly to remove the residual salt and then oven-dried overnight at 100 °C. Phases in the as-prepared product powders were identified by powder X-ray diffraction (XRD) analysis (Brukers D8 advance reflection diffractometer, Karlsruhe, Germany). Spectra were recorded at 40 mA and 40 kV using Ni-filtered CuKa radiation. The scan rate was 2.4° (2θ)/min with a step size of 0.04°. ICDD cards used for identification are $Al_8B_4C_7$ (35-1216), Al_4C_3 (35-0799), AlO(OH) (21-1307), Al (65-2869), Al_2O_3 (46-1212), Al_3BC (50-1470), AlB_2 (65-9698) and NaCl (05-0628). Microstructures and morphologies of as-prepared product powders were observed using a scanning electron microscope (SEM Nova Nanolab 600, FEI Company, Hillsboro, OR) and a JEM 2100 transmission electron microscope (TEM, 200 kV).

4.3 Results and discussion

4.3.1 Effect of firing temperature
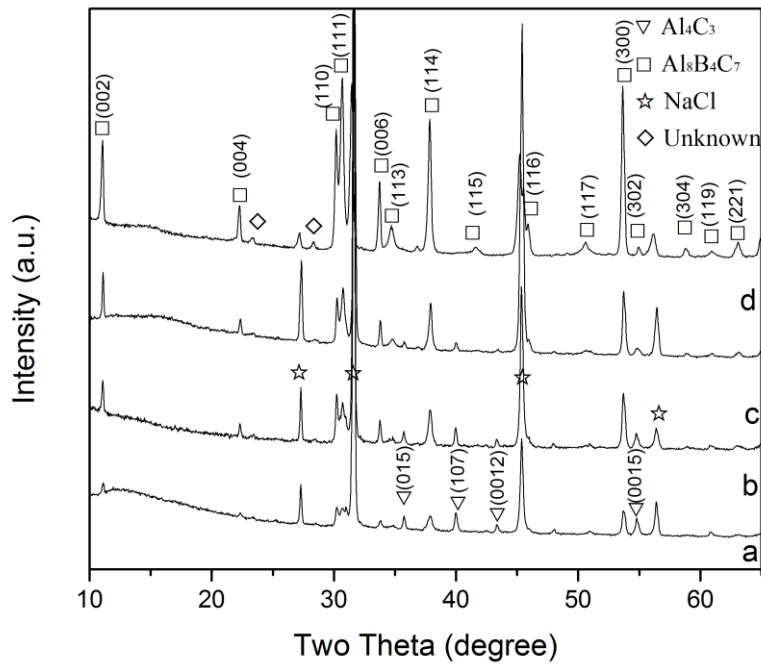
Fig. 4.1 XRD patterns of samples resultant from 6 h fired at: (a) 1100 °C, (b) 1150 °C, (c) 1200 °C, and (d) 1250 °C, respectively (prior to water washing).

Figs. 4.1 and 4.2 show XRD patterns of samples resultant from 6 h firing at different temperatures in the binary salt salts (19g NaCl + 1g NaF), before and after water-washing, respectively. According to Figs. 4.1 and 4.2, the formation of $Al_8B_4C_7$ was already evident after 6 h at 1100 °C, but the intermediate Al_4C_3 was also detected. With increasing the temperature to 1150 and then 1200 °C, $Al_8B_4C_7$ increased while Al_4C_3 decreased. Upon increasing the temperature to 1250 °C, Al_4C_3 disappeared, and only

106

$Al_8B_4C_7$ was detected. AlOOH (boehmite) was detected in the washed sample (Fig. 4.2), which was due to the hydration of Al_4C_3 originally formed at test temperatures (Reaction 4.2), during the water-washing process. AlOOH decreased with increasing the sample's firing temperature and disappeared in the sample fired at 1250 °C for 6 h.

$$Al_4C_3 + 8H_2O = 4AlOOH + 3CH_4 \tag{4.2}$$
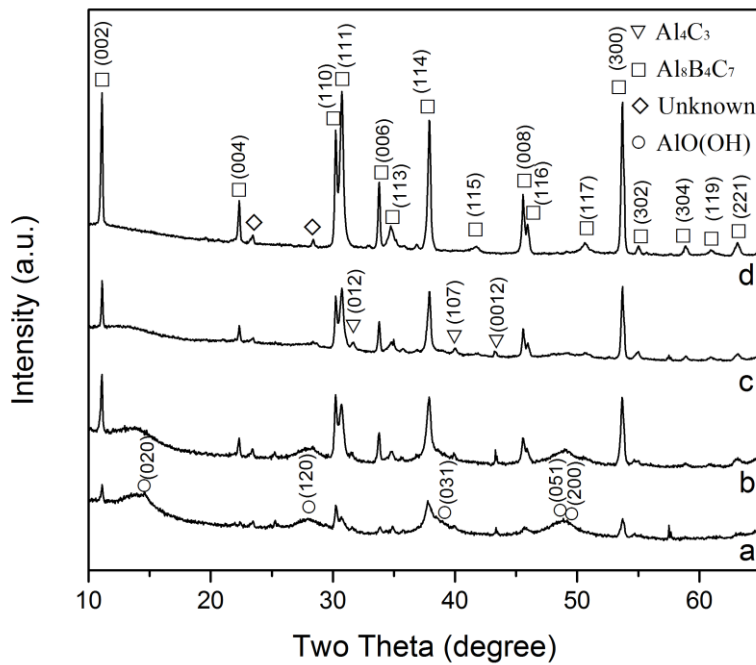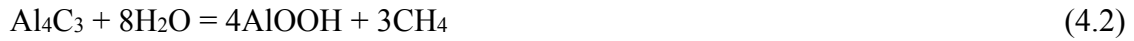
Fig. 4.2 XRD patterns of samples resultant from 6 h firing at: (a) 1100 °C, (b) 1150 °C, (c) 1200 °C, and (d) 1250 °C, respectively, and subsequent water washing.

According to the results shown in Figs. 4.1 and 4.2, the main reactions possibly involved in the synthesis process can be indicated by Reactions (4.3) and (4.4) [48,197], although more detailed reaction mechanisms will be discussed in Section 4.3.5.

$$4Al + 3C = Al_4C_3 \qquad\qquad (4.3)$$

$$2Al_4C_3 + B_4C = Al_8B_4C_7 \qquad\qquad (4.4)$$

Based on phase relationships in the Al - B_4C and Al - B_4C - C systems [198], Al_3BC and AlB_2 could be formed *via* Reaction (4.5).

$$9Al + 2B_4C = 2Al_3BC + 3AlB_2 \qquad\qquad (4.5)$$

However, they were not found in the fired samples. The reasons might be that at test temperatures, both of them were not stable, so once they were formed, they would decompose [197] and react rapidly with other phases in the raw materials to form $Al_8B_4C_7$.

4.3.2 Supplementary experiment for mechanism verification

Shown in Fig. 4.3 are XRD patterns of Al + B_4C samples after 6 h firing at 1250 ℃, and after further firing with carbon black. In the first case (Fig. 4.3-a), Al_3BC were formed as the main phases *via* Reaction 4.5. AlB_2 is not stable at high temperatures, so the AlB_2 formed from Reaction (4.5) decomposed to form Al and B (no B was detected, probably because it was amorphous). However, minor amounts of AlB_2 were still detected. They were considered to be resulted from the reaction between the residual Al and B on cooling. When the reacted Al + B_4C sample was heated further with carbon black,

108

$Al_8B_4C_7$ became the main phase (Fig. 4.3-b), suggesting that the Al_3BC formed in the sample after the first round of firing reacted further with other phases to produce $Al_8B_4C_7$ (Reactions (4.7) and (4.8)). The detection of minor amounts of AlB_2 and Al_4C_3 (Fig. 4.3-a) indicated that Reaction (4.10) might have occurred. The XRD pattern of fired Al_4C_3+B+C sample is shown in Fig. 4.4, revealing that $Al_8B_4C_7$ was formed as the major phase, along with minor amounts of carbon and Al_2O_3. This result further implied the occurrence of Reaction (4.9). The small amounts of Al_2O_3 detected (Figs. 4.3-b and 4.4) were resultant from the decomposition of $AlO(OH)$ formed from the partial hydration of Al_4C_3 and Al_3BC by the moisture in the atmosphere during the mixing.

$$AlB_2 = Al + 2B \tag{4.6}$$

$$8Al + 4B + 7C = Al_8B_4C_7 \tag{4.7}$$

$$8Al_3BC + 12B + 13C = 3Al_8B_4C_7 \tag{4.8}$$

$$7Al_4C_3 + 12B = 3Al_8B_4C_7 + 4Al \tag{4.9}$$

$$6Al_3BC = 2Al_4C_3 + 10Al + 6B \tag{4.10}$$
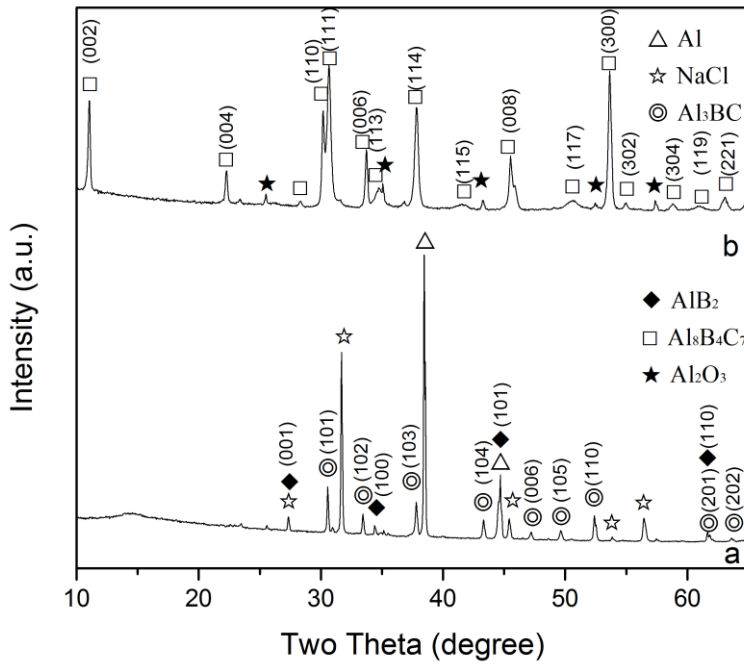
Fig. 4.3 XRD patterns of: (a) sample of Al + B_4C after 6 h firing in NaCl + NaF at

1250 ^{o}C, (b) sample resultant from further firing the sample of (a) with carbon black in

NaCl + NaF at 1250 ^{o}C for 6 h.
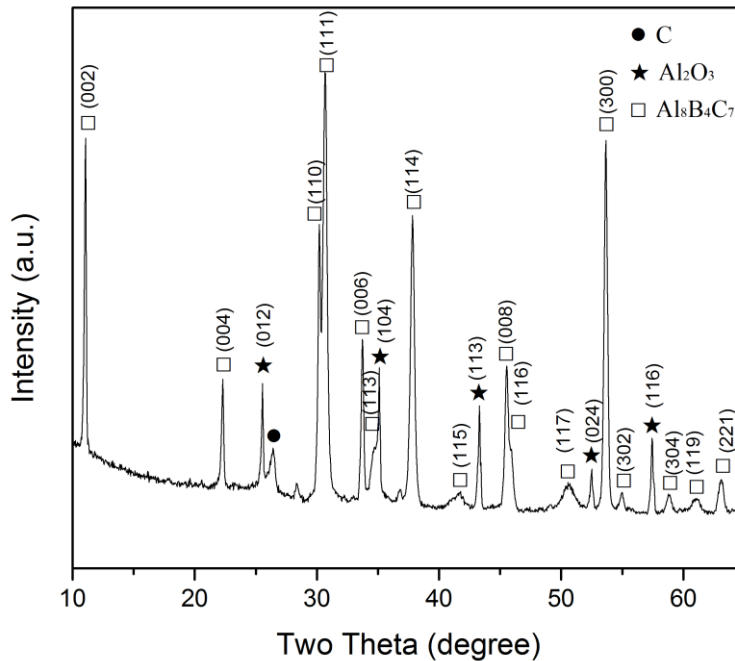
Fig. 4.4 XRD pattern of sample comprising Al_4C_3, B and C, after 6 h firing in NaCl + NaF at 1250 °C.

4.3.3 Effect of salt type/composition on the synthesis of $Al_8B_4C_7$

Fig. 4.5 demonstrates the effects of salt type/composition on the $Al_8B_4C_7$ formation. In the case of using NaCl (Fig. 4.5-a), only very minor $Al_8B_4C_7$ was formed, but large amounts of AlO(OH) were detected, indicating the limited accelerating effect of NaCl salt on the $Al_8B_4C_7$ formation. However, when small amounts (0.5g, i.e. 2.5%) of NaF was combined with NaCl, $Al_8B_4C_7$ became the main phase, although some Al_4C_3 (indicated by boehmite) was still detected, indicating the great accelerating effect of NaF addition on the overall synthesis reaction. Upon increasing the NaF amount further to 1g (i.e., 5%), Al_4C_3 disappeared and only $Al_8B_4C_7$ was formed (Fig. 4.5-c). Based on the

111

above results it can be considered that the optimal salt type/composition in the present case is 95% NaCl + 5% NaF.
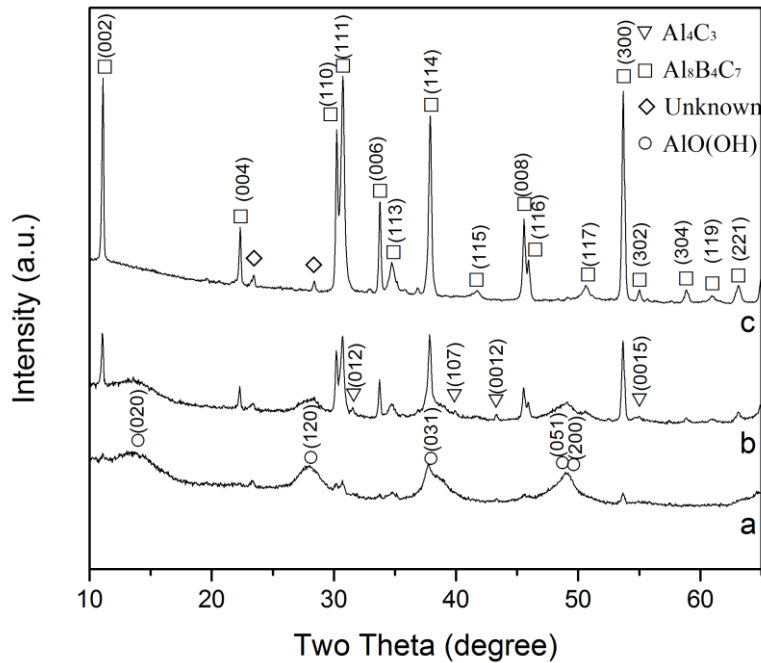
Fig. 4.5 XRD patterns of samples resultant from 6 h firing at 1250 °C in: (a) 20g NaCl, (b) 0.5g NaF + 19.5g NaCl, and (c) 1g NaF + 19g NaCl, respectively, and subsequent water washing.

The accelerating effect of NaF addition can be explained as follows. Al has very limited solubility in molten NaCl [201], but can slightly dissolve in it when it is combined with NaF [199-200]. It is believed that the increased solubility of Al in the case of NaF addition accelerated the reaction between Al and B_4C, promoting the formation of B. The formed B also slightly dissolved in the molten salt [202-203] and reacted rapidly with Al_4C_3 to form $Al_8B_4C_7$ (Reaction (4.9)).

112

4.3.4 Microstructure of product powder
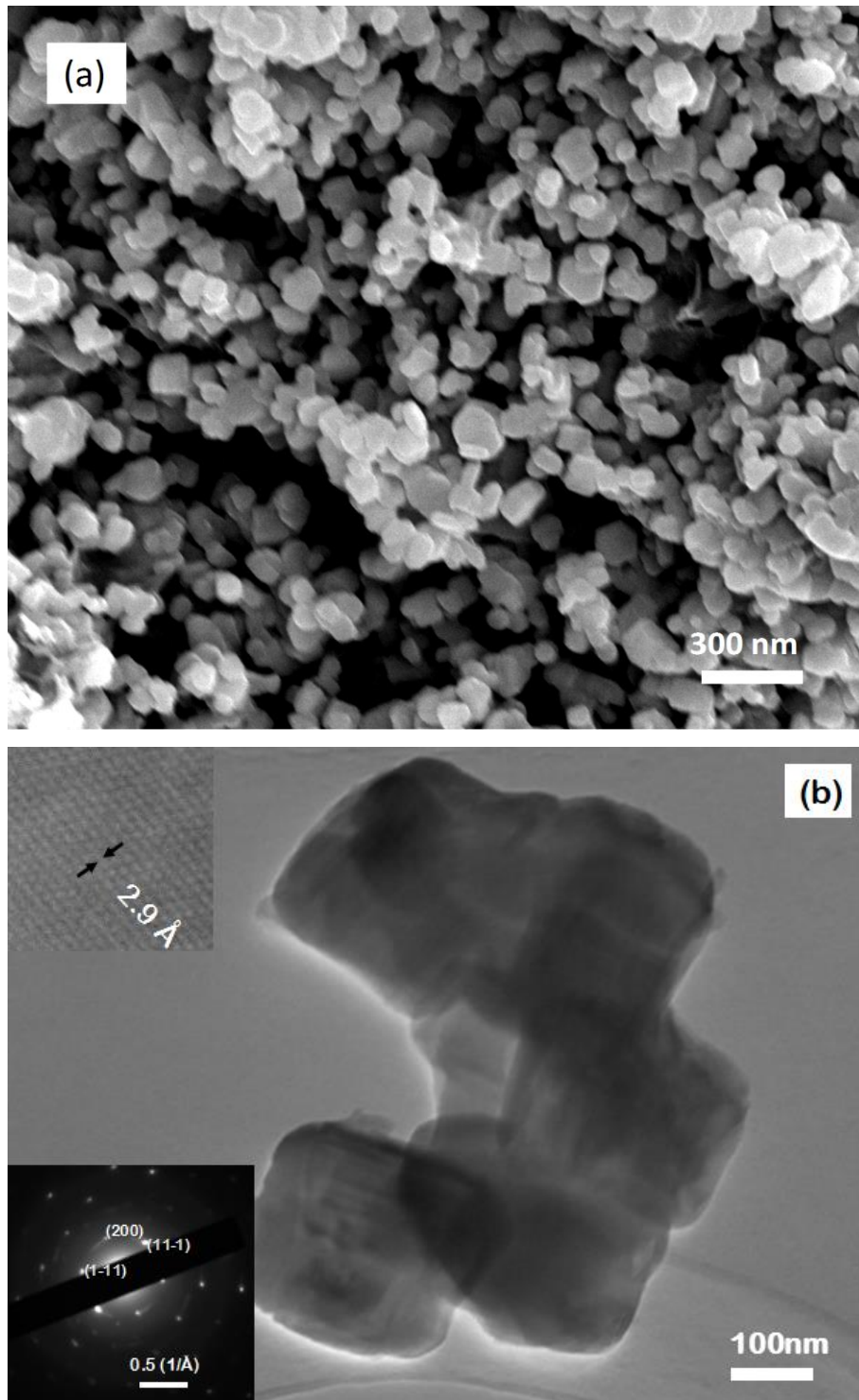
Fig. 4.6 (a) SEM and (b) TEM images of $Al_8B_4C_7$ product powder prepared at 1250 °C

for 6 h in NaCl+NaF.

Fig. 4.6 presents microstructure of the product powder prepared at 1250 °C for 6 h in 95%NaCl + 5%NaF, revealing   irregular shapes of product particles and their average size of about 200 nm. The lattice interlayer distance (one of the insets in Fig. 4.6) was measured as around 0.29 nm, which corresponds to the (111) plane of hexagonal $Al_8B_4C_7$. This, along with the SAED patterns (the other inset in Fig. 4.6) and XRD results in Figs. 4.1 and 4.2, confirm that they were $Al_8B_4C_7$.

114

4.3.5 Reaction mechanism
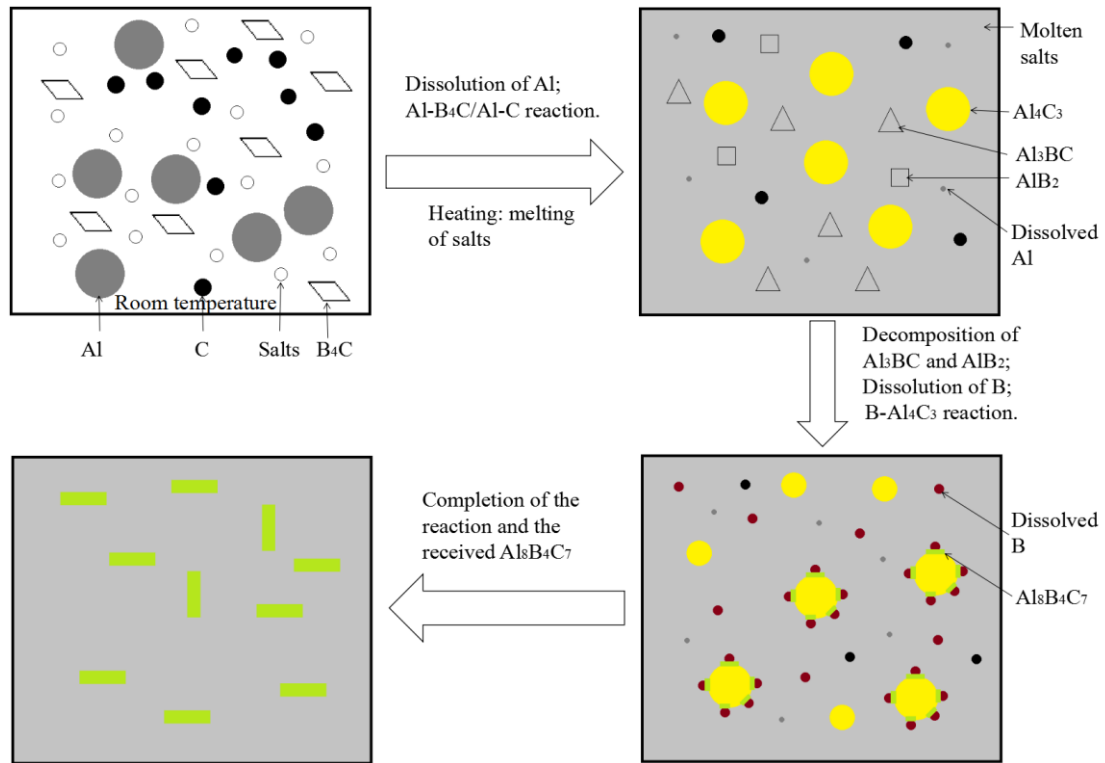
Fig. 4.7 A schematic illustrating the MSS synthetic mechanisms of $Al_8B_4C_7$.

Based on the results presented (Figs. 4.1-4.6) and discussed above, the main mechanisms

of $Al_8B_4C_7$ formation can be illustrated in Fig. 4.7, and described as follows. At the test

temperatures, NaCl (meting point: ~714 °C) and NaF (meting point: ~743 °C) interacted

with each other, forming a liquid medium in which Al slightly dissolved [199,201]. The

dissolved Al diffused rapidly through the liquid medium onto the surfaces of C and B_4C,

and then reacted with them to form Al_4C_3, and Al_3BC + AlB_2, according to Reactions

(4.3) and (4.5) respectively. AlB_2 decomposed at >1000 °C to give Al and B (Reaction

(4.6)). The formed B also slightly dissolved into the molten salt and then diffused

through the molten salt rapidly onto the surface of the Al_4C_3 formed earlier, to form

115

Al$_8$B$_4$C$_7$ according to Reaction (4.9). On the other hand, the formed Al$_3$BC also decomposed to give Al$_4$C$_3$, Al and B *via* Reaction (4.10). Similarly, the newly formed B would also dissolve slightly in the salt and diffuse onto the surface of Al$_4$C$_3$ and react with it to form Al$_8$B$_4$C$_7$ according to Reaction (4.9). The increase in the temperature increased the solubility values of Al and B in the salts and also accelerated their diffusion rates in the molten salt. As a result, the Al-B$_4$C reaction and the subsequent B-Al$_4$C$_3$ reaction would be greatly facilitated. Due to the insolubility of Al$_4$C$_3$ and B$_4$C in the molten salt and the low synthesis temperature used, Reaction (4.3) was in practice not likely to take place.

4.4 Conclusions

Phase pure Al$_8$B$_4$C$_7$ particles with the average size of about 200 nm were synthesized after 6 h firing at a much lowered temperature of 1250 °C *via* a molten-salt-mediated route using Al, B$_4$C and C powders as the main raw materials. NaF in the binary salt played very important role in the reaction process. As-prepared Al$_8$B$_4$C$_7$ powders were generally well dispersed. The overall synthesis mechanism can be described as follows: at test temperatures, NaCl and NaF interacted with each other forming a eutectic liquid medium in which Al partially dissolved. The dissolved Al diffused rapidly through the molten salt onto the surface of C to form Al$_4$C$_3$, and also diffused through the salt rapidly onto the surface of B$_4$C and reacted with it to form Al$_3$BC and AlB$_2$. B from the decomposition of AlB$_2$ also slightly dissolved in the salt, diffused onto the surface of

116

Al_4C_3 formed earlier, and reacted with it to form $Al_8B_4C_7$. On the other hand, the Al_3BC formed earlier also decomposed to give Al, B and Al_4C_3. The latter two would similarly react to form $Al_8B_4C_7$ according to the procedure described above. Compared to the conventional synthesis techniques used previously, the synthesis temperature in the present case was significantly lower (about 500 ^{o}C lower), which was attributable to the great accelerating-effect of the molten salt containing NaF.

However, there are still drawbacks for this method and some future work is worthwhile to do. Firstly, for comparison with previous work, the present work still used the composition corresponding to $Al_8B_4C_7$. However, it might be worthwhile to do further synthesis work based on the composition corresponding to "Al_3BC_3", and compare. Secondly, expensive B_4C was used in the present work to synthesize $Al_8B_4C_7$. It could be replaced by much cheaper boron oxides (or borates) for the synthesis of the target materials. In addition, the synthesis temperature remains a bit high (although much lower than required by the conventional methods) which suggests that further optimizing the molten salt synthesis conditions is still needed. Last, the sintering behavior/densification of aluminum boron carbide needs to be investigated, and microstructures and physicochemical properties of the sintered bulk samples need to be examined, providing further fundamental data for their future applications.

117

Chapter 5. Low temperature molten salt synthesis and characterisation of MoAlB fine powders

5.1. Background

MAX phases are layered carbides or nitrides with the general formula: $M_{n+1}AX_n$ (M is an early transition metal, A is Al or Si and X is C and/or N [52]. Ternary transition metal borides M_2AlB_2 (M = Cr, Mn, Fe) and MAlB (M = Mo, W) [52] have similar layered structures to MAX phase materials. Among them, MoAlB has attracted particular attention because of its several excellent properties, and great application potential. It has a relatively high electrical/thermal conductivity, low thermal expansion coefficient, low hardness, high compressive strength, and good fractural toughness [15-19,113]. MoAlB is stable up to 1400 °C in an inert atmosphere [16]. Differently from MoB, the aluminum bilayers between two MoB layers in the crystal structure of MoAlB render it very oxidation resistant because of the formation of a dense alumina scale from the initial oxidation on heating [15-16,20-21]. Therefore, MoAlB could be used as lubricant additives in metals [289] and promising high-temperature [20-21] and nuclear [56] applications.

118

Bulk or powder-formed MoAlB can be synthesized by using various techniques/methodologies, including the Al flux method, SPS, hot pressing and the conventional mixed powder route. The Al flux method [52,54-55,170], required a very high operation temperature (between 1400 and 1800 °C), and was mainly used to synthesize MoAlB single crystals (>100 μm). SPS [56] and hot pressing [16,20-21] required a much lowered synthesis temperature (1100~1200 °C) but a high pressure. They were mainly used to prepare bulk MoAlB from MoB and Al raw material powders The only method which has been attempted to synthesize MoAlB powder was the conventional mixed powder route [19,57], i.e., by directly heating a mixture of MoB and Al (always 30~ 60 % excessive) at 1100 °C. Unfortunately, with this technique it was difficult to prepare high quality (phase pure, good dispersion and fine size) MoAlB powders, as some impurity phases (e.g. MoB_2) almost always remained in the final product.

In the work presented in this Chapter, a low temperature molten salt synthesis technique was further developed to synthesize high quality MoAlB fine powder from Mo, Al and B powders. The effects of key processing parameters on the synthesis process and microstructure/morphology of the product powder were investigated and the reaction mechanisms clarified.

5.2. Experimental procedure

5.2.1 Raw materials and sample preparation

Al (purity: 99.7%, overall size: <25 μm), B (purity: 95%), and Mo (purity: ≥99%, overall size: <250 nm) powders from Sigma-Aldrich (Gillingham, UK) were used as raw materials, and NaCl (≥99%) was used to form a molten salt medium. The three raw materials were mixed in the stoichiometric ratio indicated by Reaction (5.1), or a non-stoichiometric ratio with excessive Al, followed by combination with 20g NaCl in an agate mortar. The mixed powder batch was contained in a graphite crucible covered with a lid and placed in an alumina tube furnace which was heated at 5°C/min to a temperature between 850 and 1200 °C in argon and held for 6 h.

$$Mo + Al + B = MoAlB \tag{5.1}$$

The fired samples were washed repeatedly with distilled water to remove the residual salt. The sample with 140% excessive Al, after firing, was subjected further to acid leaching with 6M HCl solution (for a week) and rinsing with distilled water. All the purified samples were oven-dried overnight at 100 °C for further characterisation.

5.2.2 Sample characterization

Phases in the product powders were identified by powder X-ray diffraction (XRD) analysis (Brukers D8 advance reflection diffractometer, Karlsruhe, Germany). Spectra were recorded at 40 mA and 40 kV using Ni-filtered CuKa radiation. The scan rate was 2.4° (2θ)/min with a step size of 0.04°. ICDD cards used for identification are MoB (51-0940), Al_2O_3 (46-1212), Al (65-2869), MoAlB (65-2497), Al_5Mo (44-1102), Al_4Mo (65-7072) and Al_8Mo_3 (65-1231). Microstructures and morphologies of as-prepared product powders were observed using a scanning electron microscope (SEM Nova Nanolab 600, FEI Company, Hillsboro, OR) and a JEM 2100 transmission electron microscope (TEM, 200 kV).

5.3. Results and discussion

5.3.1 Effect of temperature on the MoAlB formation in the sample with the stoichiometric composition
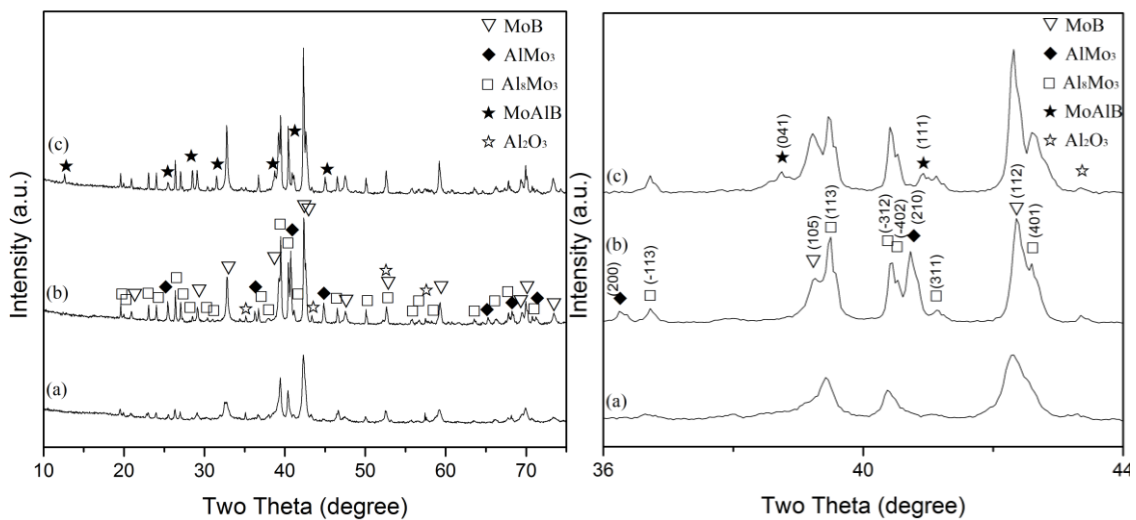
Fig. 5.1 XRD patterns of samples with the stoichiometric composition after 6 h at

(a)850, (b)900 and (c)950 °C, respectively.

Fig. 5.1 shows XRD patterns of the stoichiometric composition samples after 6 h at different temperatures. At 850 °C, Al_8Mo_3 and MoB were formed as the primary phases along with minor $AlMo_3$ and impurity Al_2O_3 (most likely resultant from minor oxidation of Al by the impurity O_2 in the Ar gas), but no MoAlB was detected. Upon increasing temperature to 900 °C, the same phases were detected, and their contents increased

evidently, in particular, in the case of AlMo$_3$. MoAlB was not formed either. Upon further increasing temperature to 950 °C, AlMo$_3$ disappeared and MoAlB started to appear. Mo$_8$Al$_3$ and MoB were also formed and the content of the latter was slightly higher than at 900 °C. It is believed that the consumption of Al caused by the formation of Mo-Al compounds was the main reason why only little MoAlB was formed at temperature as high as 950 °C when the stoichiometric amount of Al was used.
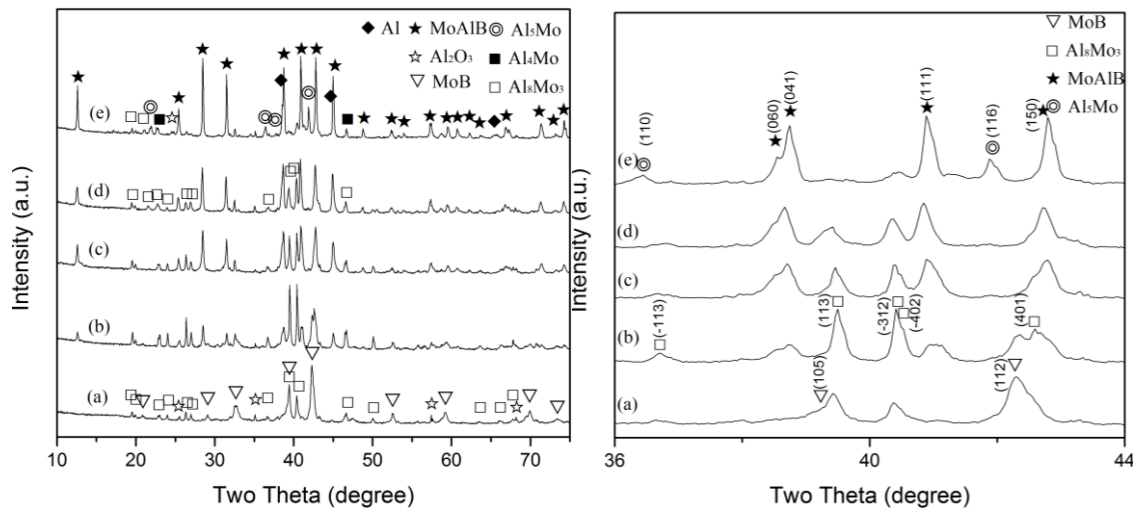
Fig. 5.2 XRD patterns of samples heated at 850 °C for 6 h with (a) stoichiometric amount of Al, (b) 60 % excessive Al, (c) 80 % excessive Al, (d) 100 % excessive Al, (e) 120 % excessive Al.

5.3.2 Effect of excessive amount of Al on phase formation and reaction extent

Fig. 5.2 shows the effects of excessive amount of Al on the phase formation and reaction extents in samples resultant from 6 h firing at 850 $^{\circ}$C. When the stoichiometric amount of Al was used (Fig. 5.2a), no MoAlB was detected, and Al_8Mo_3 and MoB were formed as the primary phases, along with minor impurity Al_2O_3 (most likely resultant from minor oxidation of Al by the impurity O_2 in the Ar gas). Upon increasing the excessive Al to 60~80%, the formation of MoAlB became evident, but MoB and Al_8Mo_3 still remained as the main phases. Upon further increasing the excessive Al to 100%, MoAlB increased whereas MoB and Al_8Mo_3 generally decreased. In addition to these two phases, small amounts of Al_4Mo was detected (Fig. 5.2d and Fig. 5.2e). Upon finally increasing the excessive Al to 120%, MoAlB increased whereas MoB and Al_8Mo_3 decreased. In addition, minor Al_5Mo was identified. The above results indicated that increasing the excessive Al generally favored the MoAlB formation, and inhibited the formation of intermediate phases. The intermediate phases detected were mainly Al-Mo binary phases and very small amounts of MoB, indicating that there should be some unreacted B (though not detectable by XRD due to its amorphous nature) which still remained in all the samples. The formation of Al-Mo phases in all the samples indicated they were stable in the presence of B at 850 $^{\circ}$C. Therefore, a higher synthesis temperature had to be used to avoid their formation and to complete the MoAlB formation reaction.

124
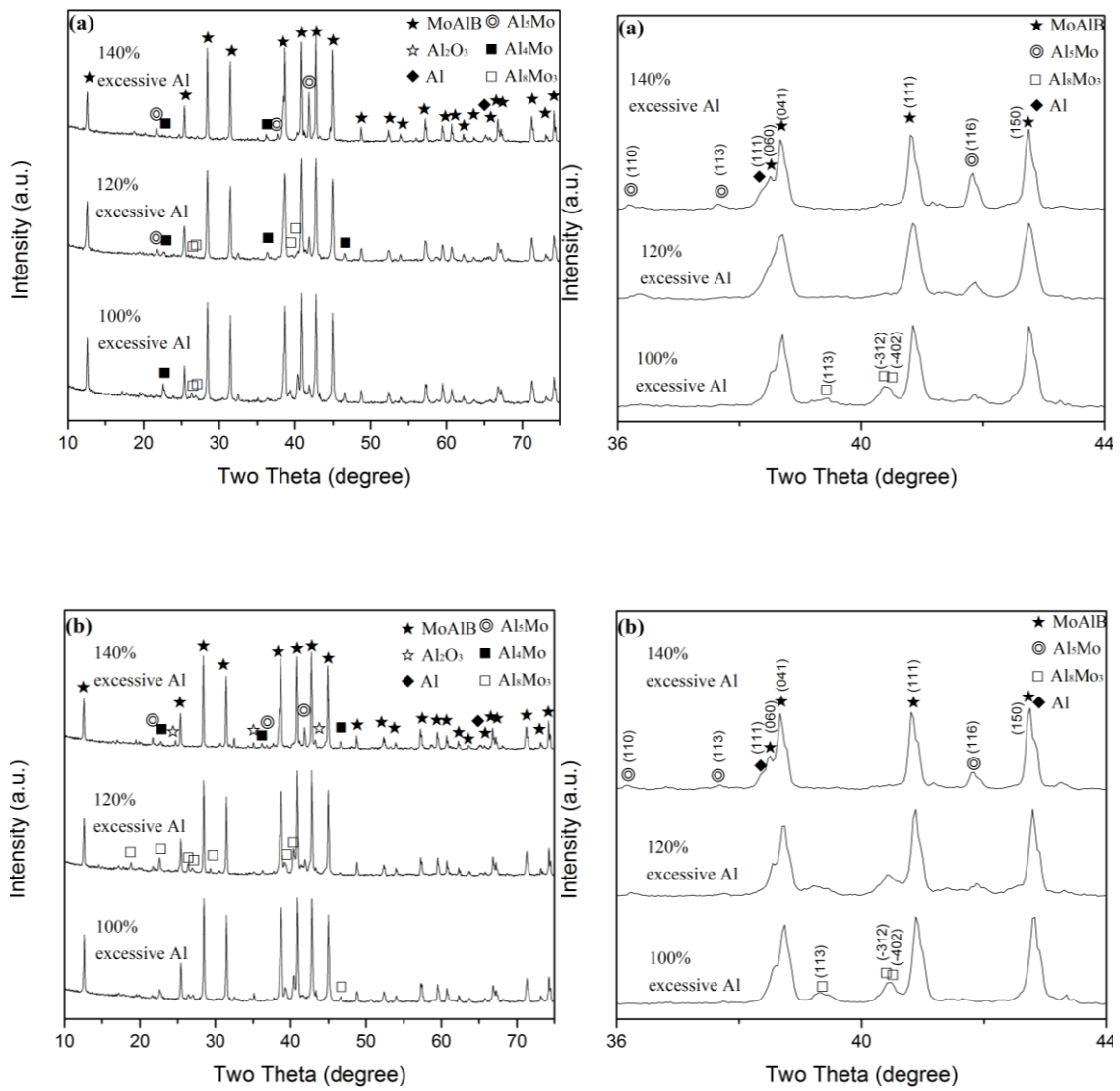
Fig. 5.3 XRD patterns of samples with various excessive amounts of Al, after 6 h firing

at (a) 900 °C and (b) 950 °C, respectively.

5.3.3 Combined effects of excessive Al and temperature on phase formation and reaction extent and optimization of synthesis condition

To illustrate the combined effects of excessive Al and temperature on phase formation and reaction extent, and to further optimize the synthesis conditions, samples with various excessive amounts of Al were fired at various temperatures. Fig. 5.3, as an example, shows XRD patterns of samples with 100-140% excessive Al after 6 h firing at 900 and 950 $^{\circ}$C, respectively, revealing similar phase formations in both cases, although slightly more MoAlB and less intermediate phases were formed at 950 $^{\circ}$C than at 900 $^{\circ}$C. When the excessive Al was 100%, Al_8Mo_3 and MoB were the main intermediate Mo-Al phases. However, with increasing the excessive Al, these two phases decreased, but two other Al-rich Al-Mo phases, Al_5M and Al_4Mo, were formed. The above results revealed that the sample with 140% excessive Al fired at 950 $^{\circ}$C had the highest MoAlB formation and the least formation of impurity (Al-Mo) phases, among all the samples, further indicating that the increase in the excessive Al along with firing temperature was beneficial to the MoAlB formation. So, to make further purer MoAlB, samples with 120 and 140% Al were further fired at 1000 $^{\circ}$C for 6 h. As seen from Fig. 5.4, when 120% excessive Al was used, apart from the primary phase of MoAlB, only minor Al_8Mo_3 and residual Al, were detected in the sample. However, upon increasing the excessive Al to 140%, all the intermediate Al-Mo phases disappeared, nearly phase pure MoAlB, along with minor residual Al (and minor Al_2O_3 as mentioned above) was formed. After leaching out the minor residual Al and Al_2O_3

126

with HCl, phase pure MoAlB was finally obtained (Fig. 5.5-a). The removal of aluminum was proved by peaks at around 65° (Fig. 5.4-left) and 38.5° (Fig. 5.5-b). The synthesis temperature in the present case was at least 100 °C lower than required by other synthesis routes [16,20-21,52,54-56,170].
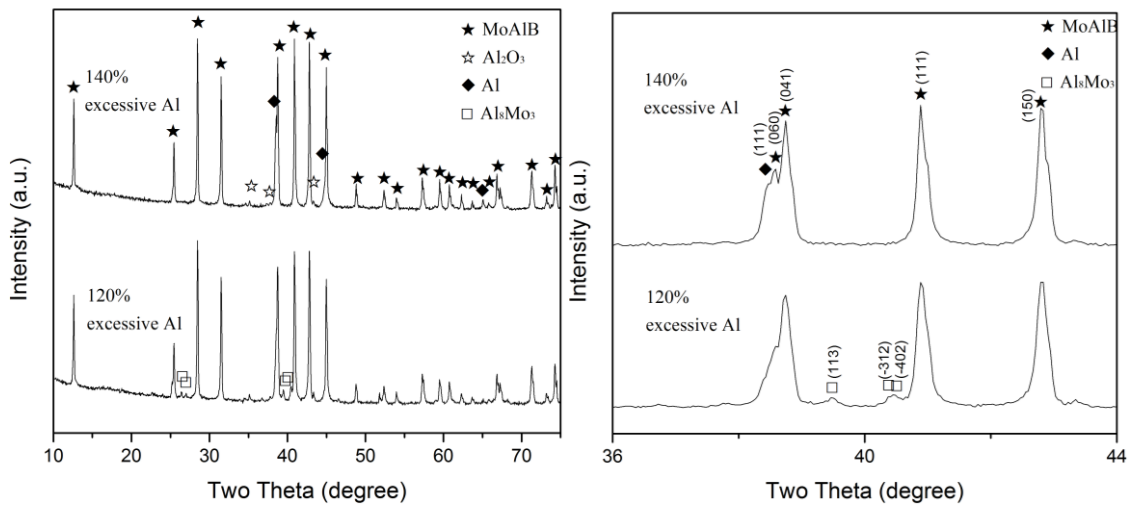
Fig. 5.4 XRD patterns of samples with 120 and 140% excessive Al, respectively, after 6 h firing at 1000 °C.
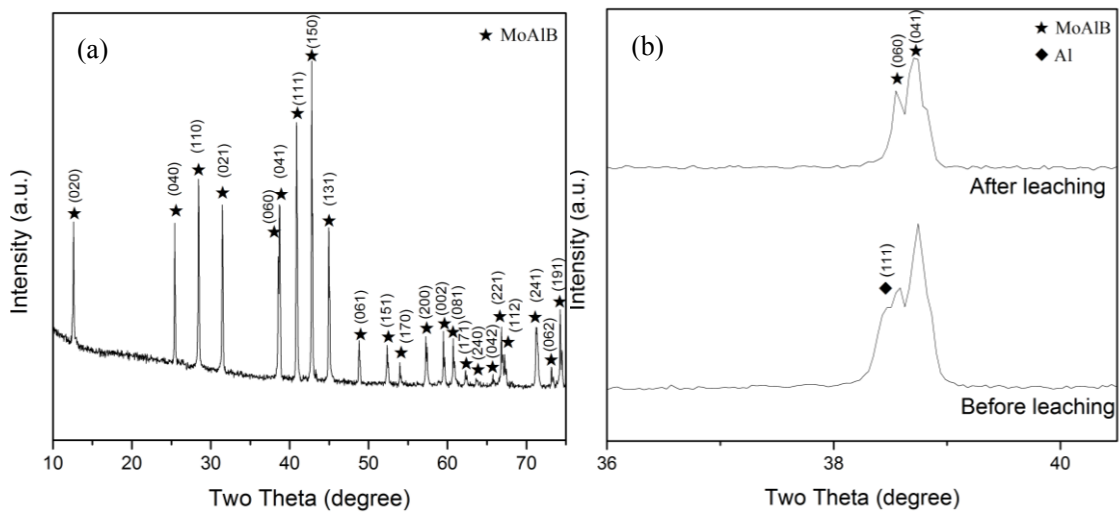
Fig. 5.5 XRD pattern of (a) the sample resultant from 6 h firing at 1000 °C and subsequent acid leaching and (b) comparation of sample resultant from 6 h firing at 1000 °C before and after acid leeching.

5.3.4 Microstructural characterization of product powder
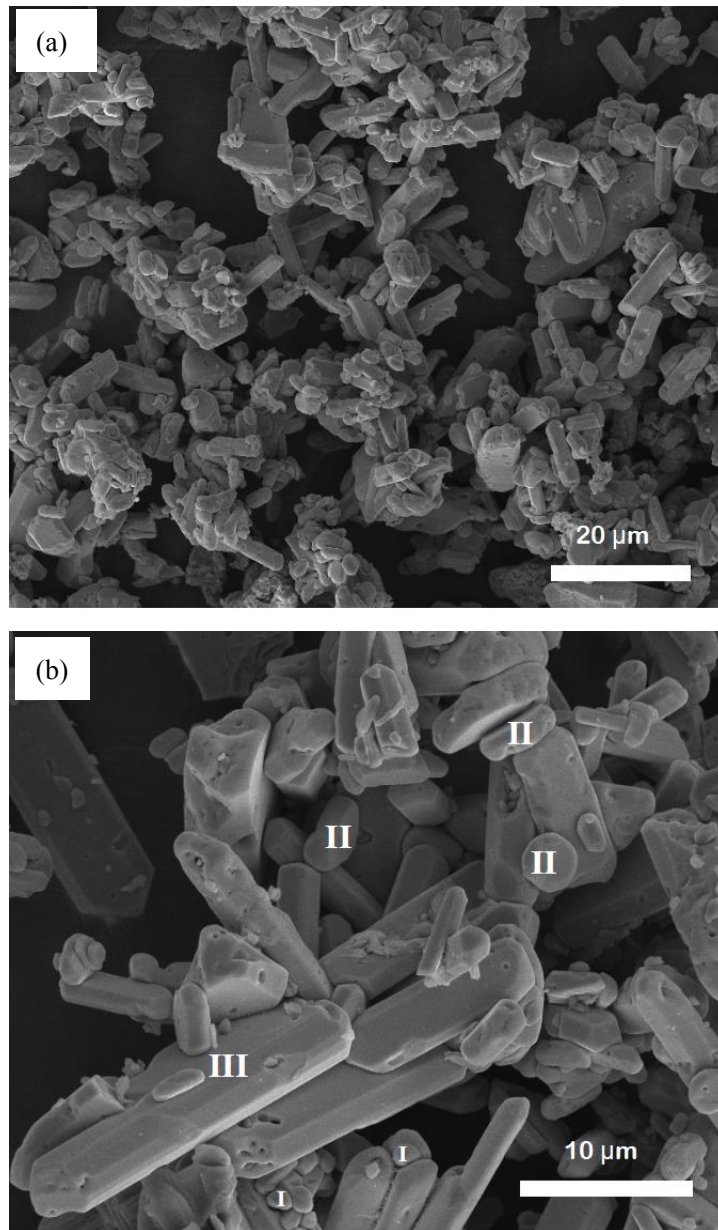
Fig. 5.6 (a) Low and (b)high magnification SEM images of MoAlB powder resultant

from 6 h firing at 1000 ºC and subsequent acid leaching.
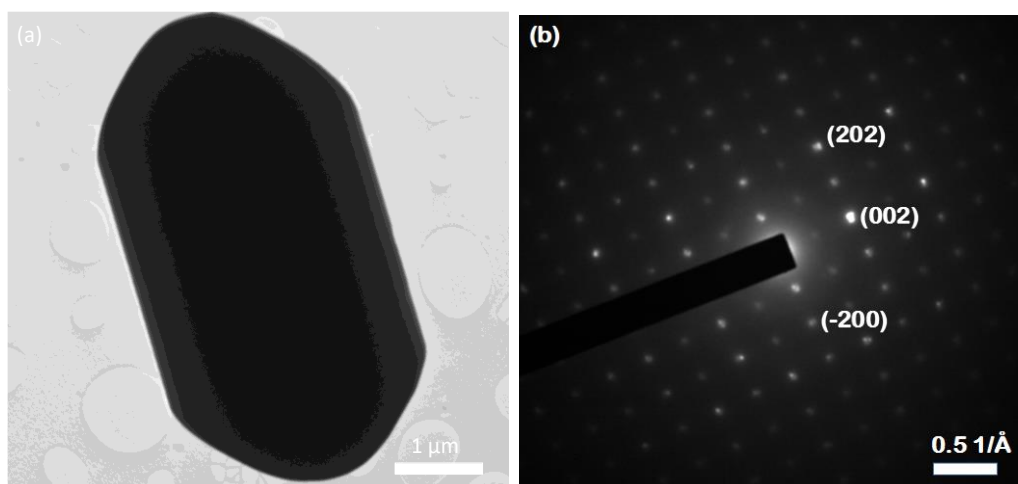
Fig. 5.7 (a) TEM images and (b) SAED of a MoAlB particle in the sample whose

microstructure is shown in Fig. 5.6.

Fig. 5.6 gives SEM images of MoAlB product powder resultant from 6 h firing at 1000

°C and further purification with HCl, revealing three different morphologies of particles.

The first was small rounded particles with a typical size of 1~3 μm (indicated by "I" in

Fig. 5.6), the second was plate-like (disc-like) particles <5 μm in diameter (indicated by

"II" in Fig. 5.6), and the third was columnar crystals up to 20 μm in length and 3-5 μm

in diameter (indicated by "III"). These three forms of particles looked similar to those

prepared by Shi et al. [265] *via* the conventional route using Al and MoB as the starting

materials. Some small spots were seen on the surface of the type "III", which was similar

of that reported by Kota and Shi et al [21,265]. although the reason for this was not clear.

Fig. 5.7a further gives a TEM image of a representative particle from the sample whose microstructure is shown in Fig. 5.6. Due to its micron-scale thickness, no lattices information could be obtained. Fig. 5.7b displays the SAED pattern of the particle which is similar to that reported by Alameda et al. [266]. It confirms that the particle had the crystal structure of MoAlB and had grown preferentially along its [010] direction.

5.4. Further discussion and synthesis mechanism

Based on the results shown in Figs. 5.1-5.7, and discussed above, the effects of processing parameters on the synthesis process of MoAlB can be further discussed, and the relevant mechanism proposed as below. At test temperatures, NaCl (melting point: ~714 °C) melted, forming a homogeneous molten salt medium. Although the actual solubility values of Al, Mo, and B in the salt are not available, based on the previous studies on the molten salt synthesis of Mo_2C [267], borides [202,268-269] and TiB_2-Al_2O_3 [270], it is considered that the solubility values should be in the following order: Mo> Al> B. At low temperatures (850-900 °C), Mo slightly dissolved in the molten salt, and diffused rapidly through it onto the surfaces of Al droplets (or met with dissolved Al) and B particles, and then reacted to form intermediate phases Al_8Mo_3 and MoB according to Reaction (5.2) and Reaction (5.3), respectively (Figs. 5.1a & 5.2a). No intermediate Al-B phases (such as AlB_2) were detected by XRD at these temperatures (Fig. 5.1a). The reason might be that all of the Al had been consumed by reacting with

131

Mo, so no Al was left for its reaction with B. Due to the this and the very limited solubility of B, once Al_8Mo_3 and MoB were formed, it would be difficult for them to be converted into MoAlB *via* reacting respectively with B and Al, i.e, Reactions (5.4) and (5.5) would not occur at these temperatures. This explained the absence of MoAlB in the sample with the stoichiometric amounts of Al after firing at 850-900 °C (Figs. 5.1a & 5.2a). With increasing the excessive Al, MoAlB increased whereas MoB decreased, indicating the occurrence of Reaction (5.5) and its gradually enhanced extent (Fig. 5.2). Apart from this, some of the excessive Al would reacted with the Al_8Mo_3 formed earlier, forming Al-rich Al-Mo phases (Reactions (5.6) and (5.7)), Al_4Mo and Al_5Mo (this phase is not stable at test temperatures, so it should be formed on cooling from the same composition of eutectic liquid, in terms of the Al-Mo phase diagram, [264]). This was responsible for the increased Al_4Mo/Al_5Mo and decreased Al_8Mo_3 upon using large excessive Al (Figs. 5.2 & 5.3). In addition to the positive effect of using excessive Al on the MoAlB formation, firing temperature affected significantly the MoAlB formation, in both cases using and without using excessive Al. This was because with increasing the firing temperature, the solubility of B in the molten salt would be increased. So, the dissolved B would diffuse through the molten salt onto the remaining Al-Mo phases (mainly Al_4Mo and Al_8Mo_3), and reacted with them to form MoAlB according to Reactions (5.4) and (5.8) (Fig. 5.1c, Fig. 5.3 & Fig. 5.4). Based on the above discussion, it can be considered that phase pure MoAlB could only be prepared by using appropriate amounts of excessive Al and firing at an appropriate temperature (in the present work, 140% excessive Al and at 1000 °C). The overall reaction process, along with the relevant

132

reaction mechanisms can be schematically shown in Fig. 5.8. It is believed that the multiple reaction steps and different formation routes of MoAlB were responsible for the different shapes and sizes of MoAlB product particles (Figs. 5.6 & 5.7), although future work is still needed to classify this further.
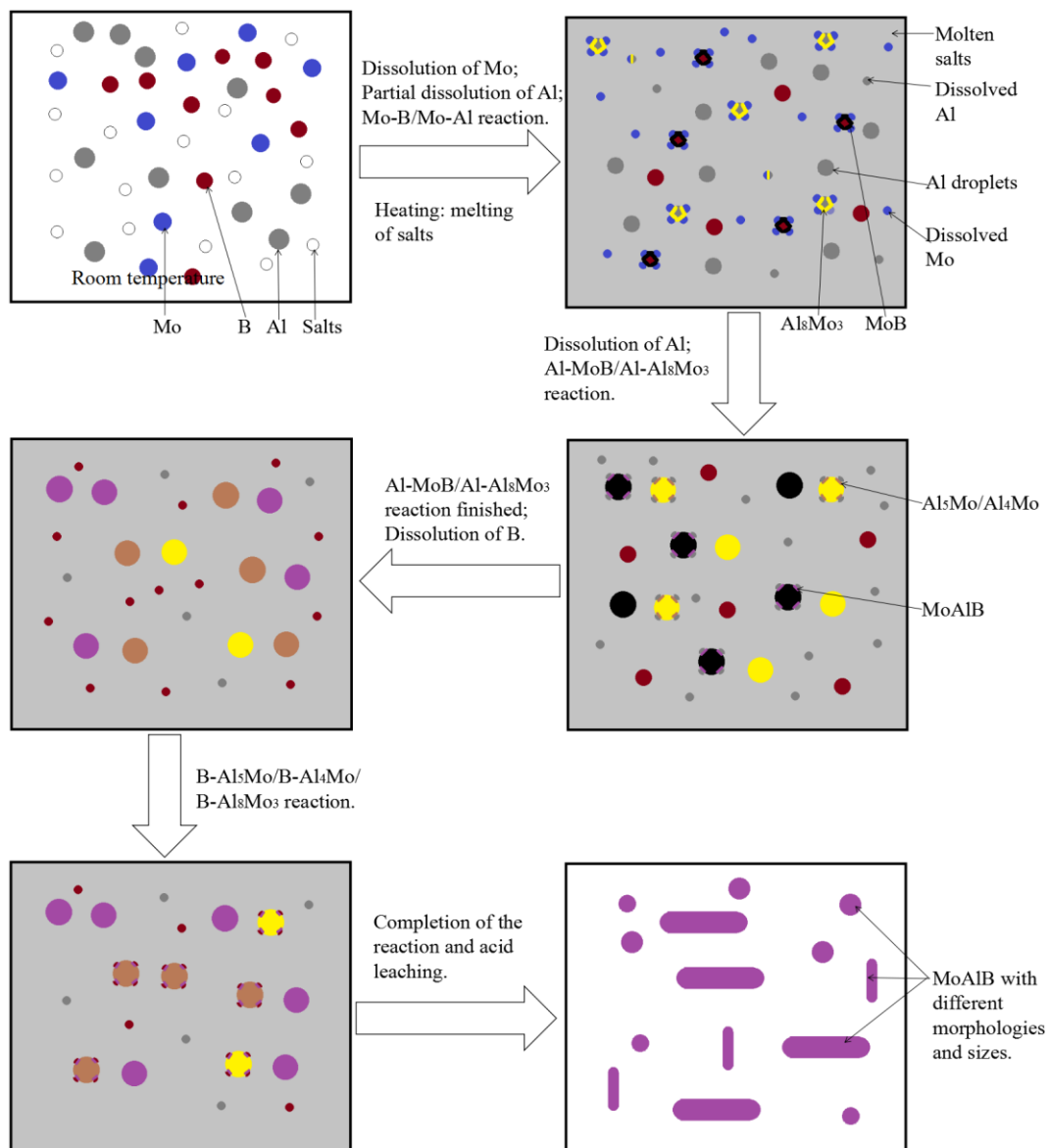
Fig. 5.8 A schematic illustrating the MSS synthetic mechanisms of MoAlB.

$$8Al + 3Mo = Al_8Mo_3 \tag{5.2}$$

$$Mo + B = MoB \tag{5.3}$$

$$Al_8Mo_3 + 3B = 3MoAlB + 5Al \tag{5.4}$$

$$MoB + Al = MoAlB \tag{5.5}$$

$$Al_8Mo_3 + 4Al = Al_4Mo \tag{5.6}$$

$$Al_8Mo_3 + 7Al = 3Al_5Mo \text{ (liquid at the test temperatures)} \tag{5.7}$$

$$Al_4Mo + B = MoAlB + 3Al \tag{5.8}$$
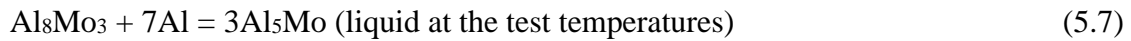
5.5 Conclusions

MoAlB fine particles were synthesized *via* a molten-salt-mediated route at a relatively low temperature using Al, B and Mo powders as the raw materials and NaCl to form the liquid reaction medium. As-prepared MoAlB particles exhibited three different morphologies: rounded particles (1~3 μm), plate-like particles (<5 μm in diameter) and columnar crystals with various lengths (up to 20 μm) and diameters (up to 5 μm). It is believed that they were formed *via* different reaction routes (Fig. 5.8). To prepare phase pure MoAlB, an appropriate amount of excessive Al has to be used and an appropriately high firing temperature is required. In the present work, the optimal synthesis condition was: use of 140% excessive Al and firing at 1000 °C for 6 h. This synthesis temperature

134

was at least 100 °C lower than required by other synthesis techniques. The overall synthesis process/reaction mechanism can be described as follows: at test temperatures, NaCl melted, forming a homogeneous liquid medium. If the temperature was low (at 850-900 °C), Mo and Al slightly dissolved in the molten salt but B almost did not dissolve. In this case, the dissolved Mo reacted with dissolved or undissolved Al and undissolved B, forming intermediate phases Al_8Mo_3 and MoB. If excessive Al was present, it would dissolve in the salt and diffuse onto the surfaces of MoB and Al_8Mo_3 and react to form MoAlB and Al-rich phases (Al_4Mo or an Al-Mo liquid with the same composition of Al_5Mo), respectively. With increasing the temperature to >900 °C, the dissolution of B in the salt became more evident. The dissolved B would diffuse through the molten salt onto the surfaces of the intermediate Al-Mo phases formed earlier, and reacted with them to form more MoAlB. The molten salt played an important role in the whole synthesis process by improving the mixing between the reactant species and facilitating their diffusion processes.

Based on the work of this chapter, some future work seems to be needed. Cheap boron oxides (or borates) could be used to synthesize MoAlB to replace the much more expensive B. Further optimizing the molten salt synthesis conditions could be needed to reduce the amounts of excessive Al. The sintering behavior/densification of MoAlB needs to be investigated, and microstructures and physicochemical properties of the sintered bulk samples need to be examined, providing further fundamental data for their future applications.

Chapter 6. Facile *In-situ* Formation of High Efficiency Nanocarbon Supported Tungsten Carbide Nanocatalysts for Hydrogen Evolution Reaction

6.1 Background

As an alternative to traditional fossil fuels, hydrogen (H_2) is considered as a promising future clean energy source with high energy density [219-225]. Compared to many other H_2 production techniques [226-228], the electrochemical hydrogen evolution reaction (HER) has several advantages, in particular the relatively high production efficiency [220]. However, high overpotential with this direct water splitting process still causes much energy loss and hinders further improvement in the overall efficiency [221,223-224]. One strategy commonly adopted to tackle this problem is the use of a highly efficient catalyst with a low free-energy of the adsorbed H [229]. Unfortunately, the most efficient HER electrocatalysts developed so far are still precious metal based (*e.g.* Pt), which are expensive and unsustainable.

For these reasons, considerable efforts have been made to develop alternative efficient HER catalysts, some of which were monolayered transition metal chalcogenides and their porous counterparts with tailored structures and improved electrical conductivity

[230-237]. Nevertheless, their preparation processes generally were complex, not cost-effective and/or not scalable. In recent years, low cost transition metal carbides have attracted a great deal of attention because of their great potential for HER applications [238-243], including molybdenum carbide [244-249] and tungsten carbide (WC) nanomaterials [27,243]. In the case of a WC nanomaterial, overpotentials of 165 to 323 mV and Tafel slopes of 85 to 119 mV dec^{-1} were achieved *via* loading WC on carbon substrates [28-29]. Diverse methods have been used to prepare such WC catalysts. The conventional solid-solid reaction process commonly exhibits several disadvantages, in particular, a high firing temperature and a long reaction time, resulting in uncontrollable sintering/heavy agglomeration of product particles and poor catalytic activity [30]. To avoid these problems, some other techniques relying on gaseous carbon sources have been attempted, and the synthesis temperatures could be reduced to 800~1000 °C. However, a carbon film was always deposited on the catalyst particles, which separated WC nanoparticles (NPs) from the reactant species, reducing their catalytic activity. Recently, Hunt *et al.* [65] have prepared well-dispersed WC NPs free from carbon covering by using a "removable ceramic coating method". Nevertheless, this method still suffers from several drawbacks such as a complex process, long processing time, the use of hazardous precursors and low production yield. On the basis of the above review, it can be considered that development of an alternative facile fabrication method for WC catalysts is key to their performance and future application in efficient HER.

137
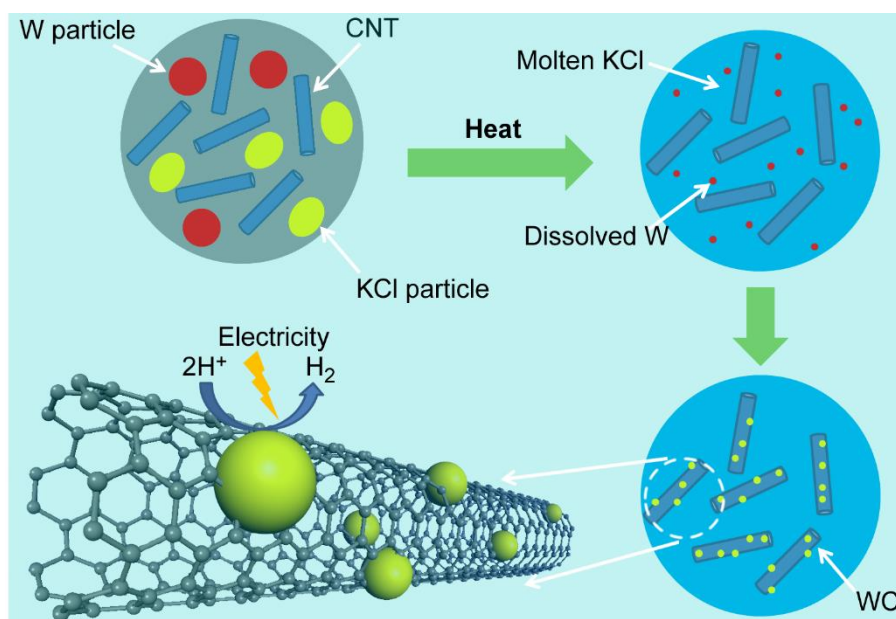
Fig. 6.1 Schematic of the molten salt synthesis process used in the present work.

In this chapter, highly efficient nanocarbon-supported WC nanocatalysts with substantially improved HER performance were fabricated *via* a novel one-step low temperature molten salt synthesis (MSS) technique. As illustrated in Fig. 6.1, WC NPs were formed *in-situ* and firmly anchored on nanocarbon substrates (nanosized carbon black/CB or carbon nanotube/CNT). Different from other synthesis techniques, the present MSS used only common raw materials and required a relatively low firing temperature. Such simple preparation process and the resulted unique catalyst structure conferred dramatically increased surface area and electrical conductivity on the catalyst, improving greatly the overall catalytic performance in HER. We report here the excellent HER electrocatalytic activity and stability of tailored WC nanocatalysts, along with a facile synthesis strategy potentially applicable to future commercial productions of a range of nanocatalysts for various important applications.

6.2 Experimental

6.2.1. Raw materials and sample preparation

0.29 g WO_3 (< 100 nm), 0.12 g Mg (> 99% purity), and 0.06 g multi-walled carbon nanotube (CNT, > 95% purity) or carbon black (CB, N990) (*i.e.*, in the molar ratio of WO_3 : Mg : C = 1 : 4 : 4) were ultrasonically dispersed for 1 h in ethanol, and dried in an oven at 80 °C for 2 h. The dried powder was further mixed with 15 g KCl (> 99% purity) and contained in an alumina crucible. A tube furnace protected by following Ar was used to fire the alumina crucible to 950 °C (5 °C min^{-1}). After 4 h at this temperature, the crucible was allowed to cool in the furnace to room temperature. The solidified mass in the crucible was repeatedly washed with distilled water and 1 mol L^{-1} HCl solution. The resultant powder sample free from residual salt and byproduct MgO was further dried at 80 ºC overnight and characterized as described below.

6.2.2. Sample characterization

A Brukers D8 X-ray diffractometer (Cu Kα, λ = 0.154 nm, 40 mV, 40 mA) was used to identify crystalline phases in samples from 20° to 80° (2θ) with a scan rate of 2.4°/min and step size of 0.04°, and an SSI S-Probe X-ray photoelectron Spectrometer was used to record their X-ray photoelectron spectra (XPS, samples in the case were pressed to

139

form a thin pallet). Prior to the XPS test, the areas to be examined were cleaned with argon etching for a few minutes. A JEM 2100 transmission electron microscope (TEM, 200 kV) was used, along with an energy-dispersive X-ray spectroscope (EDS), to examine microstructures and phase morphologies of samples (samples were sonicated in ethanol for 30 min prior to the TEM characterization).

6.2.3. Electrochemical Measurements

Electrochemical tests were performed on a CHI 602D electrochemical workstation with a three-electrode cell (counter electrode: Pt; reference electrode: Ag/AgCl, 1 mol L^{-1} KCl; working electrode: catalyst on glassy carbon). Powder catalyst (4 mg) and Nafion solution (5 μl) were dispersed in 1 ml water/ethanol solution. Then, 14 μl prepared dispersion (containing about 56 μg catalysts) was mounted onto the glassy carbon electrode (3 mm in diameter). The linear sweep voltammetry was conducted at a scan rate of 2 mV s^{-1} in a 0.5 M H$_2$SO$_4$ electrolyte (pH ≈ 0.3). All the potential values were calibrated versus a Reversible Hydrogen Electrode (RHE), based on the Nernst equation [231]. In the case of electrochemical impedance spectroscopy (EIS), a frequency range was from 10^5 to 0.01 Hz and the amplitude was 10 mV (in a potentiostatic mode).

6.3 Results and discussion

6.3.1. Characterization of tungsten carbide/carbon nanocatalysts

Before evaluation of the catalytic activity, as-prepared samples were subject to detailed characterizations. Fig. 6.2-a gives XRD patterns of samples using CB (WC/CB) and CNT (WC/CNT) respectively as the carbon source, showing similar diffraction peaks in both cases. WC and W_2C were formed as the primary phases, along with some residual carbon (ICDD cards: No. 20-1315 and 51-0939). The (002) graphite diffraction peak of WC/CNT (at 25.5º) is slightly lower than that of WC/CB (at 26.5º), which is reasonable since CNTs generally have lower crystallinity and larger layer distance than pure graphite or CB. A similar diffraction peak around 25.5º in the case of CNTs was also found in our previously work [250]. The above results indicated that the reduction of WO_3 by Mg (Reaction 6.3 below) and the subsequent W-C reactions (Reactions 6.1& 6.2 below) had been completed under the firing conditions.

$$W + C = WC \tag{6.1}$$

$$2W + C = W_2C \tag{6.2}$$

$$WO_3 + Mg = W + MgO \tag{6.3}$$
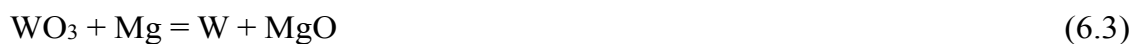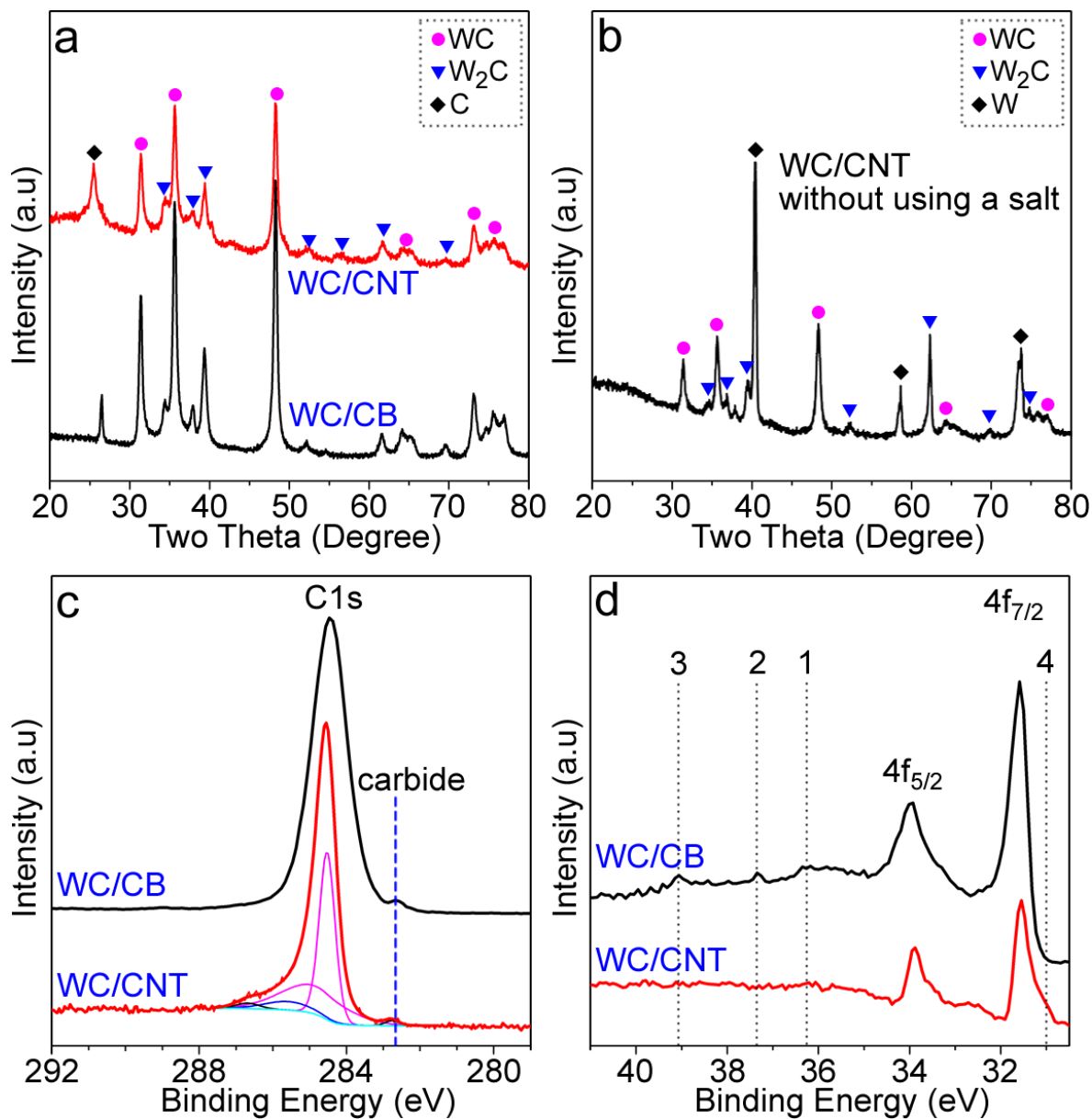
Fig. 6.2 (a) XRD patterns of as-prepared WC/CB and WC/CNT samples. (b) The XRD

pattern of WC/CNT sample after 4 h firing at 950 °C without using any salt. (c) C1s

and (d) W4f XPS of as-prepared WC/CB and WC/CNT samples.

The advantage of the present MSS technique can be further illustrated by comparing

reaction extents in the samples prepared *via* different routes. Fig. 6.2-b, as an example,

presents the XRD pattern of the WC/CNT sample fired under the identical conditions

142

(950 °C for 4 h) *via* the conventional solid-solid reaction route (without using a molten salt), showing that W (ICDD cards: No. 04-0806) was formed as the primary phase, along with small amounts of WC and W_2C. Comparison of Fig. 6.2-b and Fig. 6.2-a reveals that the present MSS technique is much more effecient than the conventional solid-solid synthesis technique, which can be attributed to the molten salt reaction medium formed in the case of the former, as will be discussed later in this paper.

Fig. 6.2-c&d are XPS spectra of as-prepared WC/CNT and WC/CB samples. C 1s profiles of both samples (Fig. 6.2-c) shows C-C (~285.3) and C=C (~284.6 eV) from CNT and CB. Both CNT and CB were defected with small proportions of O-containing groups, giving binding energy values slightly higher than those of C-C and C=C (Fig. 6.2-c) [250-253]. Deconvolution of the C 1s XPS also gives two peaks at around 285.7 and 286.5 eV, which can be ascribed to the tiny amounts of oxidized C phases [250-253]. XPS analyses also reveal that the surfaces of WC in both WC/CNT and WC/CB samples were essentially free from impurities. Specifically, the W 4f electron shows a strong doublet signal (33.9/31.7 eV, Fig. 6.2-d), which represents the characteristic peaks for WC [254]. There was no oxidized W phase detected in WC/CNT. The oxide phases of W in WC/CB were minimal, as indicated by the weak peaks of WO_x at around 36.3 and 37.3 eV (peaks 1 & 2; the peak 3 at 39.1 eV cannot be attributed to any oxidized W) [253]. The presence of this oxidized W phase would suppress the catalytic performance in HER due to the high free-energy of the adsorbed H [255]. Compared to WC/CB, the W 4f XPS of WC/CNT is also contributed by the small portion of the binding energy at
143

around 31 eV (peak 4 in Fig. 6.2-d), which might be from the metallic W and defected

WC phases with C vacancies [253].
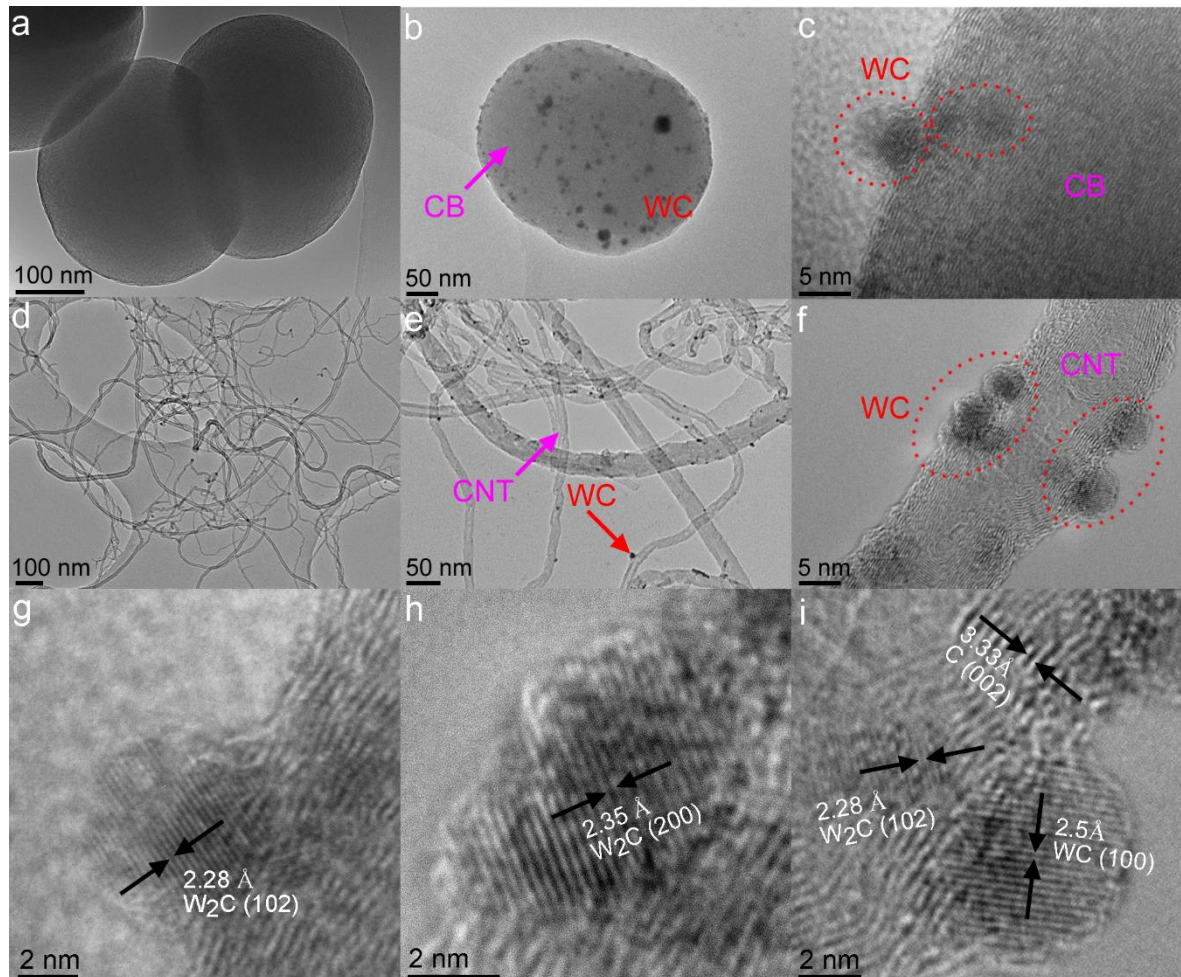
Fig. 6.3 (a) TEM image of as-received CB. (b-c) TEM images of as-prepared WC/CB

sample. (d) TEM image of as-received CNTs. (e-f) TEM images of as-prepared

WC/CNT sample. (g-i) HRTEM images of WC particles anchored on CB (g) and CNT

(h,i).

Fig. 6.3 presents TEM images of as-received CB and CNT, and as-prepared WC/CB and WC/CNT samples. As-received CB and CNT showed clean and smooth surfaces (Fig. 6.3-a&d). As-prepared WC/CB and WC/CNT samples were composed of unreacted carbon spheres or nanotubes (grey contrast) and newly-formed NPs (dark contrast) (Fig. 6.3-b&c, Fig. 6.3-e&f). The former still retained the overall morphologies and dimensions of as-received CB or CNT (Fig. 6.3-a&d), and the latter were monodispersed particles with sizes in most cases smaller than 5 nm (Fig. 6.3-b,c,ef, Fig. 6.3-g,h&i). EDS mapping under TEM (Fig. 6.5) futher reveals good dispersion and distribution of the NPs on both CB and CNT, and confirms that the NPs comprised mainly W and C (Fig. 6.4). The *in-situ* reaction between the carbon substrate and W, enabled the NPs to be firmly anchored onto the remaining carbon substrates (Fig. 6.3-c&f). The NPs were highly crystalline, giving clear lattice fringes of WC and W_2C under high-resolution TEM (HRTEM). The (102) (Fig. 6.3-g, on CB) and (200) lattices (Fig. 6.3-h, on CNT) of W_2C were clearly seen. As revealed by the HRTEM image of WC/CNT shown in Fig. 6.3-i, some W_2C and WC nanocrystals are connected with one another. The formation of monodispersed tungstern carbide nanocrystals on the carbon substrates could not be achieved *via* the conventional solid-solid synthesis route. Fig. 6.6, as an example, gives a TEM image of a WC/CNT sample prepared *via* the conventional solid-solid synthesis route, showing much larger (> 100 nm) W based particles and heavy agglomeration. In addition, it should be noted that the surafce of as-prepared tungsten carbon NPs on C substrates were clean and covering free, avoiding the surfacial carbon deposition problem commonly encountered by other techniques using gaseous carbon sources and

145

the degeneration in the final catalytic performances [31,59,61-64] (Fig. 6.3-c&f).
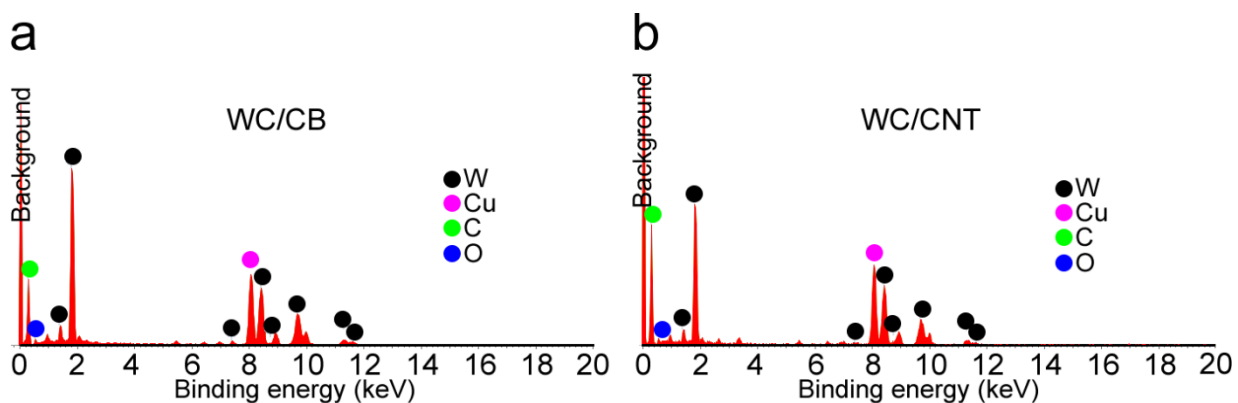
Fig. 6.4 EDS spectra of (a) WC/CB and (b) WC/CNT under TEM observations.
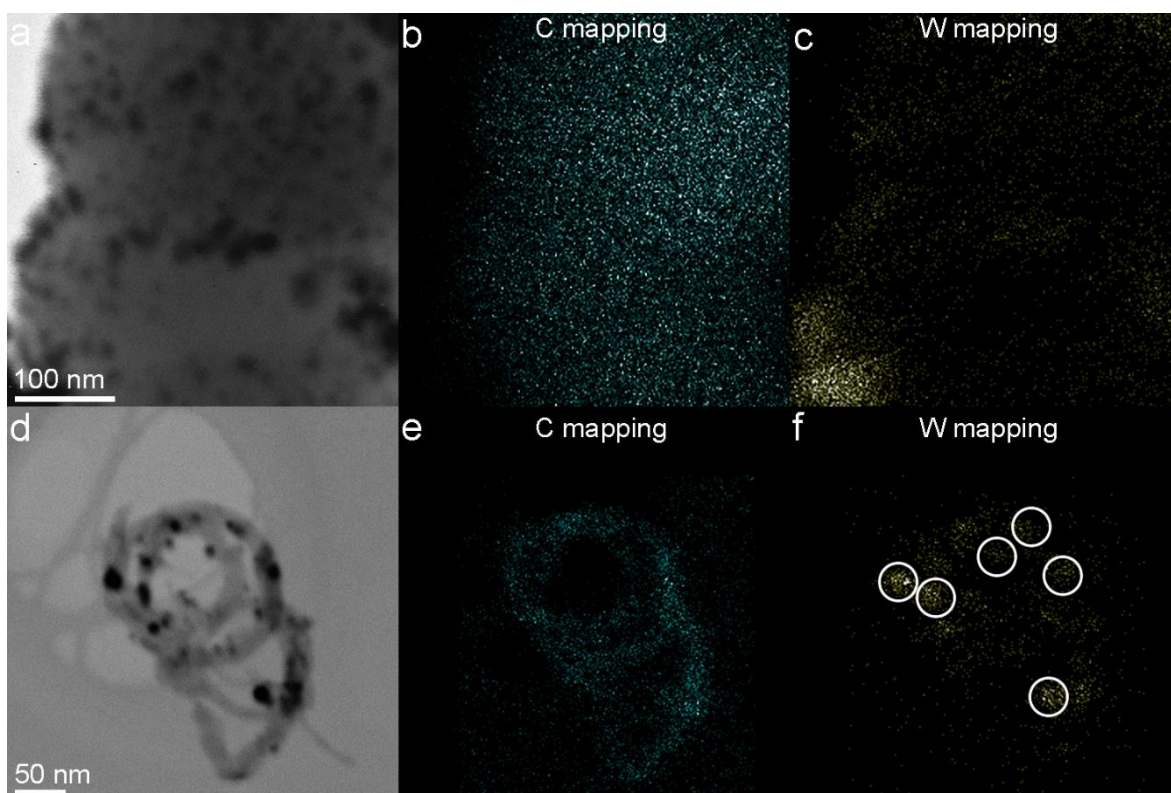
Fig. 6.5 (a-c) TEM image of as-prepared WC/CB sample and corresponding elemental

mapping of C and W. (d-f) TEM image of as-prepared WC/CNT sample and

corresponding elemental mapping of C and W.

146
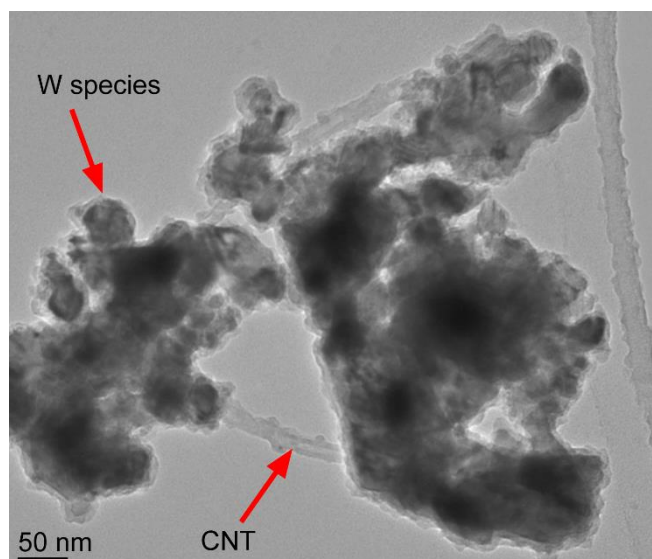
Fig. 6.6 TEM image of WC/CNT preapred *via* the conventional solid-solid synthesis route.

Based on the above characterizations, it could be considered that highly-dispersed tungsten carbon NPs (< 5 nm, in the majority of cases) had been successfully formed *in-situ* on the nanocarbon substrates by using the present MSS technique. The *in-situ* formation of high quality (*e.g.* monodispersed with clean covering-free surface) nanocarbon supported tungsten carbide nanocatalysts was attributable to the molten salt medium formed in the MSS process. The detailed reaction mechanism could be suggested as follows: At 600 °C, WO_3 NPs were initially reduced by Mg to W (Reaction (6.3)) [256]. Upon increasing the temperature to above 776 °C (the melting point of KCl), KCl melted, forming a molten salt medium into which the initially formed W partially disssolved [257]. The dissolved W diffused rapidly through the molten KCl medium onto the surfaces of CB or CNT, and reacted efficiently with carbon atoms, forming *in-situ* tungsten carbide nanocrystals (Reactions 6.1 and 6.2 described above).

147

6.3.2 HER performances
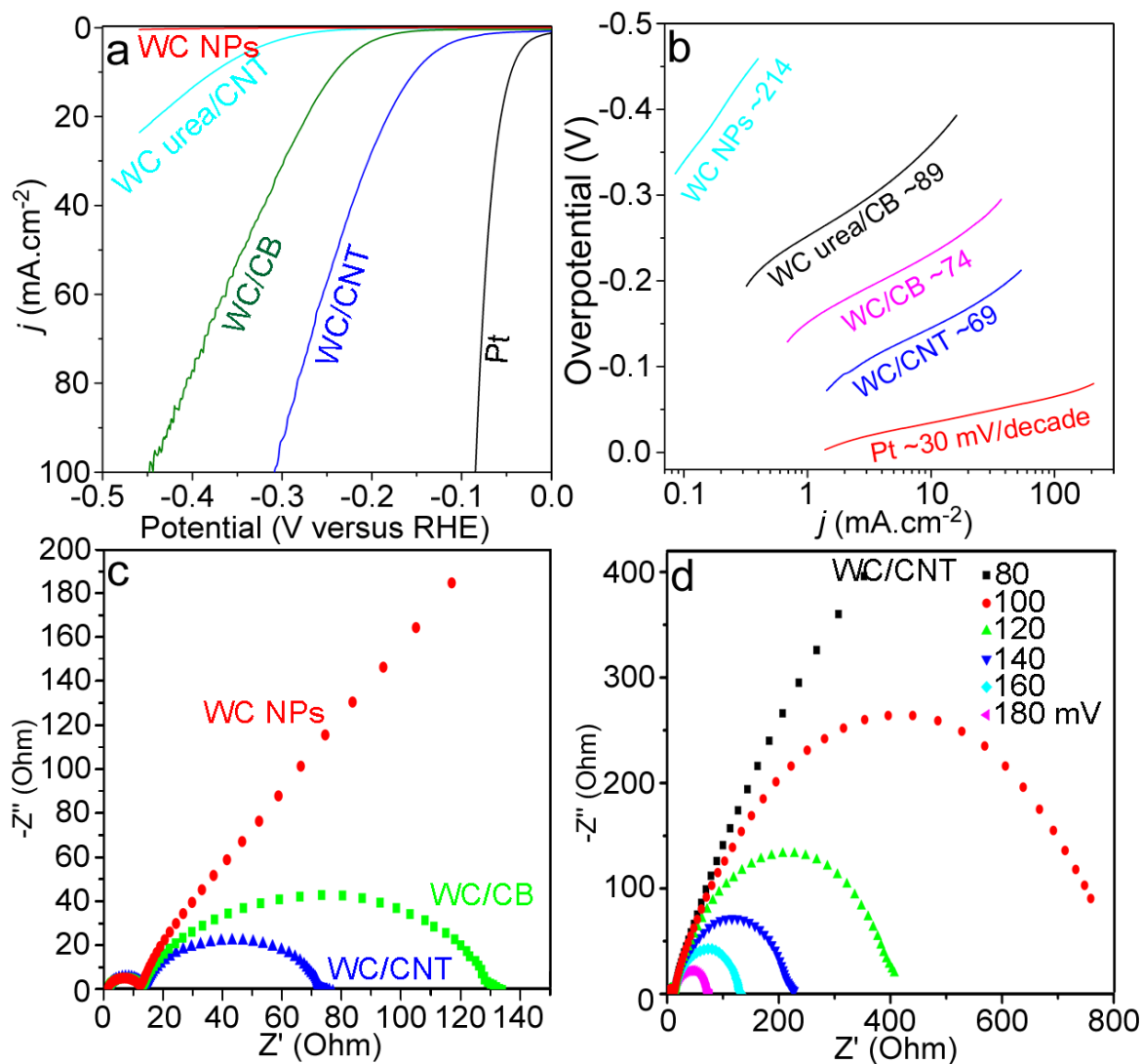
Fig. 6.7 (a) Polarization curves and (b) corresponding Tafel plots in the cases using commercial WC NPs, WC urea/CNT, WC/CB, WC/CNT, and Pt electrode. (c) Nyquist plots showing EIS (frequency range: 10^5 to 0.01 Hz; amplitude: 10 mV) responses of WC NPs, WC/CB and WC/CNT at the potential of 180 mV in 0.5M H_2SO_4. (d) Nyquist plots showing EIS (frequency range: 10^5 to 0.01 Hz; amplitude: 10 mV) responses of WC/CNT nanocatalyst at various potentials in 0.5M H_2SO_4.

The clean covering-free monodispersed WC NPs anchored onto carbon substrates exhibited much improved catalytic performance in HER. To illustrate this, we systematically evaluated and compared the HER electrocatalytic performances of as prepared WC/CB and WC/CNT nanocatalysts, commercial WC NPs (from Sigma Aldrich), WC nanocatalysts on CNT prepared *via* the "urea glass" route [59] (referred to as WC urea/CNT sample) and Pt (Fig. 6.7). The commercial WC NPs were almost inactive for HER, with negligible current density at 400 mV (Fig. 6.7-a) and Tafel slope of 214 mV dec^{-1} (Fig. 6.7-b). Although WC NPs prepared *via* the urea glass route were small enough (in most cases <5 nm, Fig. 6.8-a) to provide high surface area, the overpotential (244 mV, measured as the starting point of the linear Tafel curve) and Tafel slope (89 mV dec^{-1}) still remained high (all the potential values were with respect to Reversible Hydrogen Electrode/RHE). This was due to the amorphous carbon film deposited on NPs' surface (Fig. 6.8-b), which separated the catalytically active sites from the electrolytes. By contrast, WC/CB nanocatalysts from MSS exhibited a considerably improved HER performance, exhibiting much lower Tafel slope (74 mV dec^{-1}) and overpotential value (170 mV), and higher current densities (*e.g.* 31.3 mA cm^{-2} at 300 mV).
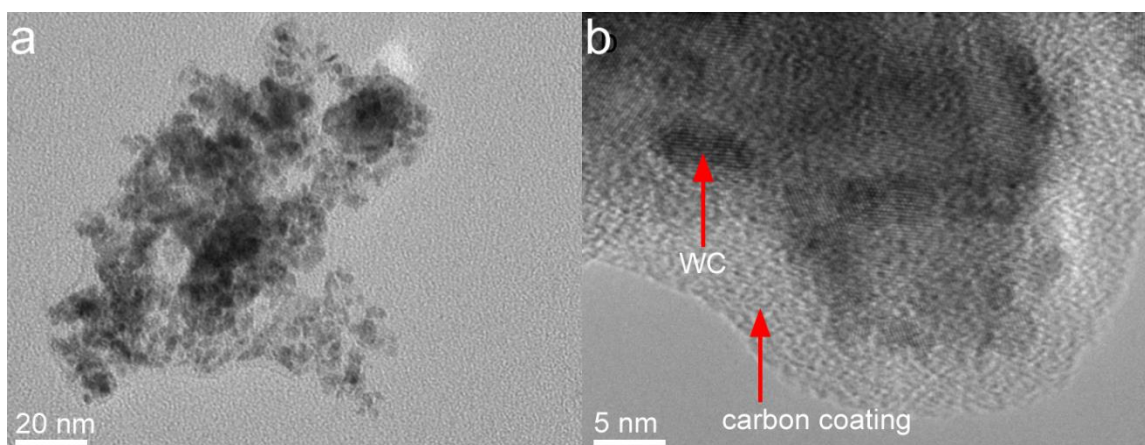
Fig. 6.8 (a) TEM image of WC urea/CNT. (b) HRTEM image of an individual WC particle prepared *via* the "urea glass" route [28], showing clearly deposition of a carbon coating on its surface.

Among the four WC based catalysts, WC/CNT nanocatalysts prepared *via* MSS showed the best HER performance with Tafel slope of ~69 mV dec^{-1} and onset overpotential of ~90 mV (Fig. 6.7-a&b). The cathode current densities of WC/CNT nanocatalysts at 300 and 200 mV were as high as 93.2 and 27.7 mA cm^{-2}, respectively. HER performance data of the above four WC catalysts are also summarized in Table 6.1.

Table 6.1 Comparison of HER performances of four different forms of WC based catalysts

Materials	Overpotential (mV)[a]	Tafel slope (mV dec^{-1})	j_{200} (mA cm^{-2})	J_{300} (mA cm^{-2})
WC/CNT	90	69	28	93.4
WC/CB	170	74	3.18	31.3
WC Urea/CNT	244	89	0.28	2.59
WC NPs	334	214	~0	0.06

Note: (a) recorded at the onset point of the linear Tafel curve.

Although the Tafel slope and overpotential of as-prepared WC/CNT nanocatalysts were still not close enough to those of commercial Pt electrode (Tafel slope of ~ 30 mV dec^{-1} and overpotential of ~23 mV), their overall HER performance was already one of the best among tungsten carbide based catalysts [27-28,31-33] (Tafel slope of 69~137 mV dec^{-1} and overpotential of 145~500 mV), and comparable to the performances of some molybdenum carbide based catalysts [248,258-259] (Table 6.2). The WC/CB catalysts (Tafel slope of ~74 mV dec^{-1} and onset overpotential of ~170 mV) were slightly less effective than the WC/CNT catalysts, but their overall performance was still better than most of the other tungsten carbide based catalysts. This could be attributed to the following reasons: (1). Monodispersed WC NPs on nanocarbon substrates had much greater surface areas, providing many more catalytically active sites. The WC on CNT had also small portions of metallic state and/or carbon vacancies (see W 4f XPS in Fig. 6.2-d), which might additionally improve the catalytic performance; (2). The WC NPs connected with one another *via* conductive CNT substrates (Fig. 6.3-e,f); (3). The H_2 bonding strength on single phase WC was too much stronger (compare with that on Pt), resulting in an inhibited H_2 desorption process [34]. However, in the present case, this bonding strength was considerably reduced since the anchored WC induced a charge transfer from W to C, downshifting the *d*-band center of W [239].

151

Table 6.2 HER performances of various types of WC and Mo$_2$C catalysts.

Materials and Synthesis methods	Overpotential (mV)	Tafel slope (mV dec^{-1})
Salt flux method from W and C [27]	345	137
WCx/C by combustion-carbothermal reduction method [28]	264	85
WC/C from a polyaniline/tungstic acid hybrid precursor *via* the annealing process at 1200 ºC [29]	220	93
High temperature reaction of W and C [30]	300	N/A
W layers deposited on the tips of vertically arrayed CNTs and heated at ~1000 °C [31]	145	72
Carbonization of SiO$_2$/WO$_x$ nanosphere [65]	260	N/A
Co and N co-doped WC [32]	500	N/A
WC thin films by Magnetron sputtering [33]	300	91
W$_2$C thin films by Magnetron sputtering [33]	200	69
High temperature reaction between ammonium molybdate and carbon cloth [248]	140	124
Carbon coated Mo$_2$C nanoparticles (reaction between MoO$_3$, Mg and polypropylene) [258]	101.4	79.5
Mo$_2$C nanoparticles decorated on graphitic carbon sheets (reaction between sodium alginate and ammonium molybdate) [259]	120	62.6
WC/CB (This work)	**170**	**74**
WC/CNT (This work)	**90**	**69**
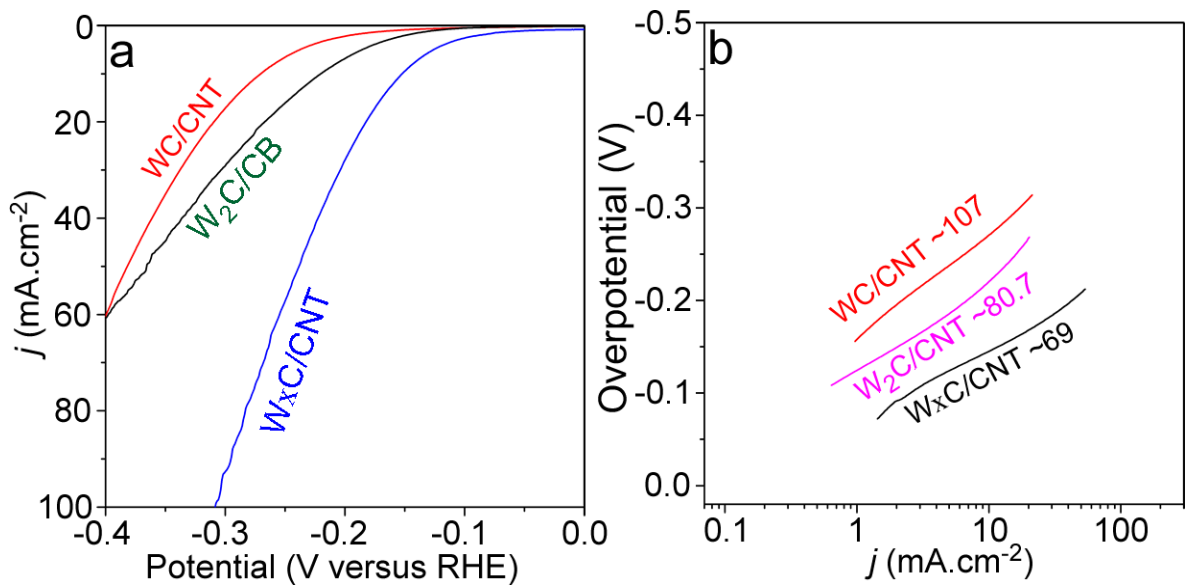
Fig. 6.9 (a) Polarisation curves and (b) Tafel slope curves of pure WC/CNT, W₂C/CNT

(the primary phase was W₂C), and WC composite/CNT (containing both WC and W₂C
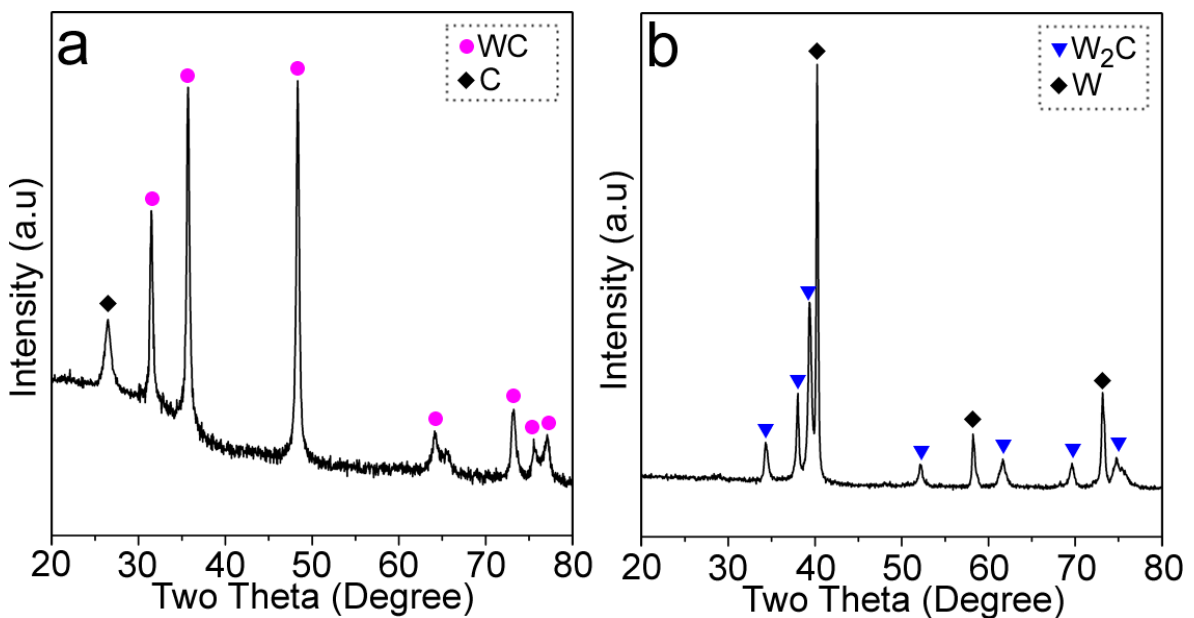
phases).

Fig. 6.10 (a) XRD pattern of single WC phase on CNTs. (b) XRD pattern of W₂C

phase on CNTs with residual W phase. Almost all of the CNTs had been reacted to

form W₂C.

We also varied the ratio of W (WO$_3$) to CNT to tailor the phase compositions (pure WC or W$_2$C) of the final product samples. Unfortunately, the HER performances of such single-phase catalysts were very poor (Fig. 6.9, also see Fig. 6.10 for their XRD patterns). W$_2$C has higher 5d-orbital electron population [260], which explains the poorer catalytic performance of single phase WC on CNTs (as a control) than that of the above discussed WC/CNT nanocatalyst (having both WC and W$_2$C phases). It was reported that the pure WC$_2$ nanocrystals had excellent HER performance with onset potential of ~50 mV and Tafel slope of 45-50 mV Dec^{-1} [35-36]. However, in the present work, after a number of attempts under different conditions (*e.g.* varying the synthesis temperature), we still failed to form single phase W$_2$C (on CNT), due to probably its metastable nature. It was found that once W$_2$C was formed, it would readily react further with CNT to form WC. Although the relative content of W$_2$C could be increased by using much more W oxide raw materials, most of the CNTs were consumed and the formation of some W particles would become unavoidable, which in turn reduce the overall catalytic activity (Fig. 6.9). Future work is still needed to find out a feasible approach to stabilization of single phase W$_2$C NPs on a conducting substrate (for example, by choosing other types of salts with higher W solubility) and to further evaluate their HER performance.

The EIS measurements at 180 mV on WC NPs, WC/CB and WC/CNT were further conducted to demonstrate the improved HER performance of our newly-developed

nanocatalysts. Nyquist plots in all the cases were characterized with two time constants at high and low frequencies (Fig. 6.7-c, the two semi-circles). The latter at lower frequency reflects the kinetics of the HER process. Compared with commercial WC NPs, the charge transfer resistances (R_{ct}) of WC/CB and WC/CNT samples were decreased significantly to 130 and 75 Ω, respectively, indicating greatly improved HER kinetics and performances (the R_{ct} of commercial WC NPs was too high and beyond the range of measurement). The lower charge transfer resistance of WC/CNT than that of WC/CB was also attributed to the higher electrical conductivity of CNT than CB, which facilitated the charge transfer process in the former. The R_{ct} values at different applied potentials in the case of WC/CNT were also measured, from which, the EIS Tafel slope was determined as 70.2 mV dec^{-1} (Fig. 6.11). This value was very close to the voltammetry Tafel slope (69 mV dec^{-1}, Table 6.1), representing the charge transfer kinetics in the case of WC/CNT. R_{ct} values in the case of WC/CNT also showed a sharp drop from 780 Ω at 100 mV to 72 Ω at 180 mV, suggesting a higher activity and faster charge transfer ability of the WC/CNT nanocatalysts at higher potentials.
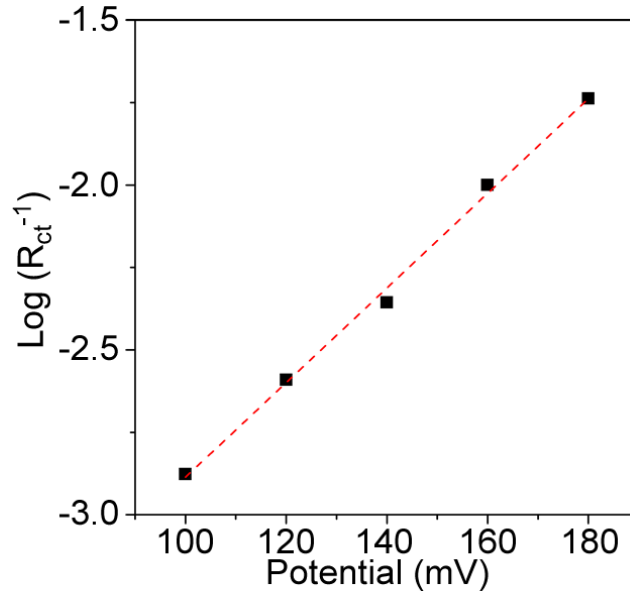
Fig. 6.11 Log (Rct^{-1}) as a function of potential.
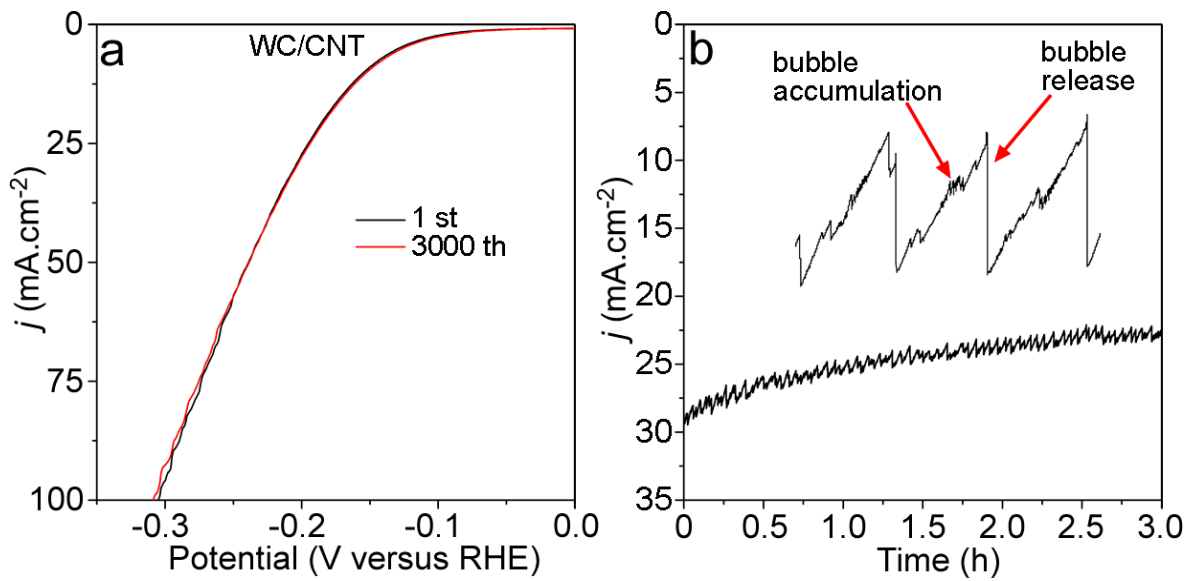
Fig. 6.12 (a) Durability test on as prepared WC/CNT catalyst showing only negligible current loss even after 3000 CV cycles. (b) Time dependence of current density at the static overpotential of 200 mV. The inset: magnified local section of the time dependent curve.

Next, we tested the stability of the WC/CNT nanocatalyst, in view of its best HER performanc among the four WC based catalysts described above (Table 6.1). The HER process was continuously run 3000 cycles in 0.5 M H_2SO_4 solution, giving highly stable polarization curves (Fig. 6.12-a) and suggesting a long-term stability of the WC/CNT nanocatalyst. Such an excellent stability was further revealed by the relationship between current density and time at a given potential (Fig. 6.12-b). As seen from Fig. 6.12-b, the current density in the case of WC/CNT at a potential of 200 mV remained stable owing to the excellent stability of the nanocatalyst and periodical changes of the HER current density during the test . It should be noted that the serrate shape was also attributed to the accumulation (which caused slight decresing of current density as the bubbles seperated the electrode and electrolyte) and release (which made the current density back to normal) of H_2 bubbles from the catalyst. (Fig. 6.12-b: the inset).
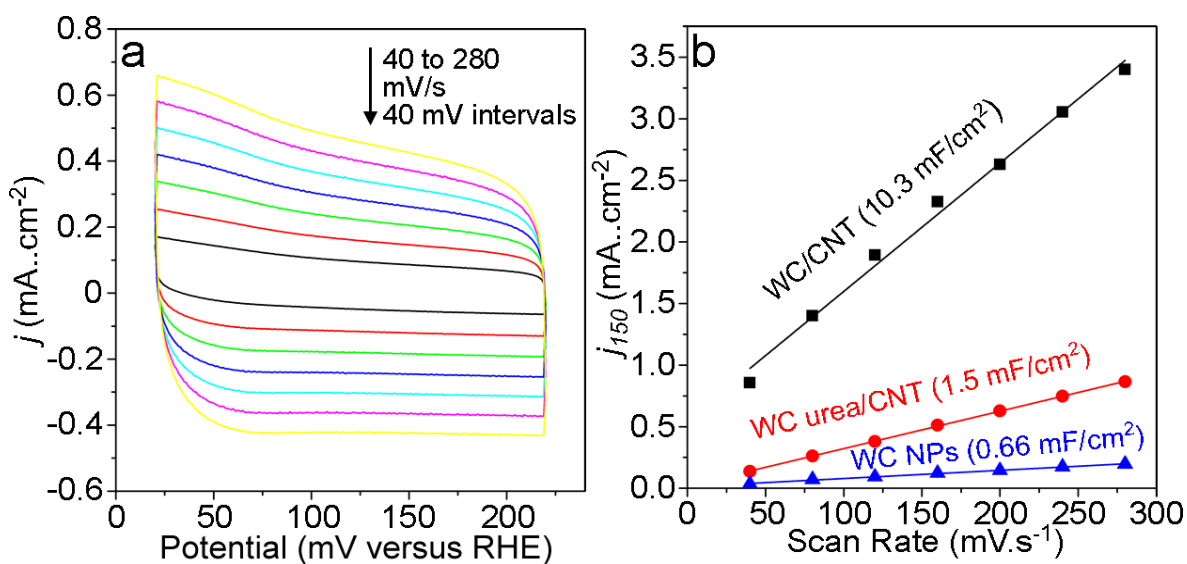
Fig. 6.13 (a) Voltammograms of the WC urea/CNT catalyst at various scan rates (40-280 mV s^{-1} with 40 mV intervals). (b) Plots of the C_{dl} of commercial WC NPs, WC urea/CNT and WC/CB.

157

Apart from the advantages of MSS technique discussed above, another important point was that the WC NPs *in-situ* formed on a nanocarbon substrate provided many more catalytically active sites than other WC-based counterparts. To illustrate this, we compared electrochemically active areas of WC/CNT, WC urea/CNT and pure WC NPs based on simple cyclic voltammetry measurements. As well documented, the effectively active surface area could be represented by the double layer capacitance (C_{dl}) of the catalyst. It can be calculated based on the plot of $\Delta j = j_a - j_c$ (where j_a and j_c are current densities at 0.15 V *vs* RHE) against the CV scan rate (the CV of WC urea/CNT) [261]. The C_{dl} value determined by this method for the WC/CNT nanocatalyst (10.3 mF cm^{-2}) was about 6 and 15 times higher than in the cases of WC urea/CNT and WC NPs, respectively. Such a great increase in the catalytically active sites further explained considerably improved HER performance of the nanocatalysts prepared *via* the present MSS route.

6.4 Conclusions

In summary, tungsten carbide (WC coexisting with W_2C) nanocrystals (in the majority of cases, <5 nm) were directly formed *in-situ* on CB or CNT substrates *via* a simple molten salt assisted reaction route. They were well dispersed and intimately anchored on the carbon substrates. Such a unique hybrid structure resulted in downshifting in the *d*-band centre of W, and decrease in the W-H bond strength. Consequently, as prepared WC nanocatalysts exhibited excellent HER performance, which was much better than

158

that achieved by most of the other WC based catalysts reported to date. In addition, as-prepared WC/C nanocatalysts showd an excellent durability. Our results suggested that as-prepared WC/C (in particular, WC/CNT) nanocatalysts could be used as very promising catalysts for HER. The work presented here provided a low cost and scalable approach to upgrade of less active conventional materials to much more active HER catalysts.

159

Chapter 7. Low temperature molten salt synthesis of SiC and ZrC nanosheets and SiC- and ZrC-coated graphite nanoplatelets

7.1 Background

Since the discovery of graphene, a monolayered carbon sheet, two-dimensional (2D) nanoscale materials or nanosheets/nanoplatelets have attracted a great deal of attention owing to their unique morphology and structure and many outstanding properties [206]. Apart from graphene, various types of 2D materials, including transition metal dichalcogenides (TMDs) [207-208], transition metal oxides (TMOs) [208-209] and nitrides [208-211], have been prepared by using different techniques/methodologies. Unfortunately, these techniques/methodologies suffered from various drawbacks, e.g., requirement of expensive and environmentally-unfriendly precursors and complex reaction vessels [271-288].

In the work presented in this chapter, a universal low temperature molten salt synthesis technique has been developed for producing several important types of nanosheets/nanoplatelets with large specific surface areas, which are difficult to prepare by using the conventional techniques used previously, including SiC nanosheets (SNS), ZrC nanosheets (ZNS), and SiC- and ZrC-coated multilayered graphene (graphite

160

nanoplatelets). The effects of key processing parameters on the reaction extent and the synthesis process were examined, and the relevant reaction mechanisms discussed.

7.2 Experimental

7.2.1 Raw materials

Multilayered graphene (graphite nanoplatelet, MG) (97% pure, thickness: 6-8 nm, overall sheet size: 5 μm, BET surface area: 100 m^2/g), silicon powder (Si, 99.6% pure), zirconium oxide powder (ZrO$_2$, <100 nm), and metallic magnesium powder (Mg), were used as main raw materials. Potassium chloride (KCl, 99% purity), sodium chloride (NaCl, 99% purity) and sodium fluoride (NaF, 99% purity) were used to form a molten salt medium. The MG was received from Strem Inc., USA and the rest were supplied by Sigma Aldrich, UK.

7.2.2 Sample preparation

As-received MG was dispersed in acetone for 30 minutes under ultrasonication followed by oven-drying at 70 °C for 24 hours. In the preparations of SiC nanosheets or SiC coated graphene (graphite nanoplatelets), Si powder and the dispersed MG were mixed homogeneously in an agate mortar, in the equimolar ratio corresponding to Reaction (7.1), and the non-stoichimetric molar ratio (1/1.5), respectively. The powder mixture

161

was further combined with a binary salt (95% NaCl + 5% NaF) in the weight ratio of 1/20.

$$Si + C = SiC \tag{7.1}$$
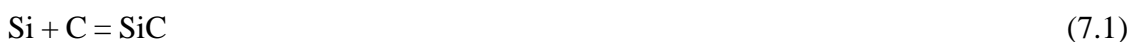
On the other hand, for ZNS and ZCG preparations, the as-received MG was dispersed in acetone for 30 minutes under ultrasonication with ZrO_2 in the equimolar mixing ratio indicated by Reaction (7.2), or non-stoichimetric ratios (1/2 and 1/4), and then oven-dried at 70 °C for 24 hours. The dispersed powder mixture was then combined with Mg powder in an agate mortar, followed by further combination with KCl in the weight ratio of 1/20.

$$ZrO_2 + 2Mg + C = ZrC + 2MgO \tag{7.2}$$

The dried batch power in each case was contained in a graphite crucible covered with a lid and placed in an alumina tube furnace protected by a constant flow of argon. The test temperature range for the preparations of SiC nanosheet and SiC coated graphite nanoplatelet was between 1050 and 1250 °C and the heating rate was 5~3~1 °C/min (5 °C/min up to 1000 °C, 3 °C/min up to 1200 °C and then 1 °C/min). The dwelling time at the target temperature was 2-6 h. On the other hand, the test temperature range for the preparations of ZrC nanosheet and ZrC coated graphite nanoplatelet was within 750~ 850 °C, and the heating rate was 5 °C/min and the holding time 2-6 h. The reacted mass

162

in each case was washed repeatedly with hot distilled water to remove the residual salt, or in the case of using Mg, further immersed in 1M HCl solution for 24 h before being washed with hot distilled water. The final product powder was oven-dried overnight at 100 °C and subjected to further characterisation.

Phases in as-prepared product powders were identified by powder X-ray diffraction (XRD) analysis (Brukers D8 reflection diffractometer). Spectra were recorded at 40 mA and 40 kV using Ni-filtered Cu Kα radiation. The scan rate was 2.4° (2θ)/min with a step size of 0.04°. ICDD cards used for phase identification are SiC (29-1131), C (65-6212), Si (65-1060), ZrC (65-4932) and Zr (65-3366). Microstructure of product samples and phase morphology were examined using a field emission gun scanning electron microscope (Nova Nanolab 600) and a high resolution TEM (HRTEM, JEM 2100 microscope), along with an energy-dispersive spectroscope (EDS) and selected area electron diffraction (SAED).

7.3 Results and Discussion

7.3.1 Fabrication and characterisation of SNS and SCG

7.3.1.1 Effects of firing temperature on the SNS synthesis
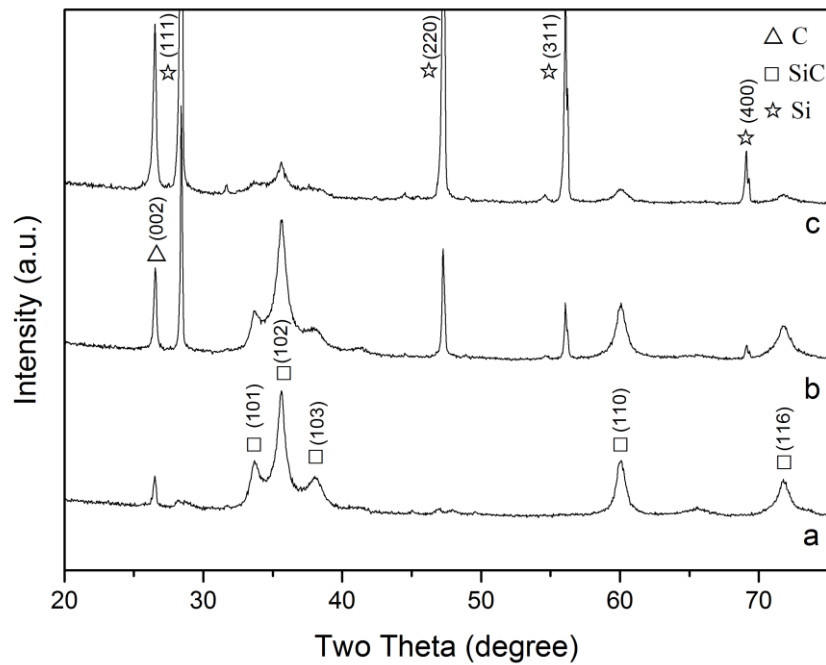
Fig. 7.1 XRD patterns of samples with Si/C = 1/1 (molar ratio) after 6 h firing in NaCl

+ NaF at (a) 1250 °C, (b) 1200 °C and (c) 1150 °C, respectively.

Fig. 7.1 illustrates the effects of temperature on the formation of SiC in the sample with

Si:C=1:1. At 1150 °C, small amounts of SiC were formed in the sample. However, large

amounts of graphite nanoplatelets and Si still remained, indicating the low extents of

164

reaction between the two. Upon increasing the temperature to 1200 °C, Si and graphite

nanoplatelet decreased while SiC increased evidently, indicating the enhanced reaction

extents. Upon further increasing the temperature to 1250 °C, all Si was consumed and

SiC phase was formed with little residual carbon.

7.3.1.2 Effects of firing temperature on the synthesis of SiC coated graphite

nanoplatelet
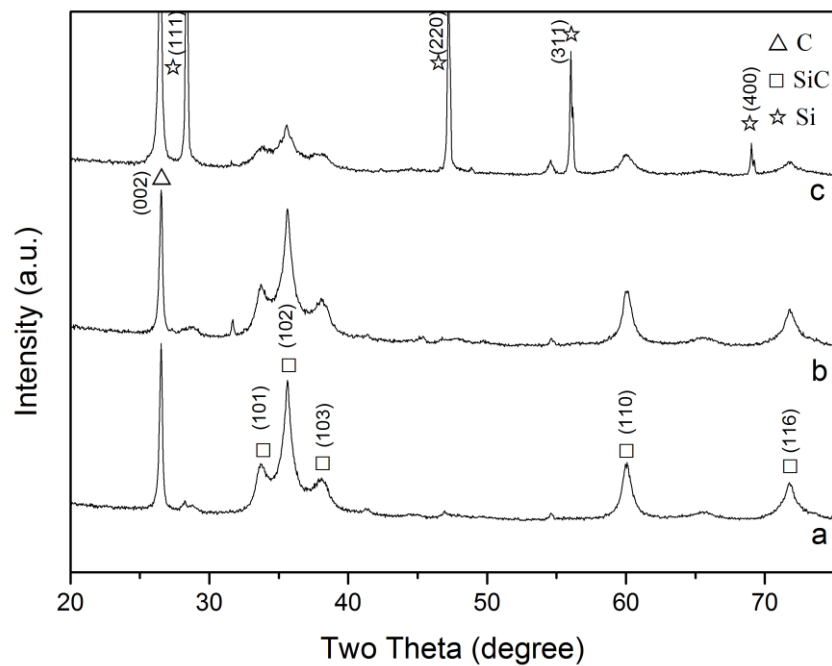
Fig. 7.2 XRD patterns of samples with Si/C = 1/1.5 (molar ratio) after 6 h firing in

NaCl + NaF at (a) 1250 °C, (b) 1200 °C and (c) 1150 °C, respectively.

Fig. 7.2 shows the effects of temperatures on the SiC formation in the sample with Si:C

= 1:1.5. At 1150 °C, only small amounts of SiC were formed, but large amounts of

165

graphite nanoplatelet, and Si were still present, indicating the limited reaction between the two. Upon increasing the temperature to 1200 °C, much more SiC was formed, along with the residual graphite nanoplatelet and minor amounts of Si, indicating that the reaction between Si and graphite nanoplatelet was nearly completed. Upon further increasing the temperature to 1250 °C, SiC increased slightly, whereas Si peaks nearly disappeared, implying that the reaction between Si and graphite nanoplatelet was nearly completed.

7.3.1.3 Effects of salt on the SiC formation and nanosheet preparation
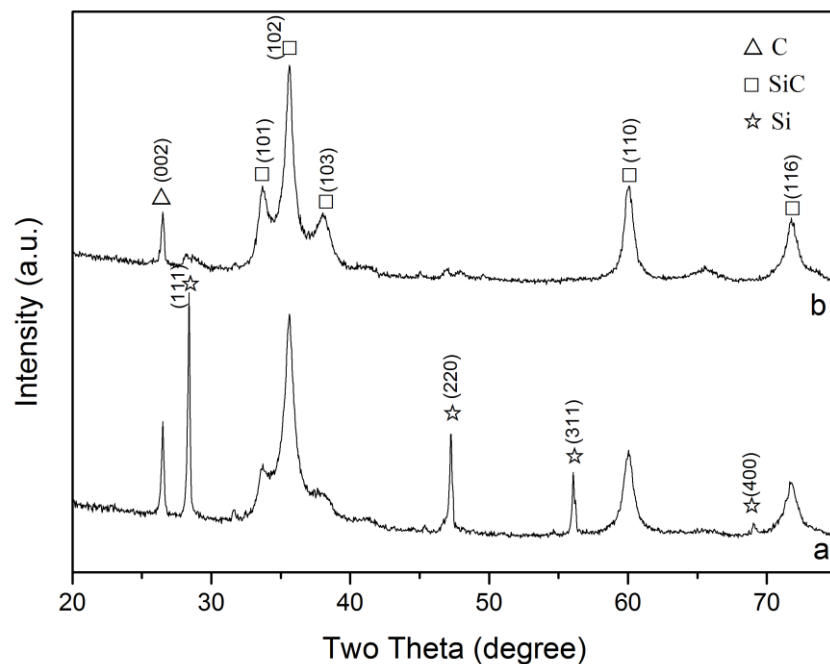
Fig. 7.3 XRD patterns of samples with Si/C = 1/1 (by molar ratio) heated at 1250 °C

for 6 h in (a) NaCl and (b) 95% NaCl + 5% NaF.

Presented in Fig. 7.3 are XRD patterns of samples with Si:C molar ratio of 1:1, after 6 h

firing at 1250 °C in single NaCl and binary NaCl-NaF salts, respectively. In the case of

using only NaCl, large amounts of unreacted Si and graphite nanoplatelet still remained.

However, in the case of using a binary NaCl-NaF salt Si peaks became nearly invisible,

indicating that the presence of NaF accelerated the SiC formation reaction. The above

results can be attributed to that the use of NaF increased solubility of Si in the salt,

although the exact solubility value is not available.

7.3.1.4 Effects of reaction time on the SiC formation and nanosheet preparation
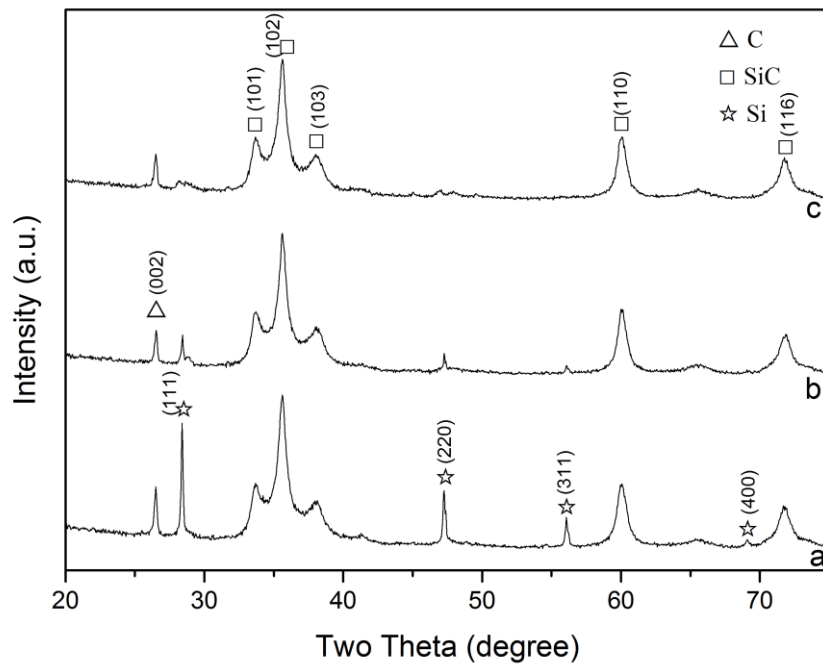
Fig. 7.4 XRD patterns of samples with Si/C = 1/1 (molar ratio) heated at 1250 °C in

NaCl + NaF for (a) 2 h, (b) 4 h and (c) 6 h, respectively.

167

Shown in Fig. 7.4 are XRD patterns of samples with Si:C ratios of 1:1 fired at 1250 °C for different time periods. As expected, with increasing reaction time, SiC increased whereas Si and graphite nanoplatelet decreased. After 6 h at the temperature, Si disappeared, nearly phase pure SiC was formed.
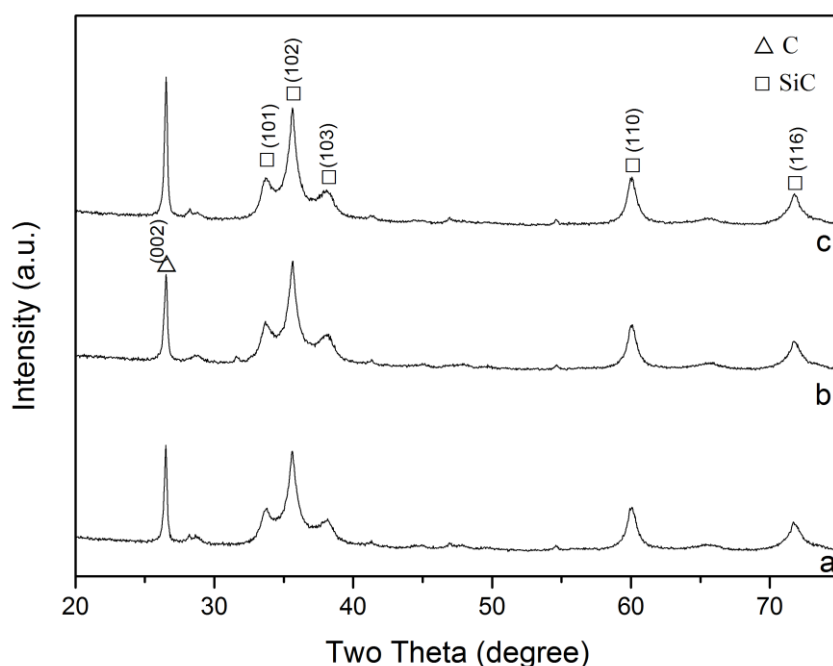
Fig. 7.5 XRD patterns of samples with Si/C = 1/1.5 (molar ratio) heated at 1250 °C in NaCl + NaF for (a) 2 h, (b) 4 h and (c) 6 h, respectively.

Fig. 7.5 further demonstrates the effects of reaction time on the SiC formation in the samples with Si:C ratio of 1:1.5. Due to the use of less Si than in the samples with Si:C ratio of 1:1, Si disappeared after just 2 h firing at the temperature. Further increasing the reaction time showed little effect on the phase formation.

7.3.1.5 Microstructural characterisation
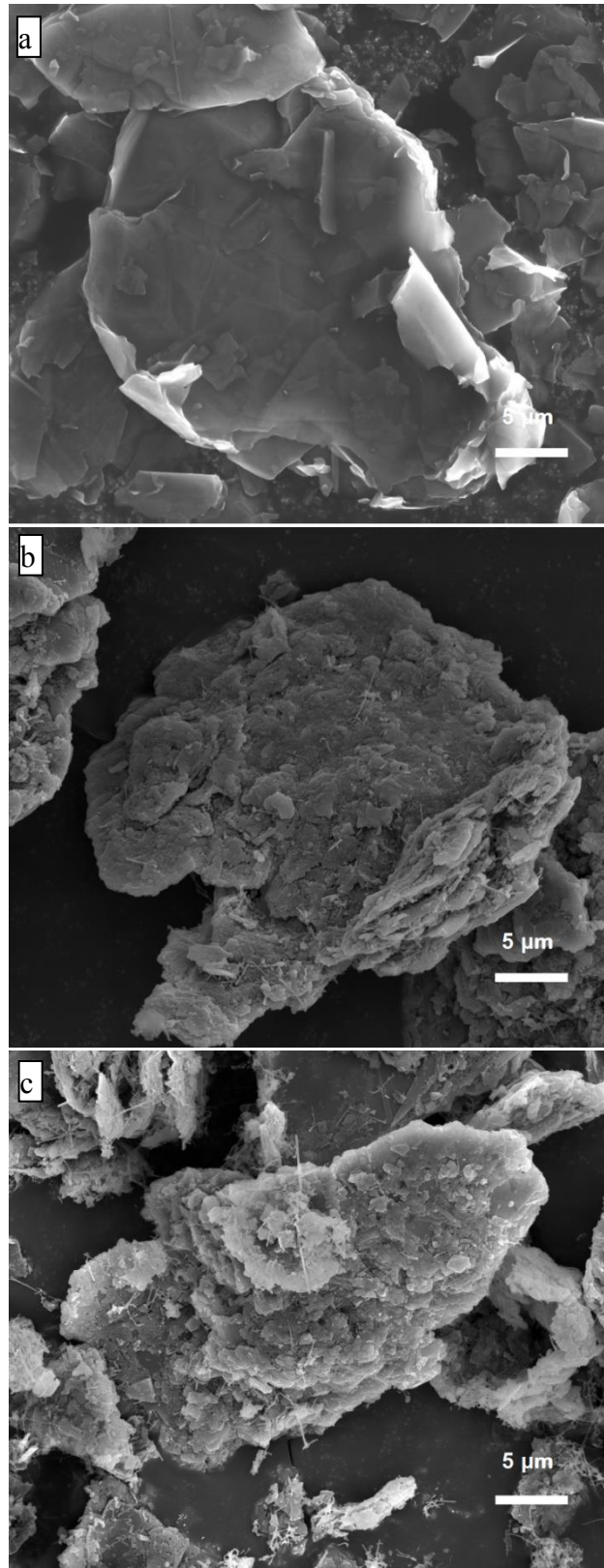
Fig. 7.6 Low magnification SEM images of (a) as-received graphite nanoplatelet, (b)

SNS, (c) SiC coated graphite nanoplatelet
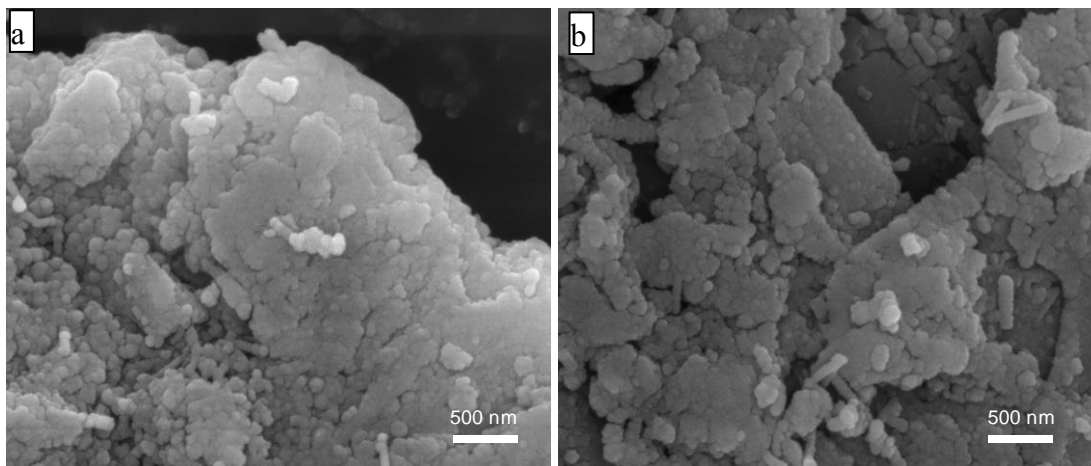
Fig. 7.7 High magnification SEM images of (a) SNS and (b) SiC coated graphite nanoplatelets.

Figs. 7.6 and 7.7 give SEM images of as-received graphite nanoplatelets, and SNS and SiC coated graphite nanoplatelets resultant from 6 h firing at 1250 ºC in NaCl-NaF. The original graphite nanoplatelets were wrinkled sheets with lateral sizes ranged from a few micrometers to about 20 μm. The as-prepared SNS overall exhibited similar morphologies, shapes and sizes to the original graphite nanoplatelets, indicating that graphite nanoplatelet acted as the template during the formation of SNS and SiC-coated graphite nanoplatelet, i.e, a template growth mechanism dominated the synthesis process. Furthermore, compared to smooth surfaces of as-received graphite nanoplatelet (Fig. 7.6-a), much rougher surfaces (Fig. 7.6-b,c) were seen in the cases of SNS and SiC-coated graphite nanoplatelet, due to the *in-situ* formation of silicon carbide particles (confirmed by XRD Figs. 7.1 and 7.2). Apart from SiC, some SiC nano-fibres were formed *via* probably dissolution and precipitation mechanism. As the main objective of this part of work is to investigate the preparation of SiC based nanosheets, no further

170

characterisation work has been done on the nanofibers.
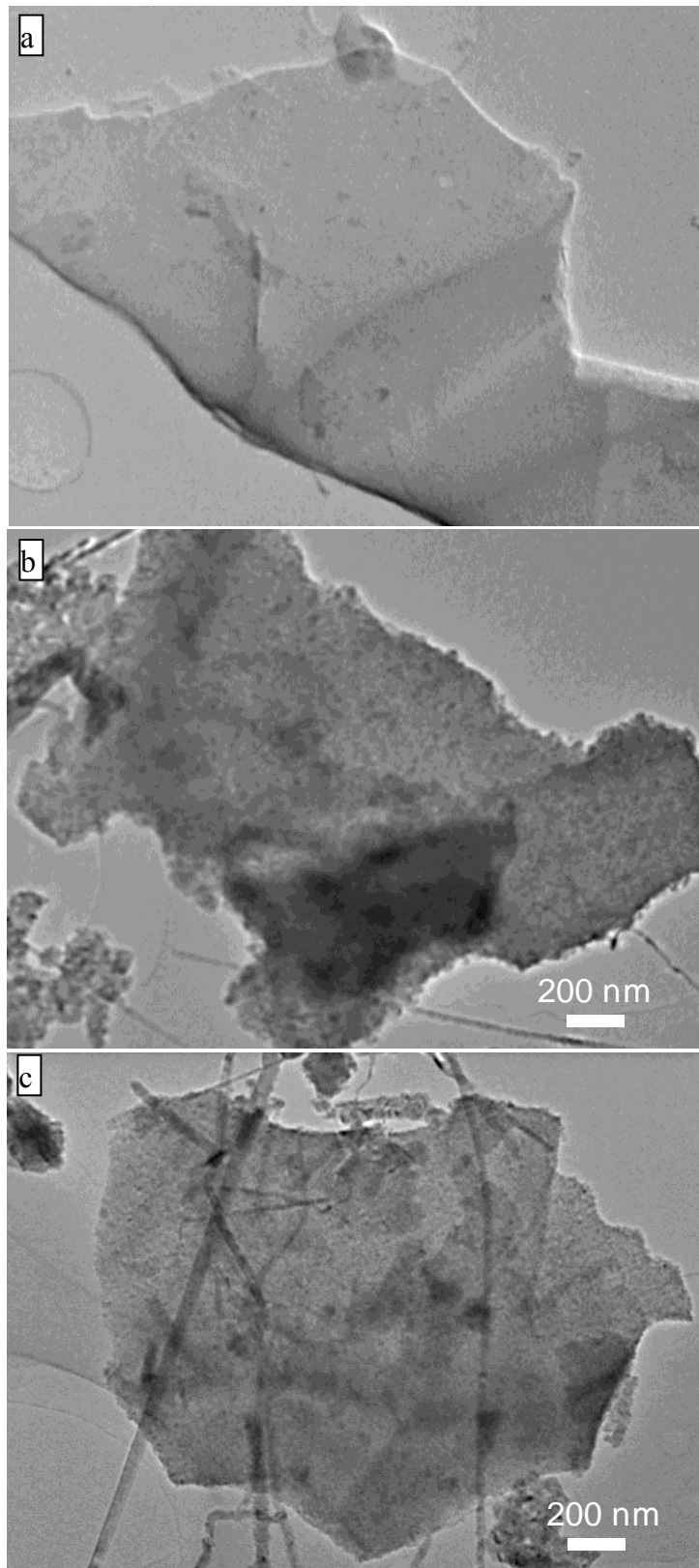
Fig. 7.8 Low magnification TEM images of (a) as-received graphite nanoplatelet, (b)

SNS, and (c) SiC coated graphite nanoplatelet.
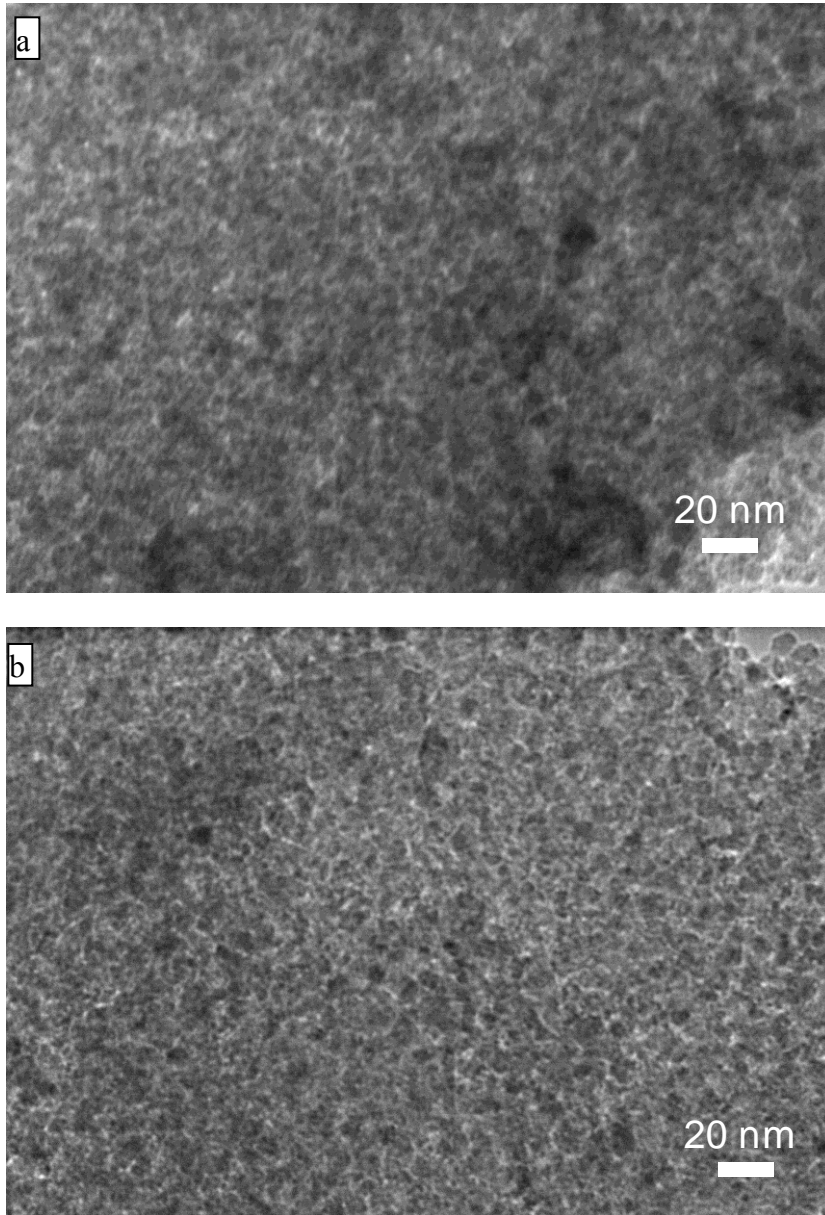
Fig. 7.9 High magnification TEM images of (a) SNS and (b) SiC coated graphite
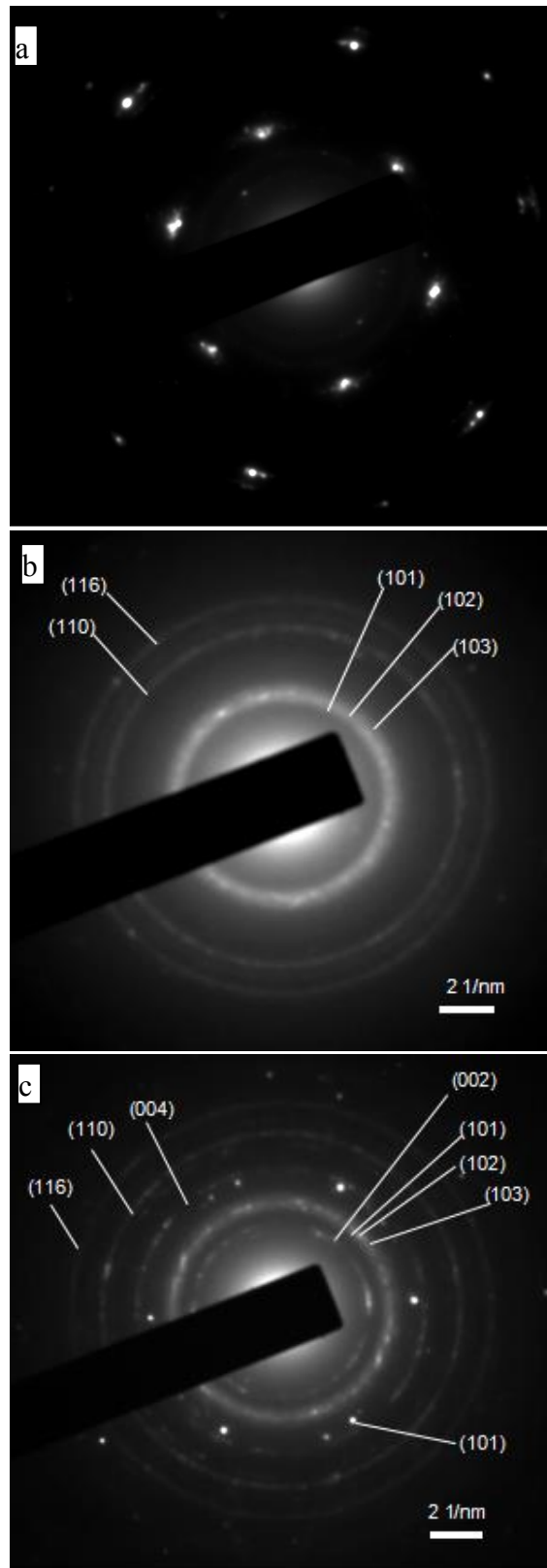
nanoplatelet.

Fig. 7.10 SAED patterns of (a) as-received graphite nanoplatelet, (b) SNS, and (c) SiC

coated graphite nanoplatelet.
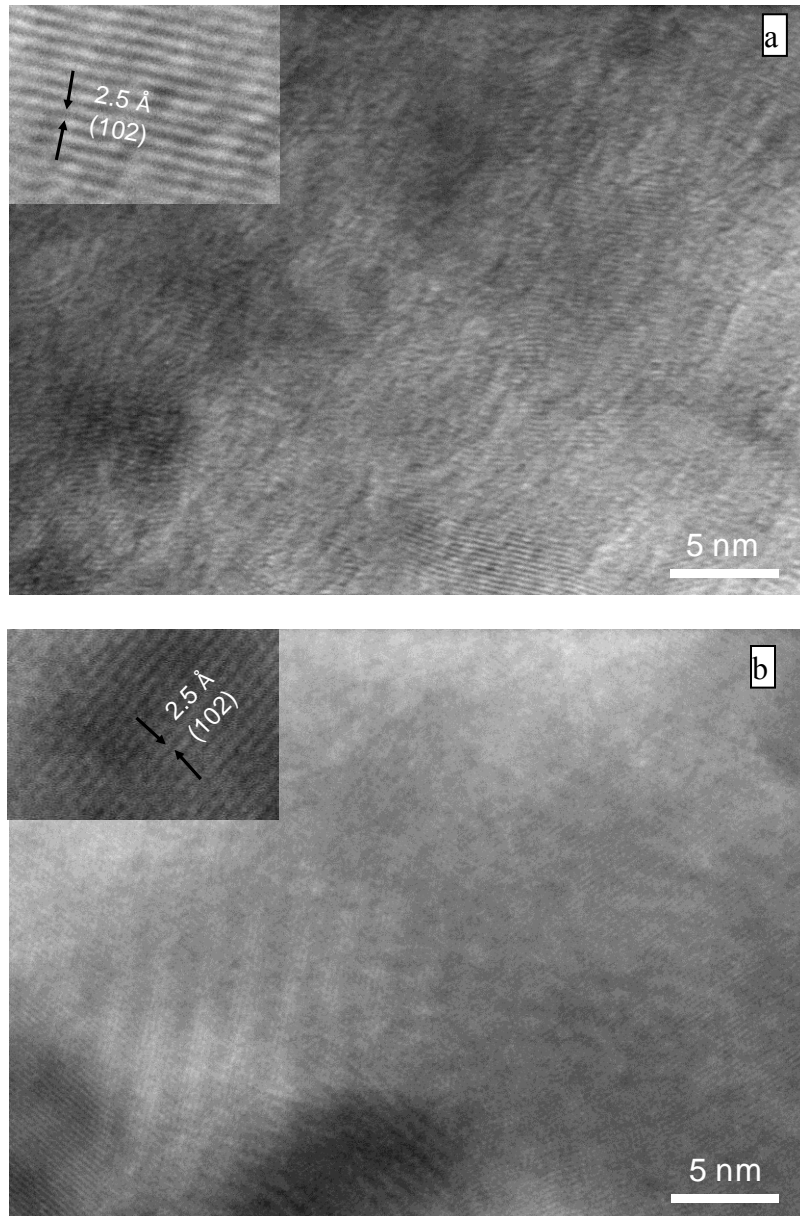
Fig. 7.11 HRTEM image of (a) as-prepared SNS and (b) SiC coated graphite

nanoplatelet.

Morphologies of as-received graphite nanoplatelet, and as-prepared SNS can be seen

more clearly from TEM (Figs. 7.8-a,b). Both materials exhibited layered 2D-

nanostructure which was supposed to have large specific surface area. Unlike graphite

nanoplatelet with smooth surface (Fig. 7.8-a), as-prepared SNS exhibited rougher

174

surface due to the formation of nanosized (20 nm) particles and some nanofibers. SAED patterns further confirm that the synthesised nanosheets were SiC (based on the diffraction rings of SiC (29-1131)) (Fig. 7.10-b,c). Those rings could be indexed to the (101), (102), (103), (110) and (116) planes, and their relative intensities matched well with those from XRD (Fig. 7.1). In contrast, in the case of as-received graphite nanoplatelet, diffraction spots indicating the hexagonal graphitic structure were obtained. As shown in Fig. 7.11, the lattice interlayer distance was about 0.25 nm, which corresponds to the (102) plane of SiC. The lattice fringes arranged in different orientations (Fig. 7.11), along with the diffraction rings in the SAED pattern (Fig. 7.10-a,b) reveal the polycrystalline nature of SNS. Similarly, as-prepared SiC coated graphite nanoplatelets also displayed rougher surfaces due to the formation of SiC nanoparticles. The lattice interlayer distance in this case was also 0.25 nm. SAED patterns (Fig. 7.10-c) also exhibited polycrystalline diffraction rings corresponding to the (101), (102), (103), (110) and (116) planes of SiC as well as (002) and (004) planes of graphite.

7.3.2 Formation mechanism

As shown in Figs. 7.6 and 7.8 and described above, as-prepared SiC nanosheet and SiC-coated graphite nanoplatelet to a large extent retained the morphology and size of the original graphite nanoplatelet. This phenomenon suggested that the template growth mechanism should have dominated the synthesis process and the graphite nanoplatelets acted as the templates because the graphite nanoplatelet had much less solubility (or

175

insoluble) than Si.
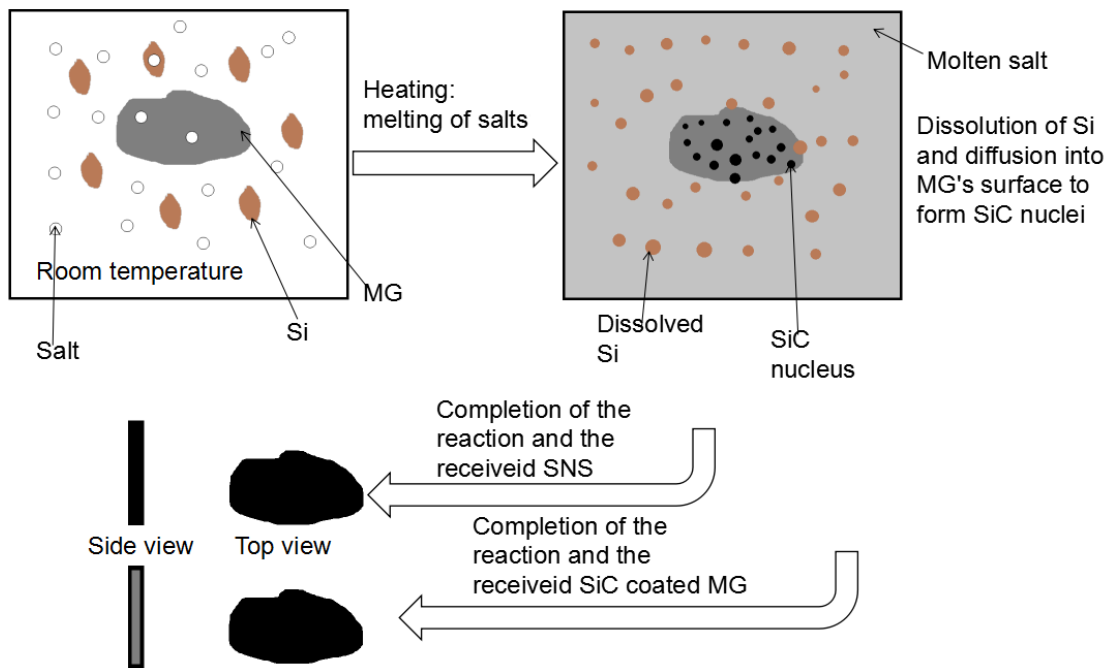
Fig. 7.12 A schematic illustrating the template growth mechanisms in

the MSS of SNS and SCMG.

The overall synthesis process can be schematically shown in Fig. 7.12, and described as

follows. At the test temperatures, NaCl and NaF melted, forming a eutectic liquid

reaction medium in which, Si slightly dissolved [214-217] and then diffused rapidly

through the liquid medium onto the surface of graphite nanoplatelet and reacted to form

in-situ SiC according to Reaction (7.1). Because of the *in-situ* formation on the graphite

nanoplatelet, the final SiC product to a great extent retained the shape and size of the

original graphite nanoplatelet template (Figs. 7.6 and 7.8).

Initially, the reaction between graphite nanoplatelet and Si was rapid, especially in the

176

case of NaF containing salt. However, with the proceeding of the reaction and formation of SiC barrier layer on the remaining graphite nanoplatelet, the reaction rate would be decreased, because Si and/or carbon had to diffuse through the barrier layer to continue the reaction. This explained why with increasing the temperature and/or time the extent of reaction was enhanced evidently (Figs. 7.1 and 7.4), and also explained the lower temperature and short time required in the case of sample with Si;C=1:1 than in the case of Si:C=1:1.5 (Figs. 7.1 and 7.2). .

7.3.3 Fabrication and characterisation of ZNS and ZrC coated graphite nanoplatelets

7.3.3.1 Effect of firing temperature
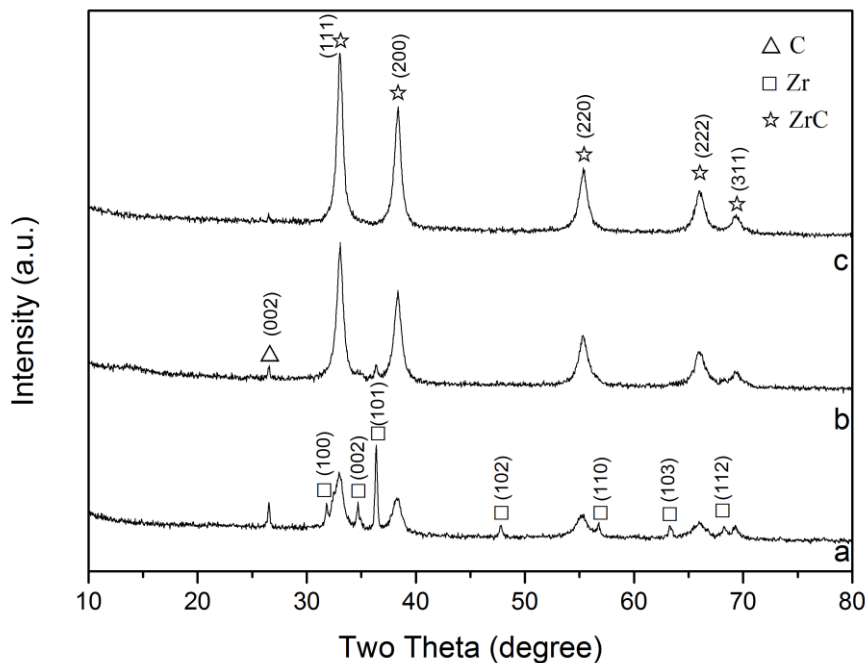
Fig. 7.13 XRD patterns of samples with Zr:C ratios of 1:1 after 6 h heating at (a) 750 °C, (b) 800 °C and (c) 850 °C, respectively.

Fig. 7.13 shows the effect of firing temperature on the phase evolution in the ZNS samples with Zr:C=1:1. At 750 °C, the formation of ZrC was already evident, but large amounts of Zr along with some carbon still remained. The ZrC peaks appeared at 33.0, 38.3, 55.3, 66.0 and 69.3° corresponded respectively to the diffraction from the (111), (200), (220), (311) and (222) planes. With increasing temperature to 800 °C, ZrC

178

increased, whereas zirconium and graphite decreased, significantly. When the temperature was increased further to 850 ℃, all of the Zr and C were consumed and phase pure ZrC was obtained.
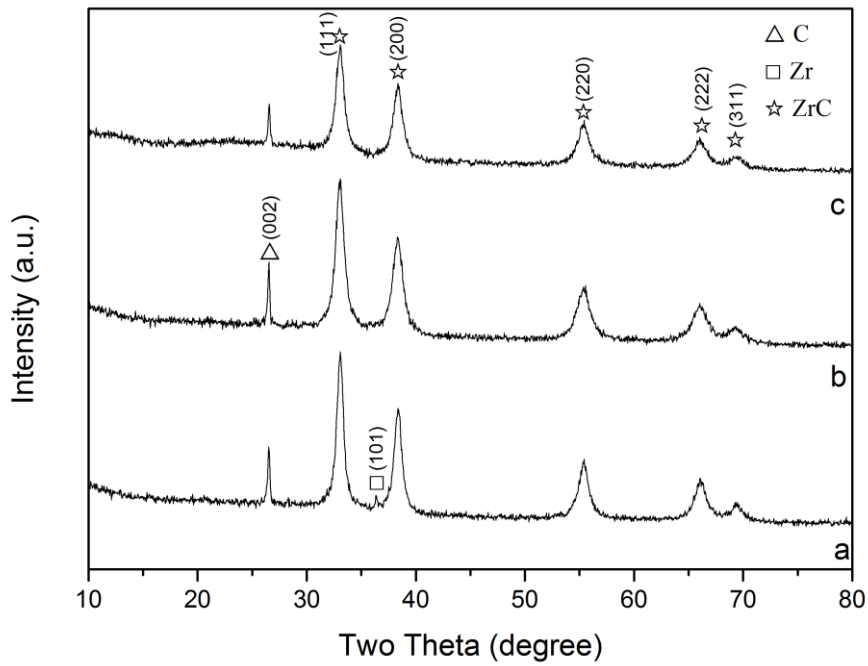
Fig. 7.14 XRD patterns of samples with Zr/C = 1/4 (by molar ratios), after 6 h heating at (a) 750, (b) 800 and (c) 850 ℃, respectively.

Fig. 7.15 XRD patterns of samples with Zr/C = 1/2 (molar ratios), after 6 h heating at

(a) 750, (b) 800 and (c) 850 °C, respectively.

Figs. 7.14 and 7.15 illustrate effect of temperature on the ZrC formation and ZCG preparation. At 750 °C, the formation of ZrC was evident in both samples, and only minor Zr remained along with the residual C (graphite nanoplatelet) (Figs. 7.14-a and 7.15-a). With increasing the temperature to 800 °C, apart from the primary phase ZrC, only minor or trace amounts of Zr was detected along with the residual C (Figs. 7.14-b and Fig. 7.15-b), indicating that the ZrC formation reaction was nearly completed. When the temperature was further increased to 850 °C, Zr disappeared completely, and only ZrC and C were detected, indicating the completion of the ZrC formation reaction (Figs. 7.14-c and Fig. 7.15-c). This temperature was much lower than required by the conventional synthesis routes [218-220].

180

7.3.3.2 Microstructure and morphology
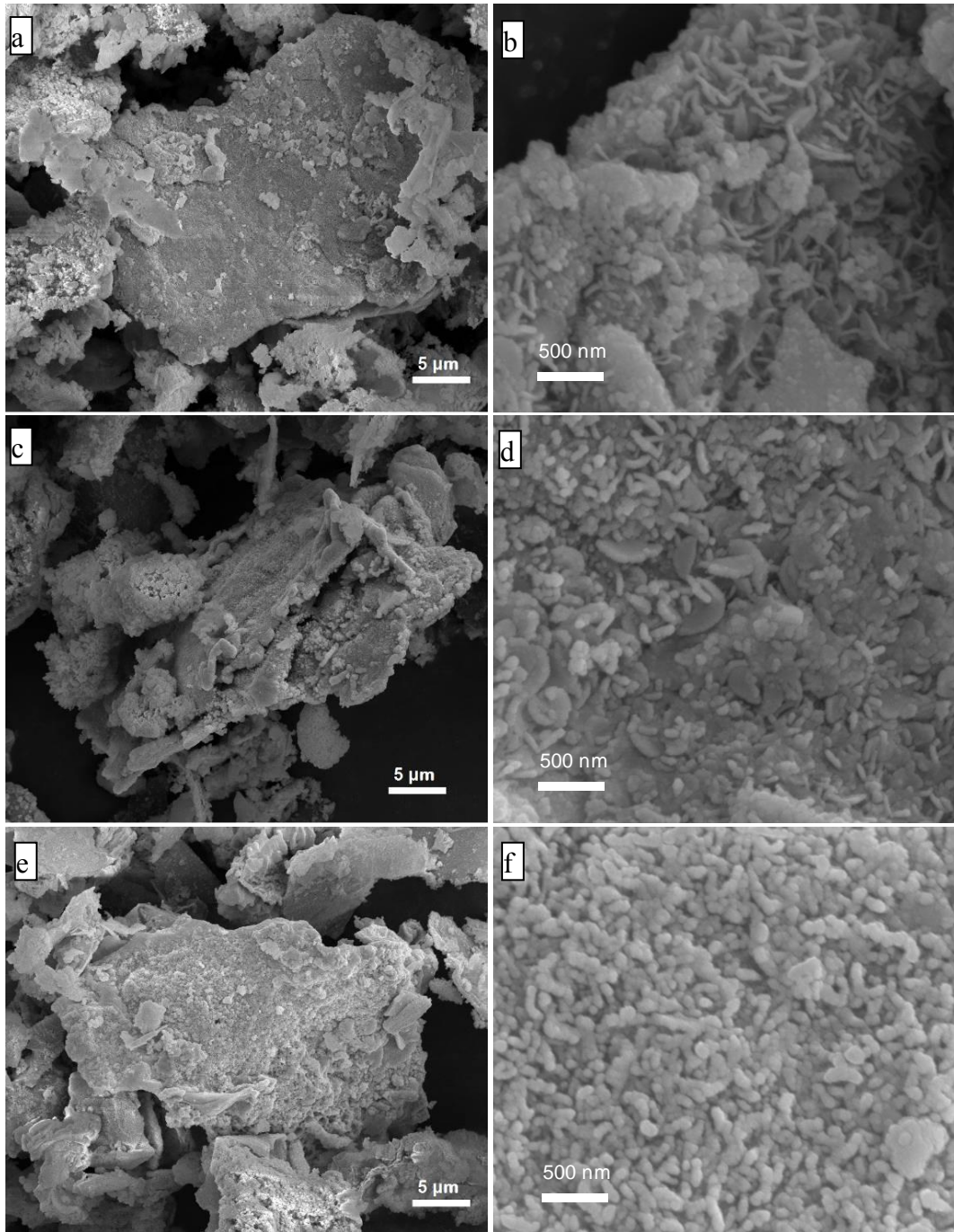
Fig. 7.16 Low magnification SEM images of samples with (a) Zr/C = 1/1, (c) Zr/C = 1/2, (e) Zr/C = 1/4; and high magnification SEM images of surfaces of samples with (b) Zr/C = 1/1, (d) Zr/C = 1/2 and (f) Zr/C = 1/4.

Fig. 7.16 compares microstructures and morphologies of, ZNS and ZrC coated graphite nanoplatelet prepared at 850 ºC for 6 h. Similarly to that seen in the cases of SNS and SiC coated graphite nanoplatelet (Figs. 7.6 and 7.7 above), as-prepared ZNS and ZrC coated graphite nanoplatelet also showed similar morphology (shape and size) to that of the original graphite nanoplatelet, indicating that the template growth mechanism discussed above (Section 7.3.2 above) also had functioned in the present cases. Rougher surfaces of ZNS and ZrC coated graphite nanoplatelet were also due to the formation of small zirconium carbide particles (confirmed by XRD in Figs 7.13, 7.14 and 7.15) on their surfaces.
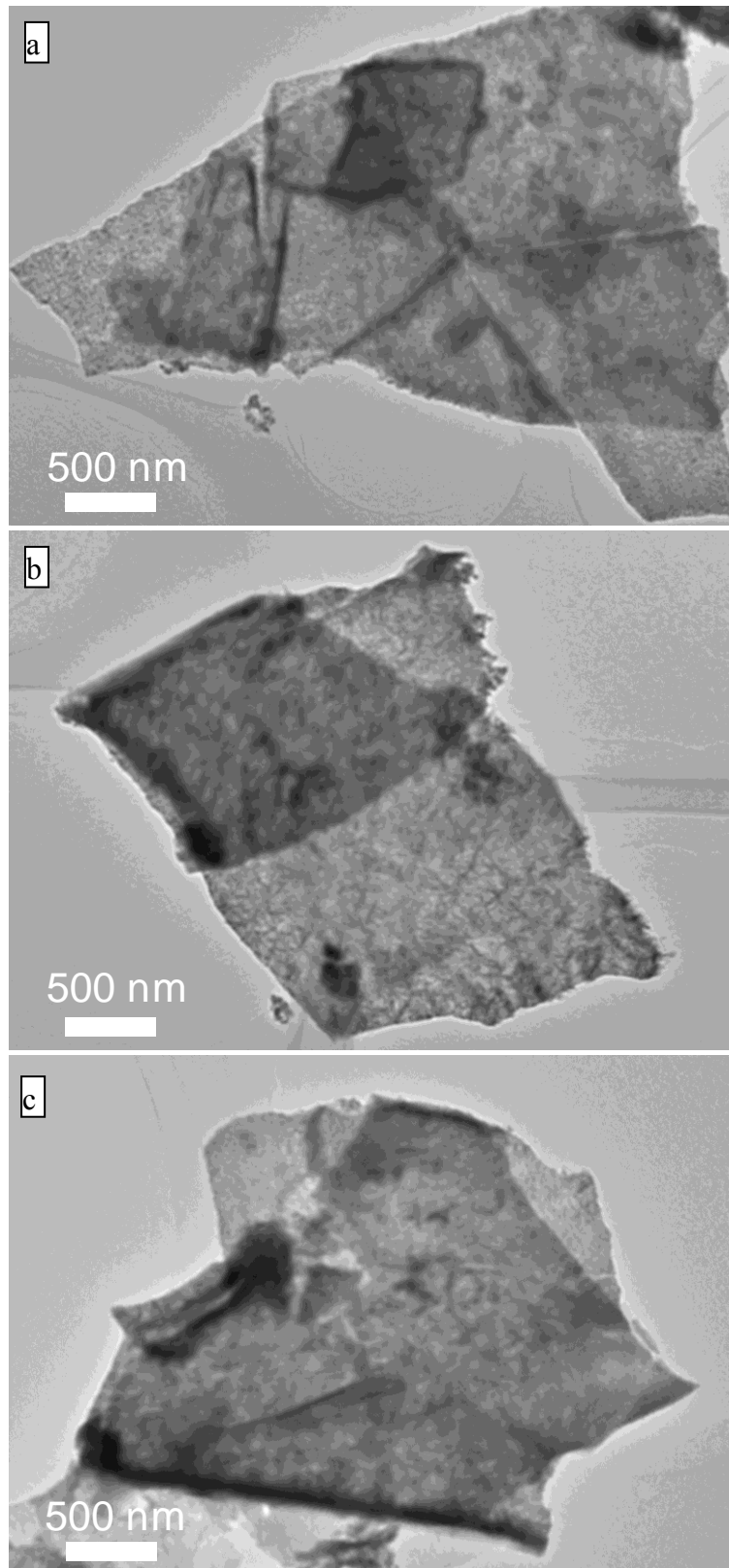
Fig. 7.17 Low magnification TEM images of (a) as-prepared ZNS; and ZrC coated

graphite nanoplatelet with Zr:C of (b) 1:2 and (c) 1:4.
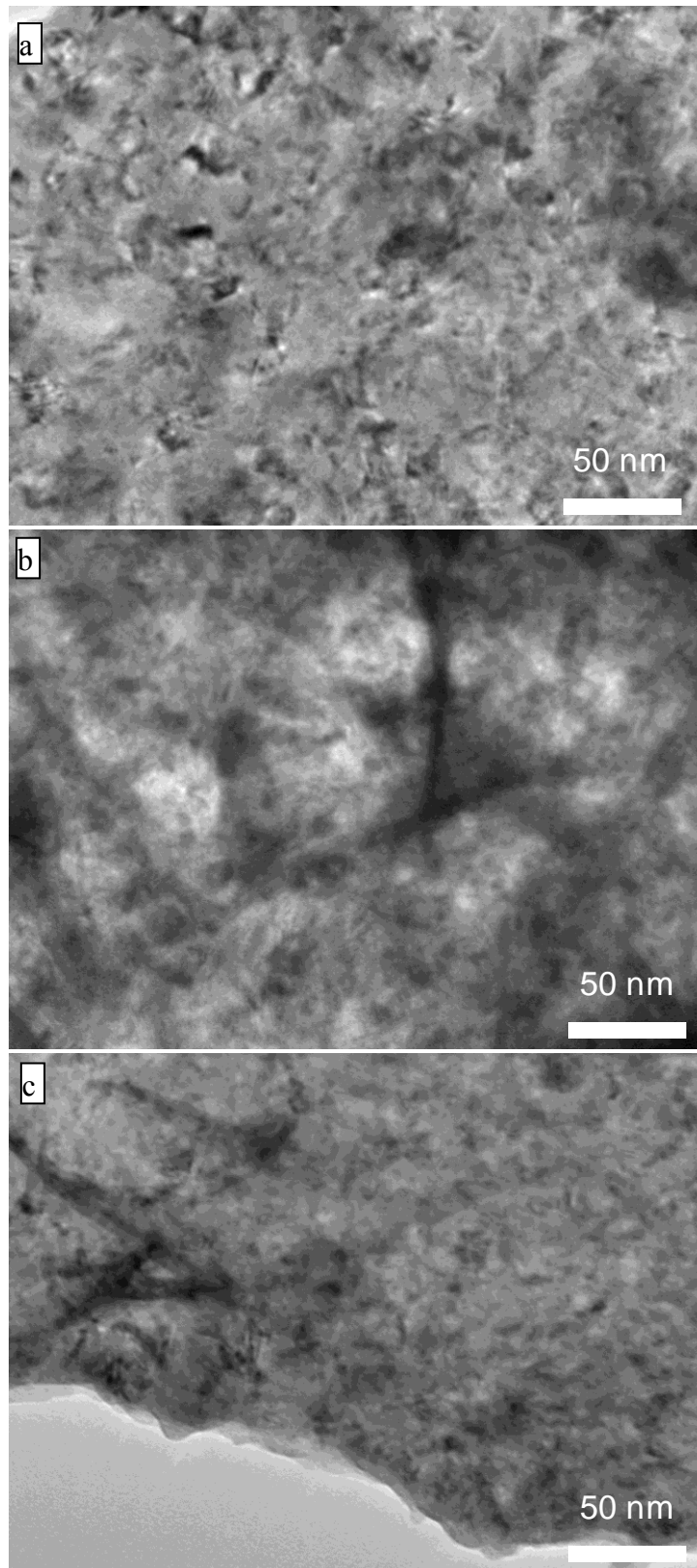
Fig. 7.18 Medium magnification TEM images and SAED patterns of (a) as-prepared

ZNS; and ZrC coated graphite nanoplatelet with Zr:C of (b) 1:2 and (c) 1:4.
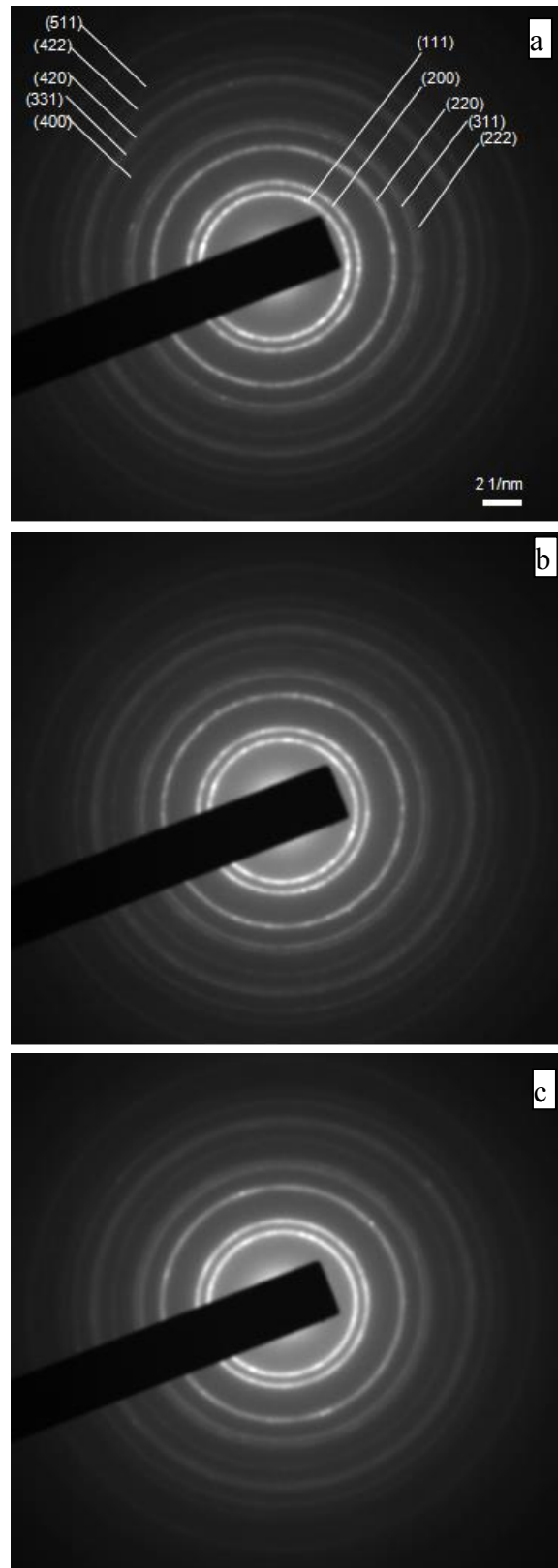
Fig. 7.19 SAED patterns of (a) as-prepared ZNS; and ZrC coated graphite nanoplatelet

with Zr:C of (b) 1:2 and (c) 1:4.
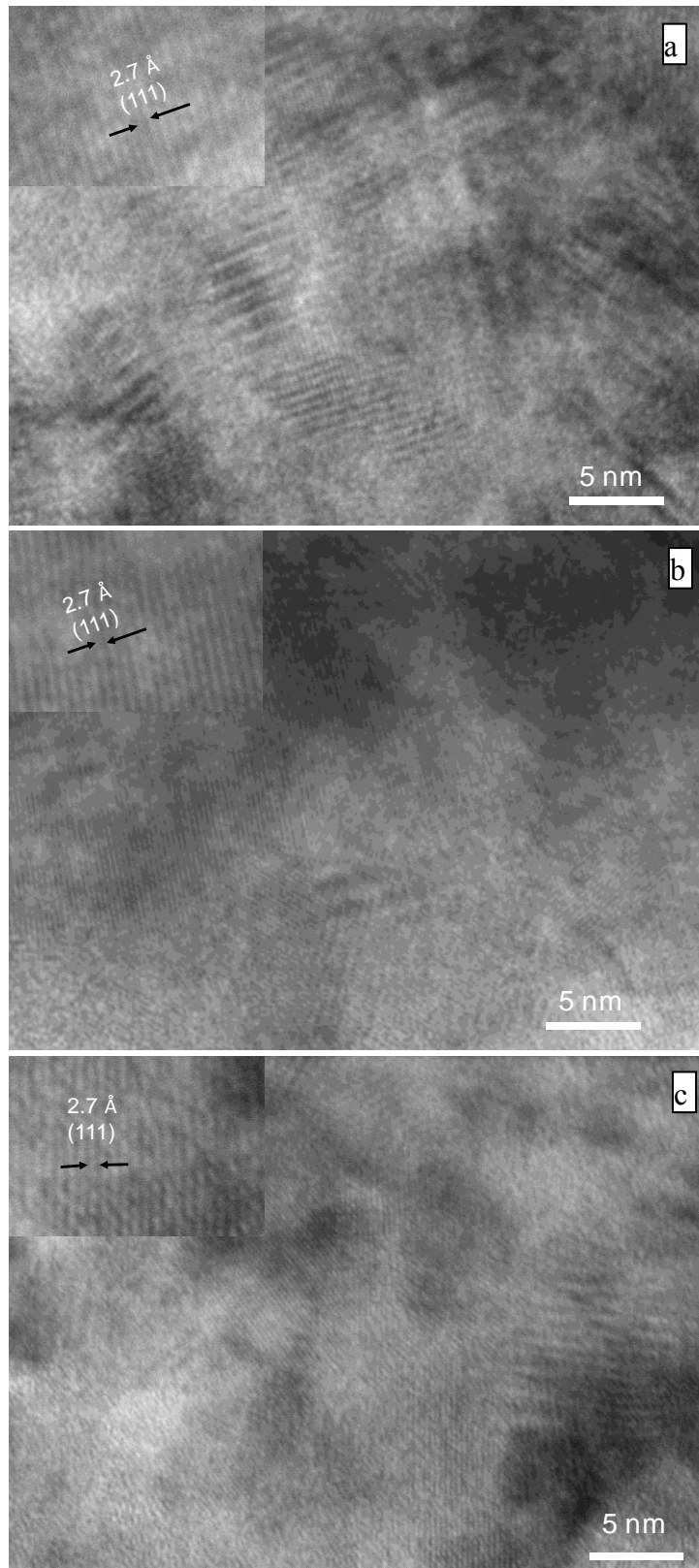
Fig. 7.20 HRTEM images revealing stacking sequences in the cases of (a) as-prepared

ZNS, and ZrC coated graphite nanoplatelet with Zr:C of (b) 1:2 and (c) 1:4.

High magnification TEM (Figs. 7.17-a and 7.18-a) reveals more clearly the surfaces of as-prepared ZNS. The rough surfaces were due to the formation of nanosized (20 nm) particles. SAED, along with the XRD results (Fig. 7.13), confirms that they were ZrC (based on the obtained diffraction rings of (111), (200), (220), (311), (222), (400), (331), (420), (422) and (511) planes of ZrC). HRTEM (Fig. 7.20-a) reveals that the lattice interlayer distance was around 0.27 nm, which corresponds to the (111) plane of ZrC. The lattice fringes were arranged in different orientations (Fig. 7.20a). This, along with the diffraction rings from the SAED pattern (Fig. 7.19-a), indicated polycrystalline nature of ZNS. Similarly, in the cases of ZrC coated graphite nanoplatelets, rough surfaces were also seen, and with increasing the molar ratio of Zr:C, the surfaces became rougher. This was also due to the formation of ZrC nanoparticles. The same lattice interlayer distance of around 0.27 nm was also determined based on the images shown in Fig. 7.20-b and 7.20-c. Furthermore, SEAD patterns (Fig. 7.19-b,c) also reveal the polycrystalline nature of ZrC shells.

7.3.4 Synthesis mechanism
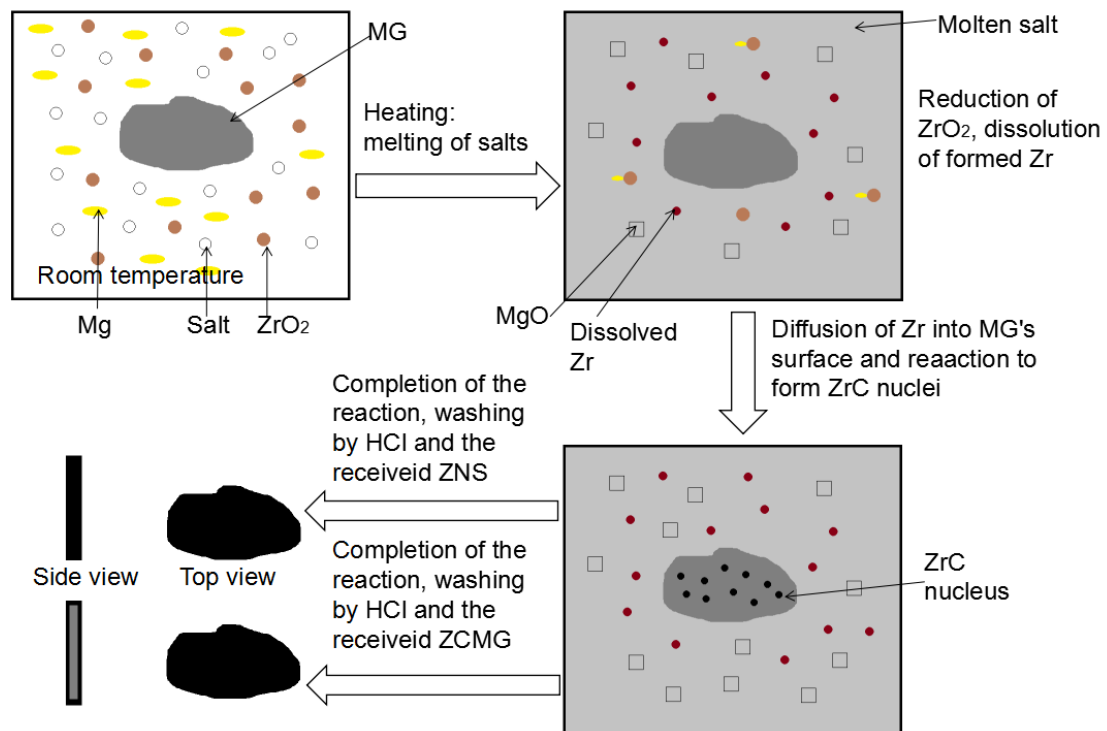
Fig. 7.21 A schematic illustrating the template growth mechanisms in

the MSS of ZNS and ZCMG.

The overall synthesis mechanisms can be schematically illustrated in Fig. 7.21, and

described as follows. At the test temperatures, the salt melted, forming a liquid medium.

Mg slightly dissolved in the salt and reduced ZrO_2 to Zr according to Reaction (7.3). The

formed Zr would also slightly dissolve in the molten salt medium and then diffuse

rapidly through it onto the surface of graphite nanoplatelet template and subsequently

reacted *in-situ* to form ZrC particles according to Reaction (7.4). As shown in Figs. 7.9-

7.11, only Zr but no ZrO_2 was detected in the fired samples, indicating that Reaction

(7.3) was very rapid under the test conditions. Therefore, Reaction (7.4) should be the

controlling step in the overall synthesis process.

$$ZrO_2 + Mg = MgO + Zr \qquad\qquad (7.3)$$

$$Zr + C = ZrC \qquad\qquad (7.4)$$

7.4 Conclusions

Novel 2D SiC nanosheet (SNS), ZrC nanosheet (ZNS), and SiC- and ZrC-coated graphite nanoplatelets were successfully prepared at relatively low temperatures, by using a molten salt synthesis technique. The effects of processing parameters such as firing temperature, time, and salt on the reaction/synthesis processes were examined, and the relevant mechanisms proposed. In all the cases, the metal (Si or Zr) slightly dissolved in the molten salt and diffused rapidly through it onto the surface of graphite nanoplatelet, and then reacted *in-situ* to form the carbides (SiC or ZrC) which retained the morphology and size of the original graphite nanoplatelet, i.e., a template growth mechanism had functioned in all the cases and the original graphite nanoplatelet acted as the template. In the initial stage, as no barrier layer was built up on the surface of the graphite nanoplatelet, so the reaction was rapid. However, with the enhancement in the reaction extent, more and more carbide product would be formed, leading to the formation of a carbide barrier layer the remaining graphite nanoplatelet. Then, the reaction process would be controlled by the diffusion process of the metal and/or carbon. Nevertheless,

189

as the molten salt medium could improve the mixing between the metal and the graphite nanoplatelet, and accelerate the diffusion process of the metal dissolved in it, the overall reaction still remained very rapid, as verified by the much lowered synthesis temperature, especially in the case of ZrC formation where Zr has a sufficiently "high" solubility in the molten salt (1250 and <850 °C respectively in the cases of SiC and ZrC formation). By controlling the ratio between the metal and graphite nanoplatelet, both carbide nanosheets and carbide-coated graphite nanoplatelet/graphene nanosheets could be readily synthesized. It is believed that the MSS presented here could be similarly used to prepare a range of other types of carbide nanosheets (e.g., WC, NbC, HfC and TaC nanosheets) for many potential applications.

Based on the conclusions above, further sintering /densification of these nanosheets/nanoplatelets is needed to make bulk samples, and their microstructures and physicochemical properties need to be examined, providing further fundamental data for their future applications.

Chapter 8. Conclusions and future work

8.1 Conclusions

In summary, $Al_8B_4C_7$, MoAlB, carbon supported tungsten carbides (WC-CB/WC-CNT), SiC nanosheet (SNS), ZrC nanosheet (ZNS), and SiC- and ZrC-coated graphite nanoplatelets nanoparticles have been successfully produced on large scale *via* molten salt synthesis technique and the optimized heat production parameters have been identified. Molten salt synthesis (MSS) is confirmed to be a highly effective route to synthesize non-oxide ceramic materials at relatively low temperatures. The main conclusions based on this thesis work can be drawn as follows:

(1) Phase pure well-dispersed $Al_8B_4C_7$ particles with the average size of about 200 nm were synthesized after 6 h firing at a much lowered temperature of 1250 °C *via* a molten-salt-mediated route using Al, B_4C and C powders as the main raw materials. NaF in the binary salt played very important role in the reaction process. The whole process was dominated by dissolution of Al and B into salts and the following Al-B_4C and B-Al_4C_3 reactions, as the former reaction provided B (decomposition from the reaction products) while the latter reaction was the main reaction to form $Al_8B_4C_7$. The synthesis temperature in the present case was significantly lower (about 500 °C lower) than the conventional synthesis techniques used previously, which was attributed to the great accelerating-effect of the molten salt containing NaF.

191

(2) MoAlB fine particles were synthesized *via* a molten-salt-mediated route at at 1000 °C (at least 100 °C lower than other techniques) using Al, B and Mo powders as the raw materials and NaCl as the liquid reaction medium. Three different morphologies of MoAlB were observed: rounded particles (1~3 μm), plate-like particles (<5 μm in diameter) and columnar crystals with various lengths (up to 20 μm) and diameters (up to 5 μm). To prepare phase pure MoAlB, an appropriate amount of excessive Al (140% in this work) has to be used and an appropriately high firing temperature (1000 °C in this work) is required. The B-Mo_xAl_y reaction was important to eliminate the byproduct and produce the pure phase. The molten salt played an important role in the whole synthesis process by improving the mixing between the reactant species and facilitating their diffusion processes.

(3) Carbon (CB or CNT) supported tungsten carbides (WC/W_2C) were prepared *via* molten salt assisted route. The nanosized carbides were intimately anchored on the carbon substrates which resulted in downshifted d-band centre of tungsten and decreased hydrogen bond strength. Therefore, as-prepared nanocatalysts exhibited excellent HER performance and durability, which was better than most other WC based catalysts. The MSS method provides a low cost and scalable approach to produce carbides based catalyst for HER application.

(4) Novel 2D carbide (SiC/ZrC) based nanosheet ceramic-coated graphite nanoplatelets were successfully prepared at relatively low temperatures, by using a molten salt synthesis technique. The lowered synthesis temperatures (1250 °C for SiC and 850 °C for ZrC) could be attributed to the molten salt medium as it improved the mixing between

192

the raw materials and accelerate the diffusion process of the metal dissolved in it. The effects of processing parameters such as firing temperature, time, and salt on the reaction/synthesis processes were examined, and the relevant mechanisms proposed. The processes were based on template growth mechanism as the products retained the morphology and size of the original graphite nanoplatelet. By controlling the ratio between metal and carbon, both carbide nanosheets and carbide-coated graphite nanoplatelet could be readily synthesized. It is believed that the MSS presented here could be similarly used to prepare a range of other types of carbide nanosheets (e.g., WC, NbC, HfC and TaC nanosheets) for many potential applications.

8.2 Future work

Based on the literature review and this thesis work, some future work which, due to the time limit, has not been done but is worthwhile to do, has been suggested as follows:

(1) There is still some controversy over the exact chemical composition of aluminum boron carbide ($Al_8B_4C_7$ or Al_3BC_3). Additional work based on the composition corresponding to "Al_3BC_3" is worthwhile to do.

(2) Boron oxide based raw materials (B_2O_3, HBO_3 or borates) could be used to replace B and B_4C to synthesize MoAlB and $Al_8B_4C_7$.

(3) Further optimizing the molten salt synthesis conditions is needed to lower the amounts of excessive Al in synthesis of MoAlB and lower the synthesis temperature of $Al_8B_4C_7$ synthesis

193

(4) Preparation of bulk samples of aluminum boron carbide, MoAlB and the carbides (carbides-carbon) nanosheets/nanoplatelets is needed to investigate further fundamental data and their potential applications.

(5) In the case of CNT supported tungsten carbide catalyst, WC along with W_2C was formed. Considering the former has poorer performance in the hydrogen evolution reaction (HER) than the latter, it would be worthwhile to optimize the synthesis conditions further to avoid the formation of the former.

(5) To assist understanding the MSS mechanisms, further work is required to investigate the interaction between the reactants and the molten salt, in particular, the solubility of the reactants in the molten salt.

(6) The MSS technique developed in this thesis work could be similarly used further to prepare many other types of carbide- and boride-based materials.

Publication

1. Liu, C., Wen, Y., Lin, L., Zhang, H., Li, X., & Zhang, S. (2018). Facile in-situ formation of high efficiency nanocarbon supported tungsten carbide nanocatalysts for hydrogen evolution reaction. International Journal of Hydrogen Energy, 43(33), 15650-15658.

2. Bao, K., Liu, C., Damavandi, B. Y., & Zhang, S. (2016). Low-Temperature Preparation of Lanthanum Hexaboride Fine Powder via Magnesiothermic Reduction in Molten Salt. Journal of Ceramic Science and Technology, 7(4), 403-408.

3. Hou, Z., Liu, C., Liu, L., & Zhang, S. (2018). Microstructural evolution and densification behavior of porous kaolin-based mullite ceramic added with MoO_3. Ceramics International, 44(15), 17914-17918.

References

[1] Wang, T., & Yamaguchi, A. (2000). Some properties of sintered $Al_8B_4C_7$. Journal of materials science letters, 19(12), 1045-1046.

[2] WANG, T., & YAMAGUCHI, A. (2000). Synthesis of $Al_8B_4C_7$ and its oxidation properties in air. Journal of the Ceramic Society of Japan, 108(1256), 375-380.

[3] Hashimoto, S., Ishihara, T., Inoue, K., Honda, S., Iwamoto, Y., & Zhang, S. (2009). Synthesis and mechanical properties of $Al_8B_4C_7$. Journal of the Ceramic Society of Japan, 117(1361), 18-21.

[4] Wang, T., & Yamaguchi, A. (2001). Oxidation protection of MgO–C refractories by means of $Al_8B_4C_7$. Journal of the American Ceramic Society, 84(3), 577-582.

[5] Lee, S. H., Kim, B. N., & Tanaka, H. (2010). Low temperature sintering of nano-SiC using a novel $Al_8B_4C_7$ additive. Journal of Materials Research, 25 (3), 471-475.

[6] Lee, S. H., Sakka, Y., Tanaka, H., & Kagawa, Y. (2009). Wet Processing and Low‐Temperature Pressureless Sintering of SiC Using a Novel Al_3BC_3 Sintering Additive. Journal of the American Ceramic Society, 92(12), 2888-2893.

[7] Wang, H., Feng, L., Lee, S. H., Chen, J., Fan, B., Chen, D., Lu, H., Xu, H., & Zhang, R. (2013). ZrB_2–Al_3BC_3 composites prepared using Al–B_4C–C additives and spark plasma sintering. Ceramics International, 39(1), 897-901.

[8] Jung, J. Y., Jung, S. H., Oh, H. C., Lee, S. H., & Choi, S. C. (2012). Spark plasma sintering of ZrB_2 using Al_3BC_3 as an additive. Journal of Ceramic Processing Research,

13(5), 641-645.

[9] Da Rocha, R. M., & de Melo, F. C. L. (2010). Sintering of B_4C by pressureless liquid phase sintering. In Materials Science Forum (Vol. 660, pp. 170-175). Trans Tech Publications.

[10] WANG, T., & YAMAGUCHI, A. (2000). Antioxidation behavior and effect of ZrB_2–Al_3BC_3 composites prepared using Al–B_4C–C additives and spark plasma sintering added to carbon-containing refractories. Journal of the Ceramic Society of Japan, 108(1261), 818-822.

[11] Yamaguchi, A., Nakano, Y., & Wang, T. (2000). Effect and behaviour of Al-BC system antioxidants added to MgO-C refractories. Canadian metallurgical quarterly, 39(4), 381-386.

[12] Zhang, S., Marriott, N. J., & Lee, W. E. (2001). Thermochemistry and microstructures of MgO–C refractories containing various antioxidants. Journal of the European Ceramic Society, 21(8), 1037-1047.

[13] Zhang, S., & Lee, W. E. (2001). Influence of additives on corrosion resistance and corroded microstructures of MgO–C refractories. Journal of the European Ceramic Society, 21(13), 2393-2405.

[14] A. I. Kharlamov and S. V. Loichenko, "Boron-Rich Solids," in Proceedings of the AIP Conference Albuquerque, USA, 1990, edited by D. Emin, T. L. Aselage, A. C. Switendick, B. Morosin, and C. L. Beckel, AIP, New York, 1991, Vol. 231, pp. 94–97.

[15] Ali, M. A., Hadi, M. A., Hossain, M. M., Naqib, S. H., & Islam, A. K. M. A. (2017). Theoretical investigation of structural, elastic, and electronic properties of ternary boride

197

MoAlB. physica status solidi (b), 254(7), 1700010.

[16] Kota, S., Zapata-Solvas, E., Ly, A., Lu, J., Elkassabany, O., Huon, A., Lee, W. E., Hultman, L., May, S. J., & Barsoum, M. W. (2016). Synthesis and characterization of an alumina forming nanolaminated boride: MoAlB. Scientific reports, 6, 26475.

[17] Li, X., Cui, H., & Zhang, R. (2016). First-principles study of the electronic and optical properties of a new metallic MoAlB. Scientific reports, 6, 39790.

[18] Lu, X., Li, S., Zhang, W., Yu, W., & Zhou, Y. (2018). Thermal shock behavior of a nanolaminated ternary boride: MoAlB. Ceramics International.

[19] Xu, L., Shi, O., Liu, C., Zhu, D., Grasso, S., & Hu, C. (2018). Synthesis, microstructure and properties of MoAlB ceramics. Ceramics International, 44(11), 13396-13401.

[20] Kota, S., Agne, M., Zapata-Solvas, E., Dezellus, O., Lopez, D., Gardiola, B., Radovic, M., & Barsoum, M. W. (2017). Elastic properties, thermal stability, and thermodynamic parameters of MoAlB. Physical Review B, 95(14), 144108.

[21] Kota, S., Zapata-Solvas, E., Chen, Y., Radovic, M., Lee, W. E., & Barsoum, M. W. (2017). Isothermal and Cyclic Oxidation of MoAlB in Air from 1100 ºC to 1400 ºC. Journal of The Electrochemical Society, 164(13), C930-C938.

[22] Kurlov, A. S., & Gusev, A. I. (2006). Tungsten carbides and WC phase diagram. Inorganic Materials, 42(2), 121-127.

[23] Pierson, H. O., (1996) Handbook of refractory carbides and nitrides: Properties, Characteristics, Processing and Applications. Noyes publications.

[24] Szutkowska, M., Boniecki, M., Cygan, S., Kalinka, A., Grilli, M. L., & Balos, S.

(2018, March). Fracture behaviour of WC-Co hardmetals with WC partially substituted by titanium carbide. In IOP Conference Series: Materials Science and Engineering (Vol. 329, No. 1, p. 012015). IOP Publishing.

[25] Kim, H. C., Shon, I. J., Yoon, J. K., & Doh, J. M. (2007). Consolidation of ultra fine WC and WC–Co hard materials by pulsed current activated sintering and its mechanical properties. International Journal of Refractory Metals and Hard Materials, 25(1), 46-52.

[26] Tsai, K. M., Hsieh, C. Y., & Lu, H. H. (2010). Sintering of binderless tungsten carbide. Ceramics International, 36(2), 689-692.

[27] Regmi, Y. N., Waetzig, G. R., Duffee, K. D., Schmuecker, S. M., Thode, J. M., & Leonard, B. M. (2015). Carbides of group IVA, VA and VIA transition metals as alternative HER and ORR catalysts and support materials. Journal of Materials Chemistry A, 3(18), 10085-10091.

[28] Chen, Z., Qin, M., Chen, P., Jia, B., He, Q., & Qu, X. (2016). Tungsten carbide/carbon composite synthesized by combustion-carbothermal reduction method as electrocatalyst for hydrogen evolution reaction. International Journal of Hydrogen Energy, 41(30), 13005-13013.

[29] Liu, C., Zhou, J., Xiao, Y., Yang, L., Yang, D., & Zhou, D. (2017). Structural and electrochemical studies of tungsten carbide/carbon composites for hydrogen evolution. International Journal of Hydrogen Energy, 42(50), 29781-29790.

[30] Wirth, S., Harnisch, F., Weinmann, M., & Schröder, U. (2012). Comparative study of IVB−VIB transition metal compound electrocatalysts for the hydrogen evolution reaction. Applied Catalysis B: Environmental, 126, 225-230.

199

[31] Fan, X., Zhou, H., & Guo, X. (2015). WC nanocrystals grown on vertically aligned carbon nanotubes: an efficient and stable electrocatalyst for hydrogen evolution reaction. ACS nano, 9(5), 5125-5134.

[32] Bukola, S., Merzougui, B., Akinpelu, A., & Zeama, M. (2016). Cobalt and nitrogen co-doped tungsten carbide catalyst for oxygen reduction and hydrogen evolution reactions. Electrochimica Acta, 190, 1113-1123.

[33] Esposito, D. V., Hunt, S. T., Kimmel, Y. C., & Chen, J. G. (2012). A new class of electrocatalysts for hydrogen production from water electrolysis: metal monolayers supported on low-cost transition metal carbides. Journal of the American Chemical Society, 134(6), 3025-3033.

[34] Michalsky, R., Zhang, Y. J., & Peterson, A. A. (2014). Trends in the hydrogen evolution activity of metal carbide catalysts. ACS Catalysis, 4(5), 1274-1278.

[35] Gong, Q., Wang, Y., Hu, Q., Zhou, J., Feng, R., Duchesne, P. N., Zhang, P. Chen, F., Han, N. Li, Y., Jin, Li., Li, Y., & Lee, S. (2016). Ultrasmall and phase-pure W_2C nanoparticles for efficient electrocatalytic and photoelectrochemical hydrogen evolution. Nature communications, 7, 13216.

[36] Ishii, T., Yamada, K., Osuga, N., Imashiro, Y., & Ozaki, J. I. (2016). Single-Step Synthesis of W_2C Nanoparticle-Dispersed Carbon Electrocatalysts for Hydrogen Evolution Reactions Utilizing Phosphate Groups on Carbon Edge Sites. ACS Omega, 1(4), 689-695.

[37] Andrievskii, R. A., Strel'nikova, N. S., Poltoratskii, N. I., Kharkhardin, E. D., & Smirnov, V. S. (1967). Melting point in systems ZrC-HfC, TaC-ZrC, TaC-HfC. Soviet

Powder Metallurgy and Metal Ceramics, 6(1), 65-67.

[38] Nino, A., Tanaka, A., Sugiyama, S., & Taimatsu, H. (2010). Indentation size effect for the hardness of refractory carbides. Materials transactions, 51(9), 1621-1626.

[39] Williams, W. S. (1998). The thermal conductivity of metallic ceramics. JOM, 50(6), 62-66.

[40] Elliott, R. O., & Kempter, C. P. (1958). Thermal expansion of some transition metal carbides. The Journal of Physical Chemistry, 62(5), 630-631.

[41] Ordan'yan, S. S., & Drozdetskaya, G. V. (1970). High-temperature strength of TiC and ZrC specimens prepared by different techniques. Powder Metallurgy and Metal Ceramics, 9(8), 665-668.

[42] Zhu, H. X., Pan, C., Deng, C. J., & Yuan, W. J. (2011). Preparation of $Al_8B_4C_7$ composite materials by using oxide raw materials. In IOP Conference Series: Materials Science and Engineering (Vol. 18, No. 22, p. 222008). IOP Publishing.

[43] Deng, C. J., Zhou, W., Zhu, H. X., & Yu, Y. (2009). Synthesis of $Al_8B_4C_7$ from $Al/Na_2B_4O_7 \cdot 10H_2O/C$ Mixed Powders. Advanced Materials Research (Vol. 79, pp. 1375-1378). Trans Tech Publications.

[44] Cui, P., Yuan, W. J., Deng, C. J., Zhu, H. X., & Li, J. (2013). Synthesis of $Al_8B_4C_7$ from Aluminum, Boron Trioxide and Activated Carbon Mixed Powders. In Advanced Materials Research (Vol. 634, pp. 2383-2387). Trans Tech Publications.

[45] Lee, S. H., Yin, J., Feng, L., & Lee, J. S. (2014). Synthesis of Al_3BC_3 particulates by carbo-thermal reduction process—Parameter optimization and mechanism analysis. Journal of the Ceramic Society of Japan, 122(1429), 772-776.

201

[46] Hillebrecht, H., & Meyer, F. D. (1996). Synthesis, Structure, and Vibrational Spectra of Al_3BC_3, a Carbidecarboborate of Aluminum with Linear $(C=B=C)^{5-}$ Anions. Angewandte Chemie International Edition in English, 35(21), 2499-2500.

[47] Li, F., Zhou, Y., He, L., Liu, B., & Wang, J. (2008). Synthesis, microstructure, and mechanical properties of Al_3BC_3. Journal of the American Ceramic Society, 91(7), 2343-2348.

[48] Lee, S. H., Kim, H. D., Choi, S. C., Nishimura, T., Lee, J. S., & Tanaka, H. (2010). Chemical composition and microstructure of Al_3BC_3 prepared by different densification methods. Journal of the European Ceramic Society, 30(4), 1015-1020.

[49] Che, Q. L., Ma, Q., & Lu, J. J. (2012). Fabrication of Al_3BC_3-Based Porous Ceramics by Pressureless Sintering. In Advanced Materials Research (Vol. 412, pp. 340-343). Trans Tech Publications.

[50] Gao, Y., Huang, Z., Fang, M., Liu, Y. G., Huang, S., & Ouyang, X. (2012). Synthesis of $Al_8B_4C_7$ ceramic powder from $Al/B_4C/C$ mixtures. Powder Technology, 226, 269-273.

[51] Inoue, Z., Tanaka, H., & Inomata, Y. (1980). Synthesis and X-ray crystallography of aluminium boron carbide, $Al_8B_4C_7$. Journal of Materials Science, 15(12), 3036-3040.

[52] Alameda, L. T., Moradifar, P., Metzger, Z., Alem, N., & Schaak, R. E. (2018). Topochemical Deintercalation of Al from MoAlB: Stepwise Etching Pathway, Layered Intergrowth Structures, and Two-Dimensional MBene. Journal of the American Chemical Society.

[53] Jeitschko, W. (1966). Die Kristallstruktur von MoAlB. Monatshefte für Chemie und verwandte Teile anderer Wissenschaften, 97(5), 1472-1476.

[54] OKADA, S. (1998). Synthesis, crystal structure and characterizations of the ternary borides TMAlB (TM= Mo, W) with UBC type structure. Trans. Kokushikan Univ. Fac. Eng. 7–12.

[55] Ade, M., & Hillebrecht, H. (2015). Ternary borides Cr_2AlB_2, Cr_3AlB_4, and Cr_4AlB_6: the first members of the series (CrB_2) n CrAl with n= 1, 2, 3 and a unifying concept for ternary borides as MAB-phases. Inorganic chemistry, 54(13), 6122-6135.

[56] Lou, T. (2016). Microstructure and Properties of Spark Plasma Sintered MoAlB Ceramics. PhD Thesis, University of Nebraska-Lincoln.

[57] Fuka, M. R. (2018). Synthesis and Characterization of Novel Ternary Borides (MoAlB) and Their Composites (Doctoral dissertation, The University of North Dakota).

[58] Singh, H., & Pandey, O. P. (2013). Direct synthesis of nanocrystalline tungsten carbide from scheelite ore by solid state reaction method. Ceramics International, 39(1), 785-790.

[59] Giordano, C., Erpen, C., Yao, W., & Antonietti, M. (2008). Synthesis of Mo and W carbide and nitride nanoparticles *via* a simple "urea glass" route. Nano letters, 8(12), 4659-4663.

[60] Singla, G., Singh, K., & Pandey, O. P. (2015). Synthesis of carbon coated tungsten carbide nano powder using hexane as carbon source and its structural, thermal and electrocatalytic properties. International Journal of Hydrogen Energy, 40(16), 5628-5637.

[61] Singla, G., Singh, K., & Pandey, O. P. (2014). Structural and thermal analysis of in situ synthesized C–WC nanocomposites. Ceramics International, 40(4), 5157-5164.

203

[62] Kumar, A., Singh, K., & Pandey, O. P. (2010). Optimization of processing parameters for the synthesis of tungsten carbide (WC) nanoparticles through solvo thermal route. Physica E: Low-dimensional Systems and Nanostructures, 42(9), 2477-2483.

[63] Singh, H., & Pandey, O. P. (2013). Single step synthesis of tungsten carbide (WC) nanoparticles from scheelite ore. Ceramics International, 39(6), 6703-6706.

[64] Kumar, A., Singh, K., & Pandey, O. P. (2009). Reduction of WO_3 to nano-WC by thermo-chemical reaction route. Physica E: Low-dimensional Systems and Nanostructures, 41(4), 677-684.

[65] Hunt, S. T., Nimmanwudipong, T., & Román‑Leshkov, Y. (2014). Engineering Non‑sintered, Metal‑Terminated Tungsten Carbide Nanoparticles for Catalysis. Angewandte Chemie International Edition, 53(20), 5131-5136.

[66] Ono, Y., Matsumoto, T., & Amemiya, Y. (1993). Development of the basic monolithic refractories containing hydrophilic graphite. Rep Res Lab Asahi Glass Co Ltd, 43(1), 35-46.

[67] Sakamoto, S., & Ono, Y. (1992). Castables Containing Graphite. Taikabutsu, 44, 467-467.

[68] Wang, Y. Q., Zhou, B. L., & Wang, Z. M. (1995). Oxidation protection of carbon fibers by coatings. Carbon, 33(4), 427-433.

[69] Hopfe, V., Tehel, A., Baier, A., & Scharsig, J. (1992). IR-laser CVD of TiB_2, TiC_x and TiC_xN_y coatings on carbon fibres. Applied surface science, 54, 78-83.

[70] Baklanova, N. I., Zima, T. M., Boronin, A. I., Kosheev, S. V., Titov, A. T., Isaeva,

204

N. V., Graschenkov, D. V., & Solntsev, S. S. (2006). Protective ceramic multilayer coatings for carbon fibers. Surface and Coatings Technology, 201(6), 2313-2319.

[71] Inomata, Y. (1980). Phase relation in SiC-Al$_4$C$_3$-B$_4$C system at 1800 $^{\circ}$C. J. CERAM. SOC. JAP. J. Ceram. Soc. Jap., 88(1018), 353.

[72] Oscroft, R. J., & Roebuck, P. H. (1995). Characterisation and Range of Composition for Al$_8$B$_4$C$_7$. British ceramic transactions, 94(1), 25-26.

[73] Jardin, C., Hillebrecht, H., Bauer, J., Halet, J. F., Saillard, J. Y., & Gautier, R. (2003). First-principles study of ternary metal borocarbide compounds containing finite linear BC$_2$ units. Journal of Solid State Chemistry, 176(2), 609-614.

[74] Li, F., Zhou, Y., He, L., Liu, B., & Wang, J. (2008). Synthesis, microstructure, and mechanical properties of Al$_3$BC$_3$. Journal of the American Ceramic Society, 91(7), 2343-2348.

[75] Xiang, H., Li, F., Li, J., Wang, J., Wang, X., Wang, J., & Zhou, Y. (2011). Raman spectrometry study of phase stability and phonon anharmonicity of Al$_3$BC$_3$ at elevated temperatures and high pressures. Journal of Applied Physics, 110(11), 113504.

[76] Wang, J., Zhou, Y., Lin, Z., & Liao, T. (2006). Pressure-induced polymorphism in Al$_3$BC$_3$: A first-principles study. Journal of Solid State Chemistry, 179(8), 2739-2743.

[77] Ping-Yi, Q. (2014). First-principles Prediction for Mechanical and Optical Properties of Al$_3$BC$_3$. Chinese Physics Letters, 31(6), 066201.

[78] Solozhenko, V. L., Meyer, F. D., & Hillebrecht, H. (2000). 300-K equation of state and high-pressure phase stability of Al$_3$BC$_3$. Journal of Solid State Chemistry, 154(1), 254-256.

205

[79] Halet, J. F., Saillard, J. Y., & Bauer, J. (1990). Electronic structure of the new rare earth borocarbide Sc_2BC_2. Journal of the Less Common Metals, 158(2), 239-250.

[80] Solozhenko, V. L., Meyer, F. D., & Hillebrecht, H. Synchrotron radiation studies of Al_3BC_3 at high pressures.

[81] Doerner, P. (1982). Constitutional Investigations on High Temperature Ceramics of the B-Al-C-Si-NO System by Means of Thermochemical Calculations. Thesis, Uni. Stuttgart, Inst. Metallkunde,(1982)(Calculation, Thermodyn., 126).

[82] Lee, S. H., & Tanaka, H. (2009). Thermal stability of Al_3BC_3. Journal of the American Ceramic Society, 92(9), 2172-2174.

[83] Meyer, F.D. (1998) Thesis, Albert-Ludwigs-Universität Freiburg ed., Freiburg, Germany.

[84] Zhou, A., Wang, C. A., & Hunag, Y. (2003). Synthesis and mechanical properties of Ti_3AlC_2 by spark plasma sintering. Journal of materials science, 38(14), 3111-3115.

[85] Choi, S. M. (2005). Sintering and mechanical properties of $AlZrC_2$. Journal of the Ceramic Society of Japan, 113(1314), 188-190.

[86] Barsoum, M. W., & El‑Raghy, T. (1996). Synthesis and characterization of a remarkable ceramic: Ti_3SiC_2. Journal of the American Ceramic Society, 79(7), 1953-1956.

[87] Smith, G. S., Tharp, A. G., & Johnson, Q. (1969). Determination of the light‑atom positions in Mo_2BC. Acta Crystallographica Section B, 25(4), 698-701.

[88] Zhang, S., Hashimoto, S., & Lee, W. E. (2005). Hydration of Aluminum Powder in Magnesia‑Containing Water. Journal of the American Ceramic Society, 88(4), 1057-

206

1059.

[89] Yu, J., & Yamaguchi, A. (1995). Hydration of synthesized Al_4C_3 and its prevention effect by Si addition. Journal of the Ceramic Society of Japan, 103(1197), 475-478.

[90] Liu, Y., Jiang, Y., Zhou, R., & Feng, J. (2014). Mechanical properties and chemical bonding characteristics of WC and W_2C compounds. Ceramics International, 40(2), 2891-2899.

[91] Kurlov, A. S., Rempel, S. V., & Gusev, A. I. (2011). Symmetry analysis of ordered phases of the lower tungsten carbide W_2C. Physics of the Solid State, 53(1), 175-181.

[92] Epicier, T., Dubois, J., Esnouf, C., Fantozzi, G., & Convert, P. (1988). Neutron powder diffraction studies of transition metal hemicarbides M_2C_{1-x}—II. In situ high temperature study on W_2C_{1-x} and Mo_2C_{1-x}. Acta Metallurgica, 36(8), 1903-1921.

[93] Hårsta, A., Rundqvist, S., & Thomas, J. O. (1978). A neutron powder diffraction study of W_2C. Acta Chem. Scand., Ser. A, 32.

[94] Swalin, R. A. (1957). Orientation relationships involved in the formation of α-W_2C on tungsten. Acta Crystallographica, 10(7), 473-474.

[95] RUDY, E., & Windisch, S. (1967). Evidence for Zeta Fe_2N ‐ Type sublattice order in W_2C at intermediate temperatures. Journal of the American Ceramic Society, 50(5), 272-273.

[96] Rudy, E. & Hoffman, J.R. (1967). Phasengleichgewichte im Bereich der kubischen Karbidphase im System Wolfram–Kohlenstoff, Planseeber. Pulvermetall., 15(3), 174–178.

[97] Suetin, D. V., Shein, I. R., Kurlov, A. S., Gusev, A. I., & Ivanovskiĭ, A. L. (2008).

207

Band structure and properties of polymorphic modifications of lower tungsten carbide W_2C. Physics of the Solid State, 50(8), 1420-1426.

[98] Sara, R. V. (1965). Phase Equilibria in the system tungsten—carbon. Journal of the American Ceramic Society, 48(5), 251-257.

[99] Rudy, E., & Hoffman, J. R. (1967) Phasengleichgewichte im Bereich der kubischenKarbidphase im System Wolfram-Kohlenstoff. Planseeber. Pulvermet. 15(3):174–178.

[100] Kurlov, A. S., & Gusev, A. I. (2009). Ordering of nonstoichiometric hexagonal compounds M_2X: A sequence of special figures. Physics of the Solid State, 51(10), 2051.

[101] Hiraga, K., & Hirabayashi, M. (1977). Long-range and short-range order in interstitial compounds M_2X with special reference to V_2C and Nb_2C. Le Journal de Physique Colloques, 38(C7), C7-224.

[102] Epicier, T. (1990). Crystal-Chemistry of Transition Metal Hemicarbides. In The Physics and Chemistry of Carbides, Nitrides and Borides (pp. 215-248). Springer, Dordrecht.

[103] Kurlov, A. S., Gusev, A. I. (2013). Tungsten Carbides: Structure, Properties and Application in Hardmetals. Springer.

[104] Kublii, V. Z., & Velikanova, T. Y. (2004). Ordering in the carbide W_2C and phase equilibria in the tungsten—carbon system in the region of its existence. Powder Metallurgy and Metal Ceramics, 43(11-12), 630-644.

[105] Butorina, L. N. (1960). LN Butorina and ZG Pinsker, Sov. Phys. Crystallogr. 5, 560.

[106] Suetin, D. V., Shein, I. R., & Ivanovskii, A. L. (2008). Elastic and electronic properties of hexagonal and cubic polymorphs of tungsten monocarbide WC and mononitride WN from first‐principles calculations. physica status solidi (b), 245(8), 1590-1597.

[107] Liu, Y., Jiang, Y., Zhou, R., & Feng, J. (2014). Mechanical properties and chemical bonding characteristics of WC and W_2C compounds. Ceramics International, 40(2), 2891-2899.

[108] Kurlov, A. S., & Gusev, A. I. (2011). Model for milling of powders. Technical Physics, 56(7), 975-980.

[109] Kumar, A., Jayakumar, T., Raj, B., & Ray, K. K. (2003). Correlation between ultrasonic shear wave velocity and Poisson's ratio for isotropic solid materials. Acta materialia, 51(8), 2417-2426.

[110] Taimatsu, H., Sugiyama, S., & Kodaira, Y. (2008). Synthesis of W_2C by reactive hot pressing and its mechanical properties. Materials transactions, 49(6), 1256-1261.

[111] Chaix‐Pluchery, O., Thore, A., Kota, S., Halim, J., Hu, C., Rosén, J., Ouisse, T. & Barsoum, M. W. (2017). First‐order Raman scattering in three‐layered Mo‐based ternaries: MoAlB, Mo_2Ga_2C and Mo_2GaC. Journal of Raman Spectroscopy, 48(5), 631-638.

[112] Kresse, G. (1996). G. Kresse and J. Furthmüller, Phys. Rev. B 54, 11169.

[113] Bai, Y., Qi, X., Duff, A., Li, N., Kong, F., He, X., Wang, R., & Lee, W. E. (2017). Density functional theory insights into ternary layered boride MoAlB. Acta Materialia, 132, 69-81.

[114] Greskovich, C., & Rosolowski, J. H. (1976). Sintering of covalent solids. Journal of the American Ceramic Society, 59(7‑8), 336-343.

[115] Cheung, Rebecca (2006). Silicon carbide microelectromechanical systems for harsh environments. Imperial College Press. p. 3. ISBN 1-86094-624-0.

[116] Baumhauer H. (1912) Uber die kristalle des carborundums. Z. Krist. 50, 33–39.

[117] Baumhauer H. (1915) Uber die verschiedenen modifikationen des carborundums und die erscheinung der poytypie. Z. Krist. 55, 249–259.

[118] Shaffer, P. T. B. (1969). A review of the structure of silicon carbide. Acta Crystallographica Section B, 25(3), 477-488.

[119] Gomes de Mesquita, A. D. (1967). Refinement of the crystal structure of SiC type 6H. Acta Crystallographica, 23(4), 610-617.

[120] Daulton, T. L., Bernatowicz, T. J., Lewis, R. S., Messenger, S., Stadermann, F. J., & Amari, S. (2003). Polytype distribution of circumstellar silicon carbide: Microstructural characterization by transmission electron microscopy. Geochimica et Cosmochimica Acta, 67(24), 4743-4767.

[121] Tairov Y. M. and Tsvetkov V. F. (1978) Investigation of growth processes of ingots of silicon carbide single crystals. J. Cryst. Growth 43, 209–212.

[122] http://www.ioffe.ru/SVA/NSM/Semicond/SiC/.

[123] Post, B., Glaser, F. W., & Moskowitz, D. (1954). Transition metal diborides. Acta Metallurgica, 2(1), 20-25.

[124] Shatynski, S. R. (1979). The thermochemistry of transition metal carbides. Oxidation of Metals, 13(2), 105-118.

[125] Toth, L. (Ed.). (2014). Transition metal carbides and nitrides. Elsevier.

[126] Nakamura, K., & Yashima, M. (2008). Crystal structure of NaCl-type transition metal monocarbides MC (M= V, Ti, Nb, Ta, Hf, Zr), a neutron powder diffraction study. Materials Science and Engineering: B, 148(1-3), 69-72.

[127] Yu, X. X., Weinberger, C. R., & Thompson, G. B. (2016). Ab initio investigations of the phase stability in group IVB and VB transition metal carbides. Computational Materials Science, 112, 318-326.

[128] Frantsvich, I. N., Zhurakovskii, E. A., & Lyashchenko, A. B. (1967). Elastic constants and characteristics of the electron structure of certain classes of refractory compounds obtained by the metal-powder method. Inorg. Mater., 3, 6-12.

[129] Oyama, S. T. (1996). Introduction to the chemistry of transition metal carbides and nitrides. In The chemistry of transition metal carbides and nitrides (pp. 1-27). Springer, Dordrecht.

[130] Ettmayer, P. and Lengauer, W. (1994) Carbides, Encyclopedia of Inorganic Chemistry. Wiley, New York.

[131] Chen, H. C., Begg, L., & Bohedba, B. (2007). U.S. Patent Application No. 11/421,693.

[132] Ma, B., Zhang, X., Han, J., & Han, W. (2009). Fabrication of hot-pressed ZrC-based composites. Proceedings of the Institution of Mechanical Engineers, Part G: Journal of Aerospace Engineering, 223(8), 1153-1157.

[133] Shimada, S. (2002). A thermoanalytical study on the oxidation of ZrC and HfC powders with formation of carbon. Solid state ionics, 149(3-4), 319-326.

[134] Wang, Z., Wu, Z., & Shi, G. (2011). The oxidation behaviors of a ZrB_2–SiC–ZrC ceramic. Solid State Sciences, 13(3), 534-538.

[135] Li, Z., Li, H., Li, W., Wang, J., Zhang, S., & Guo, J. (2011). Preparation and ablation properties of ZrC–SiC coating for carbon/carbon composites by solid phase infiltration. Applied Surface Science, 258(1), 565-571.

[136] Ye, J., Zhang, S., & Lee, W. E. (2013). Molten salt synthesis and characterization of SiC coated carbon black particles for refractory castable applications. Journal of the European Ceramic Society, 33(10), 2023-2029.

[137] Ye, J. (2014) Preparation and Characterisation of Novel Carbon Materials for Refractory Castable Applications. PhD thesis, University of Sheffield.

[138] YU, J., UENO, S., & HIRAGUSHI, K. (1996). Improvement in flowability, oxidation resistance and water wettability of graphite powders by TiO_2 coating. Journal of the Ceramic Society of Japan, 104(1210), 481-485.

[139] Sunwoo, S., Kim, J. H., Lee, K. G., & Kim, H. (2000). Preparation of ZrO_2 coated graphite powders. Journal of materials science, 35(14), 3677-3680.

[140] Saberi, A., Golestani-Fard, F., Sarpoolaky, H., Willert-Porada, M., Gerdes, T., Simon, R., & Liebscher, C. (2009). Development of $MgAl_2O_4$ spinel coating on graphite surface to improve its water-wettability and oxidation resistance. Ceramics international, 35(1), 457-461.

[141] W. C. ROBERTS-AUSTEN, C. B., F. R.S. (1895). The reduction of the rarer metals from their oxides. Scientific American Supplement, 1018(7), 16269-16270

[142] Iitaka, I., & Aoki, Y. (1932). Quantitative Separation of WC from W_2C and

212

Tungsten, and the Conditions of Formation of the Two Carbides. Bulletin of the Chemical Society of Japan, 7(4), 108-114.

[143] Yamada, S., Yamamoto, Y., Ichida, A., & Nagasaka, T. (1993). Metallurgy of Tungsten at Tokyo Tungsten Co., Ltd. JOURNAL-MINING AND MATERIALS PROCESSING INSTITUTE OF JAPAN, 109, 247-247.

[144] Koc, R., & Kodambaka, S. K. (1999). New process for producing submicron tungsten monocarbide powders. Journal of materials science letters, 18(18), 1469-1471.

[145] Nino, A., Takahashi, K., Sugiyama, S., & Taimatsu, H. (2012). Effects of carbon addition on microstructures and mechanical properties of binderless tungsten carbide. Materials Transactions, 53(8), 1475-1480.

[146] Zhao, J., Holland, T., Unuvar, C., & Munir, Z. A. (2009). Sparking plasma sintering of nanometric tungsten carbide. International Journal of Refractory Metals and Hard Materials, 27(1), 130-139.

[147] Kozyrev, N. A., Galevsky, G. V., Valuev, D. V., Shurupov, V. M., & Kozyreva, O. E. (2015). Surfacing With Tungsten-containing Ores. In IOP Conference Series: Materials Science and Engineering (Vol. 91, No. 1, p. 012009). IOP Publishing.

[148] Oro, R., Hryha, E., Gilardi, R., Alzati, L., & Nyborg, L. (2017). Optimizing the synthesis of ultrafine tungsten carbide powders by effective combinations of carbon sources and atmospheres. International Journal of Refractory Metals and Hard Materials, 63, 9-16.

[149] Löfberg, A., Frennet, A., Leclercq, G., Leclercq, L., & Giraudon, J. M. (2000). Mechanism of WO_3 reduction and carburization in CH_4/H_2 mixtures leading to bulk

tungsten carbide powder catalysts. Journal of catalysis, 189(1), 170-183.

[150] Yan, Q., Lu, Y., To, F., Li, Y., & Yu, F. (2015). Synthesis of tungsten carbide nanoparticles in biochar matrix as a catalyst for dry reforming of methane to syngas. Catalysis Science & Technology, 5(6), 3270-3280.

[151] Liang, C., Tian, F., Wei, Z., Xin, Q., & Li, C. (2003). The synthesis of nanostructured W_2C on ultrahigh surface area carbon materials *via* carbothermal hydrogen reduction. Nanotechnology, 14(9), 955.

[152] Sim, A. G. (2010). Reduction-Oxidation Cycling of Metal Oxides For Hydrogen Production. PhD thesis, The University of New South Wales Australia.

[153] Tan, G. L., & Wu, X. J. (1998). Mechanochemical synthesis of nanocrystalline tungsten carbide powders. Powder metallurgy, 41(4), 300-302.

[154] Kirakosyan, K. G., Manukyan, K. V., Kharatyan, S. L., & Mnatsakanyan, R. A. (2008). Synthesis of tungsten carbide–carbon nanomaterials by combustion reaction. Materials Chemistry and Physics, 110(2-3), 454-456.

[155] Borovinskaya, I. P., Ignat'eva, T. I., Vershinnikov, V. I., & Sachkova, N. V. (2004). Preparation of tungsten carbide nanopowders by self-propagating high-temperature synthesis. Inorganic materials, 40(10), 1043-1048.

[156] Won, H. I., Nersisyan, H. H., & Won, C. W. (2008). Combustion synthesis of ultrafine tungsten carbide powder. Journal of Materials Research, 23(9), 2393-2397.

[157] Fang, Z. Z., Wang, X., Ryu, T., Hwang, K. S., & Sohn, H. Y. (2009). Synthesis, sintering, and mechanical properties of nanocrystalline cemented tungsten carbide–a review. International Journal of Refractory Metals and Hard Materials, 27(2), 288-299.

[158] Hojo, J., Oku, T., & Kato, A. (1978). Tungsten carbide powders produced by the vapor phase reaction of the WCl_6-CH_4-H_2 system. Journal of the Less Common Metals, 59(1), 85-95.

[159] Fitzsimmons, M., & Sarin, V. K. (1995). Comparison of WCl_6-CH_4-H_2 and WF_6-CH_4-H_2 systems for growth of WC coatings. Surface and Coatings Technology, 76, 250-255.

[160] Giordano, C., Erpen, C., Yao, W., & Antonietti, M. (2008). Synthesis of Mo and W carbide and nitride nanoparticles *via* a simple "urea glass" route. Nano letters, 8(12), 4659-4663.

[161] Kim, J. C., & Kim, B. K. (2004). Synthesis of nanosized tungsten carbide powder by the chemical vapor condensation process. Scripta Materialia, 50(7), 969-972.

[162] Tang, X., Haubner, R., Lux, B., & Kieffer, B. (1995). Preparation of ultrafine CVD WC powders deposited from WCl_6 gas mixtures. Le Journal de Physique IV, 5(C5), C5-1013.

[163] Won, C. W., Chun, B. S., & Sohn, H. Y. (1993). Preparation of ultrafine tungsten carbide powder by CVD method from WCl_6-C_2H_2-H_2 mixtures. Journal of materials research, 8(10), 2702-2708.

[164] Leclercq, G., Kamal, M., Giraudon, J. M., Devassine, P., Feigenbaum, L., Leclercq, L., Frennet, A., Bastin, J. M., Löfberg, A., Decker, S., & Dufour, M. (1996). Study of the Preparation of Bulk Powder Tungsten Carbides by Temperature Programmed Reaction with CH_4+H_2 Mixtures. Journal of catalysis, 158(1), 142-169.

[165] Medeiros, F. F. P., De Oliveira, S. A., De Souza, C. P., Da Silva, A. G. P., Gomes,

215

U. U., & De Souza, J. F. (2001). Synthesis of tungsten carbide through gas–solid reaction at low temperatures. Materials Science and Engineering: A, 315(1-2), 58-62.

[166] Ma, J., & Du, Y. (2008). Synthesis of nanocrystalline hexagonal tungsten carbide *via* co-reduction of tungsten hexachloride and sodium carbonate with metallic magnesium. Journal of Alloys and Compounds, 448(1-2), 215-218.

[167] Yih, S. W. H., Wang, C. T. (1981). Tungsten sources, metallurgy and applications. Plenum Press, New York.

[168] Toth, L. (Ed.). (2014). Transition metal carbides and nitrides. Elsevier.

[169] Lee, S. H., Lee, J. S., Tanaka, H., & Choi, S. C. (2009). Al_3BC_3 powder: processing and synthetic mechanism. Journal of the American Ceramic Society, 92(12), 2831-2837.

[170] Kanatzidis, M. G., Pöttgen, R., & Jeitschko, W. (2005). The metal flux: a preparative tool for the exploration of intermetallic compounds. Angewandte Chemie International Edition, 44(43), 6996-7023.

[171] Zhang, S., & Lee, W. E. (2003). Improving the water-wettability and oxidation resistance of graphite using Al_2O_3/SiO_2 sol-gel coatings. Journal of the European Ceramic Society, 23(8), 1215-1221.

[172] Kawabata, K., Yoshimatsu, H., Fujii, E., Hiragushi, K., Osaka, A., & Miura, Y. (2001). Fluidity of a slurry of the graphite powder coated with Al_2O_3-based metal oxides. Journal of materials science letters, 20(9), 851-853.

[173] Mukhopadhyay, S., & Dutta, S. (2012). Comparison of solid state and sol–gel derived calcium aluminate coated graphite and characterization of prepared refractory composite. Ceramics International, 38(6), 4997-5006.4

216

[174] Mukhopadhyay, S., Das, G., & Biswas, I. (2012). Nanostructured cementitious sol gel coating on graphite for application in monolithic refractory composites. Ceramics international, 38(2), 1717-1724.

[175] Mukhopadhyay, S., Ansar, S. A., Paul, D., Bhowmick, G., & Sengupta, S. (2012). Characteristics of refractory castables containing mullite and spinel coated graphites. Materials and Manufacturing Processes, 27(2), 177-184.

[176] Saberi, A., Golestani-Fard, F., Sarpoolaky, H., Willert-Porada, M., Gerdes, T., Simon, R., & Liebscher, C. (2009). Development of $MgAl_2O_4$ spinel coating on graphite surface to improve its water-wettability and oxidation resistance. Ceramics international, 35(1), 457-461.

[177] Liu, X., & Zhang, S. (2008). Low‐temperature preparation of titanium carbide coatings on graphite flakes from molten salts. Journal of the American Ceramic Society, 91(2), 667-670.

[178] Li, X., Dong, Z., Westwood, A., Brown, A., Zhang, S., Brydson, R., Li, N., & Rand, B. (2008). Preparation of a titanium carbide coating on carbon fibre using a molten salt method. Carbon, 46(2), 305-309.

[179] Masoudifar, S., Bavand-Vandchali, M., Golestani-Fard, F., & Nemati, A. (2016). Molten salt synthesis of a SiC coating on graphite flakes for application in refractory castables. Ceramics International, 42(10), 11951-11957.

[180] Dong, Z. J., Li, X. K., Yuan, G. M., Cong, Y., Li, N., Hu, Z. J., Jiang, Z. Y., & Westwood, A. (2008). Fabrication of protective tantalum carbide coatings on carbon fibers using a molten salt method. Applied Surface Science, 254(18), 5936-5940.

217

[181] Gaune-Escard, M., & Seddon, K. R. (Eds.). (2012). Molten salts and ionic liquids: never the twain?. John Wiley & Sons.

[182] Kimura, T. (2011). Molten salt synthesis of ceramic powders. In Advances in Ceramics-Synthesis and Characterization, Processing and Specific Applications. InTech.

[183] Lu, J. Q., Wang, X. F., Wu, Y. T., & Xu, Y. Q. (2012). Synthesis of Bi_2SiO_5 powder by molten salt method. Materials Letters, 74, 200-202.

[184] Li, Z., Zhang, S., & Lee, W. E. (2007). Molten salt synthesis of zinc aluminate powder. Journal of the European Ceramic Society, 27(12), 3407-3412.

[185] Hull, A. W. (1919). A new method of chemical analysis. Journal of the American Chemical Society, 41(8), 1168-1175.

[186] https://en.wikipedia.org/wiki/Bragg%27s_law

[187] Waseda, Y., Matsubara, E., & Shinoda, K. (2011). X-ray diffraction crystallography: introduction, examples and solved problems. Springer Science & Business Media.

[188] Epp, J. (2016). X-ray diffraction (XRD) techniques for materials characterization. In Materials characterization using Nondestructive Evaluation (NDE) methods (pp. 81-124). Woodhead Publishing.

[189] http://cfamm.ucr.edu/documents/sem-intro.pdf

[190] https://en.wikipedia.org/wiki/Scanning_electron_microscope

[191] Goldstein, G. I.; Newbury, D. E.; Echlin, P.; Joy, D. C.; Fiori, C.; Lifshin, E. (1981). Scanning electron microscopy and x-ray microanalysis. New York: Plenum Press. ISBN 0-306-40768-X.

[192] Colliex, C. (2014). Seeing and measuring with electrons: Transmission electron microscopy today and tomorrow–An introduction. Comptes Rendus Physique, 15(2-3), 101-109.

[193] https://en.wikipedia.org/wiki/Transmission_electron_microscopy

[194] Kamarulzaman, N., & Jaafar, M. H. (2012). Synthesis and Stoichiometric Analysis of a Li-Ion Battery Cathode Material. In Stoichiometry and Materials Science-When Numbers Matter. InTech.

[195] https://slideplayer.com/slide/4935271/16/images/2/Electron+Diffraction+Geome try+for.+e-diffraction.+%EF%81%B1+e-+Bragg%E2%80%99s+Law%3A+l+%3D+2dsin%EF%81%B1+l%3D0.037%C3%85+%28at+100kV%29.jpg

[196] https://en.wikipedia.org/wiki/X-ray_photoelectron_spectroscopy

[197] Ren, D., Deng, Q., Wang, J., Li, Y., Li, M., Ran, S., ... & Huang, Q. (2017). Densification and mechanical properties of pulsed electric current sintered B4C with in situ synthesized Al₃BC obtained by the molten-salt method. Journal of the European Ceramic Society, 37(15), 4524-4531.

[198] Viala, J. C., Bouix, J., Gonzalez, G., & Esnouf, C. (1997). Chemical reactivity of aluminium with boron carbide. Journal of Materials Science, 32(17), 4559-4573.

[199] Yoshida, K., & Dewing, E. W. (1972). The apparent solubility of aluminum in cryolite melts. Metallurgical Transactions, 3(7), 1817-1821.

[200] Haarberg, G. M., Armoo, J. P., Gudbrandsen, H., Skybakmoen, E., Solheim, A., & Jentoftsen, T. E. (2011). Current efficiency for aluminium deposition from molten

cryolite-alumina electrolytes in a laboratory cell. In Light Metals 2011 (pp. 461-463). Springer, Cham.

[201] Yoshida, K., & Dewing, E. W. (2016). The Solubility of Aluminum in Cryolite Melts. In Essential Readings in Light Metals (pp. 12-18). Springer, Cham.

[202] Bao, K., Wen, Y., Khangkhamano, M., & Zhang, S. (2017). Low‐temperature preparation of titanium diboride fine powder *via* magnesiothermic reduction in molten salt. Journal of the American Ceramic Society, 100(5), 2266-2272.

[203] Zhang, S., Khangkhamano, M., Zhang, H., & Yeprem, H. A. (2014). Novel Synthesis of ZrB_2 Powder *Via* Molten‐Salt‐Mediated Magnesiothermic Reduction. Journal of the American Ceramic Society, 97(6), 1686-1688.

[204] http://resource.npl.co.uk/mtdata/phdiagrams/almo.htm

[205] Saunders, N. (1997). The Al-Mo system (aluminum-molybdenum). Journal of phase equilibria, 18(4), 370.

[206] Zhu, Y., Murali, S., Cai, W., Li, X., Suk, J. W., Potts, J. R., & Ruoff, R. S. (2010). Graphene and graphene oxide: synthesis, properties, and applications. Advanced materials, 22(35), 3906-3924.

[207] Manzeli, S., Ovchinnikov, D., Pasquier, D., Yazyev, O. V., & Kis, A. (2017). 2D transition metal dichalcogenides. Nature Reviews Materials, 2(8), 17033.

[208] Xu, M., Liang, T., Shi, M., & Chen, H. (2013). Graphene-like two-dimensional materials. Chemical reviews, 113(5), 3766-3798.

[209] Kalantar-zadeh, K., Ou, J. Z., Daeneke, T., Mitchell, A., Sasaki, T., & Fuhrer, M. S. (2016). Two dimensional and layered transition metal oxides. Applied Materials

220

Today, 5, 73-89.

[210] Wasey, A. A., Chakrabarty, S., Das, G. P., & Majumder, C. (2013). h-BN monolayer on the Ni (111) surface: a potential catalyst for oxidation. ACS applied materials & interfaces, 5(21), 10404-10408.

[211] Kiss, J., Révész, K., Klivényi, G., & Solymosi, F. (2013). Preparation of a boron nitride single layer on a polycrystalline Rh surface. Applied Surface Science, 264, 838-844.

[212] Chen, K., & Bao, Z. (2012). Synthesis and characterization of carbide nanosheets by a template-confined reaction. Journal of Nanoparticle Research, 14(9), 1141.

[213] Wu, Z. P., Zhao, M., Hu, J. W., Zhang, W. B., Yin, Y. H., Hu, Y. Y., Li, Y. S., Yang, J. G., Xu, Q. F., & Krishamurthy, A. (2014). Preparation of tungsten carbide nanosheets with large surface area using an in situ DWCNT template. RSC Advances, 4(88), 47414-47420.

[214] Ye, J., Zhang, S., & Lee, W. E. (2013). Molten salt synthesis and characterization of SiC coated carbon black particles for refractory castable applications. Journal of the European Ceramic Society, 33(10), 2023-2029.

[215] Ye, J., Zhang, S., & Lee, W. E. (2012). Novel low temperature synthesis and characterisation of hollow silicon carbide spheres. Microporous and Mesoporous Materials, 152, 25-30.

[216] Xie, W., Möbus, G., & Zhang, S. (2011). Molten salt synthesis of silicon carbide nanorods using carbon nanotubes as templates. Journal of Materials Chemistry, 21(45), 18325-18330.

221

[217] Ding, J., Deng, C., Yuan, W., Zhu, H., & Zhang, X. (2014). Novel synthesis and characterization of silicon carbide nanowires on graphite flakes. Ceramics International, 40(3), 4001-4007.

[218] Khangkhamano, M. Novel Molten Salt Synthesis of ZrB2 and ZrC powders and Molten Salt Synthesis of Novel TiC. PhD thesis, University of Exeter.

[219] Dresselhaus, M. S., & Thomas, I. L. (2001). Alternative energy technologies. Nature, 414(6861), 332.

[220] Turner, J. A. (2004). Sustainable hydrogen production. Science, 305(5686), 972-974.

[221] Cui, W., Liu, Q., Xing, Z., Asiri, A. M., Alamry, K. A., & Sun, X. (2015). MoP nanosheets supported on biomass-derived carbon flake: One-step facile preparation and application as a novel high-active electrocatalyst toward hydrogen evolution reaction. Applied Catalysis B: Environmental, 164, 144-150.

[222] Lin, L., Miao, N., Huang, J., Zhang, S., Zhu, Y., Horsell, D. D., Ghosez, P., Sun, Z., & Allwood, D. A. (2017). A photocatalyst of sulphur depleted monolayered molybdenum sulfide nanocrystals for dye degradation and hydrogen evolution reaction. Nano Energy, 38, 544-552.

[223] Wu, Z., Fang, B., Bonakdarpour, A., Sun, A., Wilkinson, D. P., & Wang, D. (2012). WS2 nanosheets as a highly efficient electrocatalyst for hydrogen evolution reaction. Applied Catalysis B: Environmental, 125, 59-66.

[224] Ye, G., Gong, Y., Lin, J., Li, B., He, Y., Pantelides, S. T., Zhou, W., Vajtai, R., & Ajayan, P. M. (2016). Defects engineered monolayer MoS_2 for improved hydrogen

222

evolution reaction. Nano letters, 16(2), 1097-1103.

[225] Winter, C. J. (2005). Into the hydrogen energy economy—milestones. International Journal of Hydrogen Energy, 30(7), 681-685.

[226] Najafpour, M. M., & Allakhverdiev, S. I. (2012). Manganese compounds as water oxidizing catalysts for hydrogen production *via* water splitting: from manganese complexes to nano-sized manganese oxides. International journal of hydrogen energy, 37(10), 8753-8764.

[227] Allakhverdiev, S. I., Thavasi, V., Kreslavski, V. D., Zharmukhamedov, S. K., Klimov, V. V., Ramakrishna, S., Los, D. A., Mimuro, M., Nishihara, R., & Carpentier, R. (2010). Photosynthetic hydrogen production. Journal of Photochemistry and Photobiology C: Photochemistry Reviews, 11(2-3), 101-113.

[228] Allakhverdiev, S. I. (2012). Photosynthetic and biomimetic hydrogen production, Int J Hydrogen Energ, 37, 8744-52.

[229] Nørskov, J. K., Bligaard, T., Logadottir, A., Kitchin, J. R., Chen, J. G., Pandelov, S., & Stimming, U. (2005). Trends in the exchange current for hydrogen evolution. Journal of the Electrochemical Society, 152(3), J23-J26.

[230] Lin, L., Miao, N., Wen, Y., Zhang, S., Ghosez, P., Sun, Z., & Allwood, D. A. (2016). Sulfur-depleted monolayered molybdenum disulfide nanocrystals for superelectrochemical hydrogen evolution reaction. ACS nano, 10(9), 8929-8937.

[231] Wen, Y., Xia, Y., & Zhang, S. (2016). Tungsten disulphide nanorattle: a new type of high performance electrocatalyst for hydrogen evolution reaction. Journal of Power Sources, 307, 593-598.

223

[232] Voiry, D., Salehi, M., Silva, R., Fujita, T., Chen, M., Asefa, T., Shenoy, V. B., Eda, G., & Chhowalla, M. (2013). Conducting MoS_2 nanosheets as catalysts for hydrogen evolution reaction. Nano letters, 13(12), 6222-6227.

[233] Baranton, S., & Coutanceau, C. (2013). Nickel cobalt hydroxide nanoflakes as catalysts for the hydrogen evolution reaction. Applied Catalysis B: Environmental, 136, 1-8.

[234] Huang, Z., Chen, Z., Chen, Z., Lv, C., Humphrey, M. G., & Zhang, C. (2014). Cobalt phosphide nanorods as an efficient electrocatalyst for the hydrogen evolution reaction. Nano Energy, 9, 373-382.

[235] Zhao, L., Hong, C., Lin, L., Wu, H., Su, Y., Zhang, X., & Liu, A. (2017). Controllable nanoscale engineering of vertically aligned MoS_2 ultrathin nanosheets by nitrogen doping of 3D graphene hydrogel for improved electrocatalytic hydrogen evolution. Carbon, 116, 223-231.

[236] Kibsgaard, J., Chen, Z., Reinecke, B. N., & Jaramillo, T. F. (2012). Engineering the surface structure of MoS_2 to preferentially expose active edge sites for electrocatalysis. Nature materials, 11(11), 963-969.

[237] Lin, S., Liu, Y., Hu, Z., Lu, W., Mak, C. H., Zeng, L., Zhao, J., Li, Y., Yan, F., Tsang, Y. H., Zhang, X., Zhang, X., & Lau, S. P. (2017). Tunable active edge sites in $PtSe_2$ films towards hydrogen evolution reaction. Nano Energy, 42, 26-33.

[238] Levy, R. B., & Boudart, M. (1973). Platinum-like behavior of tungsten carbide in surface catalysis. science, 181(4099), 547-549.

[239] Bennett, L. H., Cuthill, J. R., McAlister, A. J., Erickson, N. E., & Watson, R. E.

224

(1974). Electronic structure and catalytic behavior of tungsten carbide. Science, 184(4136), 563-565.

[240] Zeng, M., Chen, Y., Li, J., Xue, H., Mendes, R. G., Liu, J., Zhang, T., Rümmeli, M. H. & Fu, L. (2017). 2D WC single crystal embedded in graphene for enhancing hydrogen evolution reaction. Nano Energy, 33, 356-362.

[241] Wan, C., Regmi, Y. N., & Leonard, B. M. (2014). Multiple phases of molybdenum carbide as electrocatalysts for the hydrogen evolution reaction. Angewandte Chemie, 126(25), 6525-6528.

[242] Jing, S., Zhang, L., Luo, L., Lu, J., Yin, S., Shen, P. K., & Tsiakaras, P. (2018). N-doped porous molybdenum carbide nanobelts as efficient catalysts for hydrogen evolution reaction. Applied Catalysis B: Environmental, 224, 533-540.

[243] Harnisch, F., Sievers, G., & Schröder, U. (2009). Tungsten carbide as electrocatalyst for the hydrogen evolution reaction in pH neutral electrolyte solutions. Applied Catalysis B: Environmental, 89(3-4), 455-458.

[244] Vrubel, H., & Hu, X. (2012). Molybdenum Boride and Carbide Catalyze Hydrogen Evolution in both Acidic and Basic Solutions. Angew. Chem. Int. Ed., 51: 12703-12706.

[245] Chen, W. F., Wang, C. H., Sasaki, K., Marinkovic, N., Xu, W., Muckerman, J. T., Zhu, Y., & Adzic, R. R. (2013). Highly active and durable nanostructured molybdenum carbide electrocatalysts for hydrogen production. Energy & Environmental Science, 6(3), 943-951.

[246] He, C., & Tao, J. (2015). Synthesis of nanostructured clean surface molybdenum

225

carbides on graphene sheets as efficient and stable hydrogen evolution reaction catalysts. Chemical Communications, 51(39), 8323-8325.

[247] Liao, L., Wang, S., Xiao, J., Bian, X., Zhang, Y., Scanlon, M. D., Hu, X., Tang, Y., Liu, B., & Girault, H. H. (2014). A nanoporous molybdenum carbide nanowire as an electrocatalyst for hydrogen evolution reaction. Energy & Environmental Science, 7(1), 387-392.

[248] Fan, M., Chen, H., Wu, Y., Feng, L., Liu, Y., Li, G., & Zou, X. (2015). Growth of molybdenum carbide micro-islands on carbon cloth toward binder-free cathodes for efficient hydrogen evolution reaction. J Mater Chem A, 3, 16320-16326.

[249] Liu, Y., Yu, G., Li, G. D., Sun, Y., Asefa, T., Chen, W., & Zou, X. (2015). Coupling Mo_2C with Nitrogen‐Rich Nanocarbon Leads to Efficient Hydrogen‐Evolution Electrocatalytic Sites. Angewandte Chemie, 127(37), 10902-10907.

[250] Lin, L., & Zhang, S. (2012). Creating high yield water soluble luminescent graphene quantum dots *via* exfoliating and disintegrating carbon nanotubes and graphite flakes. Chemical communications, 48(82), 10177-10179.

[251] Yumitori, S. (2000). Correlation of C1s chemical state intensities with the O1s intensity in the XPS analysis of anodically oxidized glass-like carbon samples. Journal of materials science, 35(1), 139-146.

[252] Lin, L., & Zhang, S. (2012). Effective solvothermal deoxidization of graphene oxide using solid sulphur as a reducing agent. Journal of Materials chemistry, 22(29), 14385-14393.

[253] Wagner CD, Riggs WM, Davis LE, Moulder JF, Muilenberg GE (Eds.), Handbook

226

of X-ray photoelectron specstroscopy, Perkin-Elmer Corporation, Physical Enectronics Division, Eden Prairie, Minnesota, 1979.

[254] Xiao, P., Ge, X., Wang, H., Liu, Z., Fisher, A., & Wang, X. (2015). Novel molybdenum carbide–tungsten carbide composite nanowires and their electrochemical activation for efficient and stable hydrogen evolution. Advanced Functional Materials, 25(10), 1520-1526.

[255] Zheng, T., Sang, W., He, Z., Wei, Q., Chen, B., Li, H., Cao, C., Huang, R., Yan, X., Pan, B., Zhou, S., & Zeng, J. (2017). Conductive Tungsten Oxide Nanosheets for Highly Efficient Hydrogen Evolution. Nano letters, 17(12), 7968-7973.

[256] Singla, G., Singh, K., & Pandey, O. P. (2013). Structural and thermal properties of *in-situ* reduced WO_3 to W powder. Powder technology, 237, 9-13.

[257] Zhang, S., Wen, Y., & Zhang, H. (2014). Low temperature preparation of tungsten nanoparticles from molten salt. Powder Technology, 253, 464-466.

[258] Mir, R. A., & Pandey, O. P. (2018). Influence of graphitic/amorphous coated carbon on HER activity of low temperature synthesized β-Mo_2C@C nanocomposites. Chemical Engineering Journal, 348, 1037-1048.

[259] Cui, W., Cheng, N., Liu, Q., Ge, C., Asiri, A. M., & Sun, X. (2014). Mo_2C nanoparticles decorated graphitic carbon sheets: biopolymer-derived solid-state synthesis and application as an efficient electrocatalyst for hydrogen generation. ACS Catalysis, 4(8), 2658-2661.

[260] Colton, R. J., Huang, J. T. J., & Rabalais, J. W. (1975). Electronic structure of tungsten carbide and its catalytic behavior. Chemical Physics Letters, 34(2), 337-339.

227

[261] Merki, D., Vrubel, H., Rovelli, L., Fierro, S., & Hu, X. (2012). Fe, Co, and Ni ions promote the catalytic activity of amorphous molybdenum sulfide films for hydrogen evolution. Chemical Science, 3(8), 2515-2525.

[262] Li, Z., Zhang, S., & Lee, W. E. (2007). Molten salt synthesis of $LaAlO_3$ powder at low temperatures. Journal of the European Ceramic Society, 27(10), 3201-3205.

[263] Xie, W., Möbus, G., & Zhang, S. (2011). Molten salt synthesis of silicon carbide nanorods using carbon nanotubes as templates. Journal of Materials Chemistry, 21(45), 18325-18330.

[264] http://resource.npl.co.uk/mtdata/phdiagrams/almo.htm

[265] Shi, O., Xu, L., Jiang, A., Xu, Q., Xiao, Y., Zhu, D., Grasso, S. & Hu, C. (2019). Synthesis and oxidation resistance of MoAlB single crystals. Ceramics International, 45(2), 2446-2450.

[266] Alameda, L. T., Holder, C. F., Fenton, J. L., & Schaak, R. E. (2017). Partial etching of Al from MoAlB single crystals to expose catalytically active basal planes for the hydrogen evolution reaction. Chemistry of Materials, 29(21), 8953-8957.

[267] Yang, R., Cui, L., Zheng, Y., & Cai, X. (2007). Molten salt synthesis of Mo_2C powder using a mechanically milled powder. Materials Letters, 61(26), 4815-4817.

[268] Bao, K., Massey, J., Huang, J., & Zhang, S. (2017). LOW-TEMPERATURE SYNTHESIS OF HAFNIUM DIBORIDE POWDER *VIA* MAGNESIOTHERMIC REDUCTION IN MOLTEN SALT. on Advanced Ceramics and Composites, 38(3), 119.

228

[269] Bao, K., Lin, L., Chang, H., & Zhang, S. (2017). Low-temperature synthesis of calcium hexaboride nanoparticles *via* magnesiothermic reduction in molten salt. Journal of the Ceramic Society of Japan, 125(12), 866-871.

[270] Bao, K. (2017). Low Temperature Synthesis of Boron-Based Materials in Molten Salts. PhD thesis, University of Exeter.

[271] Wang, H., Zhang, S., Li, Y., & Sun, D. (2008). Bias effect on microstructure and mechanical properties of magnetron sputtered nanocrystalline titanium carbide thin films. Thin Solid Films, 516(16), 5419-5423.

[272] Djafer, A. Z. A., Saoula, N., Madaoui, N., & Zerizer, A. (2014). Deposition and characterization of titanium carbide thin films by magnetron sputtering using Ti and TiC targets. Applied Surface Science, 312, 57-62.

[273] D'Alessio, L., Santagata, A., Teghil, R., Zaccagnino, M., Zaccardo, I., Marotta, V., Ferro, D. & De Maria, G. (2000). Zirconium carbide thin films deposited by pulsed laser ablation. Applied surface science, 168(1-4), 284-287.

[274] Meng, Q. N., Wen, M., Mao, F., Nedfors, N., Jansson, U., & Zheng, W. T. (2013). Deposition and characterization of reactive magnetron sputtered zirconium carbide films. Surface and Coatings Technology, 232, 876-883.

[275] Wang, X. H., Eguchi, K., Iwamoto, C., & Yoshida, T. (2002). High-rate deposition of nanostructured SiC films by thermal plasma PVD. Science and Technology of Advanced Materials, 3(4), 313.

[276] Zhou, M. J., Wong, S. F., Ong, C. W., & Li, Q. (2007). Microstructure and mechanical properties of B_4C films deposited by ion beam sputtering. Thin Solid Films, 516(2-4), 336-339.

[277] Zellner, M. B., & Chen, J. G. (2005). Surface science and electrochemical studies of WC and W_2C PVD films as potential electrocatalysts. Catalysis Today, 99(3-4), 299-307.

[278] Wang, C., Huang, N., Zhuang, H., Zhai, Z., Yang, B., Liu, L., & Jiang, X. (2016). Growth of large-scale heteroepitaxial 3C-SiC films and nanosheets on silicon substrates by microwave plasma enhanced CVD at higher powers. Surface and Coatings Technology, 299, 96-103.

[279] Xue, Z., Caulton, K. G., & Chisholm, M. H. (1991). Low-pressure chemical vapor deposition of tungsten carbide (WC) thin films. Chemistry of Materials, 3(3), 384-386.

[280] Oliveira, J. C., Oliveira, M. N., & Conde, O. B. A. U. T. D. L. (1996). Structural characterisation of B_4C films deposited by laser-assisted CVD. Surface and Coatings Technology, 80(1-2), 100-104.

[281] Lv, X., Song, J., Lai, Y., Fang, J., Li, J., & Zhang, Z. (2016). Ultrafine nanoparticles assembled Mo_2C nanoplates as promising anode materials for sodium ion batteries with excellent performance. Journal of Energy Storage, 8, 205-211.

[282] Ko, A. R., Lee, Y. W., Moon, J. S., Han, S. B., Cao, G., & Park, K. W. (2014). Ordered mesoporous tungsten carbide nanoplates as non-Pt catalysts for oxygen reduction reaction. Applied Catalysis A: General, 477, 102-108.

[283] Gao, J., Wu, S., Chen, J., Li, Y., & Li, G. (2016). Mesoporous tungsten carbide nanoslices with pure phase and superior electrocatalysis. Electrochimica Acta, 222, 728-734.

[284] Shanmugam, S., Jacob, D. S., & Gedanken, A. (2005). Solid state synthesis of tungsten carbide nanorods and nanoplatelets by a single-step pyrolysis. The Journal of Physical Chemistry B, 109(41), 19056-19059.

[285] Chen, Z., Qin, M., Chen, P., Jia, B., He, Q., & Qu, X. (2016). Tungsten carbide/carbon composite synthesized by combustion-carbothermal reduction method as electrocatalyst for hydrogen evolution reaction. International Journal of Hydrogen Energy, 41(30), 13005-13013.

[286] Chabi, S., Chang, H., Xia, Y., & Zhu, Y. (2016). From graphene to silicon carbide: ultrathin silicon carbide flakes. Nanotechnology, 27(7), 075602.

[287] Cao, Z., Qin, M., Zuo, C., Gu, Y., & Jia, B. (2017). Facile route for synthesis of mesoporous graphite encapsulated iron carbide/iron nanosheet composites and their electrocatalytic activity. Journal of colloid and interface science, 491, 55-63.

[288] Sun, L., Wang, B., & Wang, Y. (2018). A novel silicon carbide nanosheet for high‑performance humidity sensor. Advanced Materials Interfaces, 5(6), 1701300.

231

[289] Fuka, M., Dey, M., & Gupta, S. (2018). Novel Ternary Boride (MoAlB) Particulates as Solid Lubricant Additives in Ni-matrix Composites. In 2018 Joint Propulsion Conference (p. 4893).